PROCESS OF ESTIMATING THE MATERIAL PROPERTIES OF HUMAN HEEL PAD SUB-LAYERS USING INVERSE FINITE ELEMENT ANALYSIS AND SOME MODEL APPLICATIONS

NAFISEH AHANCHIAN

School of Health Sciences

University of Salford, Salford, UK

Submitted in Partial Fulfilment of the Requirements of the Degree of Doctor of Philosophy, December 2013

Table of Contents

List of Tables

List of Figures

List of Charts

Acknowledgements

I would like to express my sincere gratitude towards my supervisory team, Professor Christopher Nester, Professor David Howard and Dr Lei Ren, for their continuous support, advice and suggestions during my research and writing up.

Also, my kind regards go to Dr Daniel Parker who generously helped me in data collection from compression tests.

Finally, my thanks and appreciations go to my husband, son and parents who supported me kindly and patiently during the course of my study.

The fees and consumable items associated with this PhD thesis were funded by the University of Salford. The STRIDE device was developed by colleagues who were funded by commercial sponsorship from Scholl Footcare. The STRIDE device was used with their permission, however, no member of the sponsoring company were involved in the work in this thesis.

Abstract

The human heel pad is subject to repetitive loading and plays an important role in absorbing shocks which may cause injuries. The heel pad has a composite biological structure consisting of the fat pad and the skin. The fat pad tissue is organised into a superficial micro-chamber layer and a deep macro-chamber layer.

The heel pad sub-layers have different structures and properties. Hence, to understand the contribution of each layer to the heel problem, it is essential to develop a model with discrete structure. Currently, only plantar pressure measurements are used for diagnosis and treatment of the heel problems, whereas it has been shown that high internal tissue stress is an important factor. Because of complex geometry, discrete structure and nonlinear material behaviour of the heel pad, the external force applied to the heel may result in inhomogeneous internal stress condition. Therefore, the relationship between the plantar pressure and internal stress does not seem to be simple. Since there is no equipment to allow measurement of internal stress, a detailed multi-layered FE model of the heel pad can be used as a solution to predict the internal stress.

The main objective of this work was to obtain the hyperelastic and viscoelastic material properties of the subject-specific heel pad sub-layers *in-vivo*. For this purpose, a combined methodology of finite element modeling and experimentation was developed.

An anatomically detailed 3D FE model of the human heel area was developed using MR images of the right foot of a female subject. A combined ultrasound and indentation system was used to apply series of slow and rapid compression tests on the same foot. The force-strain responses of the heel pad and its sub-layers were used as input to the FE model to estimate properties of the heel pad sub-layers using inverse FEA.

The hyperelastic and viscoelastic FE models were then implemented to investigate the effects of experimental and geometrical factors on the heel pad responses. The model was also used to assess the robustness of the hyperelastic FE model when predicting the behaviour of other heels with different geometries. Finally, this model was used with Taguchi method to evaluate the effect of footwear design factors on the compressive stress in the heel pad tissue.

There were some key limitations in this study. For example, the properties of the heel pad sub-layers were estimated only for a specific heel pad. Also, whilst it is preferred to use

automatic segmentation and solid modeling to improve repeatability of some FE processes, some parts of the modeling process were performed manually.

1. Chapter One:

INTRODUCTION

The human heel pad plays an important role as a shock absorber reducing impact forces generated during gait and in weight bearing. It deforms under loading and distributes contact loads. The human heel pad is characterised by viscoelastic mechanical behaviour like many other biological soft tissues (1). Viscoelastic materials involving both elastic and viscous components exhibit an interesting time-dependent behaviour. Viscoelastic materials show hysteresis and energy dissipation under loading and unloading cycle.

The human heel pad has a composite biological structure with a honeycomb configuration consisting of the fat pad and the skin (2). The fat pad tissue, located between the skin and the calcaneal perichondrium, is organised into superficial micro-chamber layer and a deep macro-chamber layer (3, 4). Pathological changes, aging and overloading may affect the heel pad stiffness and its biomechanical behaviour and are potentially important factors in the development of heel pain or other foot problems.

An improved understanding of the biomechanical characteristics of each component of the heel pad can contribute to the understanding of the mechanical functionality of the foot. It may also assist research into the interaction between the foot and the surrounding surfaces, such as footwear. Detailed information about the mechanical behaviour of the heel pad constituents also contributes to the development of models simulating the biomechanical behaviour of the heel pad under compression. These models provide an opportunity to test the effects of external factors, such as choice of insole or footwear materials, on the stress experienced by heel tissues. This may reduce the need for slow and expensive experimental tests on real subjects and models could be one part of decision making process in insole and footwear design. Developing pathology (disease) or even person (patient) specific models will be critical to ensure that outcomes are relevant for clinical practice and that predicted product effects reflect real world product efficacy.

The study of the mechanical behaviour of the human heel pad can be achieved through combined experimental and numerical methods. Experimental approaches often employ ultrasound imaging to generate data about the mechanical responses and deformation of the heel pad. Different loading conditions are applied and deformations of the heel pad sub-layers are simultaneously tracked using ultrasound, generating force-deformation/strain data of the heel pad sub-layers. These data can be used as inputs for the development of numerical models.

Several studies have been conducted to obtain force-displacement/strain data required for modelling. With the use of Finite Element Analysis (FEA), researchers have developed numerical models and studied the mechanical behaviour of the heel pad under loading. In most cases hyperelastic material models were used to simulate nonlinear behaviour of the heel pad. However, this ignored the time-dependent behaviour of the heel pad (5-7). Besides, the heel pad was mostly modeled as a homogeneous single layer material which is in contrast to the inhomogeneous nature of the heel pad (5, 8, 9). In a few cases the heel pad was modeled as a composite structure with two layers, the skin and the fat pad. However, in these models the composite structure of the fat pad was ignored (7, 10, 11). In most studies the heel pad tissue was tested in an *in-vitro* state under controlled loading and boundary conditions (10, 12, 13). However, *in-vivo* and *in-vitro* mechanical examinations of the heel pad identify different properties (14, 15).

The main goal of this research was to first develop an anatomically detailed three-dimensional (3D) Finite Element (FE) model of the human heel area with a composite structure for the heel pad consisting of three layers of, ‘skin’, ‘micro-chamber’, and ‘macro-chamber’. The next goal was to perform a series of slow and rapid compression tests *in-vivo* on the same heel using a combined the ultrasound and compression system to obtain the force-strain responses of the heel pad and its sub-layers. The experimental data were then used as inputs to the

inverse FEA to estimate the hyperelastic and viscoelastic material properties of the macro-chamber, micro-chamber and skin layers using the FE model. The final purpose of this project was to show applications of the hyperelastic and viscoelastic FE models in investigation of effects of the footwear design factors on the heel stress and how experimental and heel geometrical factors affect tissue responses. The robustness of the hyperelastic FE model in prediction of the behaviour of other heels with different geometries was also assessed. This PhD thesis is divided into 5 main parts described below.

1. **Chapter Two: Literature Review**

The aim of this chapter was to critically appraise previous research into the material properties of the human heel pad and its sub-layers, with a specific focus on studies which have used numerical methods. The chapter starts with an introduction to the human heel pad followed by an investigation of the methods used to obtain mechanical properties of the human heel pad. Several numerical models developed to investigate the material properties of the heel pad or study the biomechanical behaviour of the heel pad under compression are appraised. Prior research that has used FE models of the heel to investigate footwear design issues was also reviewed. By summarising the literature at the end of this chapter, possible ways to improve numerical models and the accuracy of experimental data are outlined and specific aims and objectives for the remainder of the project established.

2. **Chapter Three and Four: Development of the FE Model of the Heel Region**

The aim of Chapter 3 was to generate an anatomically detailed 3D geometry of the human heel area incorporating macro-chamber, micro-chamber and skin layers based on MRI scan data of the right foot of a female subject. Chapter 4 details how the 3D geometry is converted to an FE model by meshing the solid geometries of the heel pad structures into discrete elements, assigning material properties to structures and applying load and boundary

conditions to the all geometries. The FE model of the heel region is used in the subsequent chapters to estimate the material properties of the heel pad sub-layers.

3. **Chapter Five: Experimental Acquisition of Force and Tissue Displacement Data**

The main objective of this chapter was to perform an *in-vivo* series of slow and rapid compression tests on the heel used to develop the FE model. This enabled the force-strain responses of the heel pad and its sub-layers at different loading conditions to be measured. The experimental data were used in the following chapter to determine the material properties of the heel pad sub-layers.

4. **Chapter Six: Inverse Finite Element Analysis**

In this chapter, the experimental data (obtained in Chapter 5) were used as inputs to inverse FEA to estimate the hyperelastic and viscoelastic material properties of the macro-chamber, micro-chamber and skin layers using the FE model (generated in Chapter 3 and 4). Data from MRI experiments was used to validate the hyperelastic FE model. Moreover, the experimental responses of the heel pad under different rapid loading conditions were used to validate the viscoelastic FE model.

5. **Chapter Seven: Model Applications**

This chapter shows applications of the hyperelastic and viscoelastic FE models. The FE models were used to investigate the effects of the experimental setup and heel geometrical conditions on the heel pad responses. Furthermore, the ability of the hyperelastic FE model to estimate the material properties of other heel pads sub-layers with different geometries was studied. Finally, the effects of footwear design factors on the heel pad compressive stress were evaluated using Taguchi method.

2. Chapter Two:

LITERATURE REVIEW

The aim of this literature review is to understand the current knowledge of human heel pad biomechanics and identify the gaps in knowledge that should be addressed to offer further innovations. In addition, to appraise various research approaches such that subsequent research can adopt the most suitable methodology and address technical failings of prior research. The literature review chapter is divided into five sections. This chapter starts with a brief introduction to the human heel pad from histological and biomechanical perspectives. Then, the methods used to obtain the material properties of the heel pad are explored. The major studies, which have used the FEA (Finite Element Analysis) method to determine the material properties of the human heel pad, are then critically appraised. By reviewing these studies, the limitations of the existing FE models are identified. Prior research using FE models of the heel in the foot and footwear research are then reviewed. The aim of this latter part of the review is to find out how an FE model can be employed to answer questions regarding foot and footwear research instead of using relatively slow to complete and expensive *in-vivo* experiments on human participants. In the last section, the aims and objectives of this PhD research project are defined, such that the subsequent work might address important issues and limitations highlighted in the literature review.

2.1 THE HUMAN HEEL PAD

Typically, the soft tissue consisting of the skin and the fat pad layer beneath the calcaneal bone is called the “heel pad” (Figure 2.1). The heel area actually consists of the heel pad, the origin of the plantar fascia, insertion of various plantar intrinsic muscles, and the calcaneal bone.

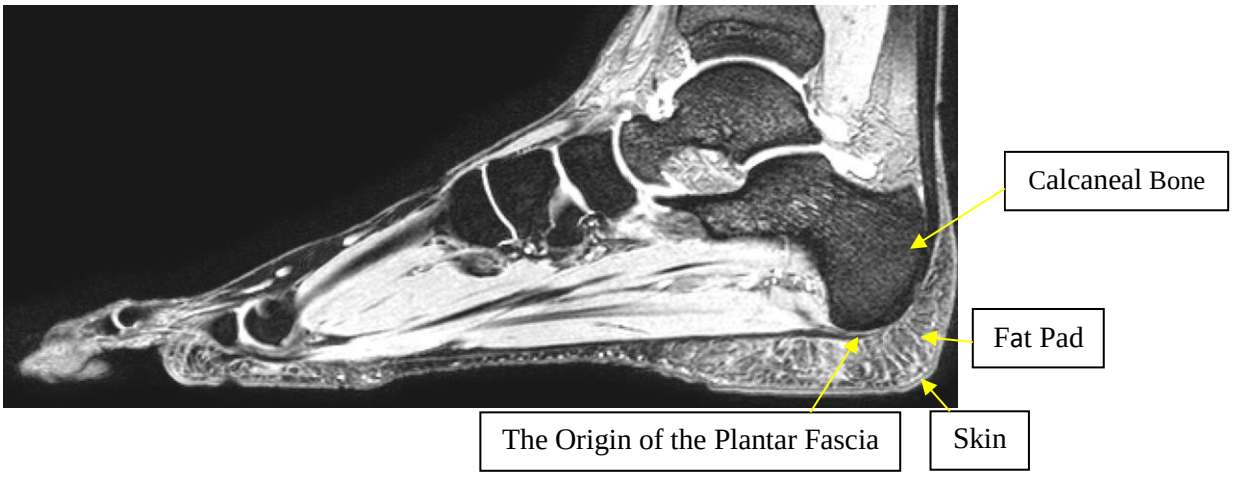

Figure 2.1: Sagittal view of the human heel area

2.1.1 The Structure

The human heel pad comprises the fat pad and the skin layers. The unloaded heel pad thickness varies between 12 to 19mm in healthy adults. Rome et al. reported the heel pad thickness of 12.5mm (SD 4.2) using *in-vivo* ultrasonic measurements on healthy volunteers (16). They measured heel pad thickness of 11 females and 4 males in the mid-section of the plantar surface of the calcaneum from the calcaneal tuberosity to the skin without compression of the soft tissue. Others have reported values of 14.3mm (SD 1.9) (17) and 16.6mm (SD 0.3) (18) for the heel pad thickness using the same technique. Levy et al. used MRI (Magnetic Resonance Imaging) to measure heel pad thickness on 5 healthy subjects. Mean pad thickness was 18.0mm (SD 4.6) (19). Steinback and Russle measured the heel pad thickness for 17.8mm (SD 2.0) using *in-vivo* radiography on normal subjects and patients with acromegaly (20). Greene also used the same technique on 8 subjects for the heel pad thickness measurement. He reported mean value of 19.0mm (SD 2.2) (21).

Using ultrasound for the heel pad thickness measurement has advantages over MRI and radiography (16). Ultrasound is a quick, non-invasive and reliable technique whereas MRI is expensive and its general availability is low. On the other hand, x-ray has its own difficulties

including accuracy issues, interpretation of the films and the health issues regarding ionizing radiation (16, 20).

- **The Fat Pad Layer**

The fat pad layer lying between the calcaneal bone and the skin has a unique honeycomb configuration. This structure consists of fibrous septa around fat cells, which is organised into chambers (Figure 2.2). The fibrous septa are arranged in U-shaped or comma-shaped columns. They are arranged in a vertical orientation in the central portions of the heel pad and in a transverse orientation in the lateral and posterior regions (22, 23). The size of the fat columns varies in different areas of the pad depending on the local loading conditions (3). For example, the largest fat columns have been found where greatest loadings are experienced by the heel pad (3).

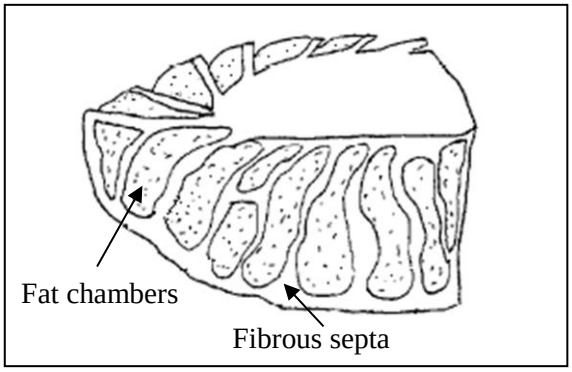

Figure 2.2: Structure of the heel pad. Derived from (22).

The fat pad layer is anatomically divided into two layers, the superficial **micro-chamber** layer with small chambers of fat, and the deep **macro-chamber** layer with larger fat filled chambers (Figure 2.3) (3, 23, 24). Hsu et al. used ultrasound to measure the unloaded and loaded thickness of the separate micro-chamber and macro-chamber layers of the heel pad of six healthy volunteers aged around 25 years old. They concluded that the unloaded thickness of the micro-chamber layer is approximately 30% of the unloaded macro-chamber layer thickness (4).

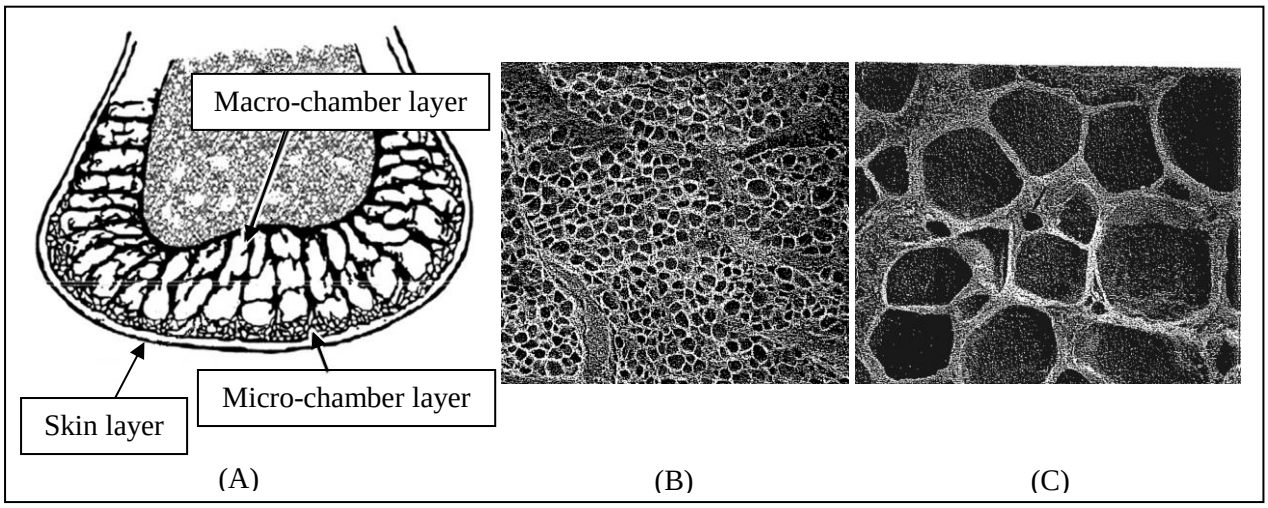

Figure 2.3: The structure of the macro-chamber and micro-chamber layers: (A) Schematic representation of the heel pad from coronal view; (B) Microscopic picture of micro-chamber layer; (C) Microscopic picture of macro-chamber layer (original magnification×100). Derived from (2, 3).

- **The Skin Layer**

The skin of the sole of the foot is thick and hairless. It is composed of an outer thinner epidermal layer and an inner thicker dermal layer (25). These two main layers are shown in Figure 2.4.

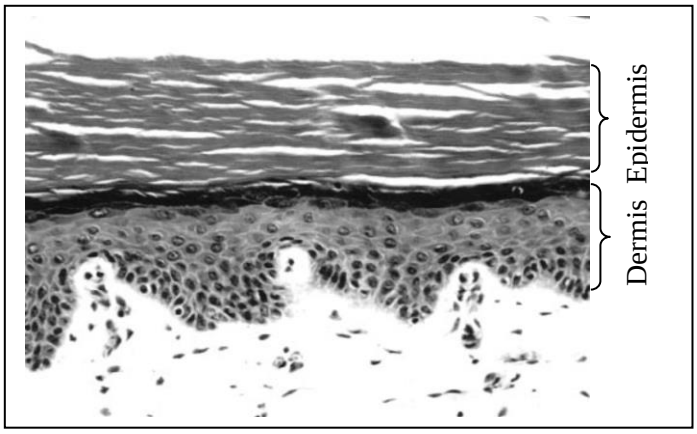

Figure 2.4: Histology of the skin of the sole of the foot (original magnification×40). Derived from (25).

The epidermis layer consists of densely packed keratinocytes and plays an important role as a barrier to physical wear and tear (26). The dermis consists of layers of collagen and elastic fibres, provides mechanical strength and elasticity (26). The thicknesses of these two layers

are different among people. The average thickness of the epidermal layer of the sole of the foot in healthy people is about 0.66 mm (27).

2.1.2 The Mechanical Properties

There is an increasing interest in studying the mechanical properties of the heel pad. Specific knowledge of heel pad mechanical properties contributes to our understanding of heel pad functionality and its role in reducing the impact forces associated with weight bearing and locomotion. The results of these researches are useful in diagnosis and treatment of foot pathologies and for footwear design.

Similar to the other biological tissues, the heel pad shows nonlinear elastic behaviour under loading. The heel pad deforms very easily and has low stiffness when initially loaded (22). Under high deformation, the collagen septa comes under tension and prevents a further change of the heel pad soft tissues, showing stiffer behaviour (22). It is accepted that the heel pad soft tissue exhibits viscoelastic behaviour under compression. The force-deformation/strain responses of these time-dependent materials depend on the velocity at which they are loaded (28). When they are suddenly deformed and deformation is kept constant, the related loads decrease with the time. This feature is called stress relaxation (28). If the viscoelastic materials are subjected to loading and then load is constant, these tissues continue to deform in time. This phenomenon is called creep (28). Moreover, under cyclic loading, the force-deformation/strain relationship in loading is different from that in unloading. This is called hysteresis (28). The area between loading and unloading curves represents the dissipated energy. These viscoelastic features are shown in Figure 2.5.

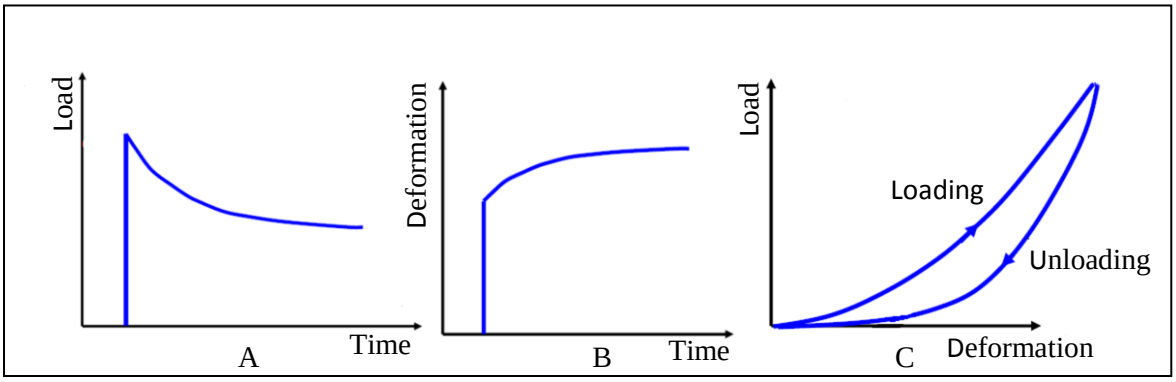

Figure 2.5: Viscoelastic features: (A) stress-relaxation; (B) creep; (C) Hysteresis.

The biomechanical properties of the heel pad vary from one person to another, and depend on whether measured *in-vivo* or *in-vitro* (14, 15). Aerts et al. showed that the *in-vivo* stiffness of the human heel pad is almost six times lower and the energy dissipation ratio is about three times higher than the *in-vitro* values (15). One possible explanation could be that the lower leg was being involved in the *in-vivo* heel pad testing and its presence had influence on the test measurements (15). It has been also shown that the geometry factors such as the heel pad thickness and the shape of the calcaneus can affect the heel pad behaviour (2, 10, 17). Although there are several studies about *in-vitro* investigation of the biomechanical behaviour of the heel pad, there are only a number of research studies about the biomechanical properties of live tissues (29-32).

When studying the mechanical properties of the heel pad, it is commonly assumed to be a homogeneous material and separate contributions of the heel pad sub-layers on the heel pad biomechanical response have not been widely reported (5, 9, 31, 32). Hsu et al. showed that biomechanical behaviours of the micro-chamber and macro-chamber layers are different under loading in 6 healthy persons aged about 25 years old (4). The thickness of the micro-chamber layer was reduced from ~3.5mm to ~3.3mm, almost 5.7% strain, under compressive loading with velocity of approximately 5mm/s up to maximum stress of 158kPa. By comparison, the macro-chamber layer changed from ~10mm to ~5.5mm, almost 45% strain, under the same loading conditions. This finding highlights the low stiffness and large

deformation behaviour of the macro-chamber layer compared to the micro-chamber layer. They concluded that the stiffness of the micro-chamber was circa 10 times greater than that of the macro-chamber layer for healthy young adults. The macro-chamber layer responds to loading with a larger contribution to tissue deformation, 96.1%, compared to the micro-chamber contribution of 3.9% (4).

In the other study on 16 healthy participants with average 55 years old, Hsu et al. showed that the stiffness of the micro-chamber layer is about 6 times of the macro-chamber layer. The 6.9% deformation contribution of the micro-chamber was very low compared to 93.1% for the macro-chamber layer (33). The difference between the mechanical properties of macro-chamber and micro-chamber layers creates contrasting functional roles. The macro-chamber layer, with lower stiffness and large deformation, is important in the heel pad resiliency (the ability of the heel pad to recover its shape after compression is removed). It is also responsible for the cushioning feature of the heel pad during gait. The micro-chamber layer, with higher stiffness, plays an important role as a constraint, preventing the macro-chamber layer from excessive deformation and maintaining critical amount of macro-chamber layer beneath the calcaneus (4). Sufficient knowledge about these layers might help better understanding the functionality of the heel pad.

Some studies have shown that age and pathological changes create changes in tissue biomechanics (34-36). Whilst there is no significant difference in unloaded thickness of the heel pad of healthy and people with diabetes, there is a good evidence that the heel pad tissue is stiffer in people with diabetes compared to those without diabetes (32, 33, 35). This might be a result of reduction in the size of the fat chambers and thickening of the fibrous septa separating the fat chambers (32, 37). Hsu et al. showed that the stiffness of the macro-chamber layer is increased in diabetic patients with Young's modulus of 239kPa compared to 181KPa for healthy adults (33). This may result in easily transferring stress from the

calcaneus to skin through the stiffened macro-chamber layer (33). On the other hand, the results of their findings indicated that the stiffness of the micro-chamber layer is decreased in people with diabetes with Young's modulus of 393kPa compared to 1140kPa for healthy subjects (33). This might be a cause of reduction in the ability of the micro-chamber in maintaining the macro-chamber tissue beneath the calcaneus and preventing the excessive deformation of the macro-chamber layer (33). The energy dissipation ratio of the heel pad is also significantly increased in people with diabetes, indicating that more energy is dissipated as heat during loading and unloading cycles (38, 39). The light microscopic examination of the diabetic heel pads revealed distorted and fragmented collagen fibres within septal walls and atrophic fat chambers (40). Higher stiffness and reduction of the shape recovery ability of the heel pad when the load is removed may contribute to the increased EDR in diabetic patients. These findings may be responsible for development of shock-induced discomfort and foot ulceration (38, 41).

In some studies, the mechanical behaviour of the human heel pad was compared between young and older adults. The results showed that the unloaded heel pad thickness and the energy dissipation ratio are increased in the aged group compared to the young group. Hsu et al. measured the heel pad thickness as 17.6mm (SD 0.2) for young and 20.1mm (SD 0.24) for older groups (36). Furthermore, they measured energy dissipation ratio of heel pad as 23.7% (SD 6.9) and 35.3% (SD 10) for young and older adults respectively (36). Their findings showed insignificantly higher stiffness of the heel pad in the older group. The average stiffness was 3.97kg/cm (SD 0.67) for older adults compared to 3.76kg/cm (SD 0.46) for young adults (36). These changes in the heel pad of older group may be explained by anatomical changes. According to the published literature, the increased fat in the heel pad leads to increased unloaded heel pad thickness and increased pressure in the sealed fibrous

chambers, which results in the loss of elasticity of the heel pad (42). Reduction in the functional capacity of the heel pad of the older group may result in discomfort and injuries.

In summary, the heel pad shows non-linear viscoelastic under loading. It has nonhomogeneous structure comprising of the macro-chamber, micro-chamber and skin layers that have different mechanical properties. Some studies showed that the age and disease affect the mechanical properties of the heel pad sub-layers and in overall the biomechanical behaviour of the heel pad.

2.1.3 The Function

The heel pad as the most distal part of the human locomotion system is subjective to repetitive loading associated with locomotion. Hence the heel pad plays an important role in shock absorption, shock reduction and protecting foot against local stress (22). The honeycomb structure of the heel pad is designed to withstand strain and pressure. The heel pad absorbs shocks occurring at the heel strike by dissipating mechanical energy as heat when foot hits the ground and thereby protects foot against possible injuries (22). The level of hysteresis prevents bounce and allows grip.

The shock reduction is achieved by the heel pad deforming under loading. Deformation of the soft tissue distributes effects of applied forces over larger areas of skin and attenuates peak forces (43). Under compression, the volume of fat-filled chambers must remain constant. Therefore, under any external compression the chambers expand in lateral and anterodorsal directions dissipating applied forces (Figure 2.6). The heel pad deforms easily under low loadings and then becomes gradually stiffer when fibrous septa stiffen and absorb energy, as the fibres are compressed and straightened under increased loadings. The chambered structure of the heel pad protects the heel bone by spreading the load over the whole plantar surface of the bone and potential its sides too (22).

The macro-chamber layer with lower stiffness is responsible for the cushioning feature of the heel pad during gait and it is important in the heel pad resiliency. The protection of the structure of the heel pad from severe bulging and excessive deformation is guaranteed by the micro-chamber layer with higher stiffness as a heel constrain (4).

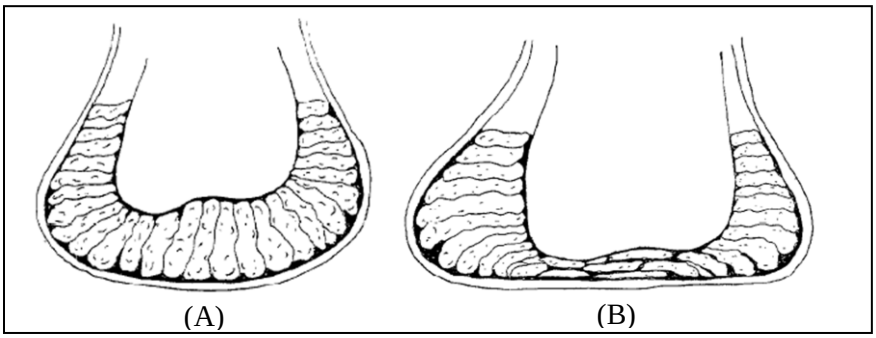

Figure 2.6: Changes of the heel pad under compression: (A) Unloaded; (B) Loaded. Derived from (22).

2.1.4 Mechanism of Injuries

High internal stress and strain are believed to be causes of heel pad problems and increase the risk of soft tissue injury (45-47). The exact nature of how the forces applied to the soft tissue are distributed depends on the material properties and geometry of the soft tissue and the external soft tissue supports (45). While stiffer tissues create areas with high stress, softer tissues tend to have large deformations (high strain). The results of analytical and clinical studies have shown that stress and strain are high in deep tissues before high stress and strain are seen in superficial tissues. Studies suggested that the applied force increases the stress and damage initially in deep tissue and close to bony interface and prominences and then in superficial tissues near the skin surface (45, 46, 48, 49).

Heel pain is a very common foot problem. The loss of elasticity in the heel pad, which results in increase of internal tissue stress, might be one possible cause of plantar heel pain (32, 44). The loss of elasticity might be either because of fat loss compared to fibrous septa or fragmented collagen fibres with uneven distribution within septal walls of the heel pad (32).

The relative percentage of each component (fat globules and fibrous septa) are different in macro-chamber and micro-chamber layers (38).

Heel ulcers are one of the most serious lower extremity ulcers which are painful and expensive to treat and can severely limit mobility. The change of the elasticity of the heel pad could be one of the possible explanations for heel ulcers (32, 41). Heel ulcers can clinically appear as an open wound or tissue damage under intact skin, which is a deep tissue injury (DTI). High stress in soft tissue layer adjacent to bony prominence is believed to be the cause of DTI. It has been suggested that the tissue wound forms first in deep soft tissues and then progresses to the skin surface (46). In this situation, it remains undiagnosed until breakdown of the skin occurs. If it is detected at early stage, injured tissues may be saved using different strategies such as unloading to reduce tissue stress.

The internal cause of heel pain and progression of heel ulcers from sub-dermal tissues to the skin indicates how important it is to estimate the internal stress and strain in plantar soft tissues. The heel pad is composed of three sub-layers (macro-chamber, micro-chamber and skin) with different structures, compositions and material properties, which make it difficult to understand the effect of the elasticity of the heel pad on heel pain and ulcer formation. Therefore, it is important to study the material properties of the heel pad sub-layers and their changes made by age, pathological changes and severe mechanical loading conditions to gain a better understanding of effect of the elasticity of the heel pad on increasing the internal stress and risk of pain and injuries in the heel. In the absence of a tool to experimentally measure the internal tissue stress and strain, valid numerical models can predict the distribution of stress and strain in tissue and subsequently the area where ulcers are likely to develop.

2.2 DIFFERENT METHODS TO OBTAIN THE HEEL PAD MATERIAL PROPERTIES

Several studies tried to investigate the material properties of the heel pad using different methods. Depending upon the method used to measure material properties, different mechanical properties were obtained for the heel pad. Thus, selection of method is critical in terms of ensuring validity. Dynamic impact test on live tissues has been commonly used to quantify the mechanical properties of the heel pad (50-52). Impact tests have provided the heel pad load-displacement behaviour without showing true stress-strain response. Indentation test has also been widely used to assess the biomechanical properties of biological tissues. Ultrasound imaging technique has been used in some studies for obtaining information associated with the human heel pad thickness and deformation under loading (18, 22, 53). In some new studies ultrasonic indentation method has been used to visualise and measure the displacements of the soft tissue with a load cell measure the applied external force concurrently (36, 54). Different methods, used to study the biomechanical behaviour of the heel pad and its sub-layers, are fully reviewed in this section and their limitations are summarised at the end of the section.

- ***In-vivo* examinations**

In some, the human heel pad mechanics were described based on either load-deformation/strain or stress-deformation/strain relations deducted from *in-vivo* experiments. Nigg & Denoth performed impact tests with controlled vertical drop of the foot of 10 seated subjects to evaluate the stress-deformation response of the heel pad to impact. The stress levels of $100N.cm^{-2}$ for deformation ranging from 2.5 to 8mm were reported (55). Although the contact area under the heel is rapidly changing under loading, they used a constant value to estimate the heel pad stress.

Kinoshita et al. examined the behaviour of 16 heel pads of adults and 5 children using a drop-impact tester with weight of 5kg and 40mm diameter contact head in order to study the shock-absorbing characteristics of the heel pad (Figure 2.7). The average peak deformations of the heel pad were 9.5mm (SD 1.0) and 11.3mm (SD 1.0) at impact velocities of 0.72 and 0.93m/s (representing impact velocities during actual running) for adults respectively. Results showed that approximately 77.4% (SD 3.5) and 78.8% (SD 3.6) of energy could be absorbed by the heel pads at lower and higher velocities respectively. The peak deformation and maximum energy absorption of children heel pads was 8.3mm (SD 0.8) and 73.9% (SD 2.9) at 0.72m/s.

They concluded that the mechanical properties of the heel pad of children differ from those of adults. The heel pad of children showed less deformation and less energy absorption (52). This can be related to less unloaded thickness of the heel pad of children who have less fat than adults do. A research study done by Jorgensen et al. showed the relationship between the heel pad thickness and the energy loss with thinnest pads displaying lowest shock absorption characteristics (56). This might reflect the effect of the age on the mechanical properties of the heel pad.

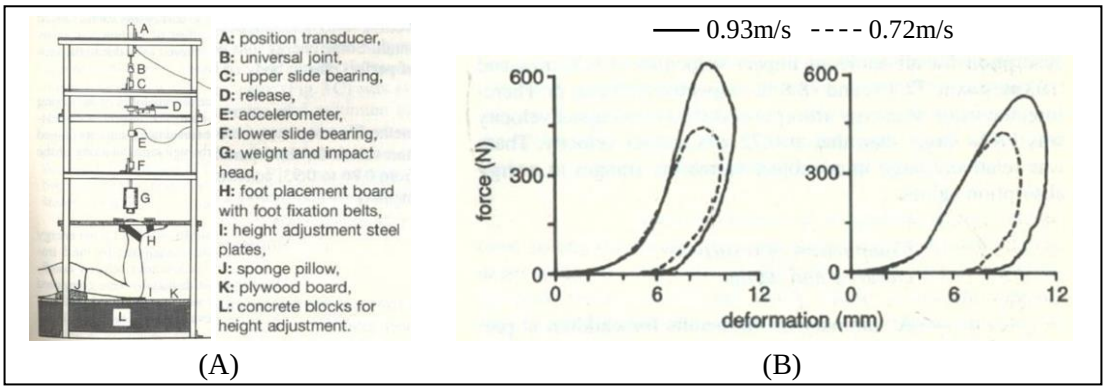

Figure 2.7: The impact test on the heel pad: (A) The impact tester; (B) Force-deformation responses of the heel pad for 2 adults. Derived from (52).

Cavanagh et al. used a ballistic pendulum with mass of 1.9 to 4.0kg to characterise the mechanical properties of the heel pad under impact conditions thought to be similar to those during running. A flat 88mm diameter circular aluminium plate was chosen as an impact

surface moving at velocities of 1.03 and 1.44m/s to perform impact tests on the heel of 10 subjects (Figure 2.8). The average peak deformations of the heel pad were measured approximately 8.8 and 10.9mm under maximum forces of 338 and 676N respectively. The energy absorption capacities of the heel pads were measured ranging from 85 to 90% for the above velocities. They used force-deformation curve to show the results (50). Although the impact velocities correspond to the vertical velocity of the foot during running, using this method could not achieve to the high load expected during running which is almost 1.5 to 3 times body weight (57).

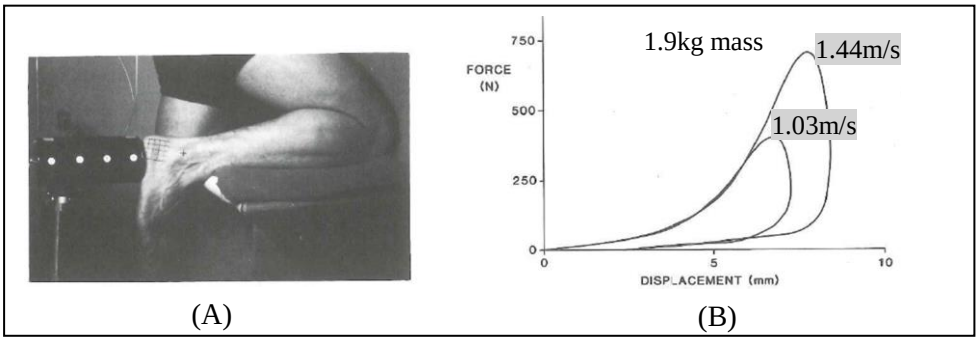

Figure 2.8: Heel pad impact test: (A) Impact test using ballistic pendulum; (B) The effects of changing velocity on the heel pad impact hysteresis curve. Derived from (50).

Aerts and De Clercq performed impact test using a pendulum on the heel region of one subject to investigate the load-deformation characteristics of the heel pad. A cylindrical pendulum with contact surface of 32.2cm^2 was used to hit the subject's heel pad at impact velocities ranged from 0.37 to 0.96m/s. The corresponding deformation was measured using deceleration during impact and load-deformation characteristics recorded for different velocities, ranging from approximately 9 to 11mm. They reported initial compliance behaviour with a subsequent stiffer behaviour for the heel pad. The increase in impact velocity resulted in an increase in the stiffness of the heel pad from 52 to 150kN/m (51).

Although the method of the compression of the heel pad and the position of the subject was similar to that in the research project developed by Cavanagh et al. (50), the findings were

different. Although the range of velocity was less than that used in the project of Cavanagh et al. corresponded to walking and moderate running, the higher load was measured in inducing similar deformation to the heel pad. Since in both projects large indenters (within and larger than the range of typical heel widths of 50-70mm) were used, the size of tested heels might be the reason for the difference. Furthermore, Aerts and De Clercq reported stiffness of the heel pad based on impact test on a single subject. The mechanical properties of the tested heel pad might be higher than the average values.

While impact tests provided valuable information about the heel pad responses to impact loading, but they could not evaluate the heel pad responses during the actual gait. De Clercq et al. tried to study the deformation characteristics of the heel pad of two healthy subjects at running speed of 4.5m/s. They used high-speed two-dimensional cineradiography to film the heel strike whilst subjects ran across a force platform to measure the vertical component of the ground reaction force. The deformation of the subcalcaneal fat pad was measured for each of the 150 film frames per second. They reported average maximum deformation of 9mm (SD 0.5) equal to strain value of 60.5% (SD 5.5) at almost 1m/s vertical velocity of the heel (58). Such a large deformation was also reported in studies using impact tests. Compared to previous studies, which were based on impact tests, this study obtained the characteristics of the human heel pad during the actual heel strike for first time.

Gefen et al. used a technique integrating two measurement methods to study heel pads behaviours of two adult volunteers at gait velocities between 0.5 to 0.9m/s (Figure 2.9). A digital radiographic fluoroscopy system was used to measure the thickness of each heel pad during gait while a contact display optical method simultaneously provided plantar pressure data (31). They concluded that the heel pad could be compressed up to 40% during walking which is lower than the 60-66% deformation reported by De Clerq et al. during running. The heel pad energy dissipation was measured 17.8% (SD 0.8) in slow to moderate velocities

which is considerably lower than values of 79-90% reported for the heel pad under impact tests (50, 52).

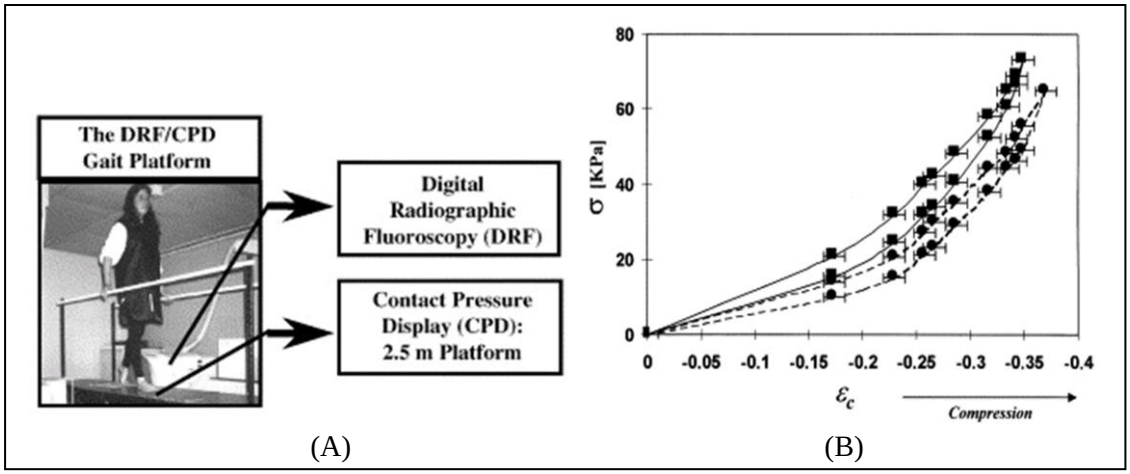

Figure 2.9: Mechanical characterisation of two subjects heel pad: (A) Experimental setup; (B) The stress-strain relation. Derived from (31).

In this study by adding the optical pressure-sensitive plate to a clinical fluoroscopic imaging system, it was possible to obtain rapidly changing contact stresses in addition to the vertical ground force provided by the setup developed by De Clerq et al. Although using the radiographic method allowed measuring the deformation of the heel pad during actual heel strike, there was not any control on the direction of the applied force, which might lead to divergent results.

In some studies, indentation was used to study the material properties of the heel pad. Robbins et al. used a hand-held, spring-loaded indentation system with a 10mm spherical end to compress the heel pad in 100 healthy subjects (14-64 years old). They also used another two 10 and 23mm spherical end indenters to compress heel pads of 17 male runner subjects (59). Their purpose was to quantify the relationship between the localized load and pain and between load and deformation of the heel pad. The indenter was pressed into the plantar surface at increments of 1.8kg to a maximum of 9kg. They reported that the pain sensitivity of the plantar surface varies in different locations with the heel pad highest. This confirmed the

protective behaviour of the heel pad against excessive stress. The results showed no significant difference in biomechanical behaviours of heel pads in two groups of younger and older adults. Moreover, the results revealed that to apply the same deformation to the heel pad, more force is required using indenter with bigger size (Figure 2.10). This is not because of the changes in the material properties but it is due to the increased contact area while using a bigger size indenter. This finding means that the size of the indenter should be considered carefully when comparing force-deformation/strain data obtained from literature.

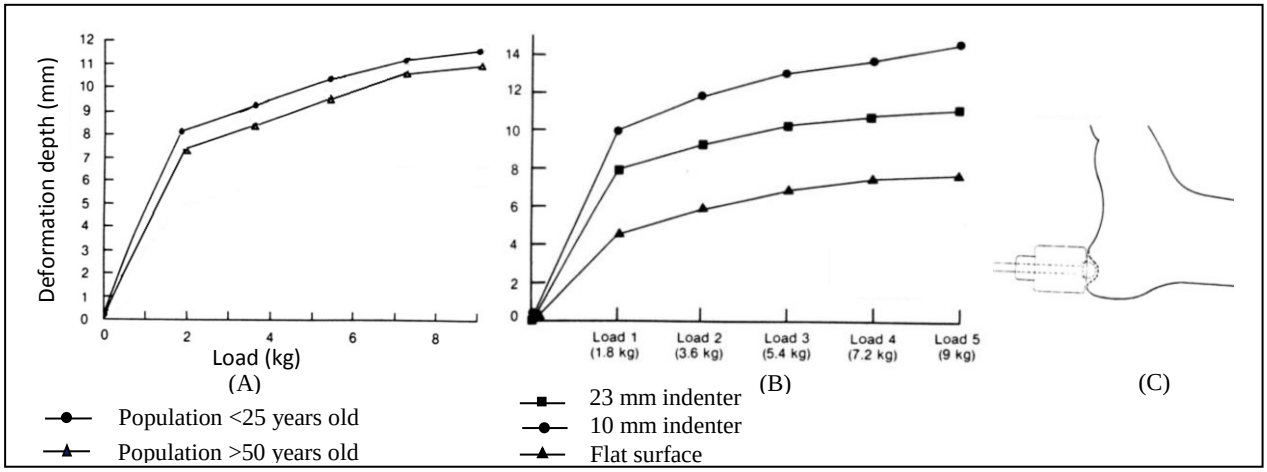

Figure 2.10: Deformation characteristics of the heel pad: (A) Different age groups, (B) Different indenter size, (C) Indentation of the heel pad. Derived from (59).

Hsu et al. used ultrasound to visualise deformation of the heel pads in 33 healthy subjects, younger than 40 years or older than 60 years of age, during loading-unloading cycles (36). Their main objective was to compare the mechanical properties of the heel pad of young and older adults. A 7.5-MHz linear-array ultrasound transducer with the contact area of $6cm^2$ was placed in a loading-unloading device to measure the thickness of the heel pad at different loads. Figure 2.11 shows the loading-unloading device with the subject in the prone position and a 90^o flexed knee.

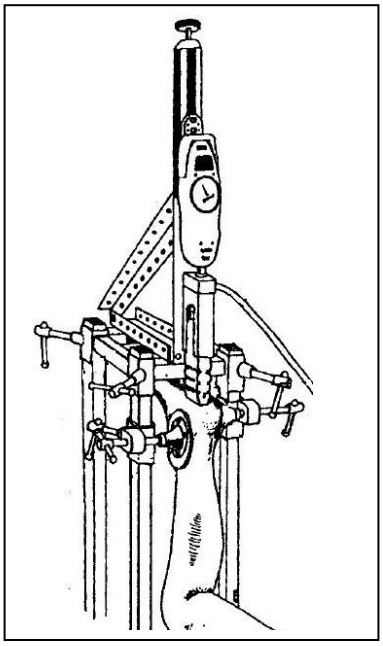

Figure 2.11: The ultrasound indentation test on the heel pad. Derived from (36).

High-resolution ultrasonography could provide dynamic information about deformation of the heel pad under loading. The heel pad was loaded at a speed of approximately 0.0006m/s up to maximum load of 3kg. The shock absorbency of the heel pad was measured 23.7% (SD 6.9) and 35.3% (SD 10.0) in the young and the elderly group respectively. Based on load-deformation relations the stiffness of the heel pad showed an increase from 3.76kg/cm (SD 0.46) to 3.97kg/cm (SD 0.67) for the young to older groups indicating loss of the elasticity of the heel pad in older people (36). Since the velocity has shown to be important factor affecting the behaviour of the heel pad, their findings are only accepted for almost static situation. In kinds of studies which used small size indenter (smaller than the maximum heel width) to investigate the heel pad behaviour, effects of large deformation and boundary conditions caused by small indenter were ignored. Although they provided valuable data about the heel pad stiffness and its energy absorbing properties, their results could not represent the heel pad behaviour during actual gait.

Tong et al. used a device combining ultrasound and force transducers to measure displacement and compression force of the heel pad under compression (Figure 2.12) (32). The material properties of 21 healthy heels were investigated and compared to those obtained for 17 heels of patients with plantar heel pain and 17 heels of patients with diabetes. The heel pad was compressed by a flat surface from 5 to 30N in 5N steps. Neither the indentation velocity nor the indenter size was reported for the experiments.

In agreement with the findings reported by Hsu et al., an insignificant increase found in the unloaded thickness of the heel pad from healthy to the diabetic patients (33). Although Hsu et al. reported no statistically difference for stiffness and strain between the healthy and diabetic groups under maximum 98N, the results of the work of Tong et al. revealed low stiffness and significantly higher strain in the healthy group compared to two other groups. Different age,

test devices, indenter with different contact surfaces and test velocities may be the sources of the divergence.

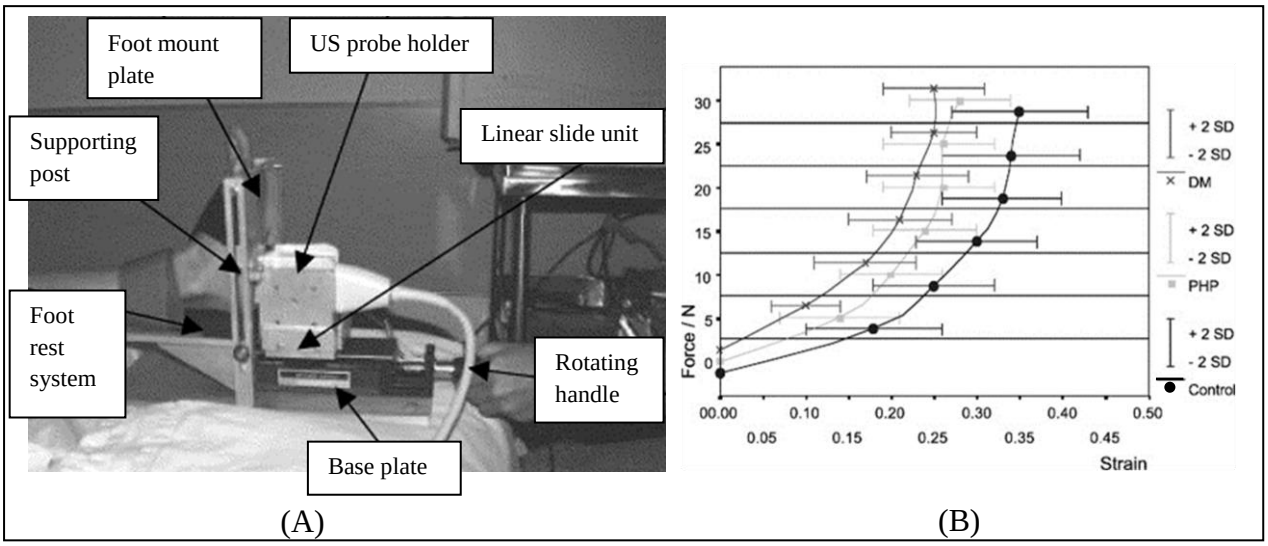

Figure 2.12: Indentation of the heel pad: (A) Test rig, (B) Force-strain data for three subject groups. Derived from (32).

Since the findings of the reviewed studies were influenced by: (1) the **geometry of the heel pad** such as the heel pad thickness and the shape of the calcaneus, (2) **experimental conditions** such as loading velocity, indenter size and position of the heel during loading and (3) **effects of the other systems of the lower leg** such as ankle and knee, the structural properties of the heel pad tissue was found instead of material properties. Some researchers investigated the behaviour of the heel pad by testing cadaveric heel pad samples to obtain the material properties of the heel pad without being affected by the surrounding tissues.

- ***In-vitro* examinations**

In some studies, the human heel pad mechanics were described based on load-deformation/strain or stress-deformation/strain relationships deducted from *in-vitro* experiments. Although *in-vitro* testing has ethical and cost advantages over *in-vivo* and can offer better control on the experimental system, the results obtained from *in-vitro* testing cannot reflect the heel pad mechanics during gait and the results are different from those

obtained from *in-vivo* experiments. Bennett and Ker tested 11 heel pad tissue specimens (49-78 years old) under compression in an Instron material testing machine (60). 7 of the specimens were tested while still were attached to the part of the calcaneus and 6 of them were tested when removed from the calcaneus. All of the specimens were mounted on the Instron machine and subjected to sinusoidal compressive loading of up to -2kN at frequencies of 0.1 to 70Hz (Figure 2.13).

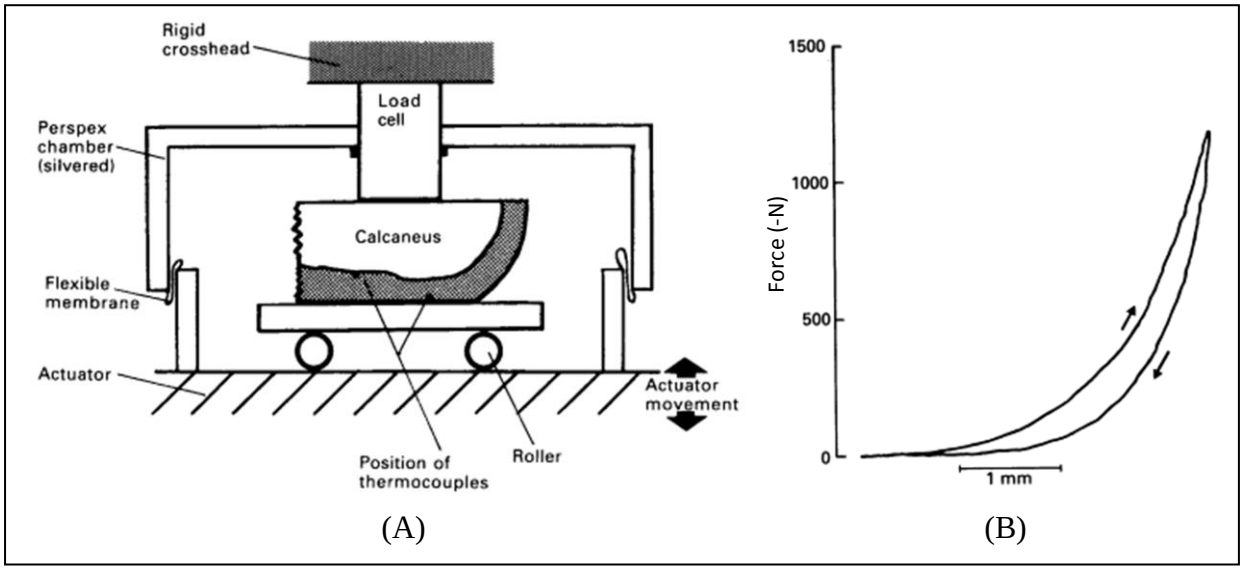

Figure 2.13: The human heel pad under compression: (A) Experimental arrangement for the heel pad compression test; (B) A typical load-displacement record. Derived from (60).

Radiographs were taken to measure the thickness of the heel pads. The load versus actuator displacement was recorded for typical compression test. They reported that the energy dissipation ratio and the stiffness of the heel pad do not change greatly over the range of frequencies for the same maximum load. The energy dissipation ratios of 28.6% (SD 6.9) and 32.3% (SD 5.4) were found for pads attached to the calcaneus and isolated pads respectively for the maximum load of -1kN (60). This difference reveals the effect of the surrounding tissues on the heel pad mechanics. The average energy absorbed of about 30%, is much smaller than those values of 85% and 95% observed in the pendulum studies. While the results of the *in-vitro* test represent the properties of the fat pad, the pendulum impact results may show the properties of the lower leg as a whole (15, 50).

Miller-Young et al. measured the nonlinear viscoelastic material parameters of heel pad tissue samples. They cut cylindrical samples (8mm diameter and 10mm high) from heel pads of 20 older feet (61-99 years old). The samples were subjected to three different compression tests: (1) quasi-static tests at the speed of 0.01 and 0.001mm/s in order to obtain the hyperelastic material properties of the fat pad, (2) stress-relaxation tests to determine the viscoelastic time constants, and (3) rapid compression tests at speeds of 175 and 350mm/s to get the viscoelastic relaxation material coefficients. The maximum stress was calculated 9.2kPa for 50% deformation at quasi-static test. At the maximum deformation of 47%, the stress was measured 33.7 and 25.5kPa for loading rates of 350 and 175mm/s respectively (12). These results showed the dependence of the heel pad biomechanical behaviour on the loading velocity and confirmed its viscoelastic characteristics.

Ledoux and Blevins determined the material properties of the fat pad by testing skinless 2 x 2cm samples from 11 young (21-46 years old) , non-diabetic donors. The specimens were placed between two plates and compressed at five frequencies ranging from 0.005 to 10Hz. The applied force and the corresponding distance of two plates were recorded to measure the material properties. For 30% strain the peak stress at the fat pad was 89.5kPa (SD 4.0) and the energy absorption was 36.0% (SD 3.0) (13). In contrast with findings of Bennett and Ker study (60), they reported that the peak stress, stiffness and the energy loss increase with frequency. However, it should be noted that Bennett and Ker used older cadavers (49-78 years old) in their study. The results suggest that the frequency sensitivity is higher in the younger subjects than the older subjects. This may be explained by a decrease in water content in heel pads of older people (61, 62) which leads to reduction in heel pad viscoelastic characteristics. The above reviewed studies are summarised in the following table and their issues and limitations are explained.

Table 2.1: Review of the studies carried out to characterise the biomechanical behaviour of the human heel pad.

Research	Experiments				Type of test		Subjects or samples			Data collections		Reported data				
	Impact test		Compression	Indentation	*In-vivo*	*In-vitro*	Number of subjects or samples	Age	Heel pad condition	Geometry of indenter	Velocity	Max deformation (mm)	Peak force (N)	Strain (%)	Peak stress (kPa)	Energy absorption (%)
	Pendulum	Vertical drop														
Nigg & Denoth (1980)		*			*		10 subjects	adults	-	-	300-1800 mm/s	2.5-8	-	30	1000-1500	-
Kinoshita et al. (1993)		*			*		16 subjects	adults	-	-	720-930 mm/s	11.3	-	-	-	75-89
Cavanagh et al. (1984)	*				*		10 subjects	adults	-	88 mm dia flat	1030 mm/s	8.8	338	-	-	85
Aerts & De Clercq (1993)	*				*		1 subjects	Young adult	Healthy	32 mm dia flat	960 mm/s	11	1000	-	-	-
De Clercq et al. (1993)			*		*		2 subjects	21-22	Healthy	Force Platform	1100±100& 1200±200 mm/s	-	1479-2192	60.5±5.5	-	-
Gefen (2001)			*		*		2 subjects	27-35	Healthy	Gait platform	2.5±0.5 s^{-1}	-	-	33.9-36.6	~68-75	17.8±0.8
Robbins et al. (1989)				*	*		17 subjects	16-64	Healthy	10 mm dia flat	1 s^{-1}	~15	9 kg	-	-	-
										23 mm dia flat	1 s^{-1}	~11	9 kg	-	-	-
Hsu et al. (1998)				*	*		33 subjects	18-36	Healthy	600 mm^2	0.6 mm/s	~7.97	3 kg	-	-	23.7±6.9
								62-78	Healthy	600 mm^2	0.6 mm/s	~7.55	3 kg	-	-	35.3±10
Tong et al. (2003)			*		*		14 subjects	21-65	Healthy	Flat plate	-	-	~30	0.35±0.08	-	-
							9 subjects	25-83	With diabetes	Flat plate	-	-	~30	0.25±0.06	-	-
							12 subjects	19-65	With PHP	Flat plate	-	-	~30	0.28±0.06	-	-

Research	Experiments				Type of test		Subjects or samples			Data collections		Reported data				
	Impact test		Compression	Indentation	*In-vivo*	*In-vitro*	Number of subjects or samples	Age	Heel pad condition	Geometry of indenter	Velocity	Max deformation (mm)	Peak force (N)	Strain (%)	Peak stress (KPa)	Energy absorption (%)
	Pendulum	Vertical drop														
Bennett & Ker (1990)			*			*	11 samples	49-78	Patients with Vascular disease	Flat plate	Frequencies of 0.1-70 Hz	-	-	-	-	~30%
Miller-Young et al. (2002)			*			*	2 samples	61-99	Healthy	Flat plate	0.01 & 0.001 mm/s	-	-	50	~8.5-9	-
							20 samples				175 & 350 mm/s	-	-	50	~25-50	-
Ledoux & Belvin (2007)			*			*	11 samples	21-46	Healthy	Flat plate	0.005-10 Hz	-	-	30	89.5±4	36±3.0

Most of the reviewed studies showed agreements in the following results:

- The heel pad exhibits non-linear behaviour under compression, with increase in the stiffness as the applied force increases.
- The biomechanical behaviour of the heel pad is affected by the loading rate.
- The energy is absorbed by the heel pad during loading-unloading cycle.

Depending on the method which was used to study the biomechanical behaviour of the heel pad, the reviewed studies obtained different results. The limitations of the approaches are explained here.

- Impact tests were frequently used to study the properties of the human heel pad *in-vivo* (15, 50, 52, 55). As Aerts et al. showed, the *in-vivo* and *in-vitro* tests obtained different properties for the heel pad. While the *in-vitro* mechanical testing on the pads specimens gave the properties of the heel pad, the *in-vivo* impact test provided the properties of the lower leg as a whole (15). In the *in-vivo* impact tests the measurements were affected by the geometry of the heel pad and confinement by the surrounding tissues as well as the material properties of the tissue. Therefore, these studies measured structural properties of the heel pad rather than material properties. Besides, impact tests could not evaluate the heel pad responses during gait.
- Kinoshita et al. and Cavanagh et al. measured the energy absorption to be 79-85% using *in-vivo* impact tests whereas it was found to be about 30% on *in-vitro* heel pads (50, 52, 60). This divergence might be explained by the fact that in *in-vivo* impact tests, the energy was absorbed by the heel/foot/leg system and it was impossible to obtain the actual contribution of the heel pad tissue in the energy absorption.
- The studies using the impact test method reported the properties of the heel pad based on force-deformation relationships. Only Nigg and Denoth presented the results in the

form of stress-deformation. Their study was based on the assumption of constant contact area during the experiments which put the accuracy of the calculated stress under question (55).

- The cineradiography or radiography made it possible to measure the deformation of the heel pad during actual heel strike. Gefen et al. also measured the contact pressure using the display optical method and created the heel pad stress-strain relationships (31). However, they measured the structural properties instead of material properties because the results are still affected by the heel pad geometry, loading and boundary conditions. Although they could measure the deformation of the heel pad during actual heel strike, they did not have control on the direction of the applied force.
- Indentation experiments performed by small indenter were also used to study the behaviour of the heel pad (36, 59). In some cases, ultrasound method was simultaneously used with indentation method for better visualisation of the deformation of the heel pad during loading and unloading (32, 36). Robbins et al. showed that the deformation of the heel pad varies by changing the size of the indenter for the same value of the compression load (59). In such studies which used small size indenter, the effects of large deformation and boundary conditions caused by the small size of the indenter have not been considered. Therefore, they failed to represent true stress-strain responses of the heel pad during actual gait.
- To overcome the effects of surrounding tissues on the heel pad behaviour and measure the material properties of the heel pad, some studies used *in-vitro* tests on isolated heel pad specimens (12, 29, 60). These studies were limited by the use of assumptions concerning no change of the heel pad during compression, such as ignoring the change of the amount of water exist in the tissue sample. Moreover, in *in-vitro* measurements, material properties of soft tissue are affected when tissue is dissected from a living

body and neurovascular supply is impaired (63, 64). Finally, it is not possible to use *in-vitro* measurements to characterise subject-specific material properties of the heel pad.

2.3 USE OF INVERSE FEA IN DETERMINATION OF THE HUMAN HEEL PAD MATERIAL PROPERTIES

Many authors have identified that inverse FEA, a tool commonly used for structure and material analysis in engineering applications, could be appropriate for investigation of the biomechanical properties of the heel pad (5, 7, 9, 11). Indeed, inverse FEA is appropriate to obtain the material properties of the heel pad sub-layers. Using inverse FEA allows modelling of the geometry and boundary conditions of the physical experiments and therefore obtaining true material properties of the heel pad. It also allows to go further and characterise the heel pad sub-layers which is impossible using *in-vivo* mechanical testing.

Inverse FEA can accommodate the force-deformation/strain measurements of the heel pad and determine the appropriate material properties by modelling the realistic geometry, loading and boundary conditions of the experiment. In recent years, several studies have used inverse FEA in order to characterise the heel pad biomechanical behaviour during loading-unloading cycle.

2.3.1 Introduction to FEA

FEA is a numerical method, which describes many of the continuous physical phenomena in engineering which are modelled by partial differential equations. FEA represents an engineering problem with a physical geometry, material properties, and loading/boundary conditions to determine unknown values of variables like displacement in solid mechanics. FEA divides the structure into an equivalent system of a finite number of smaller bodies called elements. The elements are then reconnected at “nodes” that holds elements together and make a grid called a “mesh”.

Many engineering problems are solved based on linear approximations. Linear models use linear Hookean material and assume that the deformations are small and loads are independent of displacements (65). Therefore, a set of linear equations are used to describe behaviours of FE models as bellow:

$$[K]\{X\} = \{F\} \tag{2.1}$$

In equation 2.1, [K] is the stiffness matrix, which defines the geometric and material properties of elements, F represents the loading/boundary condition, and X is unknown deformation of the engineering problem. For linear analysis in which the stiffness never changes, the unknowns can be found by solving the equations for once and no need to update anything while the structure is deforming (66). In reality, behaviours of most of structures are nonlinear. For example, when large deformation occurs under loading or the material behaves nonlinearly, an engineering problem needs nonlinear solution. These kinds of nonlinearity lead to an equation with a stiffness response which is not constant and depends on the deformation (u) (67).

$$[K(x)]\{X\} = \{F\} \tag{2.2}$$

Problems involving contact mechanics also cause nonlinear behaviour. They include a boundary condition which is dependent on the deformation and produce a nonlinear formulation (67).

$$[K(x)]\{X\} = \{F(x)\} \tag{2.3}$$

FEA has been used for engineering problems for many years and applied to biomechanical research fields. For instance, FEA was used in modelling shoulder, cervical spine, eye and many more human body parts to reach a better understanding of their functionalities (68-70). There are three steps to perform FEA on a single component structure or on an assembly of components:

1. Pre-processing

- Development of a physical geometry model of a problem in 2D (two-dimensional) or 3D (three-dimensional) using CAD (Computer Aided Design) software such as SolidWorks;
- Dividing components of the CAD geometry into many contiguous small parts called elements (meshing);
- Assignment of material properties to the components;
- Applying loads and boundary conditions to the components and define interactions or contacts between the components.

The pre-processing stage is interactive and time-consuming for the analyst. A simple example is used to show the pre-processing steps in Figure 2.14.

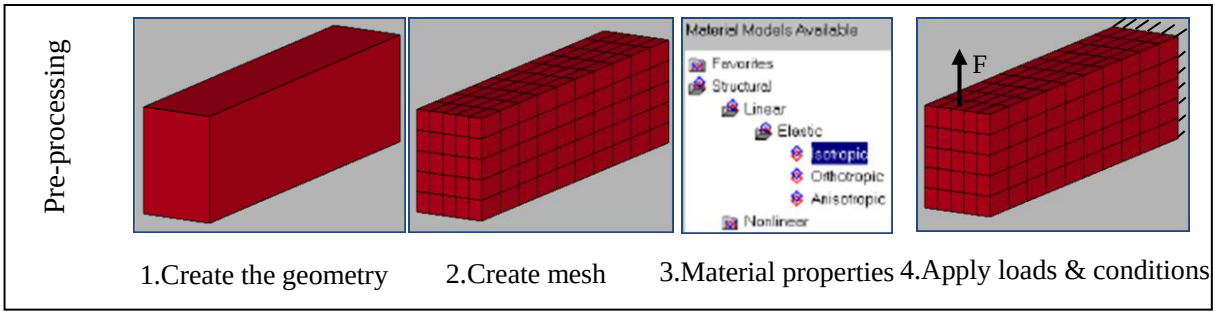

Figure 2.14: Pre-processing steps of FEA.

2. Processing

- Running the analysis and compute the unknowns;

During this stage, the model is analysed in commercial FEA software such as ANSYS, Abaqus and Ls-Dyna. This stage proceeds by assembling the governing equations for each element into a matrix form and solving it numerically. This process depends on the type of analysis (e.g. static or dynamic), type of elements, material properties and boundary conditions (71).

3. Post-processing

- Displaying the results

Once the analysis is completed, the variables such as stress, displacement and deformed shape of the model can be graphically viewed using visualization tools (Figure 2.15).

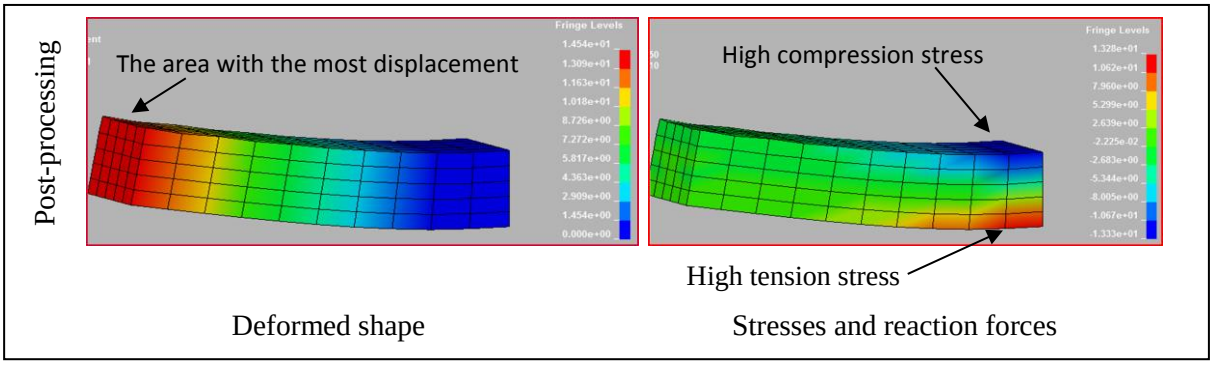

Figure 2.15: Visualization of FEA results in the post-processing stage.

In FEA method, it is common to apply some simplifications to the problems (e.g. geometry simplifications, loading and boundary conditions simplifications) to avoid huge and complicated models which are not efficient for analysis. Therefore, to ensure the accuracy of the model simulation, it is vital to validate the FE model by comparing predicted results with experimental results.

2.3.2 Using Inverse FEA to Study the Biomechanical Properties of the Human Heel Pad

In several studies, an inverse FEA has been used to characterise the heel pad biomechanical behaviour under loading. This frequently used technique combines numerical and experimental approaches. The advantage of this method is to use the experimental data obtained from physical testing on live tissues in obtaining the material properties of the heel pad and its sub-layers. In this method, a FE model of the heel pad is required to represent accurate geometry and boundary conditions of the heel pad and ideally the conditions under which the heel pad is being experimentally tested. In doing so, FEA allows corrections for the effects of confinements by surrounding tissues, loading and boundary conditions on biomechanical behaviour of the heel pad. Numerical and experimental results are then compared in an iterative scheme. In each iterative step parameters are adjusted until the model

predictions converge with the experimental data. A review of studies adopting this approach now follows.

Lemmon et al. developed a simplified FE model of the heel pad to determine soft tissue material properties (72). They used Mooney-Rivlin hyperelastic material model to represent the incompressibility of the soft tissue as it was thought that this model best could represent the incompressibility of soft tissue. This material model employs second-order polynomial strain energy with the form of:

$$U = \sum_{i+j=1}^{2} C_{ij} (\bar{I}_1 - 3)^i (\bar{I}_2 - 3)^j + \sum_{i=1}^{2} \frac{1}{D_i} (J-1)^{2i} \quad (2.4)$$

Where U is the strain energy; C_{ij} and D_i are material parameters; J is the elastic volume ratio and I_1 and I_2 are the first and second deviatoric strain invariants. Material properties were calculated using inverse FEA based on the uniaxial stress-strain data adopted from the *in-vivo* compression tests on the heel. The stress-strain data of the tissue were collected on five subjects using an ultrasound device to measure the deformation of the heel and a load cell to measure the force on the heel simultaneously. The final coefficient values are given in Table 2.2. These material parameters used to simulate the hyperelastic behaviour of the heel pad in another two studies (73-76).

Table 2.2: The parameters of the hyper-elastic material model obtained for the plantar soft tissue.

Material Parameters	C_{10}	C_{01}	C_{20}	C_{11}	C_{02}	D_1	D_2
Values	85.55	-58.40	38.920	-23.100	8.484	4.37	6.811

Units are kPa for C_{ij} and mm^2N^{-1} for D_i.

Verdejo and Mills generated a 2D axisymmetric heel pad model to study the stress distribution at the heel pad/shoe midsole interface (9). A geometrically simplified homogeneous single layer model was used to represent the heel pad and the calcaneus geometry (Figure 2.16).

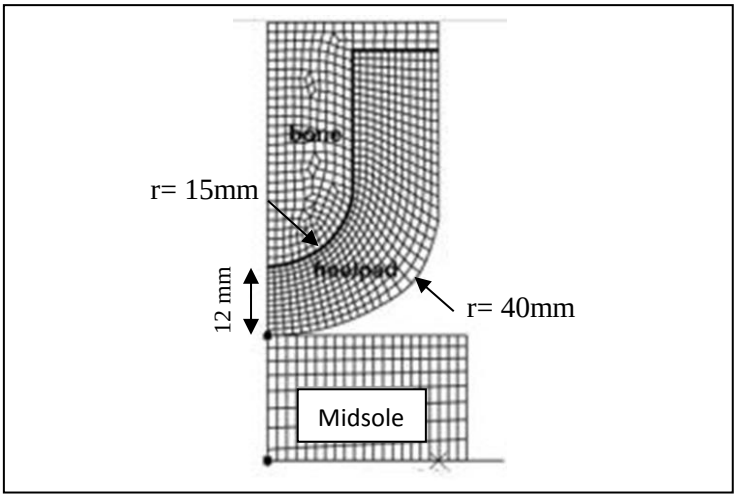

Figure 2.16: An axisymmetric 2D model of the heel area and midsole. Derived from (9).

In this study, the heel pad was simulated using hyperelastic material model. The heel pad strain energy was represented by Ogden strain energy function:

$$U = \sum_{i=1}^{N} \frac{2\mu_i}{\alpha_i^2} \left[\left(\lambda_1^{\alpha_i} + \lambda_2^{\alpha_i} + \lambda_3^{\alpha_i} - 3 \right) + \frac{1}{D_i} (J-1)^{2i} \right] \quad (2.5)$$

Where λ_i are the principal extension ratios; J is the elastic volume ratio; μ_i are shear modulus and α_i is dimensionless exponent. The material parameters (μ and α) were found by curve fitting the model predicted force-deformation data to those obtained from an impact test performed on an isolated heel of 24 year old male by Aerts et al. (29). The best fit was obtained for initial shear modulus $\mu_1=\mu_2=50$kPa and deviatoric exponents $\alpha_1=30$ and $\alpha_2=-4$. The predicted pressure distribution at skin/midsole interface was validated by the F-scan data. In this study, it is not clear which loading velocity was used to compress the FE model to replicate the experimental conditions. Therefore, it is difficult to comment on the quality of their results. However, it is obvious that using a simplified geometry for the FE model and using impact experimental data of another heel with different geometry as input to the FE model, ignored effects of the heel pad geometry on determination of material properties of the heel pad.

Erdemir et al. also used a combined method of inverse FEA and ultrasound imaging to determine the material properties of the heel pad. He indented left and right heels of 20

diabetic subjects and 20 healthy subjects using 25.4mm diameter rigid probe. The heel pad unloaded thickness and its deformations under load were measured using ultrasound while the indentation forces were recorded simultaneously. They used a 2D axisymmetric rectangular shape model, adjusted to represent individual heel thickness, for inverse FEA (Figure 2.17). They modelled the heel pad as a homogeneous single layer material using Ogden material model (5). Iteratively adjusting the material properties of the heel pad they minimised the error between the model predicted force-deformation data and those measured in experiments. The mean value of initial shear modulus, μ, for healthy subjects was measured as 16.45kPa (SD 8.27) and the value of deviatoric exponents, α, was found to be 6.82 (SD 1.57).

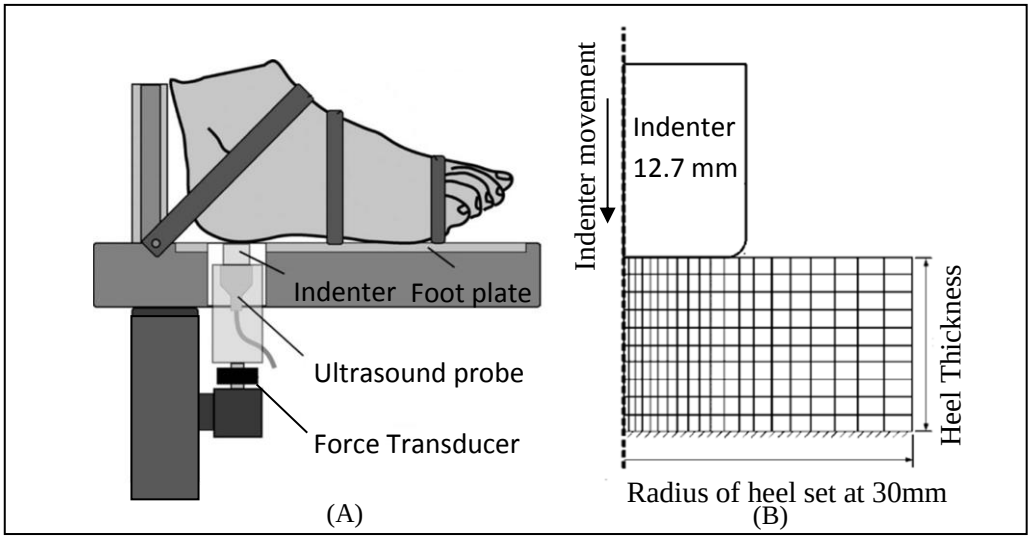

Figure 2.17: Inverse finite element analysis: (A) Force-controlled ultrasound device for indentation of the heel; (B) Finite element model of the heel under indentation. Derived from (5).

Although they have provided valuable data for material properties of the heel pad by examining several subjects, using such a simplified FE heel pad model, ignoring the shape of the calcaneus and inhomogeneous nature of the heel pad, could not appropriately represent the heel pad behaviour in actual testing. Besides, using small size indenter for physical testing could cause large deformation and stress concentration around the edges of the indenter so the

experimental data, used for material properties determination, did not represent biomechanical responses of the heel pad during actual gait.

A plane strain model of the heel pad was then created based on MRI of the heel of 23 year old male volunteer for model validation (Figure 2.18). The peak pressure predicted by model was measured at maximum loading of the heel during the first step of barefoot walking. This value was validated with experimental measurements using Novel Emed pressure platform. A peak pressure of 439kPa was predicted under maximum loading compared to experimental measurements of 426kPa (SD 21) (5). RMS error of 7% between the results of simulations run using average material properties and heel-specific material properties indicates the importance of not using the heel-specific geometry with material properties of different heel (5).

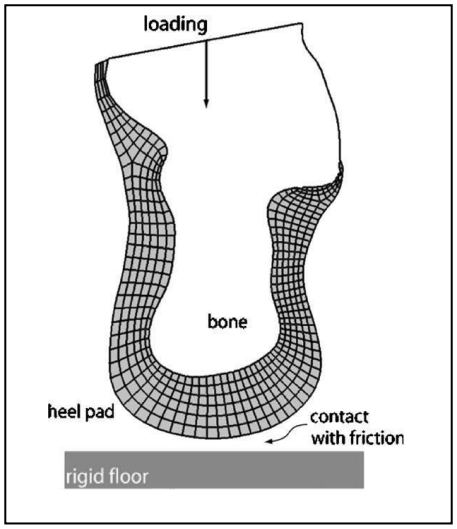

Figure 2.18: A 2D plane strain model of the heel pad used for measuring the plantar pressure. Derived from (5).

Spears and Miller-Young used FEA to study the stiffness of the heel pad in terms of stress-strain data (10). In contrast with the previously reviewed studies, the realistic geometry was developed for the heel pad based on CT images of the heel area available in the National Library of Medicine dataset (Figure 2.19). In this model, the fat pad and skin were considered as two different layers. The model was meshed using 2D axisymmetric elements and scaled to achieve the heel pad thickness of 15.5mm, which is the average heel pad thickness of healthy people measured by Tong et al. (32). A non-linear Mooney-Rivlin and viscoelastic material model was chosen to represent the fat pad and the skin biomechanical behaviours.

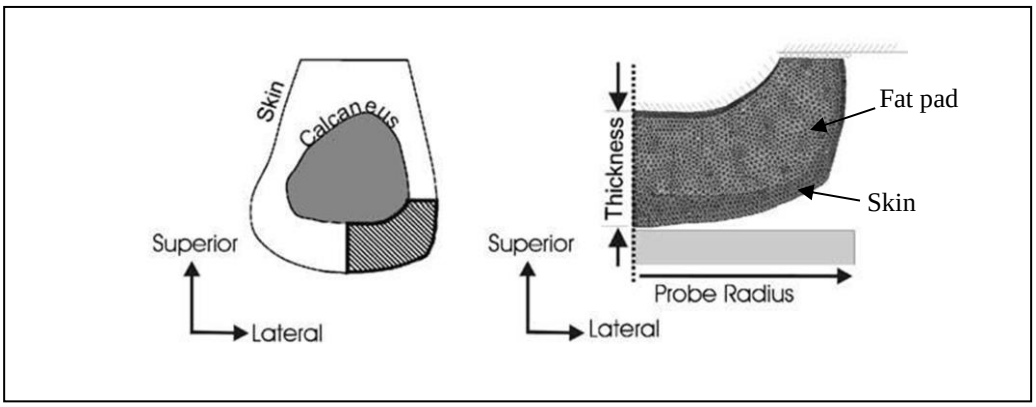

Figure 2.19: A heel pad model. Derived from (10).

The initial material properties of the fat pad and the skin were incrementally derived by comparing the predicted force-displacement results with corresponding experimental data obtained for the skinless and intact cadaveric heel. For this purpose, the intact heel pad of a cadaveric foot of a male subject was first indented with 20mm diameter indenter with speeds of 175mm/s and 350mm/s. The skin was then removed and the fat pad specimen was indented at velocities of 1mm/s and 350mm/s. The data from skinless specimen was used in a heel model with only elements representing the fat pad to determine the initial material properties of the fat pad. Subsequently, skin layer elements were added to the outer surface of the fat pad model and its parameters were adjusted until the predicted results at different velocities were as close as possible to the experimental data obtained for the intact cadaveric heel. Since the material properties were derived based on experiments on cadaveric specimens, the skin-fat stiffness ratio and viscoelasticity were maintained and then nonlinear parameters were adjusted until the force-displacement results were within 5% of those *in-vivo* experimental data obtained from Tong et al. at static situation (32). The material parameters are shown in Table 2.3. The FE model was validated by comparing predicted stress-strain data with those obtained *in-vivo* by Gefen et al. (31). For this purpose, the model was scaled to match the subject's heel dimensions.

This study for the first time characterised the fat pad and the skin layers separately and their viscoelastic parameters were determined as well as hyperelastic parameters. However, they modelled the fat pad with single homogeneous layer and ignored the effect of the shape of the calcaneus of the heel on the collected experimental data.

Table 2.3: Hyperelastic and viscoelastic material properties for the fat pad and the skin

Fat pad					Skin				
Hyperelastic			Viscoelastic		Hyperelastic			Viscoelastic	
C_{10} (kPa)	C_{20} (kPa)	C_{30} (kPa)	g	τ (s)	C_{10} (kPa)	C_{20} (kPa)	C_{30} (kPa)	g	τ (s)
81.3	81.3	81.3	0.99	0.001	6533.8	6533.8	6533.8	0.99	0.001

In another case, Spears et al. developed a 2D model of the heel pad to study the effect of the heel counter on the heel pad stress (11). Non-weight bearing MRI data of the foot of a healthy subject was used as a base for creating the heel pad geometry with the heel pad thickness of 18mm and the maximum heel width of 60mm (Figure 2.20). Loaded MRI at 52N was also taken from the same subject. In this model, the heel pad was made of two layers of the fat pad and the skin. The model was then scaled in vertical direction to represent thicker heel pads.

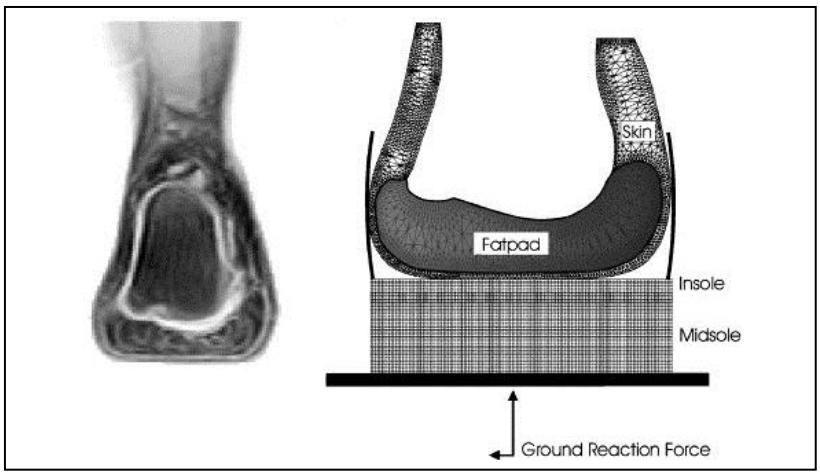

Figure 2.20: A FE model of the heel pad based on MRI data. Derived from (11).

The hyperelastic Ogden material model (equation 2.6) was chosen to represent nonlinear behaviour of the heel pad and material properties of the fat pad derived by fitting the predicted stress-strain data to the experimental data obtained by Miller-Young et al.

$$U = \sum_{i=1}^{n} \frac{\mu_i}{\alpha_i} (\lambda_1^{\alpha_i} + \lambda_2^{\alpha_i} + \lambda_3^{\alpha_i} - 3) \quad (2.6)$$

The experimental data was obtained by performing compression tests on 8mm diameter fat pad tissue at speed of 0.01mm/s (12). The material properties for the skin layer were then incrementally adjusted until the maximum vertical strain in the model under 52N matched the 0.25 strain measured in the MRI. The hyperelastic material parameters for the fat pad and the skin are given in Table 2.4.

Table 2.4: Hyperelastic material properties for the fat pad and the skin

Fat pad		Skin	
μ (kPa)	α	μ (kPa)	α
0.29	8.8	640	6.8

The results of this study were restricted to a single subject and were obtained under only static loads. However, for the first time they studied the internal stress in the skin and the fat pad separately. They found the material properties of the fat pad based on *in-vitro* test on a cadaver sample not being affected by the heel pad geometry. They compared the plantar pressure predicted by the homogenous single-layer model (heel pad) and the composite two-layer model (skin and fat pad) with the *in-vivo* experimental data (Figure 2.21). The results showed that the homogeneous model overestimated pressure at the centre of the model (>60%) and underestimated pressure in medial and lateral regions (>100%). The composite model predicted the plantar pressure evenly distributed under the heel pad and the results were close to the experimental data (within 10%). It means that both layers could be highly influential on the pressure and stress distribution. It might therefore be expected that further sub division of the layers into parts that represent the real differences in anatomical structures should further add to the quality of a model.

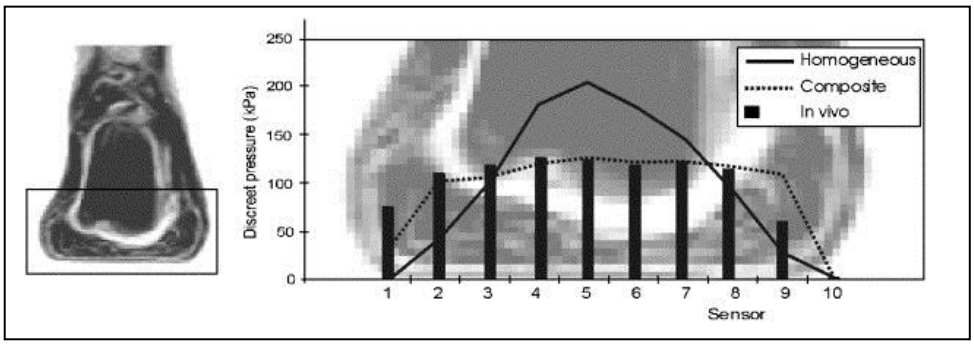

Figure 2.21: A comparison of predicted plantar pressures in the homogenous and composite models with experimental data. Derived from (11).

Gu et al. generated a 3D complex model of the heel pad consisting of four foot bones, the fat pad and the skin layers (Figure 2.22) (7). This model was developed based on subject-specific CT and MRI data. In this study, they were interested in obtaining the material properties of the skin and investigating the effects of the skin layer on the function of the heel pad. The hyperelastic Ogden material model with the following equation was used to describe the behaviour of the fat pad and the skin layers.

$$U = \frac{2\mu}{\alpha^2}(\lambda_1^\alpha + \lambda_2^\alpha + \lambda_3^\alpha - 3) \tag{2.7}$$

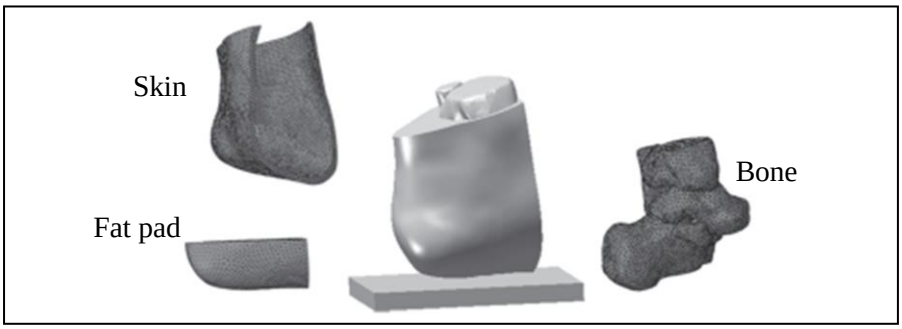

Figure 2.22: A 3D finite element model of the hind foot. Derived from (7).

The other tissues were considered as linearly elastic materials. The material properties of the fat pad were determined by comparing stress-strain numerical results with the plantar fat pad stress-strain data adopted from *in-vitro* experimental measurements obtained by Ledoux and Belvins (13). They also performed some indentation tests using 8mm diameter indenter on the same subject who went for the medical imaging. The skin layer parameters were determined

from curve fitting of the model predicted force-displacement data to *in-vivo* experimental results. The hyperelastic material properties for the fat pad and the skin are listed in Table 2.5. For validating the FE model, the plantar pressure predicted by the model under the compressive load of 360N was compared with Novel Emed measurements.

Table 2.5: Hyperelastic material properties obtained for the fat pad and the skin

Fat pad		Skin	
μ (kPa)	α	μ (kPa)	α
2.2	15.96	122	18

They managed to use an anatomically detailed 3D FE model to find the material properties of the fat pad based on *in-vitro* experimentation on cadaveric samples which out being influenced by the heel geometry. However, it is not clear that if the effects of experimental conditions specifically the indenter size were considered during the determination of material properties of the skin layer.

The FE model with subject-specific skin properties was used to simulate the behaviour of the heel pad under loading. The results showed that the high pressure and stress appeared in the centre of skin layer. Furthermore, the increase in the stiffness of the skin was shown to have limited effect on the stress in foot bones and cause small increase in the skin stress, whereas the decrease in the skin stiffness reduced the peak plantar pressure and increased stress in foot bones.

The FEA was also used by Luo et al. to characterise the mechanical properties of the heel pad tissue (77). Their main goal was to use the FE model to study the effect of insole design factors on the heel pad stress, strain and strain energy density. A 2D axisymmetric FE model of the heel pad was created based on measurements of MRI scans of a subject's foot, modelling the heel pad as a composite two-layer material. The heel pad of a healthy 62 year old male was indented using ultrasound device to obtain the experimental data. At each

displacement the indenter force was recorded concurrently (Figure 2.23). The loading velocity left ambiguous and using small indenter could not provide data representing the heel pad responses during gait.

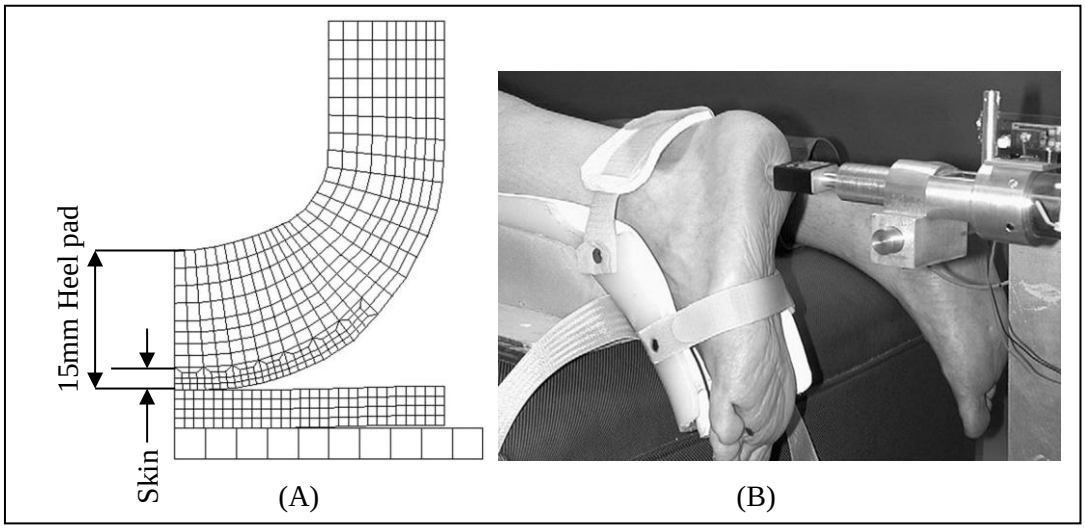

Figure 2.23: Finite element analysis of the heel pad: (A) A meshed FE model of the heel pad; (B) Measurement of the mechanical properties of the fat pad tissue. Derived from (77).

The nonlinear behaviour of the skin was modelled using a Jamus-Green-Simpson material model with the following strain energy function.

$$U = C_{10}(I_1 - 3) + C_{01}(I_2 - 3) + C_{11}(I_1 - 3)(I_2 - 3) + C_{20}(I_1 - 3)^2 + C_{30}(I_1 - 3)^3 \quad (2.8)$$

Where I_1 and I_2 are the first and second deviatoric strain invariants and C_{ij} are the material coefficients. The material parameters for the skin layer were derived from literature as C_{10}=15kPa, C_{11}=1320kPa and C_{01}=C_{20}=C_{30}=0 (78, 79). Like the FE model generated by Spears et al. (5, 7, 11), the plantar fat pad was modelled using Ogden material model (equation 2.6). The material parameters of the fat pad were determined by minimizing of the squared error between the force-displacement numerical results and those obtained from the indentation tests. The values which were obtained for the fat pad are μ_1=-680.724kPa, α_1=-0.62956, and μ_2=656.926MPa, α_2=-0.41635. It is not clear if the effects of the experimental conditions such as the loading velocity and the indenter size were considered during the

determination of material properties of the fat pad. To validate the axisymmetric FE model, the predicted plantar pressure was compared with F-Scan plantar pressure measurements.

Chokhandre et al. used inverse finite element analysis in order to calculate subject-specific material properties of the heel pad (6). Their main purpose was to use a heel pad 3D geometry along with 3D loading response of the heel pad under compression to determine heel pad properties. A 3D model of the cadaveric foot was developed for a 58 year old male donor based on the CT scan data (Figure 2.24). The hyperelastic behaviour of the heel pad was modelled using the Ogden material model (equation 2.7). Compression and shear tests were performed on the heel of the specimen using a 25.4mm diameter spherical indenter (80). The material parameters of the heel pad were obtained by minimizing the sum of squared-error between the model predicted and the experimental force-displacement data from compression tests. A total of 117 iterations were needed to find the optimized material parameters as μ=0.001084kPa and α=9.780. For the purpose of the model validation, optimised material parameters were used to compare model results with two sets of experimental data: (i) combined compression and shear loading performed by spherical indenter, and (ii) compression loading applied by flat platform.

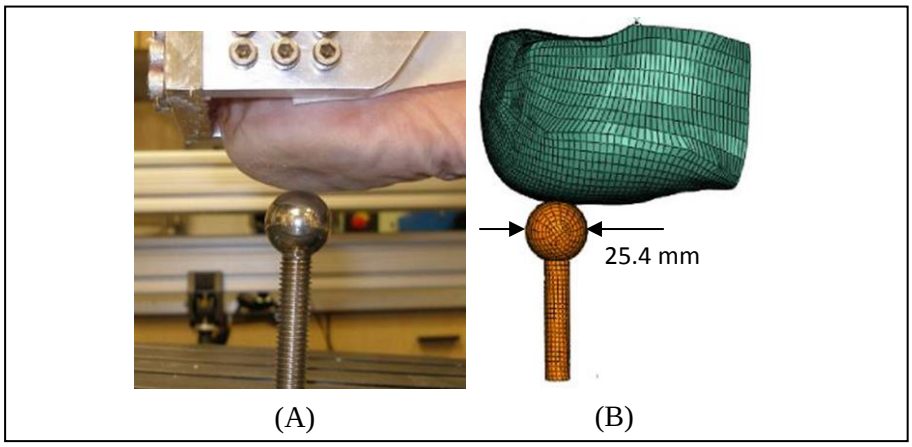

Figure 2.24: The heel pad indentation: (A) Compression test; (B) 3D model of single layer heel pad. Derived from (6).

They concluded that their model could accurately predict 3D response of the heel pad under indentation. It was the first study that used a combined compression and anterior-posterior shear loading to obtain the hyperelastic material properties of the heel pad using a spherical end indenter. However, using a homogenous single layer material to represent the heel pad structure was this study limitation. Results of this study are potentially limited to a single subject.

Some specifications of the previously published FE models and experiments carried out to obtain data upon which these models are based on, are listed in Table 2.6. The limitations of the FE models are then explained.

Table 2.6: Specifications of the reviewed FE models

Research	FE modelling												Experiment			
	FE model						Geometry		Material model							
	2D		3D													
	Axisymmetric	Plane strain		Singles layer (heel pad)	2 layers (fat pad & skin)	3 layers (macro, micro chambers & skin layers)	simplified	realistic	Hyperelastic	viscoelastic	Homogeneous	Composite	Compression	Indentation	*In-vivo*	*In-vitro*
Lemmon et al. (1997)	-	-	-	*			*		*		*		-	-	*	
Verdejo et al. (2004)	*			*			*		*		*		*			*
Erdmir et al. (2006)	*			*			*		*		*			*	*	
Spears et al. (2006)	*				*			Based on CT data	*			*		*	*	*
Spears et al. (2007)		*			*			Based on MRI data	*			*	*		S	F
Gu et al. (2010)			*		*			Based on CT & MRI data	*			*		*	S	F
Luo et al. (2011)	*				*		*		*			*		*	F	
Chokhandre et al (2012)			*	*				Based on CT data	*		*			*		*

S indicates characterisation of the skin biomechanical behaviours.

F indicates characterisation of the fat pad biomechanical behaviour.

Reviewing the projects which have used inverse FEA method to characterise the material properties of the heel pad, the gaps between the existing numerical models and what would be necessary to obtain more accurate material properties of the heel pad, have been identified. It is also evident which measurements techniques are required to address some issues relating to data collection for model development and model validation. These are summarised below:

- The heel pad is a complex structure consisting of the macro-chamber, micro-chamber and skin layers. These tissues have different structures and material properties that have direct effects on the biomechanical behaviour and stiffness of the heel pad and consequently the likely formation of the heel pain and injuries. In most studies, the heel pad was considered as a homogeneous single layer structure with a single value representing the heel pad stiffness. In four cases, the heel pad was modelled as a composite two-layer material (7, 10, 11, 77). In one of these studies it was shown how a two-layer model consisting of fat pad and skin could more accurately predict the pressure distribution under the heel than one-layer model (11). Knowing that the fat pad have inhomogeneous structure composed of two layers with different properties, which can be affected by age and pathological changes differently, it is expected that a model with a discrete three layer structure can more accurately predict the biomechanical behaviour of the heel pad.

  Moreover, presently only plantar pressure measurements are used clinically to estimate foot risk due to overloading of the foot. However, because of complex geometry, discrete internal structures and nonlinear material behaviour of the heel pad soft tissue, the external force applying to the heel may result in inhomogeneous internal stress condition (81). Therefore, the relationship between the plantar pressure and internal stress does not seem to be simple. Since some studies indicate that the heel ulcers initiate internally (49, 82) and the location immediately beneath the calcaneus tuberosity has been reported as the region of plantar heel pain (83), it is important to measure the stress within the heel tissue

for estimation and addressing the ‘at risk’ foot. In the absence of an equipment to measure the internal stress experimentally, the FEA of the heel pad can be used as a solution to predict the internal foot stress (81). Although FE models with homogenous single and two-layer heel pad can provide valuable data relating to plantar measurements at the surface of the model their usage in the prediction of internal stresses of the foot is limited by lack of multi-tissue geometry (81). Therefore, future studies should consider the heel pad as a composite material and characterise the skin, micro-chamber and macro-chamber as separate layers.

- The biomechanical behaviour of the heel pad depends on the heel pad geometry and the shape of the calcaneus as well as the interfacial biomechanical properties (84). For instance, in terms of force-deformation relationships, the thickness of the fat pad and the skin are amongst the key factors affecting the results. Increased thickness of the skin may cause increase in the heel pad stiffness. Cavanagh et al. studied the effect of calcaneus geometry on plantar pressure under the heel (17). In some studies a simplified geometry was used to model the heel pad, only the thickness of the heel pad was measured and considered in the FE modelling. Therefore, future studies should seek to use subject-specific anatomically detailed model of the heel pad to determine the accurate material properties of the heel pad and study its responses under loading.
- The heel pad exhibits nonlinear behaviour with high compliance at low force and high stiffness at increasing force. The energy dissipation occurs during a loading-unloading cycle, and the heel pad displays stiffer behaviour with increasing loading rate, demonstrating viscoelastic behaviour (12). In most studies the heel pad was modelled as a hyperelastic material rather than viscoelastic. In doing so, the heel pad was considered independent of the effect of loading rate. The hyperelastic model is only capable of simulating the heel pad response for a specific natural activity of standing, walking or

running, depending on the loading rate at which the experimental data were collected. Hence, in future studies the viscoelastic nature of the heel pad sub-layers should be considered and these sorts of properties should be determined as well as hyperelastic properties to make FE model capable of simulating the heel pad behaviour at different load/loading velocity conditions.

- The heel pad shows different biomechanical responses depending on the method under which it is examined. In some studies, either *in-vitro* or *in-vivo* measurements obtained from indentation tests using too small indenters were used to study the behaviour of the heel pad which cannot evaluate the heel pad responses during actual gait. Therefore, in future studies it is important to use quality *in-vivo* experimental data collected from a compression tests using a large indenter for development and validation of FE models capable of interpreting actual behaviour of the heel pad.

2.4 APPLICATIONS OF FEA IN FOOTWEAR DESIGN

The heel pad is under repetitive high stresses relating to cycles of loading during locomotion. Plantar pressures should be relieved in patients with plantar heel pain to both address clinical symptoms and address stress experienced by inflamed tissue. There are a range of strategies related to use of different materials and geometries around the heel to reduce load applied to the heel and related tissues. Accordingly there is a great interest in design of insoles and footwear products that might reduce the load, pressure or stress related to the heel pad. This might be through use of energy absorbing material under the heel, or changes in the geometry of the footwear/insoles around the heel to change the heel pad geometric responses to loading or a combination of both approaches.

A variety of research has been done to design footwear products using measures of plantar pressure. This information is used in designing footwear in order to redistribute and reduce

high plantar pressure under the heel and metatarsal regions. These measurements were obtained using pressure platforms and flexible pressure-sensing insoles (85, 86). However, whilst these studies can identify the changes in external loads due to variations in footwear or insole designs, they are expensive and time-consuming. Large number of physical testing on different subjects with different footwear is required to achieve reliable results. A combined FE model of the foot and footwear can provide biomechanical information about influence of the footwear on behaviour of the heel pad and thus reduce the risk of injury and tissue damage. It also allows quick and easy modification of footwear, which results in a more rapid search for optimum designs. A number of studies have used FEA to understand the effects of footwear design.

Chen et al. developed a 3D model of the foot of 24 years old subject to investigate effects of the total contact insole on redistribution of the plantar stresses (87). A homogeneous hyperelastic material model was used to represent the heel pad soft tissue (Figure 2.25). The combined heel pad and insole model was compressed by a rigid plate up to total displacement of 2.4mm at velocity of 20mm/s. They tested changes in plantar stress when using flat and two sets of insoles that their geometries were designed to match the shape of the foot and thus maximise the contact area under the foot with different material combinations. The flat insole was made of Microcell Puff. The first set of total contact insole was made of three layers: top layer of PPT; mid-layer of Microcell Puff; bottom layer of Thermocork. The second set of total contact insole was made of two layers: top layer of medium Plastazote; bottom layer of PPT. The analysis predicted reductions in peak plantar pressure and average normal stresses of 19.8% to 56.8% on various foot regions (except the mid-foot and hallux regions) by wearing total contact insoles compared to flat insole. This method had the benefit of comparing the effects of different insole conditions on a plantar pressure using the same foot

geometry, loading conditions etc. They reported that the two sets of total contact insoles used in this study reduce the plantar pressure in the heel region.

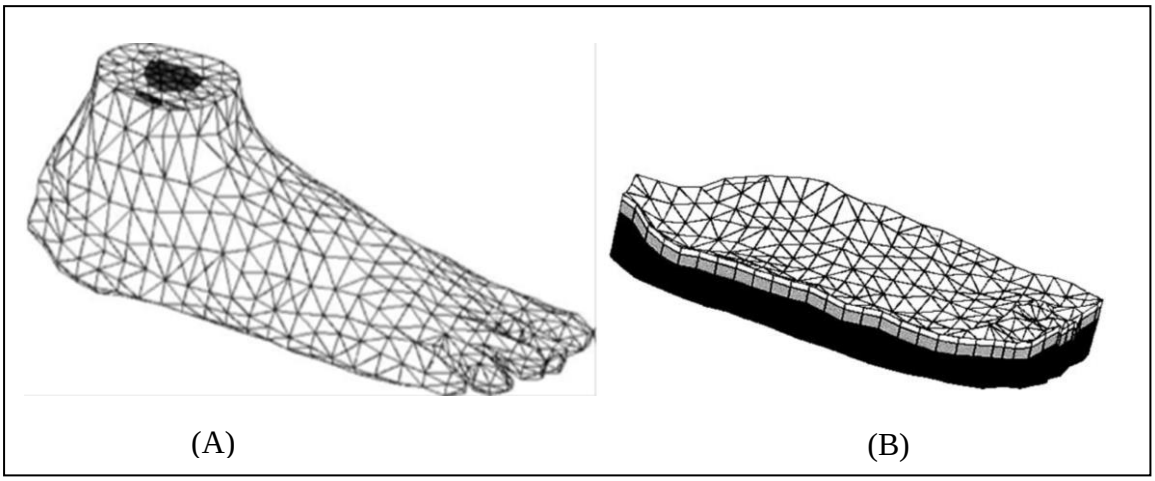

Figure 2.25: A 3D FE model of the foot and the insole: (A) The complete foot model of the bone and the soft tissue; (B) The insole model. Derived from (87).

Goske et al. used a 2D plane strain FE model of the heel pad to investigate effects of insole design parameters such as shape, material and thickness of insoles on the heel plantar pressure (88). Microcell Puff, Microcell Puff Lite and Poron cushioning were used for insole design while firm crepe and leather were used to model midsole and sidewalls respectively.

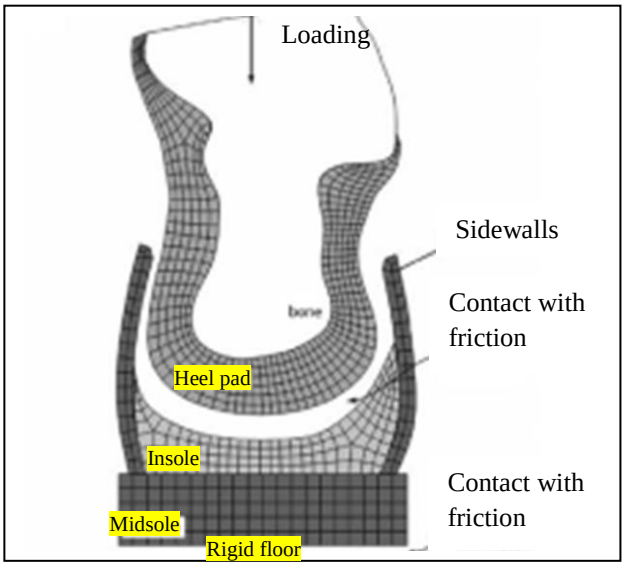

Figure 2.26: A footwear model interacting with the heel pad. Derived from (88).

FEA allowed studying 27 insole designs systematically. The single layer heel pad model was developed based on MRI data (Figure 2.26) and modelled the heel pad as a hyperelastic material. The compressive load of 678N was applied to the heel pad to simulate loading at first step of walking. They reported that the geometric conformity of the insole to the shape of the heel pad is the most important design factor affecting the heel plantar pressure, whereas

the insole material selection has the least influence on the plantar pressure. The results showed that the peak pressure was relieved by 24% using flat insole compared to barefoot condition. This value increased to 44% using full conforming insoles.

Spears et al. used a 2D plane strain two layers FE model of the heel pad to investigate the heel counter effect on the peak stress (Figure 2.27) (11). Two rigid and deformable behaviours were assigned to the heel counter with using leather material for deformable condition. They reported that in the presence of the heel counter peak compressive stress increased (16%) whereas tensile and shear stresses decreased (33% and 26%) in the skin layer. In the fat pad, compressive and shear stresses decreased (22% and 58%) and tensile stress remained negligible. These trends were mirrored by high friction, increase of thickness of the heel pad and using deformable heel counter.

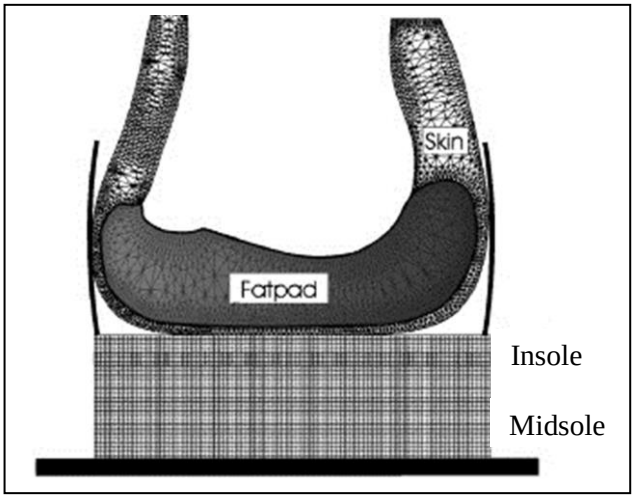

Figure 2.27: A 2D model of the combination of the heel pad and the footwear. Derived from (11).

Cheung et al. developed a 3D FE model of the human foot and ankle based on MR images (Figure 2.28). The aim of their project was to combine FEA and Taguchi method to study the sensitivity of five design parameters including arch type, insole thickness, midsole thickness, insole material and midsole material on plantar pressure reduction (74). The heel pad was

modelled as a single layer hyperelastic material and its responses were studied under 550N ground reaction force.

The foot orthosis was made of insole, midsole and outsole layers. Polyurethane (Poron-L24 and Poron-L32) and Eva foam (Nora-SL and Nora-SLW) were used for insole and midsole material. High density Eva foam (Nora-AL) was assigned to outsole layer. According to their findings, among the five design factors, arch type and insole stiffness were the first and second important factors for peak pressure reduction. The insole with custom-moulded shape and softer material had the greatest reduction on plantar pressure.

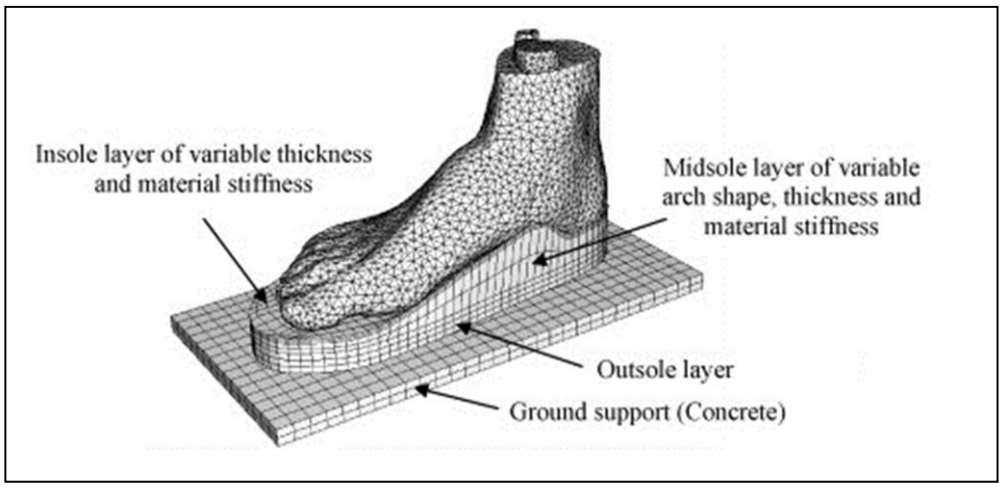

Figure 2.28: A 3D finite element model of the foot and the footwear. Derived from (74).

Luo et al. created a 2D axisymmetric model to investigate the influence of insole geometry and insole material on the heel plantar stress (Figure 2.29). The heel pad was modelled as a composite hyperelastic material with two layers namely the fat pad and the skin. Two types of insole geometries were investigated in this study: flat insoles with or without reliefs (cavities under the heel); custom contoured insoles. Three insole materials were used to study their effects on the plantar pressure: material with stiffness equal to the subject's heel pad; material with 2.5 times the stiffness of the subject's heel pad; and material with 6 times the stiffness of the subject's heel pad.

The responses of the heel pad under 200N load, about $\frac{1}{4}$ of the subject's body weight were studied. The results showed that flat insoles with reliefs reduce the pressure beneath the heel pad more than the flat insoles without reliefs. However, custom insoles provide the most reduction with value of 79%-92% in the heel plantar stress. Comparing the insole material the maximum reductions in tissue stress were 25% when the stiffness of insole material was equal to the stiffness of the subject's heel pad in flat insoles (77). This result is agreement with findings of the study conducted by Cheung et al. and Goske et al, that the softer insole material has more effect on reduction of the heel plantar pressure (74, 88).

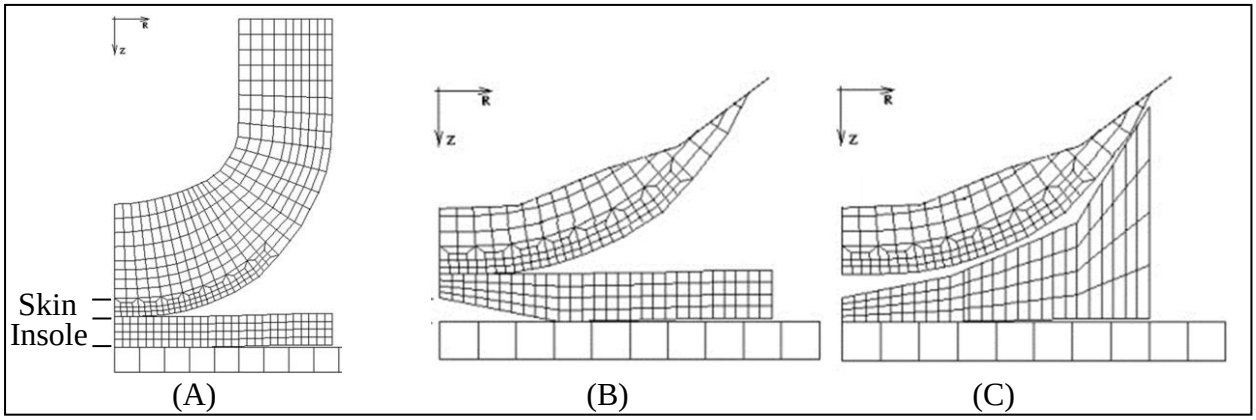

Figure 2.29: : A FE model of the heel pad interacting with different insoles: (A) Meshed model of the heel pad; (B) Flat insole with conical relief at bottom; (C) Custom contoured insole with conical relief at top. Derived from (77).

Reviewing the studies which used FEA for footwear design showed that FEA could assist design processes towards an optimum without burden of carrying out a large number of experiments. Furthermore, compared to experimental studies, not only does FEA reveal the responses of the heel pad at its outer surface (of the model) but also shows the internal reactions of the heel pad sub-layers tissues.

Apart from the use of FEA of the heel region in footwear design there are many more applications which can provide easy and quick way to reach valuable conclusions for better understanding foot functionalities and also improving physical experimentation procedures. Some of applications of the FE model of the heel region are as follows: (1) investigation of

effects of various experimental conditions (e.g. indenter size and shape) and the heel pad geometry (e.g. heel pad thickness and maximum width) on heel pad biomechanical responses. These results can be beneficial in explaining why experimental data available in the literature differs from each other and how we should be careful using and comparing them; (2) studying effects of other factors than design features such as friction, which might be influential on the heel pad behaviour; and finally (3) studying effects of stiffness of each of the heel pad sub-layers on the heel pad biomechanical behaviour. The characteristics and applications of the FE models reviewed earlier are summarized in Table 2.7.

Table 2.7: Summery of FE models used for footwear design

Research	Geometry	Material	Application
Chen et al. (2003)	3D (foot bones, cartilage, ligaments, soft tissue, foot orthosis)	Bones, cartilages, ligaments, soft tissue (linear elastic), insole, midsole (hyperelastic)	Flat and total contact insole on stress and plantar pressure distribution
Goske et al. (2006)	2D (heel pad, heel counter, insole, midsole)	Heel counter (elastic), heel pad, insole, midsole (hyperelastic)	3 insole conformity levels, 3 insole materials, 3 insole thicknesses on plantar pressure
Spears et al. (2007)	2D (skin, fat pad, insole, midsole, heel counter)	Skin, fat pad, insole, midsole (hyperelastic), heel counter (elastic)	2 heel counter materials on peak stress
Cheung et al. (2008)	3D (foot bones, soft tissue, cartilage, ligaments, fascia, foot orthosis, ground)	Bones, cartilage, ligaments, fascia, ground (elastic), soft tissue, orthosis (hyperelastic)	4 arch type levels, 4 insole thicknesses, 4 insole materials, 4 midsole thicknesses, 4 midsole materials on plantar pressure
Luo et al. (2011)	2D (skin, fat pad, insole, ground)	Skin, fat pad, insole (hyperelastic), ground (elastic)	5 insole shapes, 3 insole materials on stress, strain and strain energy density

Reviewed FE models have shown their applications in understanding of influence of heel supports on the biomechanical behaviour of the heel pad. More detailed geometry of the foot and more accurate material properties of the FE model components can advance the representation of the combination of the foot and footwear. It is no surprising to find a wide range of variations in effects of the foot support on the internal stress and plantar pressure amongst the reviewed studies. The sources of the divergence might be difference between: material properties and geometry of the footwear model, loading and boundary conditions and the degree of simplification of material properties and geometry of the foot model. Although

the reviewed models obtained different amounts of the stress or pressure relief using foot supports, similar agreements can be found in their studies: (1) decrease in stiffness of the insole material increases the reduction in stress and plantar pressure in the heel pad; (2) increase in thickness of insole material elevates the heel stress and pressure relief; (3) full conforming insole is an effective factor in pressure reduction by increasing contact area; (4) heel counter decreases the stress in the heel by preventing heel pad from excessive deformation and maintaining more soft tissue material under the calcaneus.

2.5 AIMS AND OBJECTIVES

The previous sections reviewed different experimental methods used to characterise the human heel pad, and the information and data describing its properties. The experimental and FEA modeling tools used to investigate heel pad function were also reviewed, including how different models were constructed, validated and implemented, especially to test footwear and insole designs.

Major issues of these FE models and experimental results were identified and discussed. These issues were mainly caused by using **simplified models** to simulate experiments, such as the use of hyperelastic material models to describe viscoelastic behaviour, ignoring experimental conditions and limiting models to 2D behaviour. Furthermore, the influence of the **sub-layers and geometry** of the different part of the heel area on the biomechanical response were not considered. Some of these models were developed based on experimental results obtained from cadaveric tissue samples or at conditions which do not replicate the heel pad behaviour during gait (e.g. using a small indenter to compress the heel pad and obtain its force-deformation response). Use of *in-vivo* data should provide better model performance and improved validation.

The aim of this project is to address these issues and limitations in the previous works and develop a heel pad model that can adequately represent *in-vivo* properties of the subject-specific heel pad. To achieve this aim, several objectives are defined.

1. The **first objective** of this study is to carefully develop an anatomically detailed 3D model of composite three-layer human heel pad based on unloaded MRI scan data of the heel region. The aim is to consider the effects of the shape of foot bones, the geometry of the heel and its sub-layers (macro-chamber, micro-chamber and skin) and confinements from surrounding tissues such as plantar fascia and muscle tissues on mechanical responses of the heel pad.
2. The **second objective** is to characterise the mechanical behaviour of heel pad sub-layers *in-vivo*. An existing system consisting of a high resolution ultrasound and loading system are used to measure the deformations of heel pad and its sub-layers and simultaneously measure the applied force during loading.
3. The **third objective** of this project is to determine the hyperelastic material properties for each separate heel pad sub-layers. Two nonlinear elastic material properties for each of the separate macro-chamber, micro-chamber and skin layers are determined by fitting the predicted data to *in-vivo* experimental measurements. Since the material descriptions of the heel pad sub-layers affect the mechanical behaviour of the heel pad, it is important to determine the material properties of each layer to improve the accuracy of the model predictions.
4. The **fourth objective** is to estimate the viscoelastic material properties of the heel pad sub-layers. Two viscoelastic parameters are obtained by fitting the model predicted force-strain data to *in-vivo* experimental measurements. It makes it possible to use the model with increased confidence in prediction of the heel pad behaviour at simulated gait conditions (higher loading velocity).

5. The **final objective** of this project is to implement the FE model of the heel region to address foot and footwear research questions. First the FE model is used to study the effects of the experimental setup conditions and the heel pad geometry on the biomechanical responses of the heel pad under loading. Then the FE model is used to investigate the effects of footwear design factors such as material choice and insole and midsole thickness on heel pad stress. Finally sensitivity of the FE model to subject-specific heel geometry is investigated. This is achieved by estimating the hyperelastic material properties of heel pad sub-layers of a subject other than the individual whose heel was used to construct the model.

3. Chapter Three:

DEVELOPMENT OF THE HEEL REGION GEOMETRY

3.1 INTRODUCTION

The aim of this chapter is to generate an anatomically detailed geometry of the human heel area for development of an FE model in Chapter 4. To create the geometry for the FE model of the heel region, first a surface geometry of the heel region was developed based on MRI data of the right foot of a volunteer. The surface geometry had complicated features, which made it difficult to be analysed in the FE software. Therefore, it was required to develop a 3D solid geometry of the heel, ideal for FEA. The solid geometry was developed replicating the surface geometry. To ensure about the quality of the final model, the solid model was compared with MRI data. The strategy to generate the model of the human heel region is schematically illustrated in Figure 3.1.

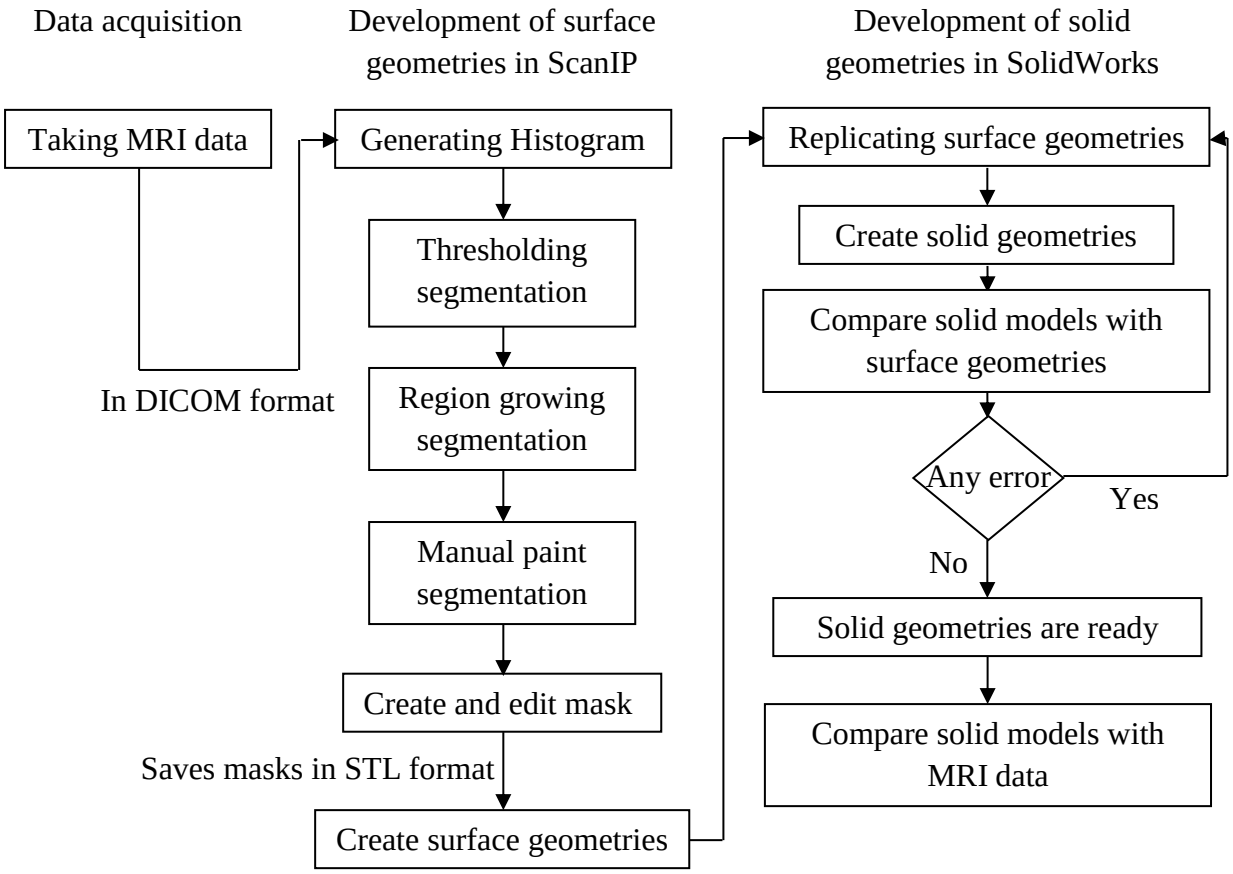

Figure 3.1: The process of development of solid geometries

3.2 METHODS

In this chapter, the methodology used to develop the 3D solid model of the human heel region is discussed in detail. This chapter is divided in to 3 main sections.

1. Data acquisition: The method of data acquisition is introduced.
2. Development of surface geometries: Generating of surface geometry for each structure in the heel region is explained. The model of the heel region includes six structures of skin, macro-chamber layer, micro-chamber layer, foot muscles, foot bones and the plantar fascia.
3. Development of solid geometries: The method for development of the final 3D solid geometries is described.

3.2.1 Data Acquisition: Magnetic Resonance Imaging (MRI)

The first step in FEA is to show the geometry of the model in the computer. The FE model can be developed as 2D or 3D according to the purpose of the analysis. 2D is a simplified model of a physical structure while 3D model is more realistic and can simulate the behaviour of a physical structure more accurately. The main disadvantage of 3D compared to 2D is the significantly increased computational time.

In this project, MRI data of the heel area was used to develop 3D geometries of different structures in the heel region. The MR images were taken from the right foot of a healthy female subject (age 34 years old, height 164cm, weight 63kg and shoe size UK5) in coronal plane at neutral position (called **Subject 1)**. The university of Salford ethical committee approved the study and data collection. MRI data were T1 weighted with flip angle of 25 degree taken using 3D fast field echo using Philips 1.5T Acheiva with dimensions of 0.286458mm×0.286458mm taken with 1.25mm intervals (Figure 3.2). A bird-cage coil (head coil) was used as a receiver antenna to make the magnetic field as homogeneous as possible

and take images with better quality. 75 series scans were taken to cover 9.25cm from the back of the foot and it took 8 minutes per session. The Wolfson Molecular Imaging Centre (WMIC) team in Christie Hospital in Manchester performed the MR scanning.

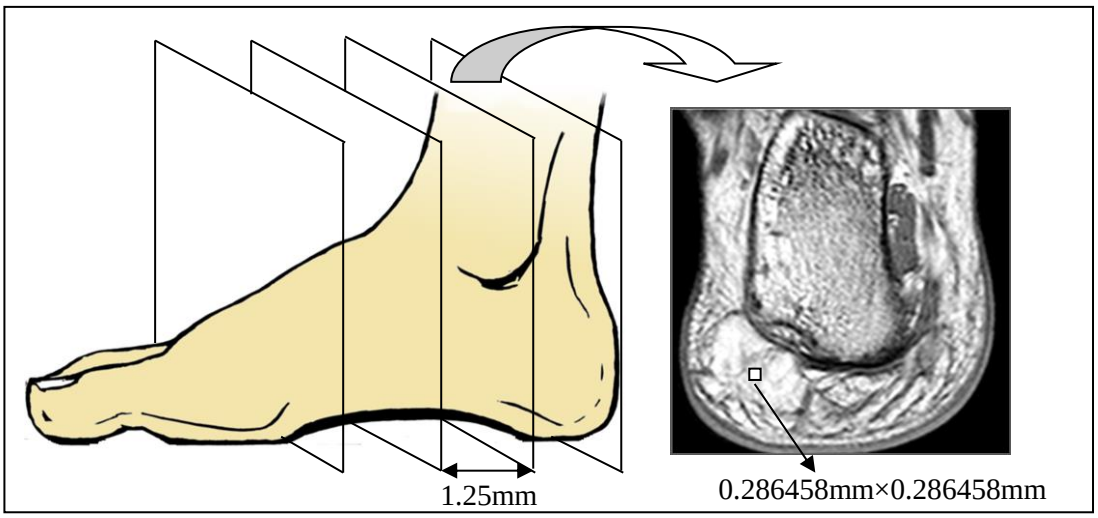

Figure 3.2: Dimensions of MRI scans

MRI is a medical imaging technique to produce detailed images of internal structures of the body. MRI uses the property of Nuclear Magnetic Resonance (NMR) to image nuclei of hydrogen atoms -single protons- inside the body (89). The hydrogen protons normally spin in random directions. If they are exposed to a strong magnetic field, they tend to line up like a compass needle. If the protons are hit by a short radio signal whose frequency is equal to the protons frequency, they will be knocked out of the alignment and flipped around. When the radio signal is stopped, the flipped protons will try to return into alignment with the magnetic field. In the process of returning, protons emit a radio signal of their own which reflects the presence of a specific tissue (90). This process is shown in Figure 3.3.

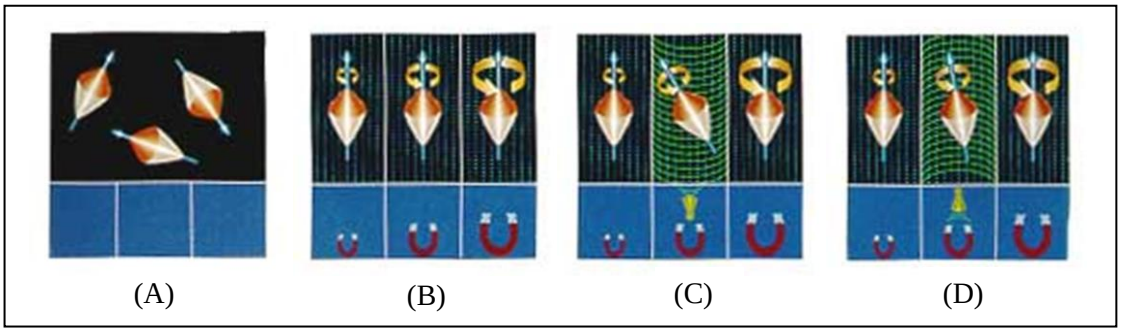

Figure 3.3: The way MRI works: (A) Hydrogen protons, (B) Hydrogen protons exposed to magnetic field, (C) Hitting proton by radio wave, (D) Proton returning to its original orientation after stopping the radio wave. Derived from (90).

In MR images the contrast between different tissues are provided by proton density, T1 relaxation time and T2 relaxation time. T1 and T2 relaxation times define the way that the protons revert back to their resting states and provide different intensities of images (91). Some tissues are contrasted better and can be differentiate easier with one technique than the other. T1 contrast shows better anatomical detail. In T1 weighted images, soft tissues like fat appears bright whereas water and fluid appears dark. In T2 weighted images, fat, water and fluid are bright. Since soft tissues were the focus of this project and it was important to obtain clear and detailed images to distinguish them, the MR data were taken in T1 weighted. An example of T1 and T2 weighted images of foot in sagittal view is shown in Figure 3.4.

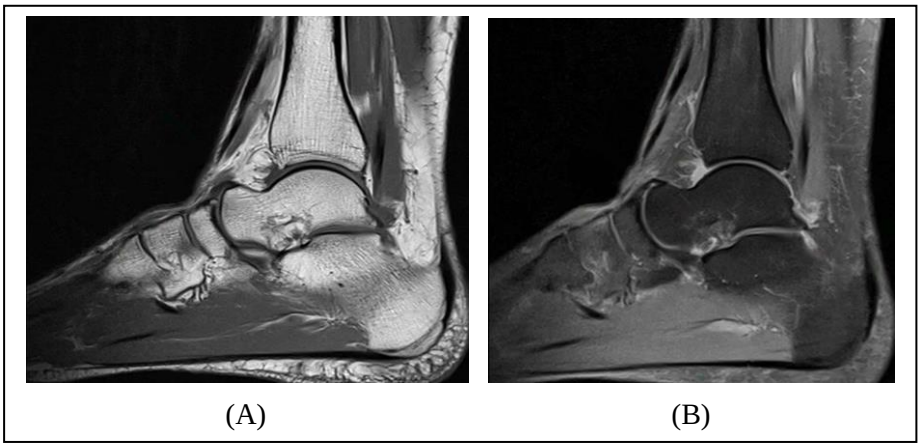

Figure 3.4: Difference between T1 and T2 weighted MR images: (A) T1 weighted; (B) T2 weighted.

The MRI data was available as a series of greyscale 2D images. Usually the 2D MR images are available in DICOM (the Digital Imaging and Communications in Medicine) format, which is a standardised medical image format. Image processing software is required to convert DICOM images to an analyse format. By putting 2D slices, each as a separate DICOM file, together a 3D picture is formed.

To get the MRI scan, the subject lies on a scan table in a type of tunnel that contains a large and powerful magnet. Part of the body to be scanned is directly lies in the centre of the magnet. The MRI scanner is shown in Figure 3.5.

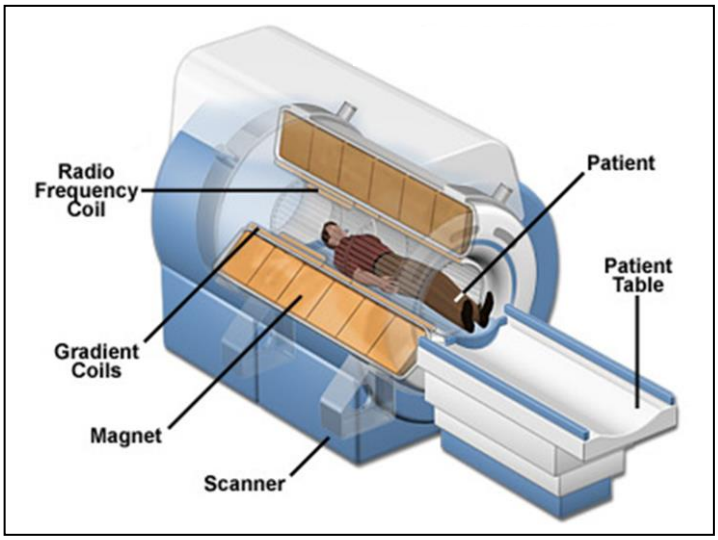

Figure 3.5: MRI scanner. Derived from (92).

3.2.2 Development of the Surface Geometries

MRI data was used to develop 3D surface geometries of different parts in the heel region. Image processing is an important step in development of surface geometries of distinct tissues that lie close to each other. Based on literature several software are available that can be used to process DICOM data of medical images to produce surface geometries such as MIMICS, Amira, ImageJ-FIJI and Simpleware. In this project Simpleware ScanIP v3.1 (Simpleware Ltd, Exeter, UK) was chosen for image processing because of the tools that it offers and the accessibility of the tools through its manual and example tutorial. This process started with

importing MRI data with DICOM format into ScanIP. Two main operations used for image processing are as follows:

- Pre-processing of MRI data
- Segmentation

3.2.2.1 Pre-processing of MRI Data

During importing MRI data into ScanIP, the histogram tool was used to reduce the noise and adjust the contrast between the region of interest and surrounding tissues (93). This tool allows seeing the frequency of the occurrence of pixels in greyscale band. In the histogram, the x axis represents the intensity value and y axis represents count of pixels in an image with the intensity value of x. Looking at the histogram of a dataset, it is clear that a certain type of tissue does not have a unique range of values and it is difficult to classify pixels of a type of tissue.

At the beginning of the pre-processing stage by deriving the histogram of the dataset and adjusting the intensity value settings, more contrast between different tissues could be generated. As it can be seen in Figure 3.6, the histogram shows peaks for intensity values which occur relatively more than others in a dataset. The first peak (largest) represents the background values while other peaks represent the object (94). To increase the contrast, the histogram was analysed by choosing "key values" such as the end of background peak and the high end of the final peak (94). By selecting the default option in window and level of the histogram tool instead of full data range option, the "histogram window and level" was set to the "key values" and thus contrast and clarity of the images were improved. By importing the series of MR images, the dataset could be seen in three different planes of coronal, sagittal, and transverse in ScanIP (Figure 3.7).

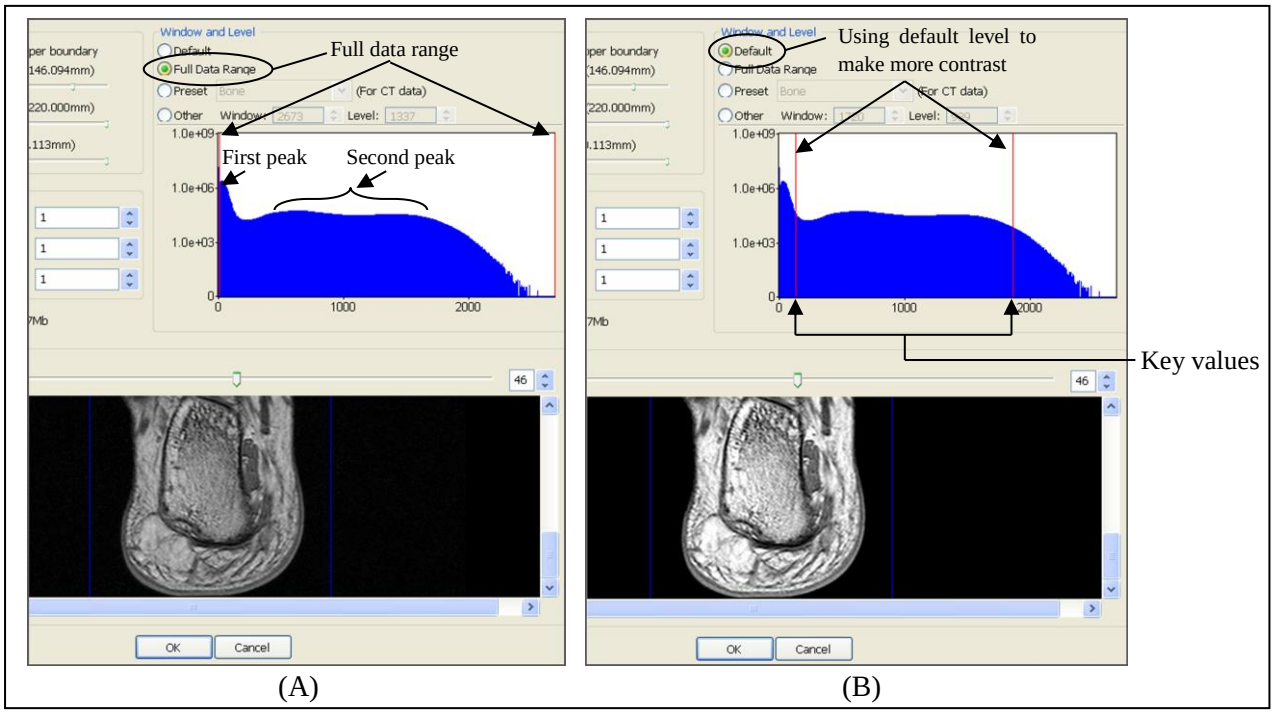

Figure 3.6: Using histogram to control the greyscale level, reduce the noise and increase the contrast between different tissues: (A) Using the full greyscale level to see the MR series of images; (B) Changing the level of greyscale to default level to better distinguish different tissues.

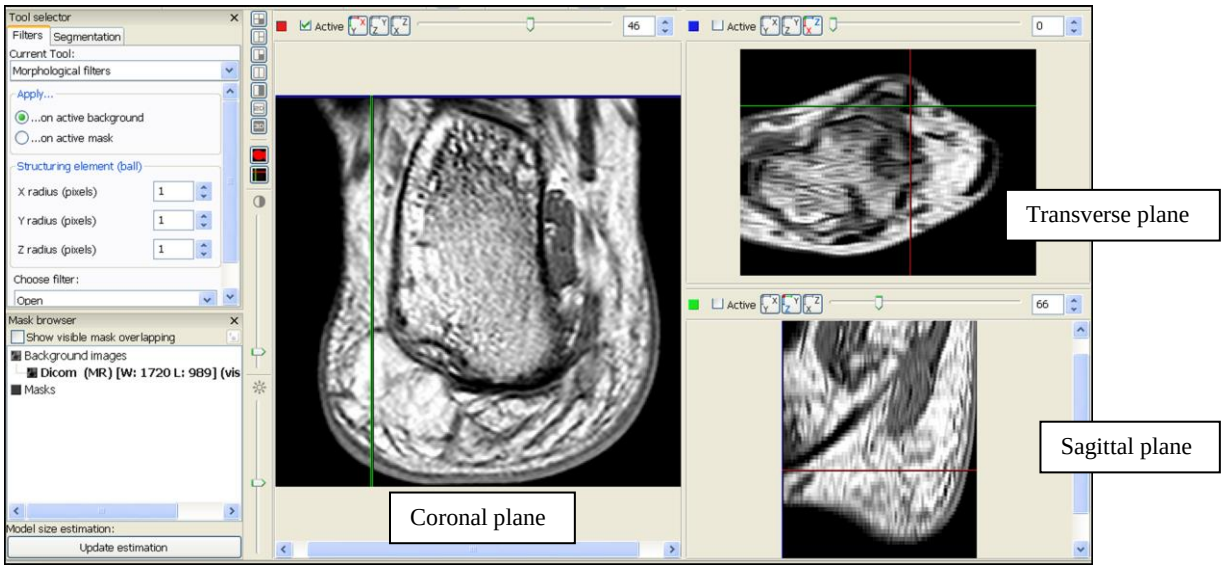

Figure 3.7: The MRI data in three views.

As it is shown in Figure 3.7, the quality of the images in the coronal plane was higher than the quality of the images in the other two planes. This was because the MR imaging was taken in

coronal plane and the pixel size in the coronal plane was 0.286458mm×0.286458mm while the pixel size in transverse and sagittal planes was 0.286458mm×1.25mm.

3.2.2.2 Segmentation

Segmentation is a process to identify a region by grouping appropriate pixels and define the boundaries of the region (94). This is very important step because the accuracy of the final model mostly depends on the initial segmentation. Since the quality of MRI data taken for this project was better in the coronal plane than the other two planes, the coronal plane was mostly used as a base plane for the segmentation. A foot atlas and reference to clinical expert was used during the segmentation to ensure about the identification of different tissues and their locations in the heel area. The segmentation was mostly based on greyscale level of different tissues. In T1 weighted MRI data, bone and soft tissues have similar greyscale values that make it very difficult to distinguish different tissues by only greyscale levels. Instead, different body tissues vary in texture and can be easily distinguished visually. Therefore, different segmentation algorithms including automatic, semi-automatic and manual segmentation tools were used for identifying different tissues in the heel area. First automated and then semi-automated segmentation tools were used as much as possible to improve the accuracy of the initial segmentation. At last, the manual segmentation tools were used to finish the segmentation by filling the holes, eliminating selected wrong pixels and tiding up the interfaces between different regions.

The skin of the heel pad was the first tissue to be distinguished and segmented. At the beginning, “threshold tool” which is one of the automatic segmentation tools was used to identify the boundary of the skin layer. Thresholding is a non-linear operation, which converts a greyscale and colour image to a binary image. During the threshold segmentation, two upper and lower parameters, known as intensity threshold levels, are used to create a partition of pixel intensities. Each pixel in the image is compared with these values. The pixels whose

intensity is between upper and lower values are grouped together to one region and the pixels with intensity less than lower value are grouped to another region and the remaining pixels are set to the third region (95). To start suitable upper and lower threshold bounds were needed and initial settings of these are very important because these two values define the contrast between different structures. To find the optimum lower and upper threshold values the dynamic threshold function was used which offers the possibility to visually determine those values by checking automated segmentation to visual inspection of tissue boundaries. Adjusting the lower and upper threshold values was continued until the outer boundary of the skin layer was selected. Figure 3.8 shows the thresholding of the skin layer. In the threshold algorithm, the pixel selection is based on greyscale level and it does not assume pixels are connected in the image. For this reason, some pixels at the boundary of the foot bone were selected during the process of identifying skin boundaries (Figure 3.8). In these cases, subsequently manual de-selection is used to modify the segmentation and remove wrong selected pixels.

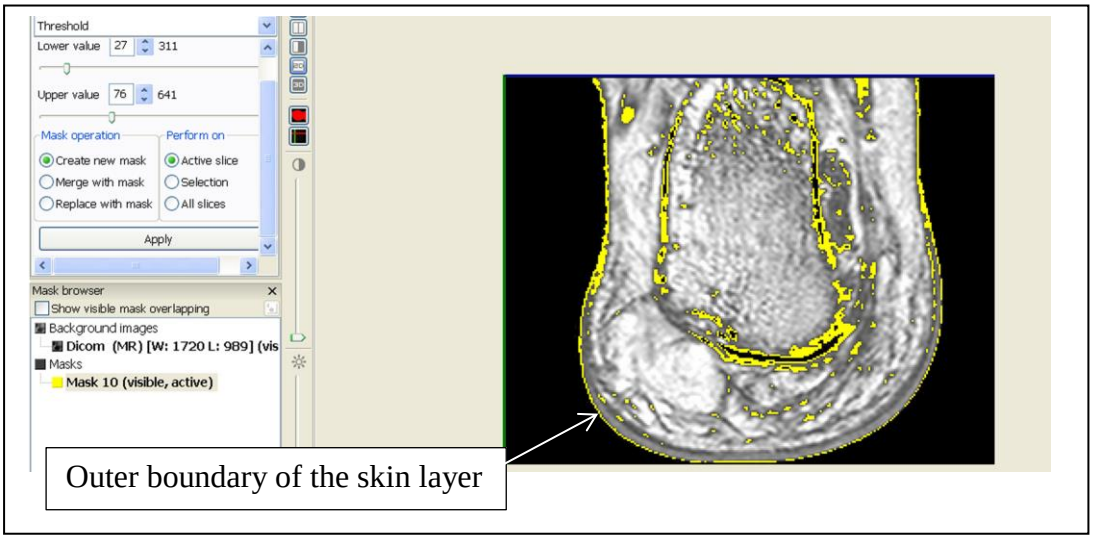

Figure 3.8: Threshold based segmentation of the skin layer with lower threshold value of 27 and upper threshold value of 76.

In the next stage, the “confidence connected region growing” algorithm was used to select the pixels inside the skin layer. The confidence connected region growing is a semi-automatic

segmentation tool which extracts connected regions in the image based on the pixel intensity. This technique requires a seed point as an input to represent the tissue of interest. Pixels in small neighbourhood region of the seed point are examined and added to the growing region on the basis of criterion such as pixel intensity. Different algorithms use different criteria to add the neighbouring pixels to the segmented region. In this method, first the "mean" (m) and "standard deviation" (σ) of the region intensity are computed for a neighbour of 8 connected, 26 connected… (depends on the algorithm) of a seed point. Neighbouring pixels are added to the segmented region if their intensities fall between m-Aσ and m+Aσ. A is the user defined multiplier, which determines the sensitivity of the algorithm. This process repeats for a user-specified number of iteration and computes m and σ at each iteration for the segmented region until no more pixels can be joined to the growing region (96). The stages of this process are illustrated in Figure 3.9. In Figure 3.9, each block represents a pixel and the number written in each block indicates the pixel intensity.

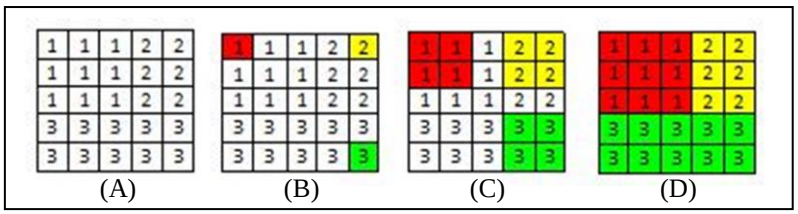

Figure 3.9: Segmentation using confidence connected region growing algorithm: (A) Pixels with three different greyscale intensity values; (B) Selecting seed points; (C) Growing segmentation; (D) Finishing segmentation.

To select pixels belonging to the skin layer, a seed point was picked inside the skin layer area and then the skin region grown by adding the neighbouring pixels if their intensity values were in the accepted range. This process was repeated until most of pixels for the skin layer were selected. As it can be seen in Figure 3.10, some wrong pixels were selected while some of the pixels that were part of the skin layer were not picked. In the following stages, the unselected skin pixels were filled and the incorrectly selected pixels were deselected using another two segmentation tools.

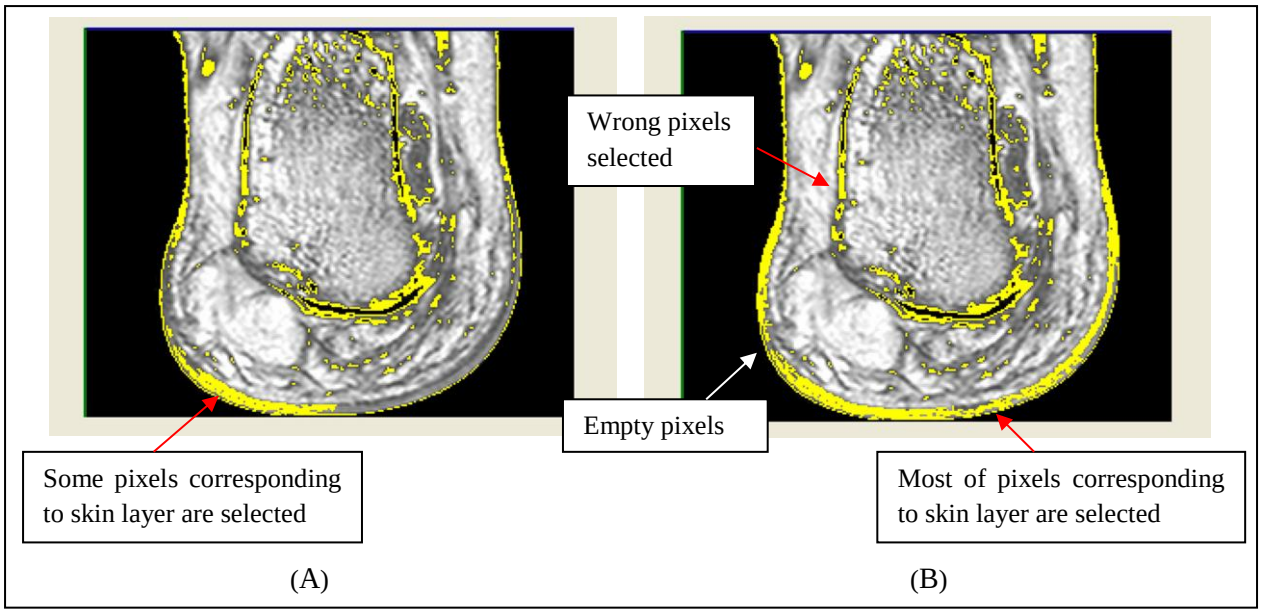

Figure 3.10: Confidence connected region growing based segmentation: (A) Partly skin layer pixel selection; (B) Full skin layer pixel selection.

In the next stage, "floodfill" algorithm was used to fill the cavities. The floodfill is a segmentation tool that selects the area that is connected to a selected pixel and fully surrounded by previously selected pixels to be included in a segmented region. In Figure 3.11, an example shows how floodfill is started by selecting a pixel inside the area and then the algorithm marks all pixels inside the area as selected and leaves borders and pixels outside the area. Figure 3.12 shows that by applying floodfill algorithm to the MR images, all empty pixels belonging to the skin layer were filled. The manual "paint" tool was the last segmentation tool used to refine the MR images by deselecting pixels that did not belong to the skin layer (Figure 3.13).

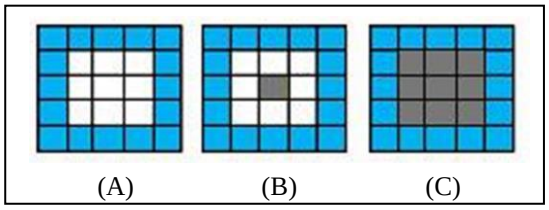

Figure 3.11: Segmentation using floodfill algorithm: (A) Unselected area surrounded by segmented region; (B) Selecting seed point; (C) Growing segmentation.

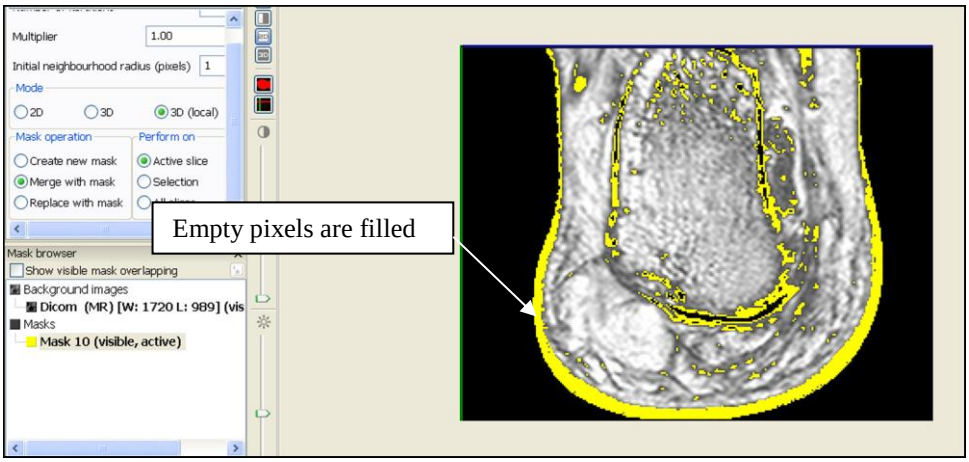

Figure 3.12: Using floodfill tool to fill the cavities in the skin layer.

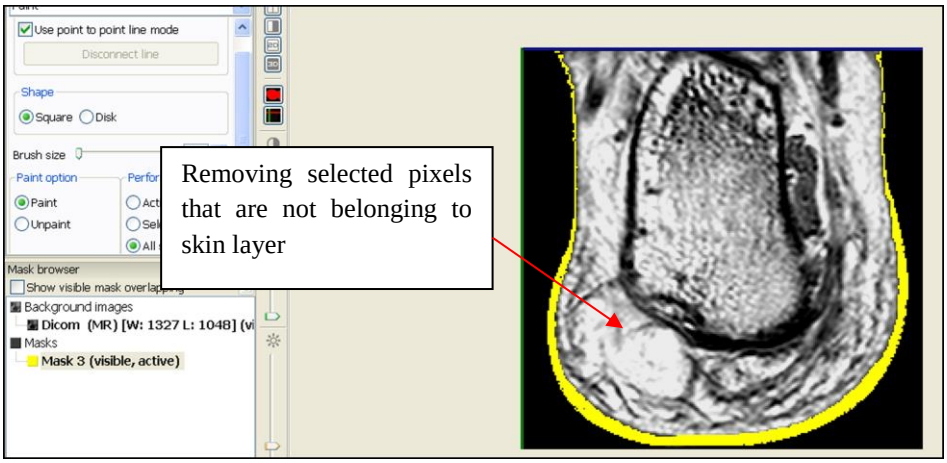

Figure 3.13: Manually refining MR images using the paint segmentation tool.

By performing, the operations discussed earlier on all 75 slices, the skin layer was segmented and differentiated in all MR images. At this point, it was possible to preview the 3D model of the skin layer (Figure 3.14). This is the 3D mask of the skin layer, which can be saved as surface model in STL (Standard Tessellation Language) file format and be exported into other engineering modelling software. STL format is a triangular representation of a 3D surface geometry.

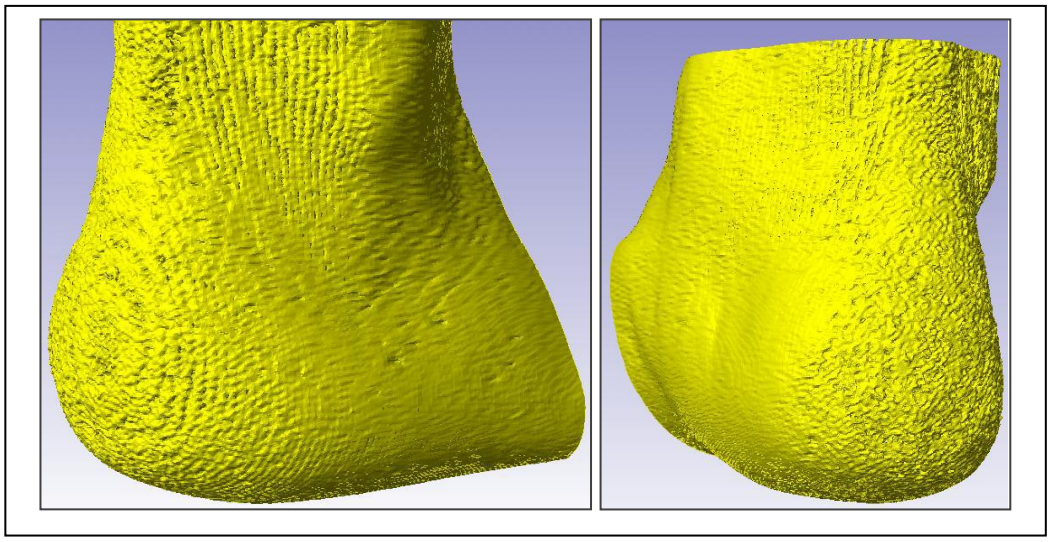

Figure 3.14: The 3D surface model of the skin layer.

The second part to be segmented was the stiff tissue in the heel pad area. This part consists of some part of calcaneus, talus, navicular, cuboid, 5th metatarsal bone and part of Achilles tendon join together to create the stiff tissue of the heel pad model. Since Achilles tendon is stiffer than the fat pad and it is far from the heel pad so it is unlikely to influence the fat tissue behaviour, it was joined to stiff tissue structure. MR images in three different planes were used to identify the boundary of the stiff tissue. Since the contours of the stiff tissue were easily distinguishable on the MR images, then this part could be mostly segmented automatically using threshold segmentation tool (Figure 3.15).

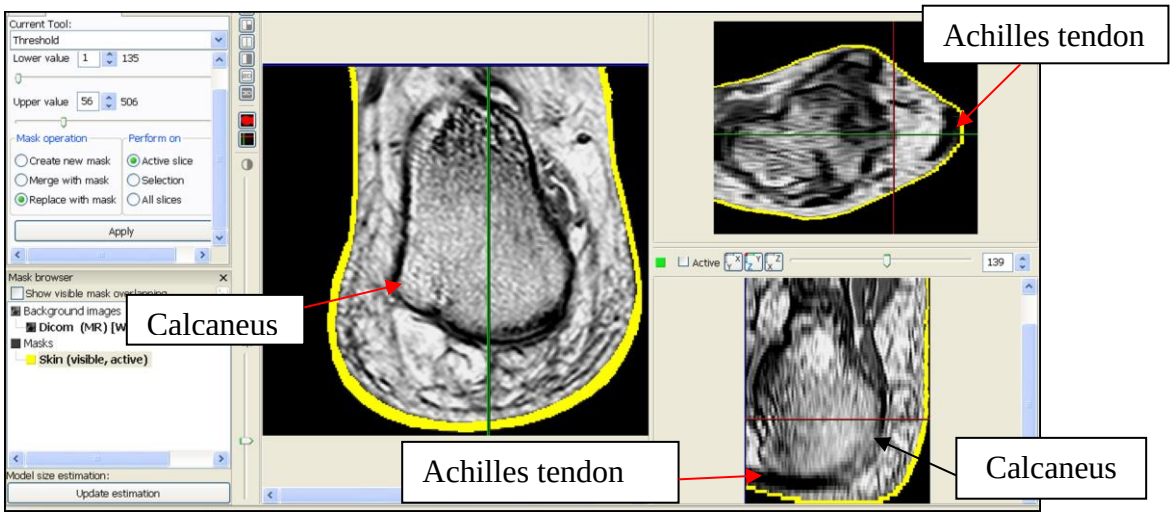

Figure 3.15: The stiff tissue in three different views.

The threshold was the first segmentation tool used for the segmentation. By adjusting the upper and lower threshold values the boundaries of the stiff tissue were identified (Figure 3.16). As it can be seen in Figure 3.16, some pixels around the skin layer were selected as well. They were not part of the stiff tissue and were deselected subsequently. On the other hand, the contour of the stiff tissue was disconnected in some areas, which was adjusted using the other segmentation tool subsequently.

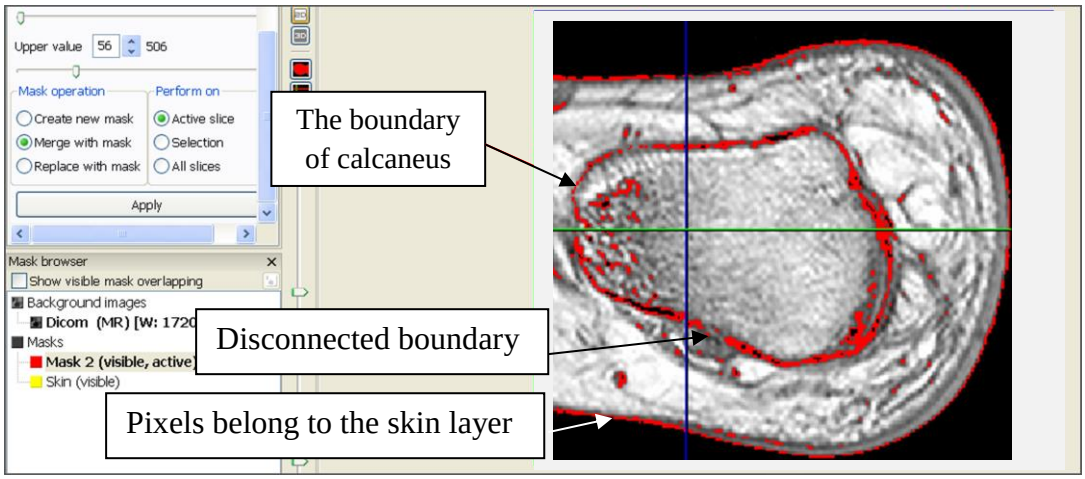

Figure 3.16: Threshold based segmentation of the stiff tissue. The disconnected boundary of the stiff tissue and selected pixels belong to the skin layer can be seen in the image.

The confidence connected region growing and floodfill tools were then used to add the unselected pixels, which belong to the stiff tissue, to the stiff tissue mask. Finally, the incorrectly selected pixels were deselected using the manual paint segmentation tool. These steps explained above are illustrated in Figure 3.17. By applying the above algorithms to all MR images the 3D surface model of the stiff tissue could be generated (Figure 3.18).

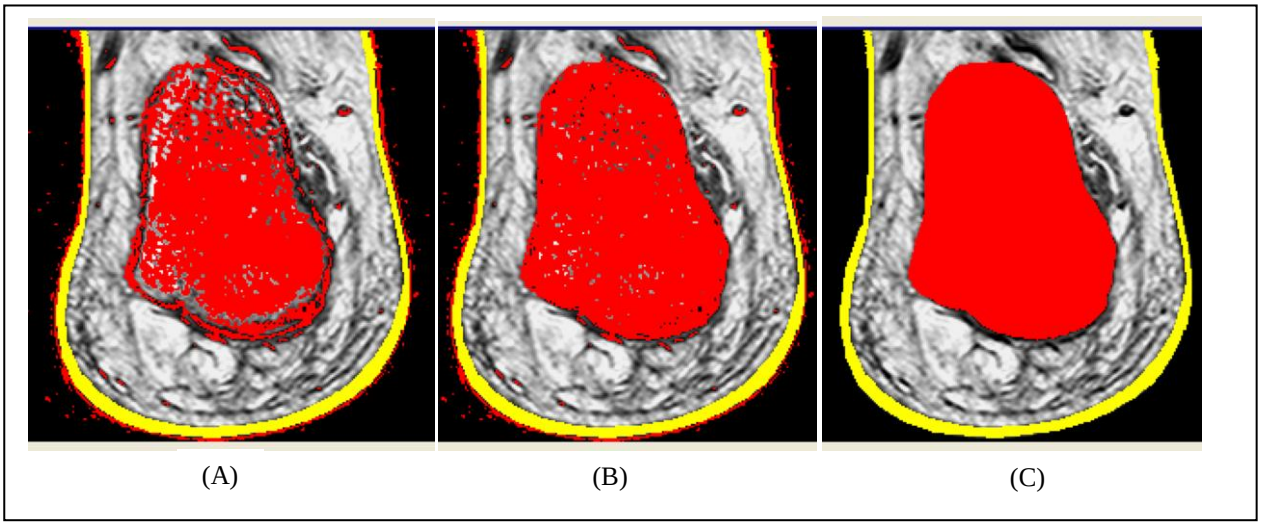

Figure 3.17: Using different algorithm for the stiff tissue segmentation: (A) Confidence connected region growing based segmentation; (B) Using floodfill tool to fill the cavities; (C) Using the Paint tool to refine the MR image.

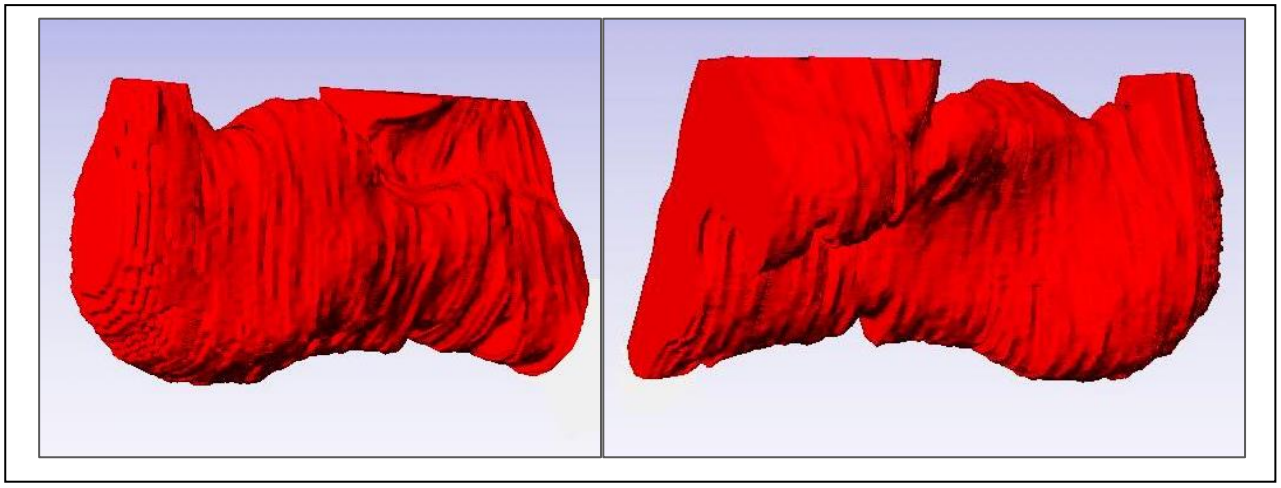

Figure 3.18: The 3D model of the stiff tissue in the heel area.

The next part to be segmented was the plantar fascia. The plantar fascia, also known as the plantar aponeurosis, is a strong layer of fibrous connective tissue initiating posteriorly from the tuberosity of the calcaneus and extending towards the toes. In Figure 3.19, section A-A shows the area under calcaneus tuberosity where the plantar fascia originates. For the foot, imaged in this project, the ultrasound measurements and MRI data agreed that the plantar fascia originated approximately 2.7cm from the back of the foot. The attachment of the plantar fascia to the calcaneus could be seen more clearly in the sagittal view (Figure 3.19). In

the MR images, the plantar fascia appeared as a dark grey homogeneous material while its internal structure was not clear.

As it can be seen in Figure 3.19, the plantar fascia shows contrast with the surrounding tissues. For segmentation of the plantar fascia, first the semi-automated confidence connected region growing algorithm was used to select the pixels belong to the plantar fascia by picking a seed point in this tissue. Then with the help of the manual paint tool, all of the unsuitable selected pixels were deselected. The 3D surface model of the plantar fascia was generated by applying these two segmentation algorithms on to the all MR images. The segmentation process is shown in Figure 3.20. The 3D model of the plantar fascia and its attachment area to the calcaneus are shown in Figure 3.21.

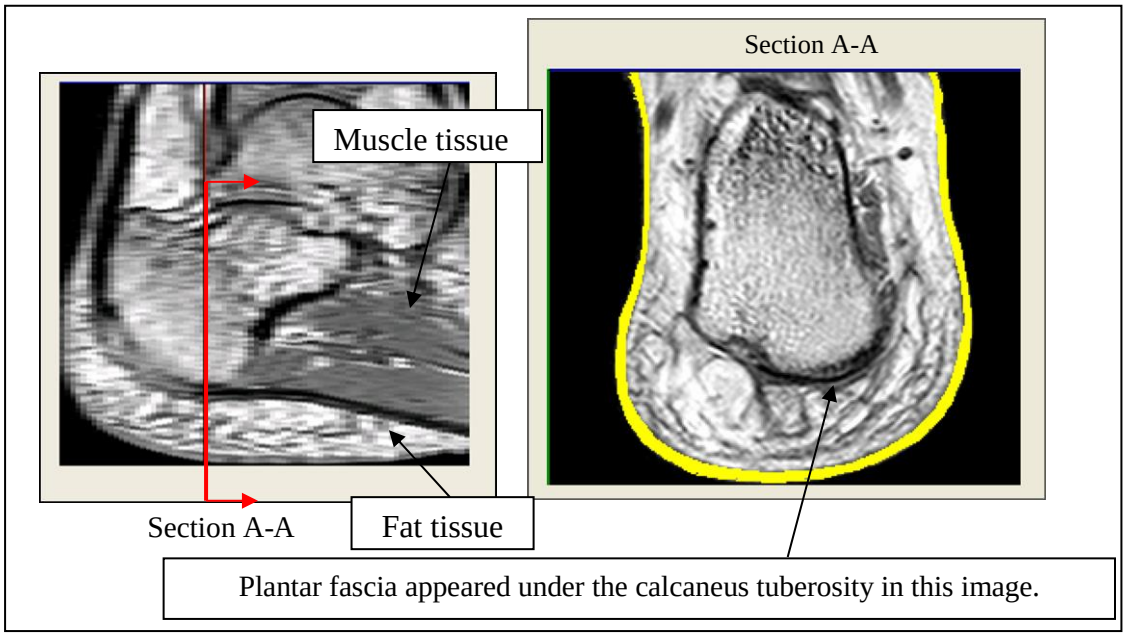

Figure 3.19: The initiation of the plantar fascia. The plantar fascia can be seen as a dark grey band separating the white fat tissue and grey muscle tissue.

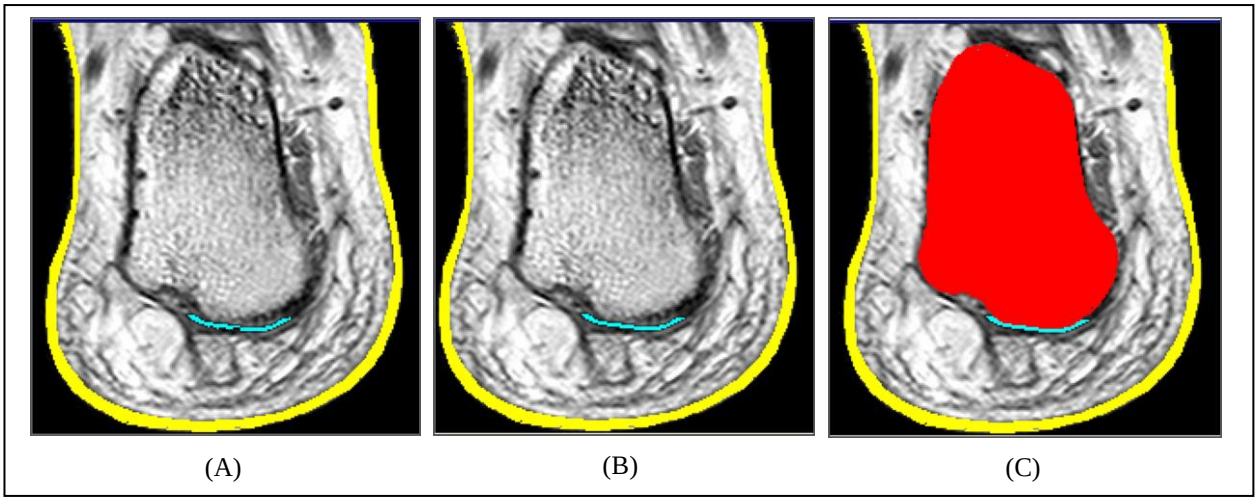

Figure 3.20: Segmentation of plantar fascia: (A) Using Confidence connected region growing to select the pixels corresponding to plantar fascia; (B) Using Paint tool to refine the automatic segmentation; (C) The calcaneus and plantar fascia

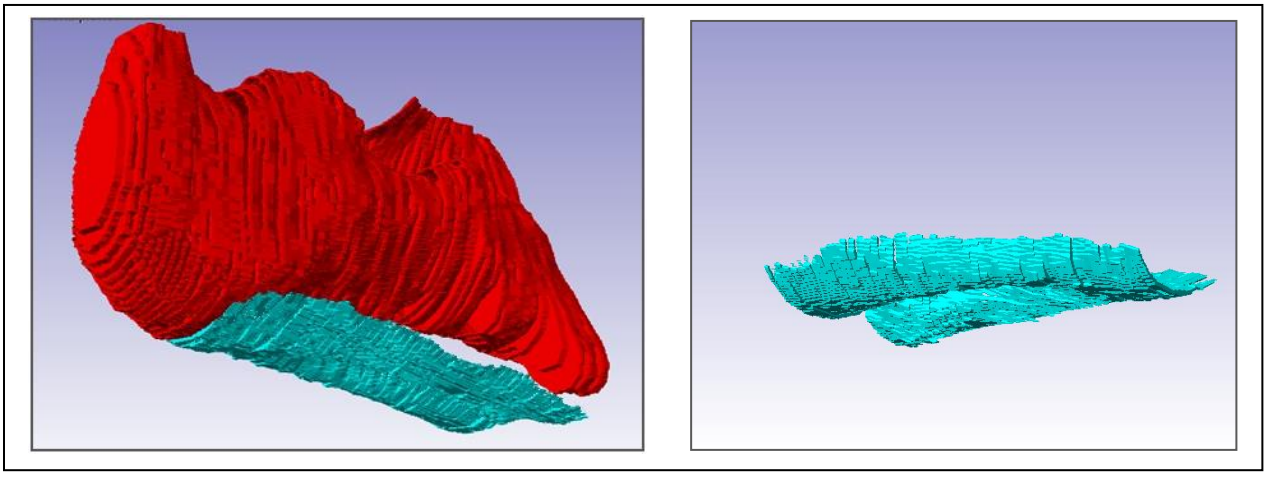

Figure 3.21: The 3D model of the plantar fascia.

After the segmentation of the plantar fascia, the muscle tissue was segmented. A visual examination of T1 weighted MR images revealed that the muscle tissue was darker than the fat tissue. It was difficult to identify the exact boundary of this tissue in the MR images. Therefore, segmentation of the muscle tissue was done with the help from anatomy studies and the use of the difference between the texture of the muscle tissue and fat and stiff tissues in MR images (Figure 3.22). The manual paint segmentation tool was used extensively and in preference to automatic and semi-automatic tools in the multi-plane segmentation approach to identify the pixels describing to the muscle tissue. In the multi-plane segmentation approach,

MR images in frontal, sagittal and transverse planes were iteratively reviewed for an accurate segmentation.

At the interface of the muscle tissue and fat tissue, the outer pixels with lower intensity value (darker) were selected as the border of the muscle tissue. At areas where the difference between the intensity values of the corresponding tissues (muscle tissue and fat tissue) was not clear, no pixel was selected. Then, the MR image was inspected in other planes i.e. sagittal and transverse and segmented in the best view using the same criteria. The segmented pixels were then reflected in the all other views. This process was continued until most of the pixels corresponding to the muscle tissue and its border were segmented. Finally, in the area where no pixel was selected with the help of three planes, the border was completed by connecting adjacent pixels using a straight line and the inner area of the tissue was segmented using the floodfill tool. Figure 3.22 shows the connection between coronal and transverse planes and how the marked pixel could be seen in different views.

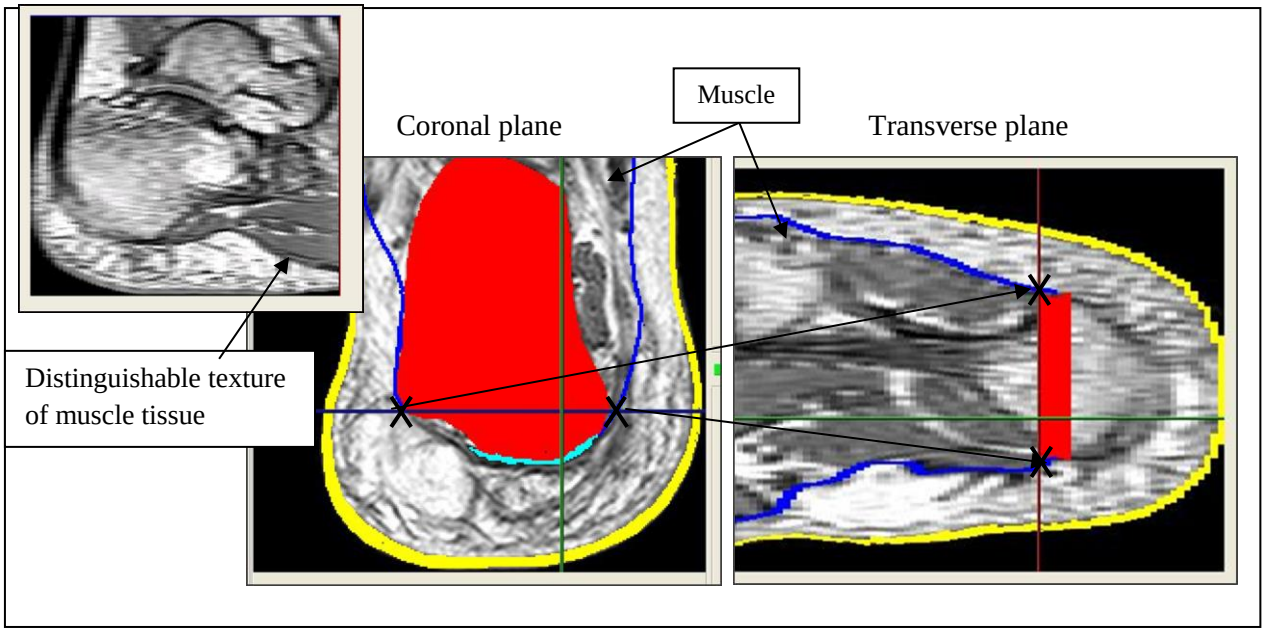

Figure 3.22: Segmentation of the muscle tissue.

Comparing the segmentation of the muscle tissue with segmentation of other tissues, which were mostly performed using automatic and semi-automatic segmentation tools, this process

required much more time and greater use of anatomical reference materials. Figure 3.23 shows the generated 3D surface model of the muscle tissue. Moreover, it can be seen how the stiff tissue is enveloped in the muscle tissue and how the plantar fascia covers the muscle group.

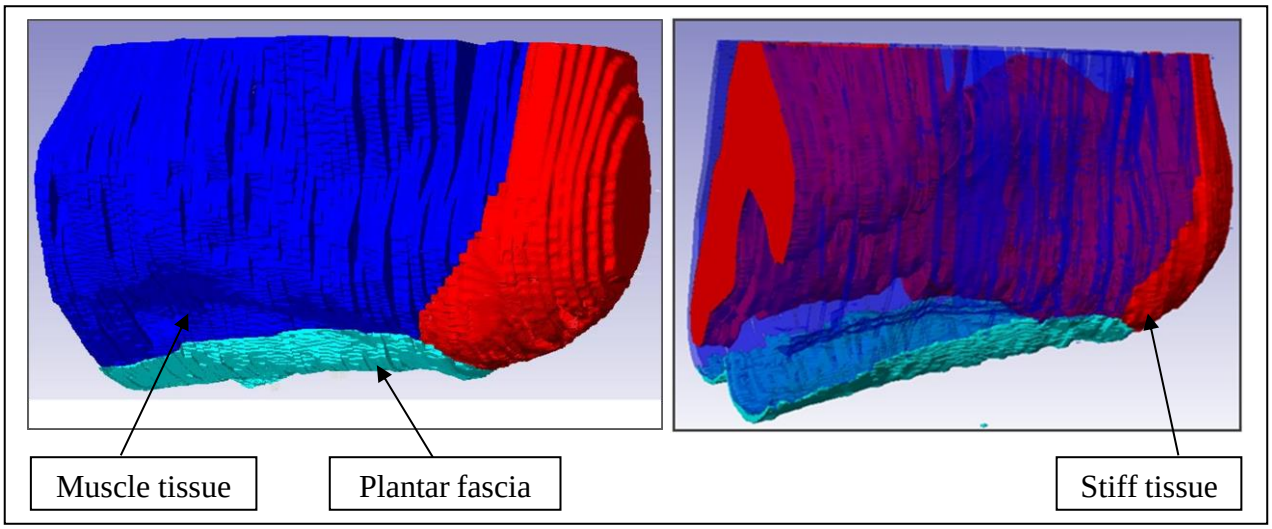

Figure 3.23: The 3D surface model of the muscle tissue.

The last two parts to be segmented were the micro-chamber and the macro-chamber layers. The greyscale levels of these two layers were quite similar whereas their textures were different. The micro-chamber layer, with smaller fat chambers connected directly to the inside of the heel skin, could be seen as a denser and slightly darker area. The macro-chamber layer, with greater fat chambers, was situated deep in the heel area directly attached to the inside of the micro-chamber layer. A dark border could be distinguished separating these two layers (Figure 3.24). Prior knowledge about these two layers, based on foot anatomy books and consultation with clinical experts, and information from ultrasound images of the foot being modelled were used to compensate for poor image contrast and missing boundaries. The only way to achieve segmentation was using the manual paint tool and the multi-plane segmentation approach. Moving from the macro-chamber layer towards the micro-chamber layer, the inner darker pixels with lower intensity values at the interface of the two layers were selected as the border of the micro-chamber layer. Similar to the process used for the

segmentation of the muscle tissue, in areas where the border was not clear, no pixel was selected. Then, the MR image was reviewed in other planes and, applying the same criteria, marked as segmented in the best view. This process was continued until most of the pixels corresponding to the micro-chamber layer and its border were segmented. The border was later completed in the area where there was a discontinuity, by connecting adjacent segmented pixels using a straight line and the inner area was segmented using the floodfill tool (Figure 3.24).

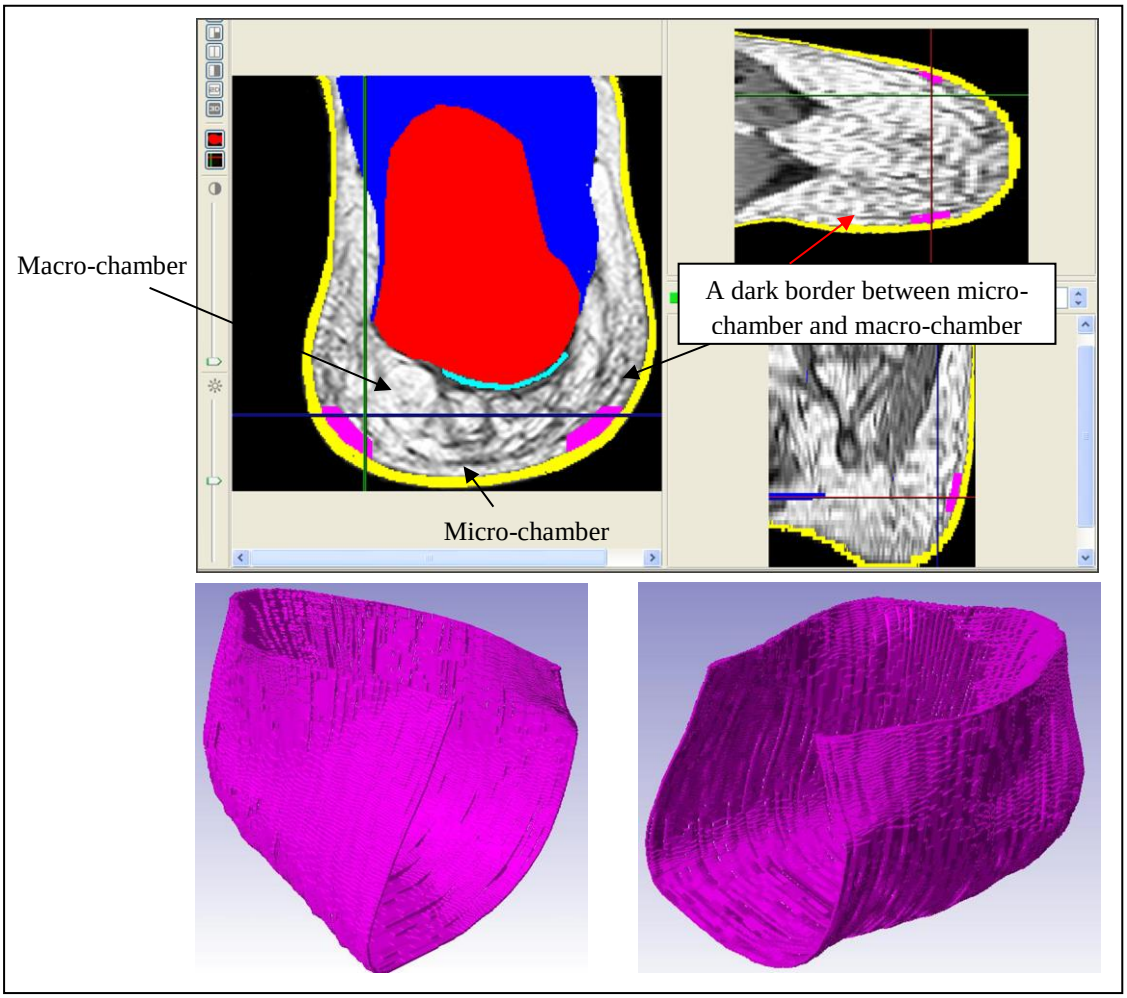

Figure 3.24: The segmentation process and the 3D surface model of the micro-chamber layer.

At the last stage, when most of the parts in the heel region were segmented, the pixels describing the macro-chamber layer were selected. The macro-chamber layer is the thick fat tissue around the stiff tissue and the muscle group. Using the floodfill segmentation tool and selecting a seed point inside the macro-chamber area, pixels surrounded by segmented areas

were marked as segmented. Some pixels belonging to macro-chamber layer, which were left unmarked, were added to the segmented region using floodfill and paint tools (Figure 3.25). The final 3D surface model of the macro-chamber is shown in Figure 3.25.

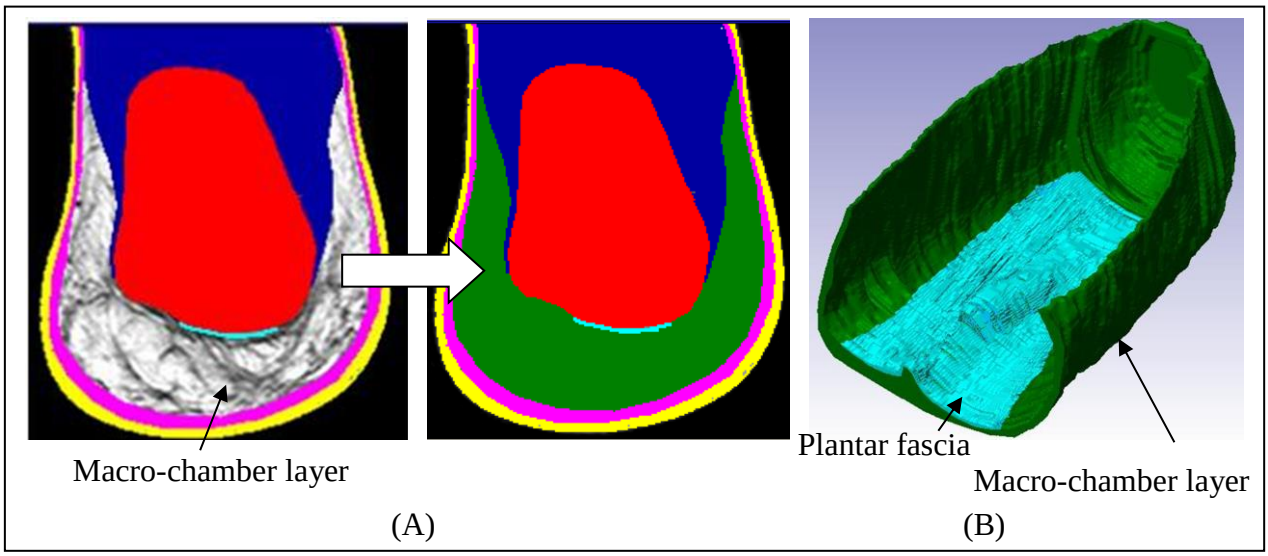

Figure 3.25: The macro-chamber layer mask: (A) The creation of macro-chamber layer mask by including all remaining pixels in the new mask; (B) The 3D surface model of the macro-chamber layer.

3.2.2.3 Repeatability of the Segmentation Procedure of the MRI Scans

The accuracy of the final model depends partially on the segmentation process. In this project, the segmentation of the MR images was performed using automatic, semi-automatic and manual segmentation tools in the ScanIP software. Therefore, it is important to test the repeatability and precision of the segmentation. Here, a simple repeatability test was performed on a sample MR image slice in the coronal plane. First, automatic and semi-automatic segmentation algorithms were applied to the image slice (Figure 3.26). Then the manual paint tool was used to distinguish the boundary between the macro-chamber and micro-chamber layers. For this repeatability test, it was sufficient to focus just on the pixel selection task. In doing this, sample pixels were selected at the boundary of each layer by a user on a fixed vertical position (e.g. x coordinates is fixed at 38.09mm) and corresponding y coordinates were recorded. There were 10 pixels to be selected in order to identify the

boundaries of different structures. These pixels were the initial and final pixels of the skin, micro-chamber, macro-chamber, plantar fascia and stiff tissue. After completion of the selection, the image was closed and reopened again to give time to the operator to clear previous selection from his/her mind.

Pixel selection process was repeated 20 times. This number of repetition was selected to reduce the error of the standard deviation reported, which can be approximately obtained using the following equation. In this equation, σ_s, σ and n stand for the error of standard deviation, standard deviation and sample size, respectively. The approximation is more accurate for larger sample sizes (n>16), and so, the number of repetitions (n) in this study was set to 20.

$$\sigma_s = \frac{\sigma}{\sqrt{2n}} \tag{3.1}$$

In Table 3.1, the results of the repeatability test show that the standard deviations for selection of the initial and final pixels for different structures in the heel area are relatively small, and even less than our image pixel size, which is 0.2864mm. Therefore, it can be concluded that a sub-pixel precision in the segmentation task was achieved. This repeatability test was performed using the segmentation results obtained by a single user. However, because the segmentation procedure is not complex, it is expected that any other user with adequate knowledge of foot anatomy and familiarity with the ScanIP segmentation tools can segment identical MR images with comparable accuracies as those obtained by the current user.

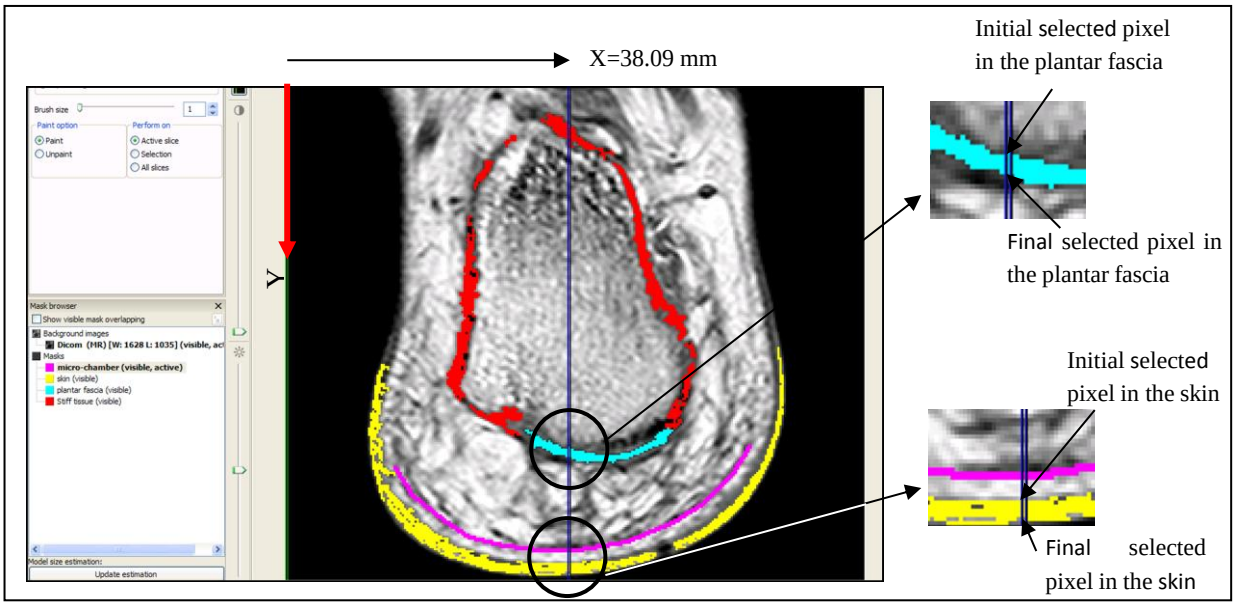

Figure 3.26: Repeatability test of the segmentation.

Table 3.1: Repeatability analysis of the segmentation

	Initial pixels		Final pixels	
	Mean on initial y coordinates	Standard deviation on initial y coordinates	Mean on final y coordinates	Standard deviation on final y coordinates
Skin	75.709 mm	0.1368 mm	77.0408 mm	0.0913 mm
Micro-chamber layer	73.332 mm	0.0622 mm	75.423 mm	0.1363 mm
Macro-chamber layer	61.289 mm	0.0905 mm	73.046 mm	0.0624 mm
Plantar fascia	60.129 mm	0.0625 mm	61.0032 mm	0.091 mm
Stiff tissue	16.253 mm	0.124 mm	59.843 mm	0.0622 mm

3.2.3 Development of the Solid Geometries

Simpleware provides the +FE module to convert surface geometries into solid models to generate volume meshes for FEA applications. This module automatically creates meshes based on voxel sizes. Since the number of elements created by +FE module for the heel region model was out of limits of computer memory and time, filtration and resampling of the model structures were necessary to improve the quality of the mesh and reduce the size of the resulting mesh. Appling filtration and resampling to the structures could also smooth all the areas. During filtration and resampling some holes appeared in thin structures (often areas

with less than 5 pixels deep) including the skin, micro-chamber and plantar fascia. Fixing these structures was not possible by filtration and they were needed to be re-created again. The thickness of these structures had to be changed during re-creation to make it possible to smooth the surfaces using filtration. Since the thicknesses of the skin and micro-chamber layers under the heel were particularly important for achievement of the main objective of this project and might influence the heel pad behaviour, it was decided not to use +FE module and find another way to generate solid models based on actual sizes of the structures. SolidWorks was chosen to develop the 3D solid model of the heel area based on surface geometries generated in the previous section. SolidWorks 2010 was used as the CAD design software as the author was familiar with SolidWorks and its attributes seemed well structured to the nature of solid modelling. The generated surface geometries, saved as STL format, were exported to SolidWorks (97). The process of the solid modelling started with modelling of the whole heel region as a single layer structure followed by scooping out each of the component layers from this region.

3.2.3.1 The Solid Model of the Heel Region as a Single Layer Structure

The surface geometry of the skin layer in STL format (extension of .stl) was imported into SolidWorks 2010 to form a smooth solid model of the heel region. The surface geometry of the skin layer, imported into the SolidWorks, is shown in Figure 3.27.

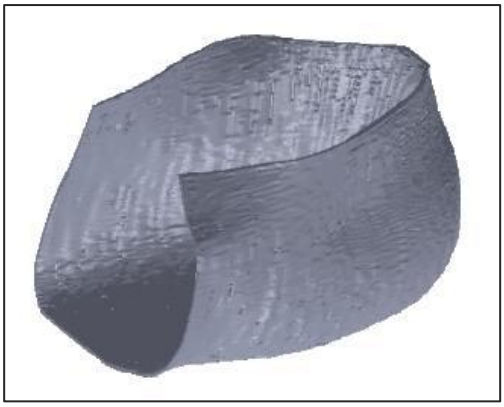

Figure 3.27: Surface geometry of the skin layer imported into SolidWorks.

The “loft” is a main feature in SolidWorks that was used for construction of the 3D solid geometries in the heel region. Referring to Figure 3.28, the loft feature allows users to create complex geometries by interpolating shapes between various cross-sections of a model. These user-defined cross-sections, which can be faces or edges, are called profiles. To better control this feature to produce desired geometries, guide curves are also used. A guide curve is a user-defined sketch that defines the path that the loft feature follows when interpolating shapes between profiles. A single sketch or different sketches can be used as guide curves (98). An example of the creation of a geometry using loft feature is illustrated in Figure 3.28.

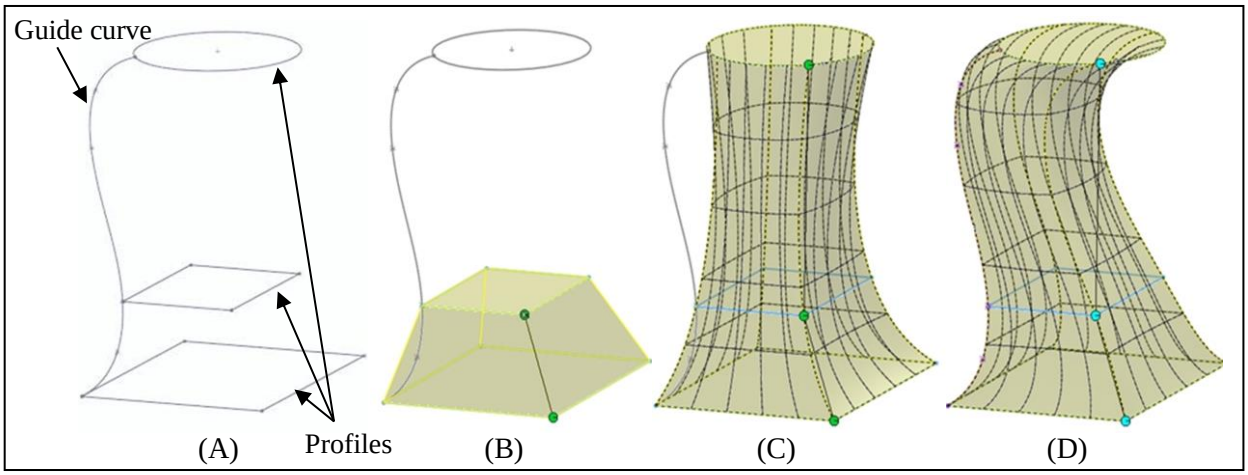

Figure 3.28: Creation of a geometry using loft feature: (A) Profiles and guide curve; (B) Insertion of surfaces between first and second profiles; (C) Continuing of inserting of surfaces between second and third profiles; (D) Using the guide curve as a path to follow for controlling the shape of the model.

Loft feature with profiles sketched around the outer surface of the skin layer and guide curves showing the curvature of the skin layer were used to create the model of the whole heel region. Creation of a model accurately replicating the outer boundary of the skin layer started with generating 3 transverse planes at the top, bottom and middle of the surface model of the skin layer (Figure 3.29). On each plane, a profile was sketched by selecting and joining points at the outer boundary of the skin layer. The profiles were sketched in a way that the associated surface model roughness, caused by stacking of MR images, was smoothed by selecting

points at spatial intervals greater than the MRI slice intervals (Figure 3.29). Three guide curves were also sketched showing the curvature of the skin layer in the medial, lateral and back of the foot (Figure 3.29). These curves were drawn on planes perpendicular to the transverse planes to capture curvature over the entire heel region. The process of sketching of the profiles and guide curves was not automatic and required patience and extra attention.

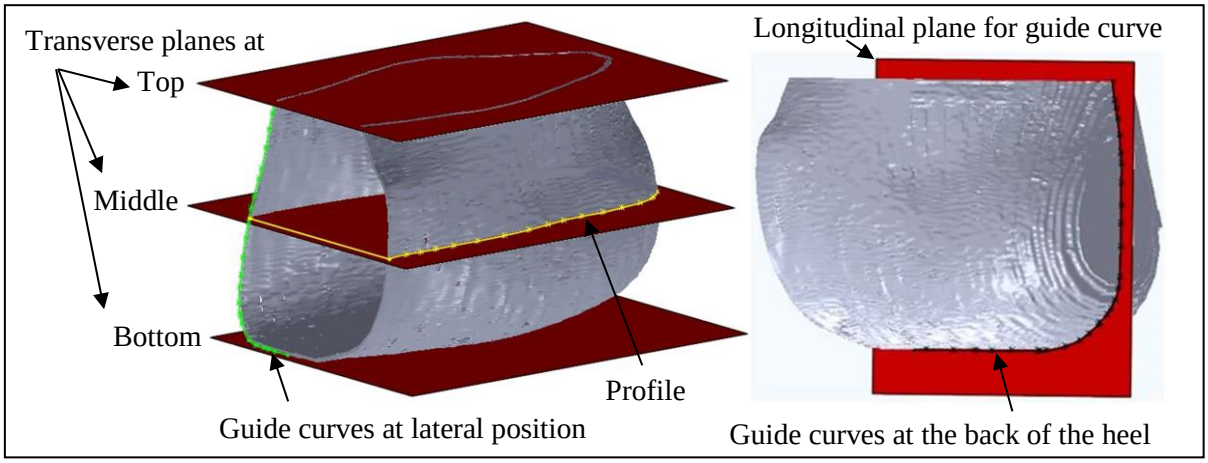

Figure 3.29: Sketching of profiles and guide curves.

The first lofted model was generated using 3 profiles and 3 guide curves (Figure 3.30). Investigation of the difference between the lofted solid model and the surface geometry revealed the maximum difference of 2.7mm close to the transverse plane approximately 40mm from the back of the heel (Figure 3.30). The difference investigation was carried out by cutting the model in coronal and transverse planes at 1mm intervals and checking the differences.

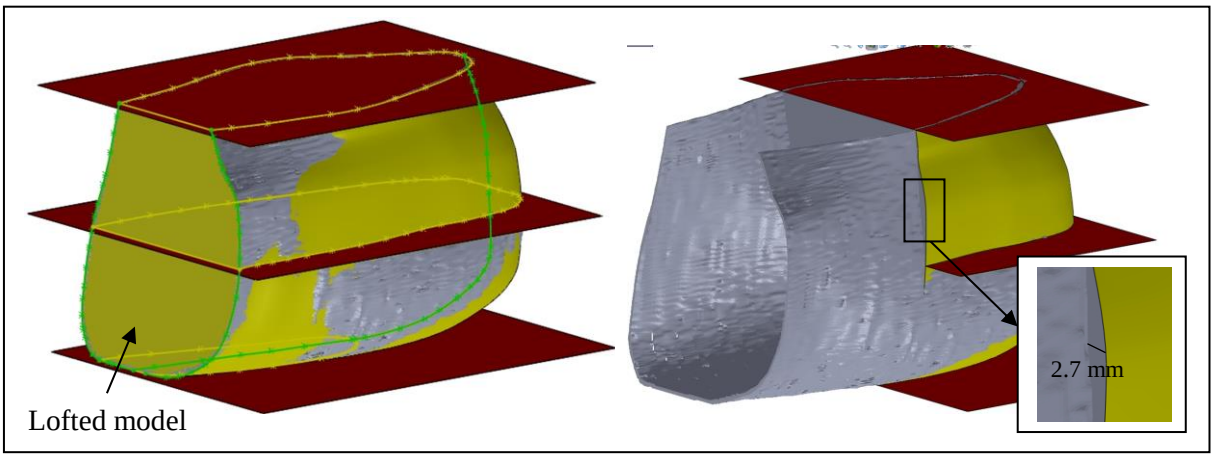

Figure 3.30: First lofted model of the whole heel region and its difference with the surface model.

Since the whole model of this project includes some thin structures such as skin layer with only 2mm thickness in some areas, the amount of 2.7mm difference was not acceptable. Only up to 0.3mm difference could be acceptable under the heel which is very important area in this project. This value almost equals to the pixel size of MR images (which is 0.286458mm) and it is the minimum value if the smoothing is required. Up to 0.9mm difference, which is almost three times of the pixel size of MR images, could be tolerated at the sides and the back of the model. Occasionally in muscle and stiff tissue structures, which were made by combining different parts in the heel area, more differences were tolerated because of the existence of discontinuous boundaries.

Since in the generated lofted model for the heel region (Figure 3.30), a large difference was found between the lofted solid model and the surface geometry, more modifications were required to achieve an accurate solid model. Therefore, more profiles were sketched on new transverse planes inserted between the existing planes. One new guide curves were also added. These additional profiles and guide curve were used in loft feature to better define the outer boundary of the skin layer. As can be seen in Figure 3.31, the maximum difference measured between the lofted solid model and surface geometry was reduced to less than 0.4mm. In an iterative approach, the number of profiles was increased until the difference

investigation showed no unacceptable difference and ensured that the solid lofted model made a copy of the surface model. Finally, the 3D solid geometry of the heel region as a single layer was created using 12 profiles and 4 guide curves on highly curved areas (Figure 3.32).

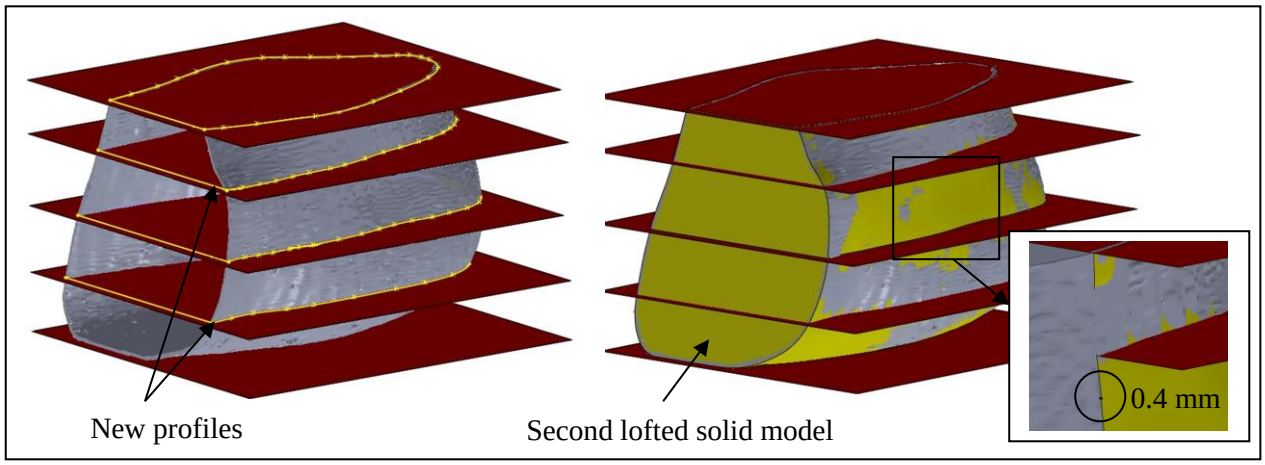

Figure 3.31: Second lofted model of the whole heel region and its difference with the surface model.

Figure 3.32: The 3D solid model of the heel region as a single layer structure.

3.2.3.2 Development of Solid Geometries of Different Tissue Layers in the Heel Region

Once the solid model of the heel region was constructed, by developing surfaces representing the interface between different structures in the heel area, it was possible to scoop out 3D solid geometries of different layers (stiff tissue, muscle tissue, plantar fascia, micro-chamber, macro-chamber and skin layers) from the heel region model. This started with the skin layer. For this purpose, a surface representing the interface between the skin and the surrounding layers was required. To create a surface model to replicate the inner boundary of the surface geometry of the skin layer the “loft surface” feature was used in SolidWorks. This feature

works the same as the loft feature but uses open profiles instead of closed. This allows creation of complex surfaces with zero thickness. By inserting these surfaces into the heel region solid model, it is possible to separate the different structures without losing any material.

Similar to the method used for creation of the heel region model, an iterative approach was used to generate necessary profiles and guide curves in order to create the surface representing the interface between the skin and surrounding tissues. Altogether 12 profiles and 4 guide curves were required to make an exact copy of the inner boundary of the skin layer and meet the difference investigation specifications explained earlier (Figure 3.33).

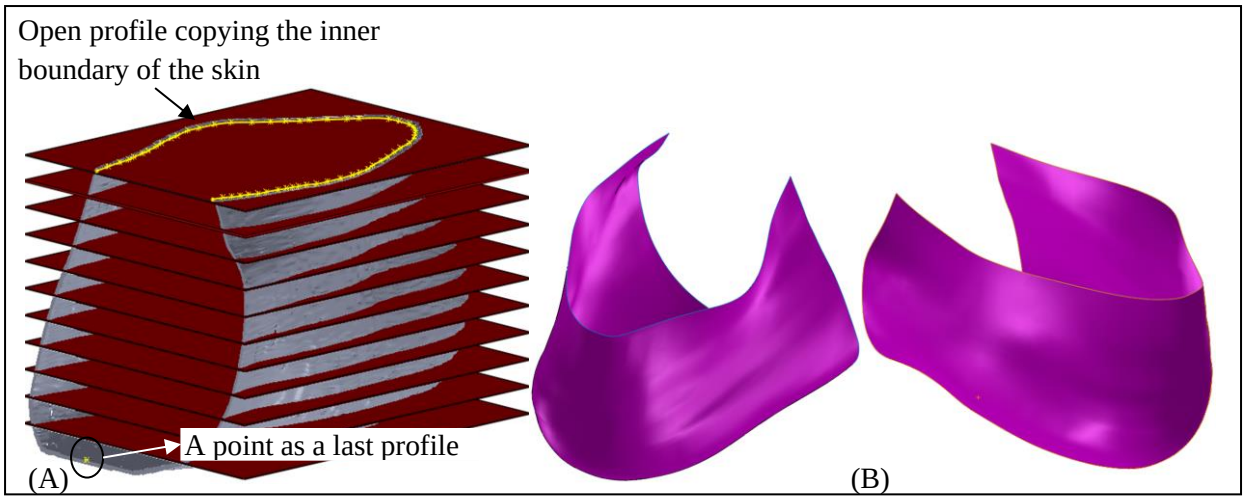

Figure 3.33: Creation of the lofted surface representing the inner boundary of the skin layer: (A) The process of sketching profiles; (B) Splitting lofted surface.

The generated lofted surface was used as a splitting surface to separate the skin layer from the 3D model of the heel region developed in the previous section. The splitting surface was located inside the heel region model and divided it into two parts. The split feature in SolidWorks divides a single solid body into multiple bodies using sketches, planes or surface bodies. This process is shown in Figure 3.34. The outer part was the solid model of the skin layer and the inside part was saved as the “remaining part-1” (Figure 3.34). The remaining part-1 was representing the 3D model of the stiff tissue, muscle tissue, plantar fascia, macro-

chamber and micro-chamber joined together. Subsequently the remaining part-1 was used to generate the solid model of the micro-chamber layer.

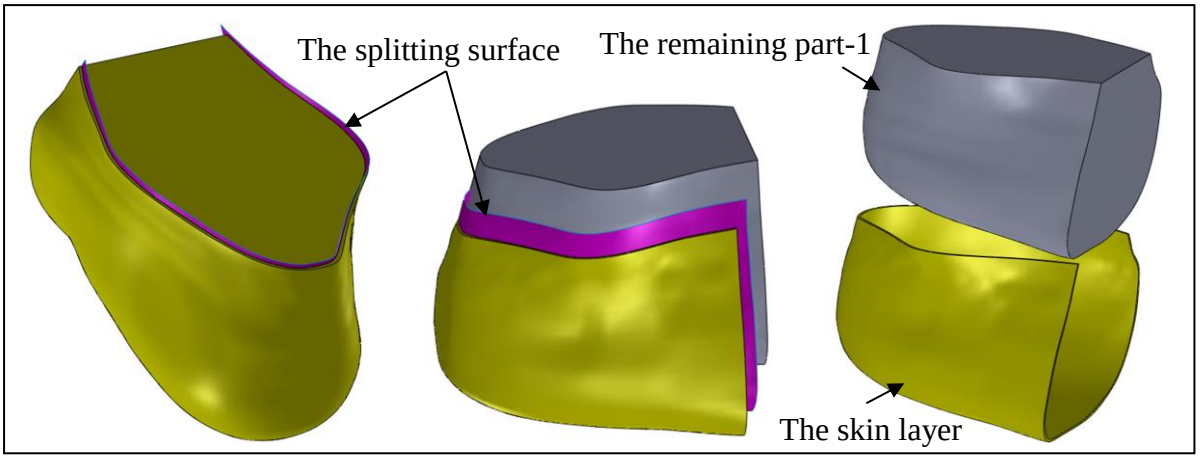

Figure 3.34: Separation of the solid model of the skin layer from the heel region model.

Same method was used to create lofted surfaces representing the interfaces between micro-chamber, macro-chamber, stiff tissue, muscle tissue and plantar fascia structures. For this purpose, the surface models of the corresponding structures (micro-chamber, macro-chamber, stiff tissue, muscle tissue and plantar fascia) which generated in ScanIP, were imported into SolidWorks with STL format. The loft surface feature was then used to create the lofted splitting surfaces. In an iterative approach, the number of profiles and guide curves were increased until the minimum difference targets between solid models and surface models were met. The images showing the creation of the lofted surfaces representing the inner boundary of the micro-chamber layer, the outer boundary of the stiff tissue and muscle tissue and the interface between the plantar fascia and macro-chamber layer are attached in Appendix A. The continuous smooth lofted surfaces were placed in the remaining part-1 subsequently and split it into five new solid parts. The images relating to the process of separation are also attached in Appendix A.

3.3 RESULTS AND DISCUSSION

The solid geometries developed in SolidWorks for the plantar fascia, muscle tissue, stiff tissue (bones and Achilles tendon), macro-chamber, micro-chamber and skin layer were assembled

together to form a complete solid model. It took about 4 months for the development of the 3D model of the heel region to be completed. However, it should be noted that with recent improvements in well-known segmentation software available in the market and using more powerful computer hardware, the model development could be achieved in much shorter time scales. Some images of the complete solid model and different layers assembled together are shown in Figure 3.35.

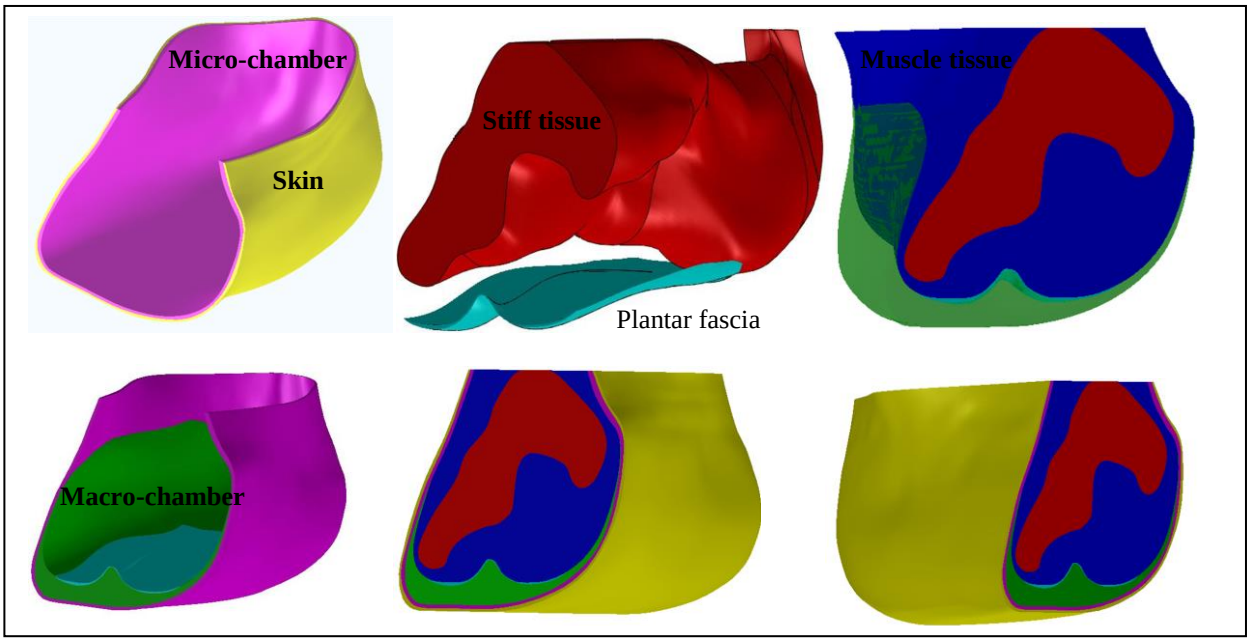

Figure 3.35: The complete solid model of the heel region.

Since the process of the creation of the geometries was very human driven and iterative, it was important to evaluate the accuracy of the model. For this purpose, the maximum width of the heel region in the model was compared with that in the experimental measurement. This maximum width (MW) is shown in Figure 3.36 for both the model and the subject's foot. The MW was measured at 9.25cm from the back of the foot in both the model and the subject's foot. The MW measurement was 7.30cm in the model, while it was 7.33cm (SD 0.13) in the subject (Figure 3.36). This means that the measurement in the model had 0.41% error compared to that in the subject. This small error suggests high accuracy of the model.

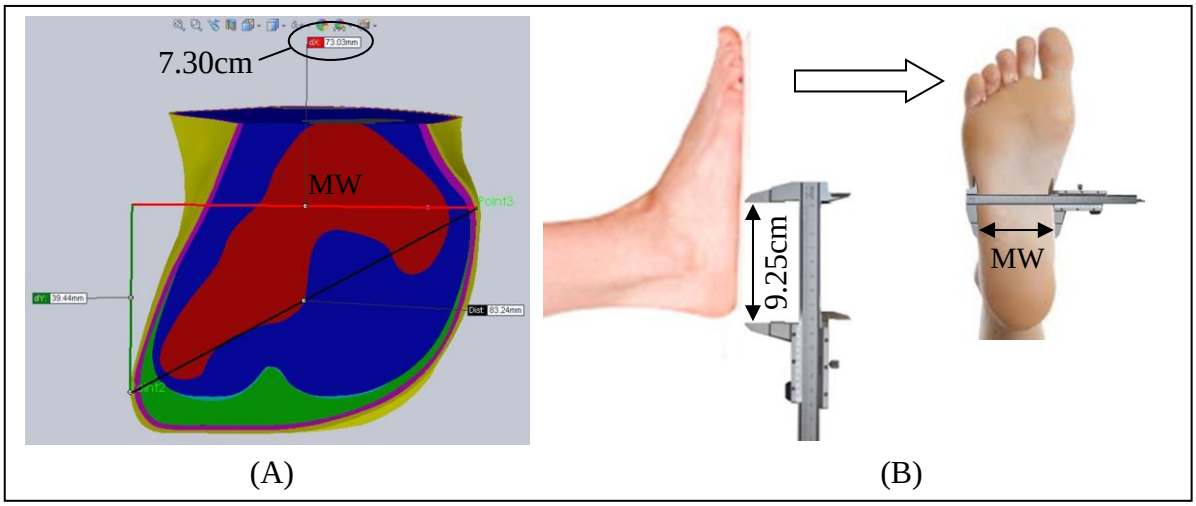

Figure 3.36: A comparison between the dimension of the final 3D model and the subject's foot: (A) Measurement of the MW at 9.25cm from the back of the foot in the model; (B) The procedure of measuring the MW of the real foot.

An alternative method to evaluate the accuracy of the model was to superimpose the final solid geometries back on to the MRI data and check for differences. To superimpose the solid geometries on to the MRI data, it was required to create a mask out of each solid geometry which can be imported to an MRI data project. To create the mask, the solid geometry was saved as STL file and then exported to Simpleware +CAD software. This software has got the tool that can convert a CAD model to a mask. Figure 3.37 shows the mask of the skin layer made out of the STL file in +CAD.

The skin layer mask was saved in ScanIP format, which makes it suitable for opening in Simpleware ScanIP software. To superimpose the created mask on to the MR images, first, the MRI data in DICOM format was imported into the ScanIP and then the created mask was imported into ScanIP as an existing mask and overlaid on the MR images. It should be noticed that the MRI data and the mask must have the same size (in pixels) and same spacing (in mm) to be imported into a same file. The resampling and rescaling were applied to both mask and MRI data to be in size of 0.2×0.2×0.2mm. Figure 3.38 shows the skin mask overlaid on the MR images.

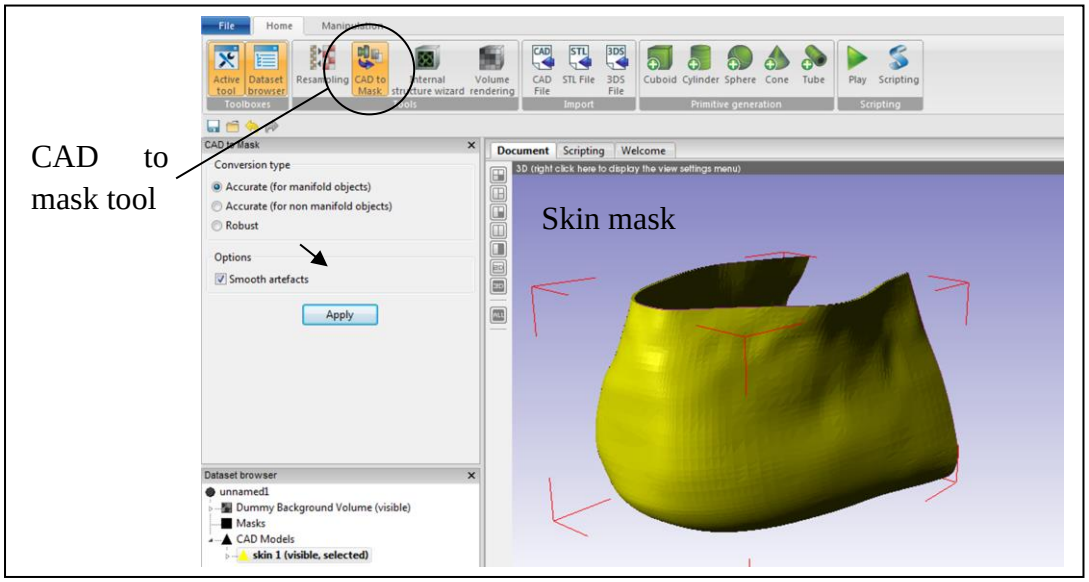

Figure 3.37: Creation of the skin mask in +CAD software from the solid geometry of the skin layer.

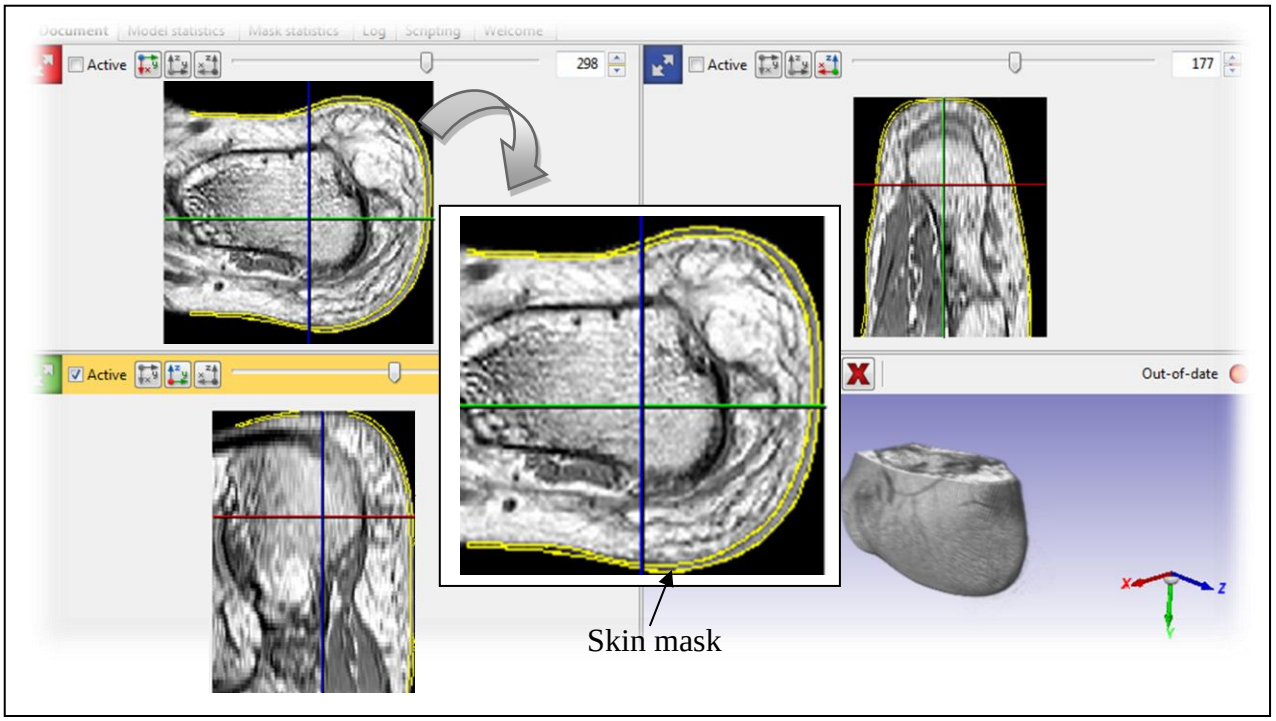

Figure 3.38: Superimposing the skin mask on to the MRI data. The laying of the mask over the MR images can be seen in coronal, sagittal and transverse views.

To see how much the mask, which is representing the solid model, differs from the MRI data, the MR images were segmented to differentiate the tissue of interest using the method used during segmentation process and then the maximum difference between the mask and the segmented MRI were provided in pixels. For all 6 structures 3 images in coronal, sagittal and

transverse planes at same positions of approximately 34mm from the back of the foot, 27mm from the medial side of the heel and 30mm from the bottom of the foot were selected to show the differences. The positions of the planes are shown in Figure 3.39.

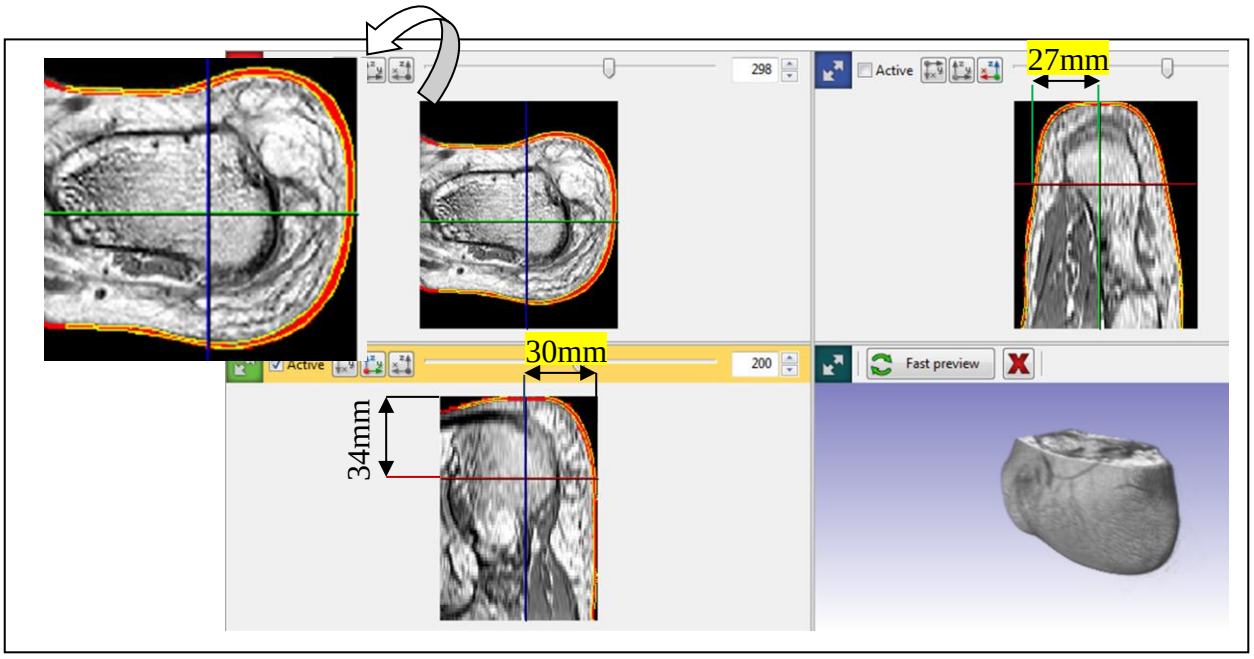

Figure 3.39: The skin mask and the segmented region of the skin layer are represented by yellow pixels and red pixels respectively in the MR images. The position of coronal, sagittal and transverse planes at 34mm from the back of the foot, 27mm from the medial side of the heel and 30mm from the bottom of the foot are shown in the MR images.

For the skin layer the maximum difference between the mask and the segmented area in coronal plane was measured 2 pixels (0.4mm) at the side of the foot. This difference increased to 3 pixels (0.6mm) in transverse plane at medial and lateral areas of the foot. In sagittal plane, the maximum difference was 1 pixel (0.2mm) under the heel and up to 3 pixels (0.6mm) at the back and under the foot away from the heel area. By subtracting the two layers (the skin mask and segmented skin layer) from each other, their difference can be visualised clearly and measured very easily. These differences were mainly because of the smoothing process performed during creation of solid geometries in SolidWorks. Figure 3.40 shows the maximum difference between the mask and segmented area in coronal, transverse and sagittal planes.

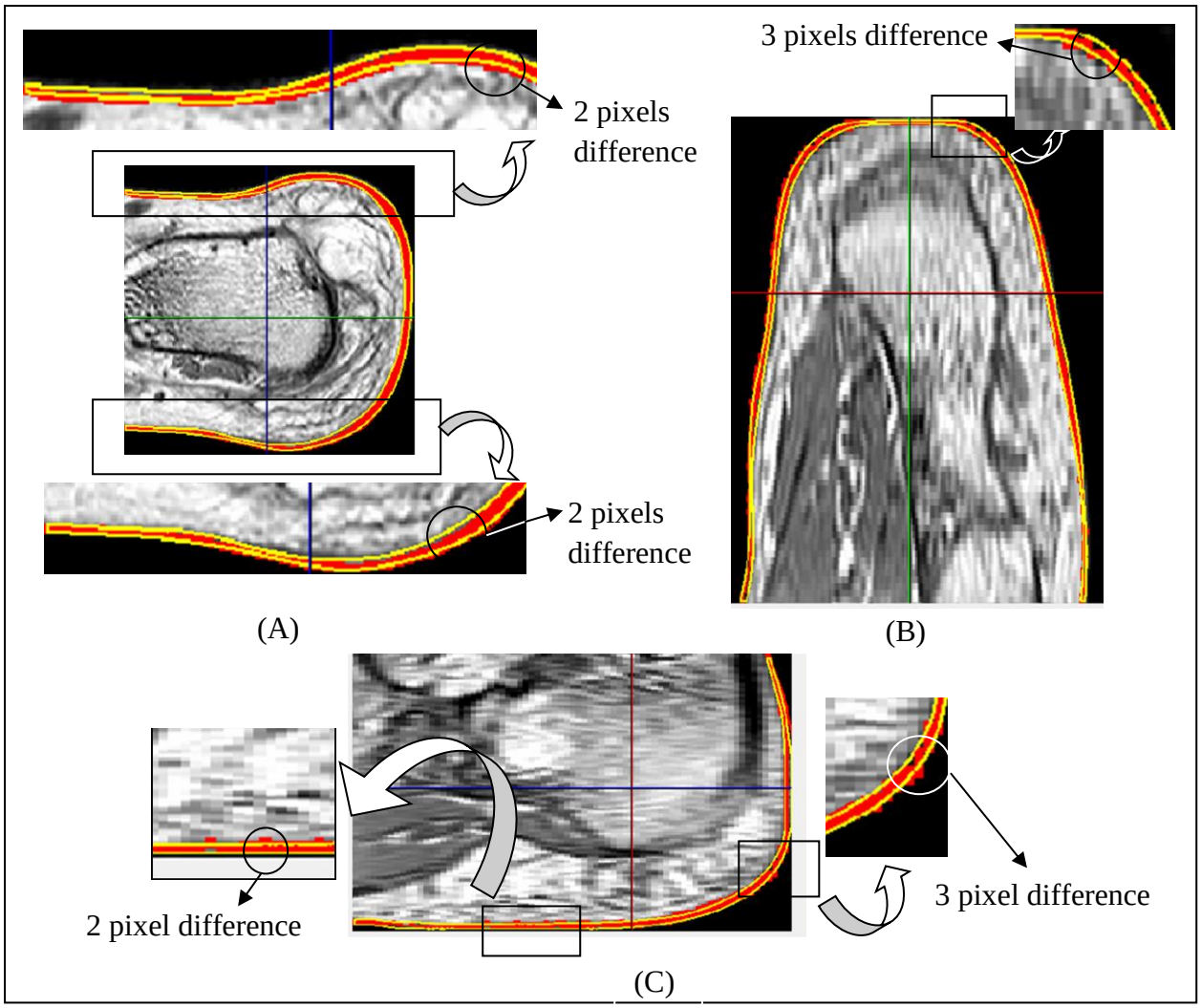

Figure 3.40: Maximum difference between the skin mask and segmented region of skin layer: (A) Maximum difference in coronal plane; (B) Maximum difference in transverse plane; (C) Maximum difference in sagittal plane.

The same procedure was repeated for the other structures in the heel region model and the maximum differences between corresponding masks representing the solid geometries of the structures and MRI data were measured. The results revealed that for the micro-chamber layer the maximum difference was up to 1 pixel (0.2mm) under the heel and 3 pixels (0.6mm) at the medial side of the foot (Figure 3.40). Since under the heel area was very important region in this project the segmentation of this region was performed with highest possible attention and solid modelling was done with high accuracy. Therefore, small difference of up to 2 pixels (0.4mm) were found at this region for the other structures. For macro-chamber layer the

maximum difference was found 4 pixels (0.8mm) at the medial side of the foot. This difference is clear in transverse plane (Figure 3.40). For the stiff tissue 3 pixels (0.6mm) difference was found under the heel and the maximum difference was 7 pixels (1.4mm) at the top of the stiff tissue in distal part of the heel region. This difference can be seen in sagittal plane (Figure 3.41).

For the muscle tissue the maximum difference of 7 pixels (1.4mm) were found at the area were the maximum difference was found for the stiff tissue and also at the distal part of the heel region. This difference is clear in sagittal plane (Figure 3.41). These maximum differences for the muscle and stiff tissue appeared in the area away from the critical area under the calcaneus tuberosity and at the top region of the stiff tissue. Higher differences for the muscle and stiff tissues were expected since they were made by combining different parts in the heel area and because of the existence of discontinuous boundaries.

The plantar fascia was very thin structure and maximum possible attention was applied during creation of this structure. The results revealed the maximum difference of 3 pixels (0.6mm) at the top part of this structure at the interface with the muscle tissue. This difference can be seen in sagittal plane in Figure 3.41. The results of this stage were consistent with the rule outlined for development of the solid geometries (Section 3.2.3).

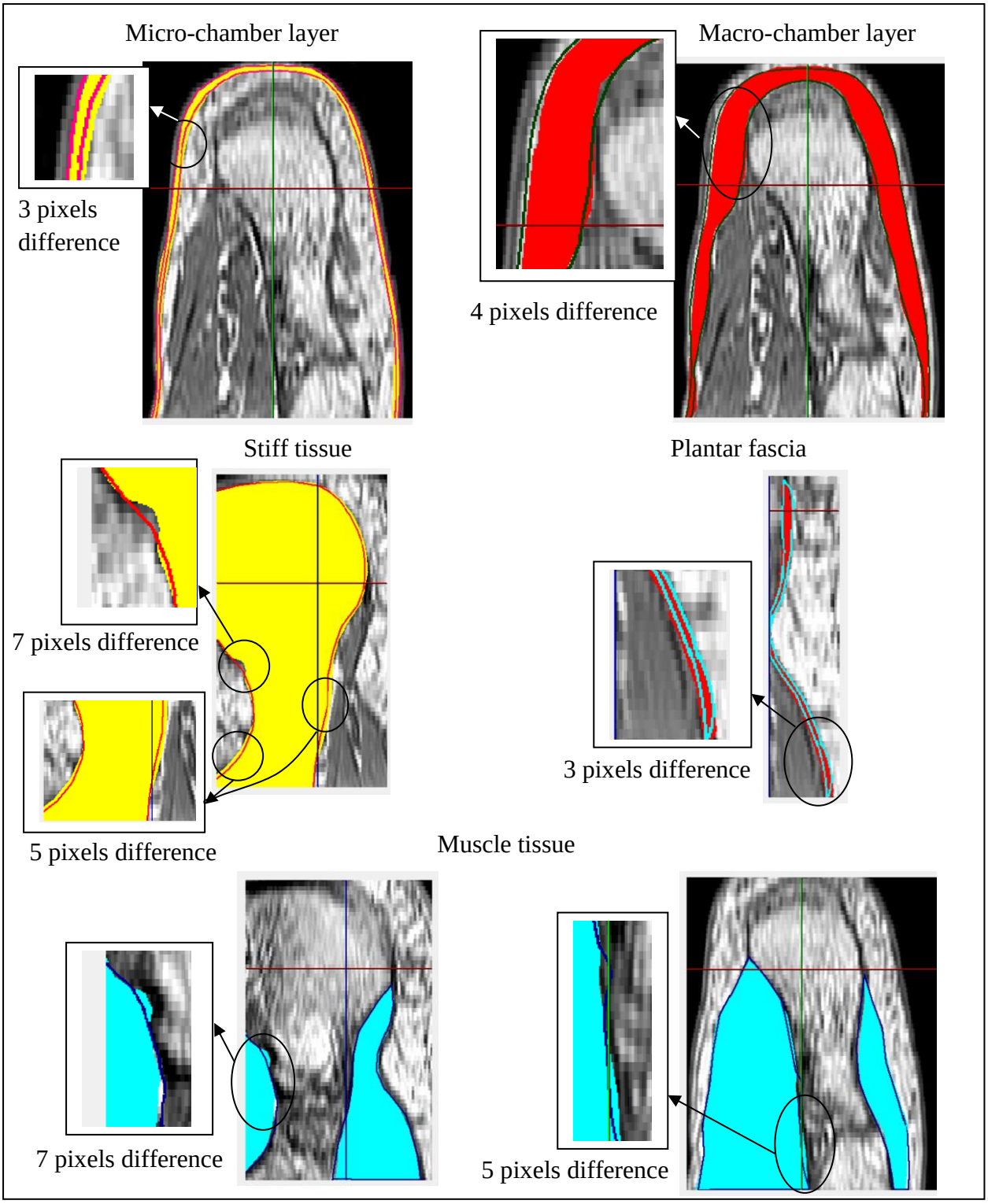

Figure 3.41: Maximum difference between the mask of each structure and the corresponding segmented region of interest.

An alternative method to evaluate the segmentation process would be to use a phantom. Such phantom would contain synthetic tissue made with materials of similar characteristics as those

in corresponding layers of the *in-vivo* sample. The phantom would be scanned with identical imaging protocol as those used for the *in-vivo* sample to generate comparable MR images. The segmentation process would then be applied to the phantom MR images in the same way as was applied to the *in-vivo* images. The segmentation results would then be compared with the reference boundaries between layers in the synthetic tissue known as priori. The design of such phantom and the statistical analysis of the corresponding MR data would be the subject of future investigation and is beyond the scope of this thesis.

3.4 CONCLUSIONS

Detailed information about the heel pad behaviour under loading is important for the human foot and footwear biomechanics research. The heel pad located beneath the calcaneal bone has a composite structure composed of three layers: the skin, micro-chamber, and macro-chamber. Each of these layers contributes to the biomechanical response of the heel pad to loading. The material properties of each of these layers contain important information about their biomechanical behaviour during gait.

Researchers have used different methods to estimate the material properties of the heel pad and characterise its biomechanical behaviour. Specifically, FEA has been a reliable method for obtaining the material properties of the heel pad and for simulating its behaviour under loading. The first step in the FEA method is to generate the geometry of the structure. In most previous studies, researchers have modelled the heel pad as a homogeneous single layer structure. In some cases, the heel pad has been modelled as a two-layer structure and skin has been modelled separately.

The main purpose of this chapter was to develop an anatomically detailed 3D model of the human heel region based on MRI data of a right foot of a subject. To achieve the main objective of this project the heel pad sub-layers were differentiated from each other and

modelled separately in the heel region model. MR images were segmented in ScanIP to generate 6 surface geometries for the skin, micro-chamber, macro-chamber, plantar fascia, muscle tissue, and stiff tissue in the heel region. The stiff tissue was composed of some foot bones and the Achilles tendon was fused to these. The surface geometries were then imported into SolidWorks to create the solid geometries suitable for FEA. Finally, the quality of the solid geometries was assessed by comparing the solid geometries with initial MRI data.

The very human driven of the segmentation process and generating of the solid geometries was the primary limitation of the development of the 3D model of the heel region. The assembly of solid geometries developed in this chapter was used as the base for generating the initial FE model of the heel region in Chapter 4.

4. Chapter Four:

INITIAL DEVELOPMENT OF THE FE MODEL OF THE HEEL REGION

4.1 INTRODUCTION

This chapter contains the description of the procedures required to develop the CAD geometry and define the material properties and loading/boundary conditions in FE model. In addition, the results of three parametrical analyses to evaluate the effects of muscle tissue stiffness, plantar fascia stiffness, and the angle of rotation of the FE model on the force-strain relation of the heel pad under loading are provided. Since the main objective of this project was to estimate the material properties of the heel pad sub-layers, a detailed 3D FE model of the heel region with distinct layers of macro-chamber, micro-chamber and skin layers under calcaneal bone was required. Therefore, the assembly of the solid geometries of the heel region structures, developed in Chapter 3, was used as the base for development of the CAD geometry and adjusted to meet the FE model requirements.

4.2 DEVELOPMENT OF THE FE MODEL

4.2.1 CAD Geometry and Mesh Generation

The solid geometry of the heel region developed in Chapter 3 was used to generate the FE model geometry. To reduce the computation time, only a portion of the solid assembly, that was required to simulate the heel pad behaviour, was to be included in the FE model. The decision on the extent of the CAD geometry and choosing the most suitable anterior and superior surfaces for the FE model was made based on a pilot study carried out on the heel pad of the same subject, used to develop the heel region geometry. The aim of the pilot study was to identify locations at which no tissue movement occurred when the heel was compressed.

In the pilot study, the subject was asked to lie down in prone position with her foot hanging over the edge of the examination table (Figure 4.1 and 4.2). Then the right heel of the subject was compressed with a flat rigid plate and simultaneously the deformation of the heel pad was

tracked using the ultrasound imaging technique. To find the minimum extent of the FE model in the anterior direction, first, the location of the calcaneus tuberosity was found using ultrasound. This location was identified at 2.7cm from the back of the heel and marked as x (Figure 4.1 A). The locations of x+3, x+4cm up to x+8cm were marked under the foot to examine if any movement of the heel tissue at these distances from the calcaneus tuberosity was possible. The ultrasound probe was placed at the marked locations while foot was compressed at the region of the calcaneus tuberosity by the flat rigid plate (Figure 4.1 B and C). The movements of the heel tissue in x and y directions (Figure 4.1) were observed. The evidence of tissue movements was interpreted that the tissue at the specific location was affected by applying compression under the calcaneus tuberosity.

The ultrasound imaging data showed that tissue at the area of x+5cm (7.7cm from the back of the foot) was far from the calcaneus tuberosity so that was not affected by the heel compression. At this location, movements of the heel tissue in both x and y directions were restricted by surrounding tissues and no movement was noticed. Based on this data, the FE model could be fully constrained in the coronal plane at 7.7cm from the back of the heel. This constraint could reproduce the reactions of the surrounding tissues distal to this point. However, because of some differences between tests conditions in this pilot study and experiments to obtain the heel pad biomechanical behaviour, and also to allow for some margin of error, a plane at 9.25cm from the back of the heel (almost 1.5cm more than what imaging results suggested) was chosen to be the distal edge of the model. This is the maximum size of the solid geometry in the anterior direction made over the final MR image in coronal plane.

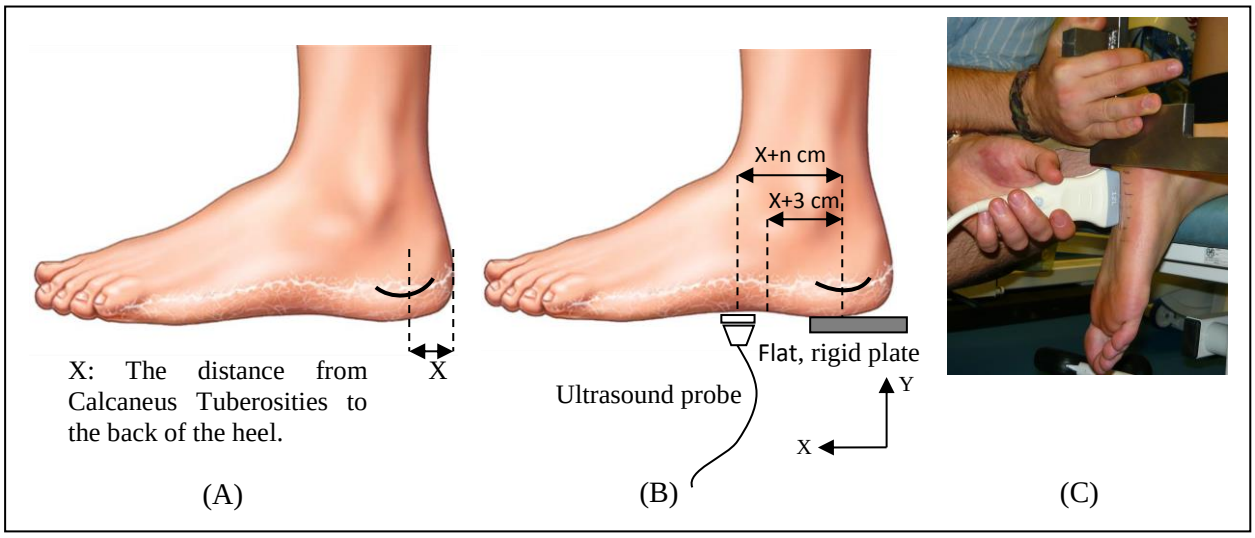

Figure 4.1: Pilot study to identify the required size for the 3D model in the anterior direction; (A) schematic image showing the location of the tuberosity,(B) schematic image showing the process of placing the ultrasound probe under the foot at different locations anterior to the tuberosity, (C) placing the ultrasound probe under the foot at different locations with cm space between them.

To identify the most suitable superior surface for the model and the minimum height of the FE model, the ultrasound probe was placed vertically at the back of the foot and tissue movements in inferior-superior direction was observed during compression of the plantar surface of the heel. As it is shown in Figure 4.2, the ultrasound probe was placed at different locations with 0.5cm space between them while the heel pad was compressed by the flat rigid plate.

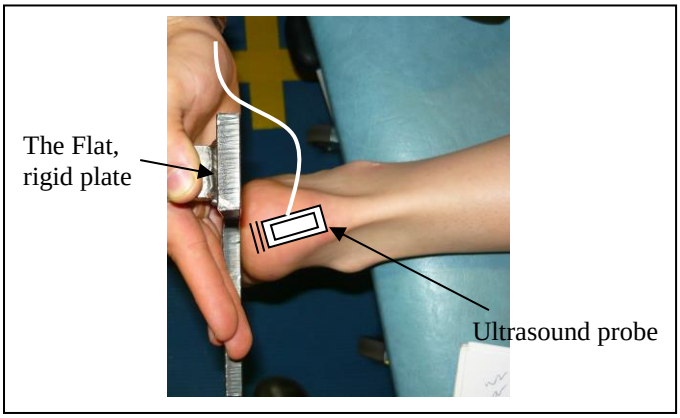

Figure 4.2: Pilot study to identify the minimum size of the FE model in the inferior-superior direction.

According to the ultrasound data, there was no movement of the heel tissue at the area of 4cm from the bottom of the foot when plantar heel was compressed. Thus, the effects of the compression of the plantar heel pad did not propagate superiorly beyond this position. Based on the ultrasound data a transverse boundary was placed at 4.5cm from the bottom of the foot (0.5cm higher than what the imaging data suggested) and this plane represented the upper boundary of the FE model. Therefore, to prepare the CAD geometry for the FEA, the 3D solid geometry of the heel region developed in Chapter 3 was cut into size of 9.25 and 4.5cm from the back and bottom of the heel respectively (Figure 4.3).

In literature, there are some studies that used heel region models (models of part of a foot) to study the behaviour of the heel pad (6, 7, 99). However, none of them selected the coronal and transverse boundaries of their models based on any experimental study. Since the bone tissue is effectively stiffer than the other structures in this human heel region model and its deformation is negligible, this structure was removed from the CAD geometry. Instead, its effect on the behaviour of the heel pad under loading was modeled in the FE model using fully constrained boundary conditions.

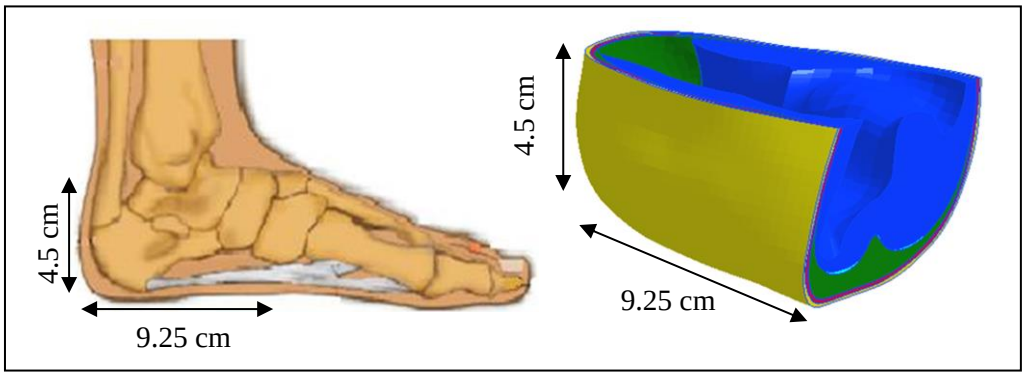

Figure 4.3: The size of the CAD geometry.

The CAD geometry composing of the muscle tissue, plantar fascia, macro-chamber, micro-chamber and skin structures generated in SolidWorks were stored in ACIS (.sat) format to be exported into Abaqus 6.10 (Dessault Systemes, USA) in order to generate the mesh. Abaqus is popular commercial FE software from the same vendor as SolidWorks, Dassault System. It

has advanced capabilities such as CAD geometry import and repair, and partitioning of complicated geometry. These capabilities make mesh creation of complex geometry simple and quick. The sat file which stands for "Standard ACIS Text" saves 3D geometry information in an ASCII text format. Though there are other formats which can be imported into Abaqus, the Abaqus documentation suggests using ACIS format for importing parts. It is because geometries created in Abaqus are in this format and also because it is possible to import all the assembly parts at once whereas using other formats may require each part of an assembly to be imported individually (100).

Abaqus provides a variety of tools which allow specifying elements shape, type and size. In this package, there are a variety of solid types of element which can be used for meshing the solid parts of the heel region. In 3D FEA, two types of tetrahedral and hexahedral elements are commonly used for mesh creation. While tetrahedral meshing is mostly automatic, hexahedral meshing requires more manual steps, time and patience of the user. Therefore, tetrahedral elements have been widely used for meshing foot and footwear models (7, 87, 101-103). However, hexahedral elements provide a more accurate solution at less cost, especially in situation when complex structures are undergoing large deformation. Besides, linear tetrahedral elements are very stiff and extremely fine meshes are required to obtain accurate results (100). A study by Tadepalli et al. demonstrated that for different conditions commonly seen in foot and footwear biomechanics, hexahedral elements consistently performed better than linear tetrahedral elements (104).

Since Abaqus cannot automatically generate hexahedral meshes for structures with very irregular shapes, each of the structures in the heel region model was partitioned into less complex sub-regions. The partitioning process was iterative and continued until all sub-regions could be meshed using hexahedral elements. The quality of the mesh and individual elements was controlled using verification tools. The quality of elements was accepted if they

met the following criteria: 1) aspect ratio (ratio between the longest and shortest edge of an element)≤ 5, 2) face corner angle (angle between two edges of a face in an element)≤160 and ≥10 degree. Adjustments were applied to the mesh where they were necessary to obtain a high quality mesh. A sensitivity analysis was conducted to establish the mesh density most appropriate to obtain more accurate solution. Each FE model part was discretised with successively finer meshes and the model predicted force results were analyzed. The model predicted peak force was measured against the number of the elements and a further increase in mesh density was stopped when no important changes was observed in the peak force (variation in peak force for subsequent mesh densities<3%). More simulations with finer meshing showed that to achieve variation in peak force under 2.5%, sometimes the increase in computation time was doubled. For instance, in macro-chamber mesh convergence study, to achieve 2.8% difference between peak forces of successive models with different meshing, the computation time was increased for 8 minutes compared to the first model with coarse meshing. The results in Figure 4.4 shows that to reduce the difference between peak forces to 1.8% by increasing the number of elements, the computation time was increased for another 11 minutes. When this increase of time is considered for more than estimated 100 iterations of running FEA to achieve the project objectives, this difference becomes very significant in terms of computation time while the effect of increasing of the number of elements on the model response was negligible.

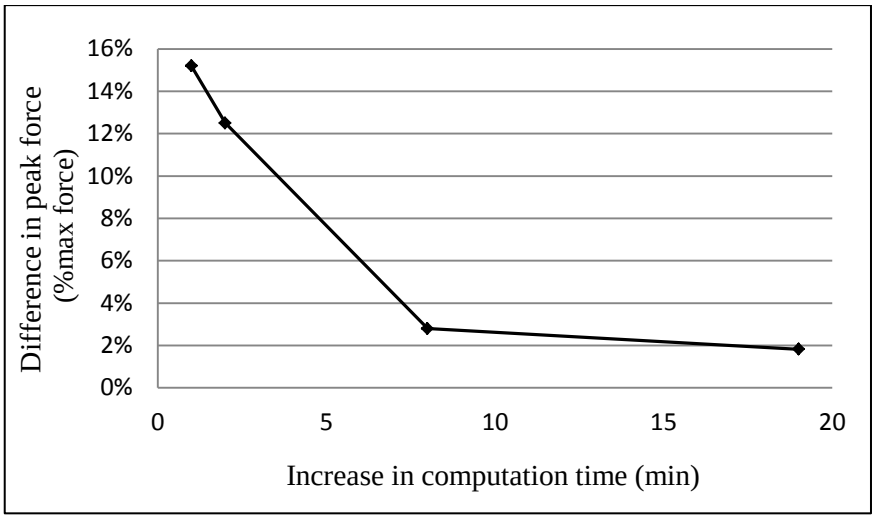

Figure 4.4: Effect of mesh density of macro-chamber layer on increase in computation time and decrease in variation in peak forces.

The total numbers of elements generated for each part in the FE model are given in Table 4.1. All elements are hexahedral with type of C3D8R which is 3D linear 8-node brick reduced integration element. Figure 4.5 also shows coarse, intermediate and fine meshes of the skin layer.

Table 4.1: Numbers of elements of the FE model parts

	Muscle tissue	Plantar fascia	Macro-chamber	Micro-chamber	Skin
Number of elements	2477	1157	2936	3364	1570

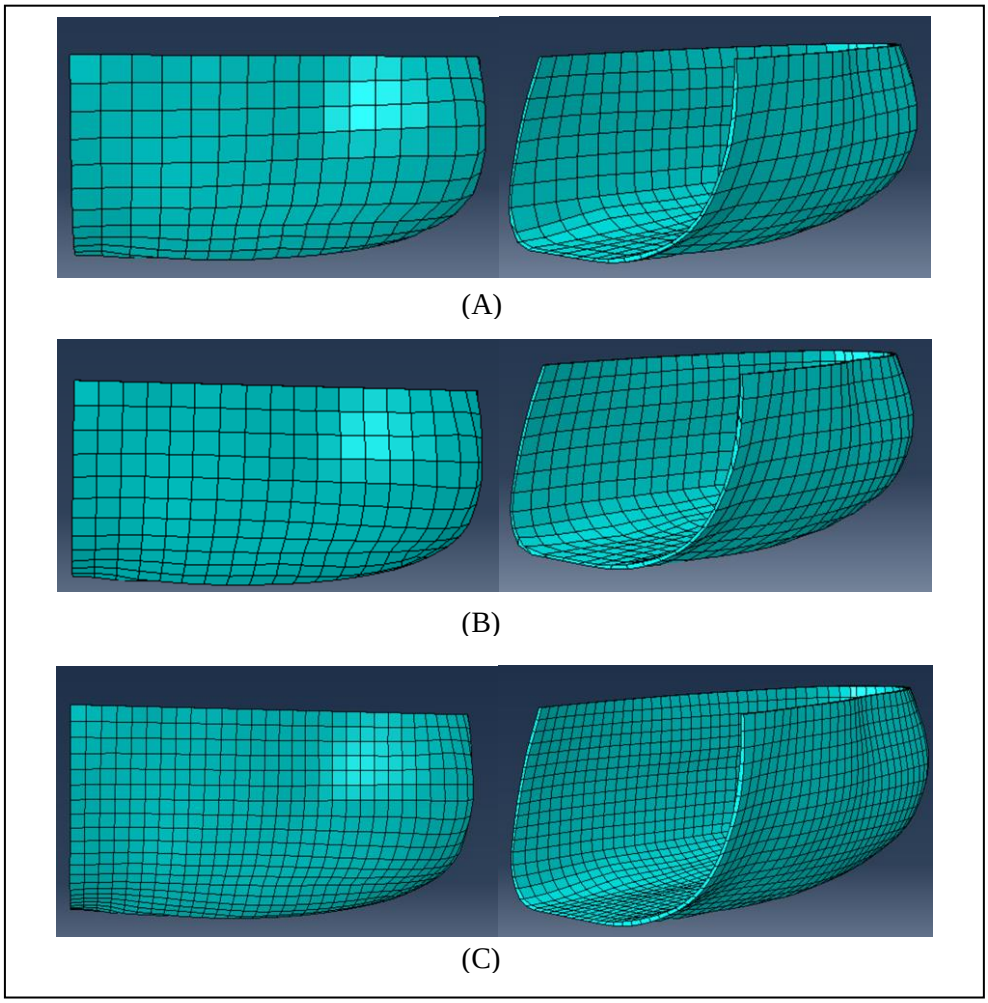

Figure 4.5: Finite Element meshes of the skin layer: (A) Coarse; (B) Intermediate; (C) Fine mesh.

After mesh creation, the FE model was exported to Ls-Dyna 2.2 (Livermore Software Technology Corporation, Livermore, USA) using Nastran file format. Ls-Dyna was selected for the FEA because of the various material models it can provide for soft tissues. Since in this project the main objective is to estimate the hyperelastic and viscoelastic material properties of the heel pad sub-layers, the selection of the material model which could be used to simulate both of these behaviours was very important. In Ls-Dyna, Ogden material model was found to be the one which meet the specifications. Using Ogden material model, not only was the incompressibility of the heel pad tissue modelled but also loading speed dependence of the tissue was simulated by using the optional viscoelastic term.

To complete the FE model so that it accurately reproduces the heel pad behaviour under loading (see sections 5.2.1 and 5.2.2), it was necessary to model the indenter and load cell located beneath the calcaneus tuberosity. During experiments in the test rig, the foot of the subject was placed in a foot brace just above the flat rigid indenter and the load cell (Figure 4.7). The ring shaped indenter with the load cell at the center of it were responsible for compressing the heel pad while the load cell simultaneously measured the reaction force under the heel pad.

In Ls-Dyna a rigid ring shaped plate with 150mm outer diameter and 21mm inner diameter was modeled to represent the indenter. A rigid 20mm diameter circular plate, located at the center of the indenter, was also modeled to represent the load cell. A gap of 0.5mm was modelled between the load cell and the indenter to exactly replicate the positions of the load cell and the indenter in the test rig and also remove any possible interactions exist between them. A total number of 20 and 105 hexahedral elements were generated to mesh the indenter and load cell respectively (Figure 4.6).

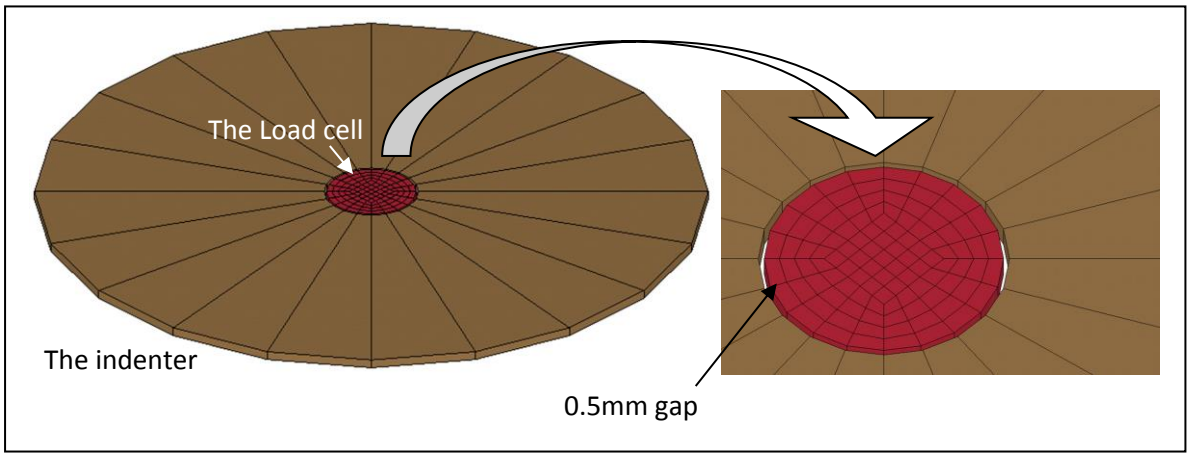

Figure 4.6: The model of the indenter and the load cell.

In actual physical testing when the foot was placed in the foot brace, it was observed that the heel region was tilted for some degree. To replicate this in the FE model the angle of rotation of the heel in the foot brace was measured. As can be seen in Figure 4.7 the heel was placed in a rectangular aperture with the size of 80×70mm in the test rig during experimentations.

Therefore, with the use of the following equation the amount of the angle of rotation of the heel could be found.

$$tan\,\theta = \frac{Y}{8-X} \tag{4.1}$$

Where θ is the angle of the rotation, X is the location of the calcaneal tuberosity from the back of the foot, and Y is the vertical measurement of the amount of the heel pad coming out of the aperture (Figure 4.7). Using the ultrasound imaging technique, the location of the calcaneus tuberosity was measured 2.7cm from the back of the foot. The amount of the heel pad coming out of the aperture was also measured 1.68cm. Therefore, the angle of rotation of the heel inside the foot brace was approximately 17.6˚. Because of the compliance within the brace system and small change of the position of the heel inside the brace, the angle of rotation of the heel could be changed for approximately ±5˚. A parametric study at the end of this chapter evaluates the effect of the variation in the angle of rotation on the heel pad behaviour.

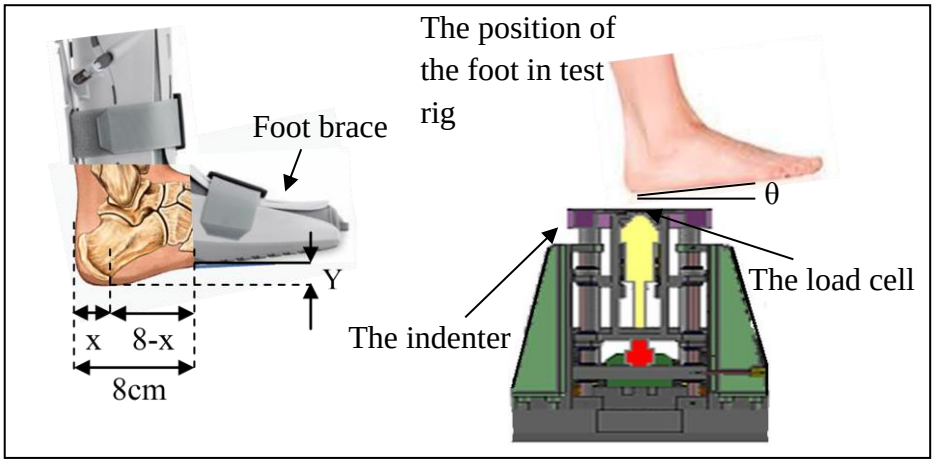

Figure 4.7: The angle of rotation of the heel in the test rig

To properly reproduce the position of the heel pad in the modeling, the FE model was rotated for 17.6 degree. The indenter and the load cell were positioned under the heel pad so that the centre of the load cell was exactly under the calcaneal tuberosity that has the minimum thickness of the heel pad. Doing so the experimental conditions, in which the centre of load cell was placed under the calcaneus tuberosity, were simulated. A parametric study was conducted to investigate the effect of the angle of rotation on the force-strain response of the

heel pad under compression (see section 4.3). The final position of the FE model is shown in Figure 4.8.

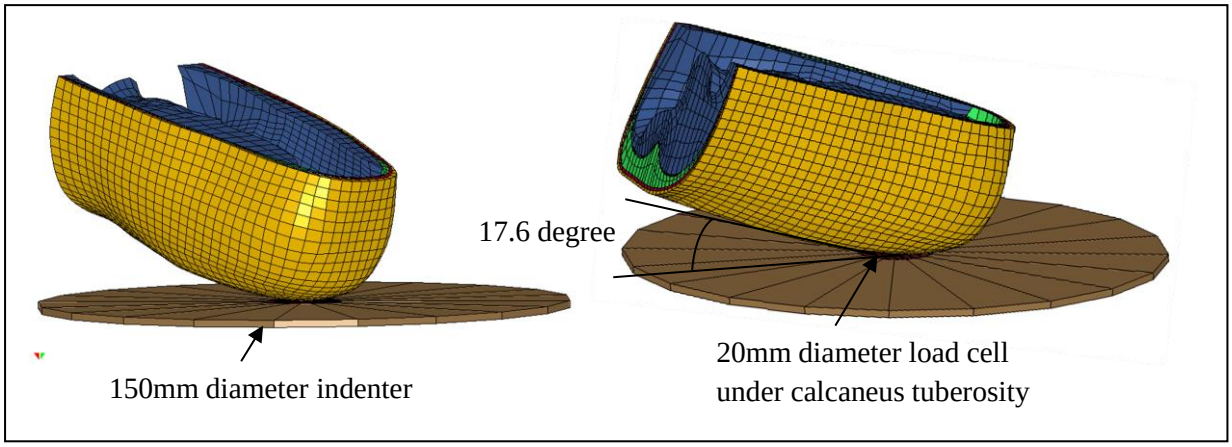

Figure 4.8: The complete meshed model of the heel region

4.2.2 Loading and Boundary Conditions of the Finite Element Model

Based on the results of the ultrasound study on investigation of soft tissues movements in superior and anterior directions, all nodes at the superior and anterior regions (flat faces) were fully constrained against movements in superior and anterior directions (Figure 4.9). The effects of the stiff tissue (foot bone and Achilles tendon) on the biomechanical behaviour of the heel pad were simulated by applying zero-displacement constraint to all nodes forming the soft tissue-stiff tissue interface. A boundary constraint was also set on the indenter and load cell to allow them to move only in the vertical direction as was the case in experiments. Figure 4.9 shows the boundary conditions applied to the heel region model.

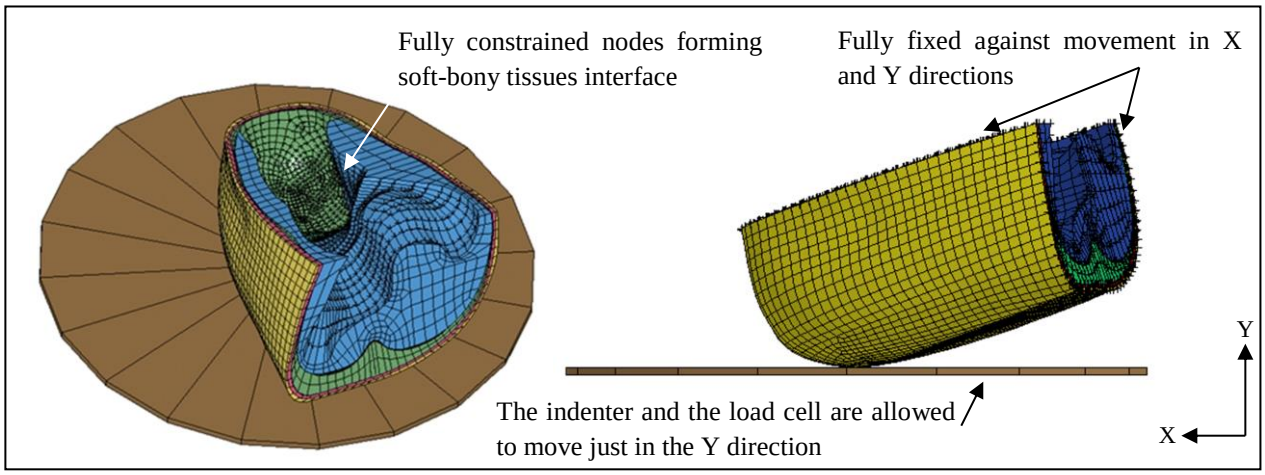

Figure 4.9: The boundary conditions applied to the FE model

The contacts between different parts in the heel model were defined. To define contacts it is necessary to distinguish the potential contact partners called master and slave. These FE terminologies refer to the way that the contact constraints are applied to the FE model during analysis. The master surface is interpolated as a smooth curve whereas all individual nodes on the slave surface are constrained so as not to penetrate into master surface (105). In the case where one of the bodies is rigid or stiffer than the other one, the stiffer surface is chosen as the master surface and the surface of contacting body is called slave surface. However, if both bodies have comparable compliance, the selection of master and slave surfaces becomes arbitrary (106).

The automatic surface-to-surface is the simplest contact type that allows the surfaces to disconnect when the loading is removed. In Ls-Dyna, the surface-to-surface contact works by checking different locations for potential penetration of a slave node through master segments. The automatic surface-to-surface contact was established between the indenter/load cell and the plantar soft tissue. Because of the lubricating nature of the ultrasound gel on the load cell during experimentations, the contact behaviour between the indenter/load cell and the soft tissue plantar surface was considered frictionless.

A tied contact is another contact type in which two surfaces of different parts are bonded together. In tied contact, any slave nodes to be tied are moved to the master surface during initialization thus any gaps between the slave nodes and master segments be eliminated. Then the slave nodes get constrained to move with the master surface (107). The tied contact was used to simulate the interactions between the skin/micro-chamber, micro-chamber/macro-chamber, macro-chamber/muscle tissue, macro-chamber/plantar fascia, and plantar fascia/muscle tissue.

4.2.3 Material Properties of the Finite Element Model

To complete the FE model, all structures included in the heel region model had to be assigned with material properties. Therefore, the material properties derived from published works were assigned to the muscle tissue and the plantar fascia. Researchers have used both linear and nonlinear elastic material models for the muscle tissue and the plantar fascia in different cases (68, 97, 108, 109). In this project, linear elastic material model was selected for the muscle tissue and the plantar fascia to reduce the complexity of the problem. The load cell and the indenter were modelled as rigid parts with material properties of steel.

The main objective of this project was to estimate the nonlinear elastic and viscoelastic material properties of the macro-chamber, micro-chamber, and skin layers. However, to start FEA, initial material properties were required for the heel pad sub-layers. Therefore, the heel pad sub-layers were assigned with initial nonlinear elastic and viscoelastic material properties obtained from literature.

4.2.3.1 Linear Elastic Material Models for Muscle and Plantar Fascia

An elastic material is a material that returns to its original shape once the applied force is removed. For a linear elastic material, the relationship between stress and deformation is represented by constitutive equation that is called Hooke's law (eq. 4.2).

$$\sigma = E\epsilon \quad (4.2)$$

Where σ is stress, ε is strain and E values are the Elastic constants, also known as Young's modulus. The stress-strain behaviour of the linear elastic materials is shown in Figure 4.10. The muscle tissue and the plantar fascia were modelled as linear elastic material. Little was found about the exact material properties of the foot muscle in the literature. In most of the FE models of the foot available in the literature, the foot muscle tissue was merged with the heel pad tissue and assigned with the material properties of the heel pad (73, 102, 110, 111). However, in one case, the foot muscle and skin layer together were modelled as linear elastic material with Young's modulus of 2.49MPa (109). In another case, the Young's modulus of 1.08, 14, and 55MPa were assigned to the muscle tissue of the foot to evaluate effects of the weak, moderate and severe muscle tensions on the behaviour of the foot (97).

In this project the muscle tissue was modelled as a homogeneous, isotropic linear elastic material with Young's modulus of 1.08MPa representing the stiffness of the muscle tissue. The material properties selection was based on the fact that between three Young's modulus values of 1.08, 14, and 55 MPa, representing different degrees of muscle tension in literature, 1.08MPa was the closest to the 2.49MPa value used for muscle tissue in the published work (109) and to 0.15MPa (7, 108) and 0.45MPa (102) used for the soft tissue (foot muscle and heel pad). Poisson's ratio of 0.49 was assigned to the muscle tissue to represent its nearly incompressible nature (109, 111). Poisson's ratio expresses the negative ratio of the strain of the contraction perpendicular to the force direction to the strain of the expansion in direction which force applies. Incompressible materials are sort of materials that their shapes are changed under loading while their volumes stay constant. Since no agreement was found in the published studies on specific material properties for the foot muscle tissue a parametric study was conducted to investigate the effects of the foot muscle stiffness on the heel pad

responses and verify the selection of Young's modulus of 1.08MPa for the foot muscle (see section 4.3).

The literature contains limited reports concerning material properties of the plantar fascia. In most of experimental studies, only the tension stiffness of the plantar fascia in its longitudinal direction has been of interest (112-114). In most of published works on FEA of the human foot, the plantar fascia was modelled with tension-only truss elements with Young's modulus of 350MPa determined from tension tests on the long axis of the plantar fascia (73, 97, 110). In one case, the plantar fascia was modelled as isotropic, linear elastic material using 2D elements and Young's modulus of 11.5MPa was assigned to it in both inferior-superior and anterior-posterior directions (111). In another study, the plantar fascia was modelled with 3D elements with Young's modulus of 350MPa (76).

Since no information concerning the behaviour of the plantar fascia in its inferior-superior direction could be found in literature, in this project the plantar fascia was modelled as an isotropic homogeneous material assigned with properties found for its longitudinal axis. Young's modulus of 350MPa was selected for the plantar fascia because this value was commonly used in published works, one for 3D elements and another 3 for truss elements. Poisson's ratio of 0.4 derived from literature was selected for the plantar fascia (31, 115). Since it was not possible to find strong reasons in the literature to verify the selection of 350MPa as Young's modulus of the plantar fascia, a parametric study was conducted to assess the effect of the alternation of the stiffness of the plantar fascia on the responses of the heel pad. Detailed information about the process and results of this parametrical study can be found in section 4.3.

4.2.3.2 Nonlinear Material Model for Macro-chamber, Micro-chamber and Skin

The macro-chamber, micro-chamber and skin layers were modelled as homogeneous, isotropic visco-nonlinear elastic materials. Their incompressible nature was simulated with the Poisson's ratio of 0.4999 obtained from literature (110). Apart from the bones, all body tissues undergo large deformations during physical activities. When the biological tissues undergo large deformation their stress-strain responses are no longer linear. This kind of material shows large deformations at the beginning of loading and becomes stiffer when the load is increased. These materials return to their original unloaded dimensions when the load is removed. Any material exhibiting such behaviour is called nonlinear elastic material, also known as hyperelastic material (Figure 4.10). The hyperelastic materials have some specific features as follows:

- Behaves nonlinear under large deformation;
- Does not have permanent deformations;
- There is not proportional relationship between the stress and the strain;
- The (E), are not constant coefficients but stress-strain relation is derived by strain energy function.

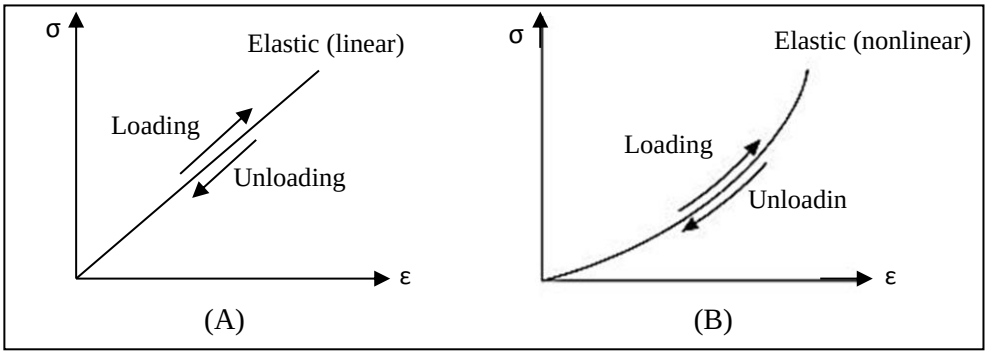

Figure 4.10: Stress-strain response of an elastic material under static loading: (A) Linear elastic material; (B) Nonlinear elastic material.

For analysing the hyperelastic material, the elasticity is considered as energy not stress. When a hyperelastic material is loaded and consequently deformed, energy (U), usually known as

strain energy, is stored and after removing the load, it brings the material back to its original state. Some forms of the strain energy function used in the literature for modelling the heel pad behaviour under loading are Neo-Hookean, Mooney-Rivlin, and Ogden hyperelastic models. The Ogden model is one the form of strain energy function for hyperelastic materials, proposed by Ogden in 1972 (116). In the Ogden material model in Ls-Dyna, the strain energy is expressed as a function of principal stretches (λ_i) as given in equation 4.3.

$$U(\lambda_1, \lambda_2, \lambda_3) = \sum_{i=0}^{N} \frac{\mu_i}{\alpha_i} ({\lambda_1}^{\alpha_i} + {\lambda_2}^{\alpha_i} + {\lambda_3}^{\alpha_i} - 3) + \sum_{i=1}^{N} \frac{1}{D_i} (J-1)^{2i} \quad (4.3)$$

Where i is the model's order, μ_i and α_i and D_i are material properties and J (total volumetric ratio) is equal to $\lambda_1\lambda_2\lambda_3$. For the incompressible material J is equal to 1. Therefore, the first order of the Ogden form for the incompressible material can be denoted by equation 4.4.

$$U(\lambda_1, \lambda_2, \lambda_3) = \frac{\mu}{\alpha} ({\lambda_1}^{\alpha} + {\lambda_2}^{\alpha} + {\lambda_3}^{\alpha} - 3) \quad (4.4)$$

The heel pad sub-layers also shows viscoelastic characteristics during loading-unloading cycle. While elastic materials return to their original state via the same path used to compress them, viscoelastic materials return via a different path and energy dissipates in a number of ways such as heat, sound, and surface energy. The relationship between stress and strain in this kind of materials depends on time. The rate dependent viscoelastic behaviour of the materials can also be modelled using the Ogden material model in Ls-Dyna. In addition to the hyperelastic model there is an optional viscoelastic contribution. This material model uses the generalized linear Maxwell viscoelastic model, which consists of dampers and springs in series (Figure 4.11).

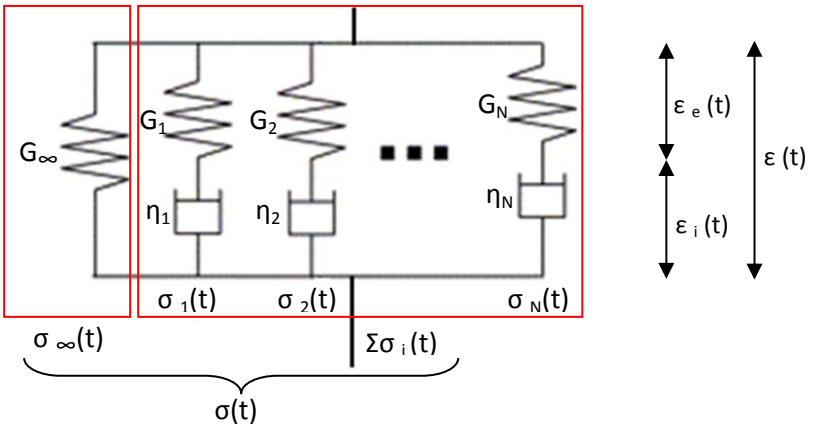

Figure 4.11: Generalised Maxwell viscoelastic model.

G represents the spring constant and η represents the viscosity of the dashpot. In this model the overall stress results from adding viscoelastic stress, $\Sigma\sigma_i$ (t), to the hyperelastic stress, σ_∞(t), derived from Ogden strain energy function.

$$\begin{cases} \sigma(t) = \sigma_\infty(t) + \sum_{i=1}^{N} \sigma_i(t)\,; \\ \varepsilon(t) = \varepsilon_e(t) + \varepsilon_i(t); \\ \sigma_i(t) = \sigma_i(0)e^{-\beta_i t} \end{cases} \tag{4.5}$$

The relaxation function is defined as:

$$G(t) = \frac{\sigma(t)}{\varepsilon_0} = G_\infty + \sum_{i=1}^{N} G_i\, e^{-\beta_i t} \tag{4.6}$$

In eq. 4.6, G_i and β_i are the viscoelastic material properties and i is the model's order. The G_i is the shear relaxation modulus and β_i is decay constant modulus. For the Ogden model in Ls-Dyna up to 6 Maxwell elements can be defined.

The main objective of this project was to estimate the hyperelastic and viscoelastic material properties of the macro-chamber, micro-chamber, and skin layers. To start FEA initial hyperelastic materials of μ=16.45kPa and α=6.82 from published literature were assigned to the macro-chamber, micro-chamber and skin layers (5). The initial viscoelastic material parameters for the heel pad sub-layers also were derived from the published work as

0.389MPa and $1ms^{-1}$ for G and β respectively (117). The material model and properties used for different structures in the heel region model are listed in Table 4.2.

Table 4.2: Material properties of each component in the FE model

	Material	Material properties	Poisson's ratio	Density (g/mm^3)	References
Muscle tissue	Linear elastic	E=1.08MPa	0.49	1×10^{-3}	(97)
Plantar fascia	Linear elastic	E=350MPa	0.40	1×10^{-3}	(73, 97)
Macro-chamber (initial) Ogden model	Hyperelastic Viscoelastic	μ=16.45kPa, α=6.82 G=0.389MPa, $\beta=1ms^{-1}$	0.4999	1×10^{-3}	(5) (117)
Micro-chamber (initial) Ogden model	Hyperelastic Viscoelastic	μ=16.45 kPa, α=6.82 G=0.389MPa, $\beta=1ms^{-1}$	0.4999	1×10^{-3}	(5) (117)
Skin layer (initial) Ogden model	Hyperelastic Viscoelastic	μ=16.45 kPa, α=6.82 G=0.389MPa, $\beta=1ms^{-1}$	0.4999	1×10^{-3}	(5) (117)
Indenter	Rigid	$E=2.07\times10^5$ MPa	0.3	7.83×10^{-3}	
Load cell	Rigid	$E=2.07\times10^5$ MPa	0.3	7.83×10^{-3}	

4.3 PARAMETRIC STUDIES

A series of parametric studies were conducted to investigate effects of variation of: (1) material properties of muscle tissue; (2) material properties of plantar fascia; (3) angle of rotation of the heel model on the force-strain FE model responses. The first two parametric studies allowed assessing the integrity of the material properties selection and estimating the potential errors that might result from not using the material properties for the test subject. The degree of rotation of the heel in the test rig was measured using ordinary measurement tools (see section 4.21). In addition, the compliance within the brace system allowed small changes in the position of the foot inside the test rig. The parametric study could estimate the errors that might be induced to results due to using imprecise angle of rotation. The predicted

relationship between compressive force and the heel pad tissue strain was used as a major sensitive index.

4.3.1 Effect of Varying the Stiffness of the Muscle Tissue

To investigate the effect of stiffness of the muscle tissue on the compressive load experienced by the heel pad a parametric study was conducted. Young's modulus of 1.08MPa, 14MPa, and 55MPa, derived from the published data, were assigned to the muscle tissue to simulate its low, medium, and high stiffness respectively and evaluate the effect of variation in the muscle tissue stiffness on the heel pad (97).

All other structures in the FE model were assigned with the material properties as per Table 4.2. The heel pad model was then compressed up to 40% of the unloaded thickness of the heel pad at the constant velocity of 5mm/s. The heel pad was compressed up to 40% strain during physical experimentations to study its hyperelastic behaviour (see section 5.2.3). The predicted compressive load measured by the load cell in the FE model is plotted against the tissue strain (Figure 4.12).

As can be seen in Figure 4.12, varying the stiffness of the muscle tissue had only a small influence on the compressive load experienced by the heel pad. The maximum difference was 0.67% max force between low and high stiffness of muscle tissue. The differences between predicted force-strain results of the heel pad obtained for muscle tissue with low, medium and high stiffness were calculated using RMS (Root Mean Squared) error (Table 4.3). RMS error provides a standardized way to measure the differences between values obtained from two different experiments. RMS error at each level of strain of the heel pad (ε) is calculated as:

$$RMS\ \text{error} = \sqrt{\frac{\sum_{\varepsilon=1}^{n}(F_{\varepsilon}-F_{\varepsilon}^{'})^{2}}{n}} \tag{4.7}$$

Where F_{ε} is the load obtained by the first experiment at strain of s and F'_{ε} is the load obtained

by the second experiment at the same strain ε. The strain is used to describe the deformation of a layer under loading. The maximum strain is defined as:

$$\varepsilon = \frac{UT-LT}{UT} \tag{4.8}$$

In equation 4.8, UT stands for the unloaded thickness of a layer and LT stands for the loaded thickness of a layer.

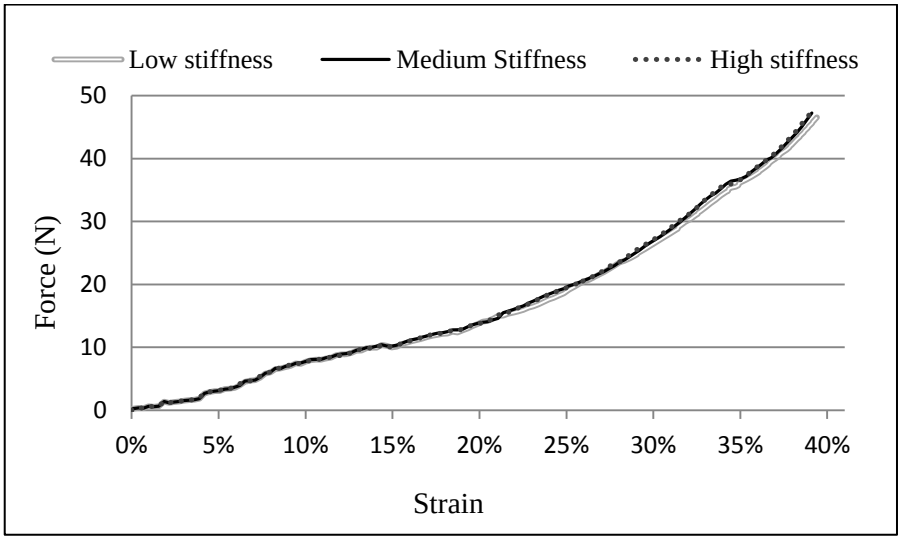

Figure 4.12: Effect of varying the stiffness of the muscle tissue.

The small differences between force-strain curves of different situations, represented by RMS error in Table 4.3, indicate that the response of the heel region model is insensitive to the variation of the muscle tissue stiffness. However, the computation time for analysis of the heel region model with high stiffness of muscle tissue was three times more than the time required for analysis of the model with low stiffness of muscle tissue. Therefore, the Young's modulus of 1.08MPa was selected as the reference material parameter for the muscle tissue during further analysis.

Table 4.3: Difference between force-strain curves obtained for the model with different muscle tissue stiffness.

Muscle Stiffness	Low vs Medium	Low vs High	Medium vs High
RMS error (N)	0.28	0.32	0.15
RMS error (% Max force)	0.60	0.67	0.33

4.3.2 Effect of Varying the Stiffness of the Plantar Fascia

The plantar fascia was modelled as an isotropic linear elastic material and 5 Young's modulus values ranging from 10 to 500MPa were assigned to this structure. These values started from 10MPa, which is close to 11.5MPa used in the literature (111), and ended up at 500MPa which represents the high stiffness of the plantar fascia. Further values such as 250 and 350MPa were selected from the literature (108, 112, 113).

Other structures in the FE model were assigned with the material properties as per Table 4.2. Similar to section 4.3.1 the heel pad model was compressed up to strain of 40% with velocity of 5mm/s to reproduce the physical tests conditions (see section 5.2.3). The model predicted compressive force-strain relationship of the heel pad is plotted in Figure 4.13.

1: E=500MPa 2: E=350MPa 3: E=250MPa 4: E=100MPa 5: E=10MPa

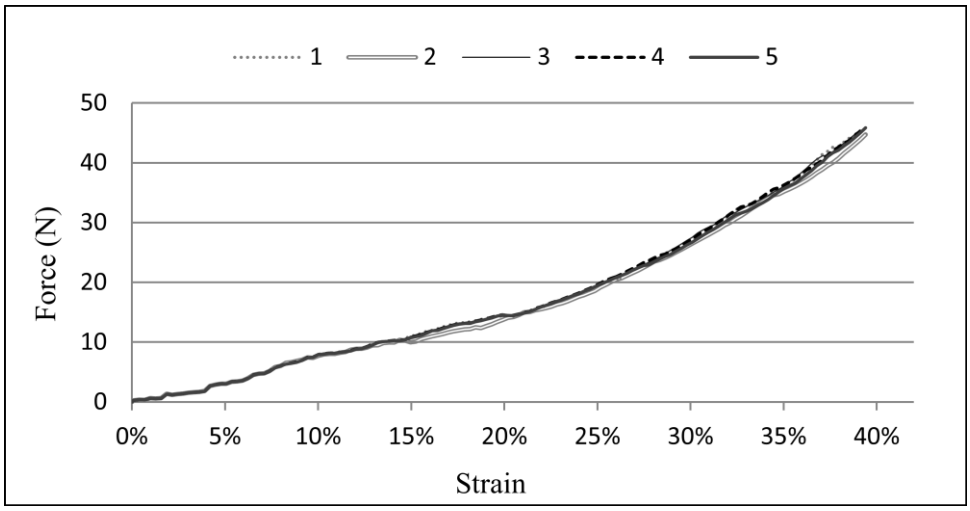

Figure 4.13: Effect of varying the stiffness of the plantar fascia.

This figure shows that the changes of the material properties of the plantar fascia had a small effect on the predicted force-strain results (RMS error<1.5% max force). Since the plantar fascia is far from the plantar heel, no difference was found in the force-strain results by variation of the plantar fascia stiffness up to 15% strain. The results of the parametric study confirmed that the response of the heel region model is not affected by the variation of the plantar fascia stiffness in range of 10 to 500MPa. Although the increase in the plantar fascia

stiffness increased the computation time, the Young's modulus of 350MPa was selected as the reference material property for the plantar fascia since this value was used in several studies.

4.3.3 Effect of Varying the Angle of Rotation of the Heel Model

To assess the effect of variation in the angle of rotation of the foot on the heel pad responses, the angle of rotation of the heel model (reference value = 17.6˚) was varied for ±1˚, ±5˚ and ±10˚. All structures in the FE model were assigned with the material properties as per Table 4.2. Similar to previous parametric studies, the heel pad model was compressed up to strain of 40% with displacement rate of 5mm/s to reproduce the physical tests conditions (see section 5.2.3). The model predicted force-strain results for reference angle of rotation and different angles are shown in Figures 4.14-4.16.

As can be seen in Figure 4.14, the predicted force-strain relationship for the models with angle of rotations of ±1˚are generally coincident with the force-strain result for the model with the reference angle of rotation (RMS error<1.5% max force). According to Figures 4.15 and 4.16 extend changes to the angle of rotation of the heel model (±5˚ and ±10˚) bring some small variations (RMS error<4% max force). Figures 4.15 and 4.16 show that for more than 25% strain, by increasing the angle of rotation the force decreases for the same depth of indentation. It can be explained by the fact that by increasing the amount of rotation of the model less material is compressed in high strains. In low strains, the amount of materials, which are required to be compressed for the same depth of indentation, are approximately equivalent for different rotation of the model.

The differences between the force-strain results obtained for the model with reference and different angles of the rotation are calculated and represented by RMS error in Table 4.4. The results indicates that for maximum 10 degree difference in angle of rotation which is ~48% average measurement error of the amount of the heel pad coming out from the aperture

induced less than 4% maximum force error to predicted force-strain results. Understanding the effect of angle of rotation of the FE model, the measurements error was kept small by repeating the examination and measurement of the amount of the heel protruded from the foot brace at different times.

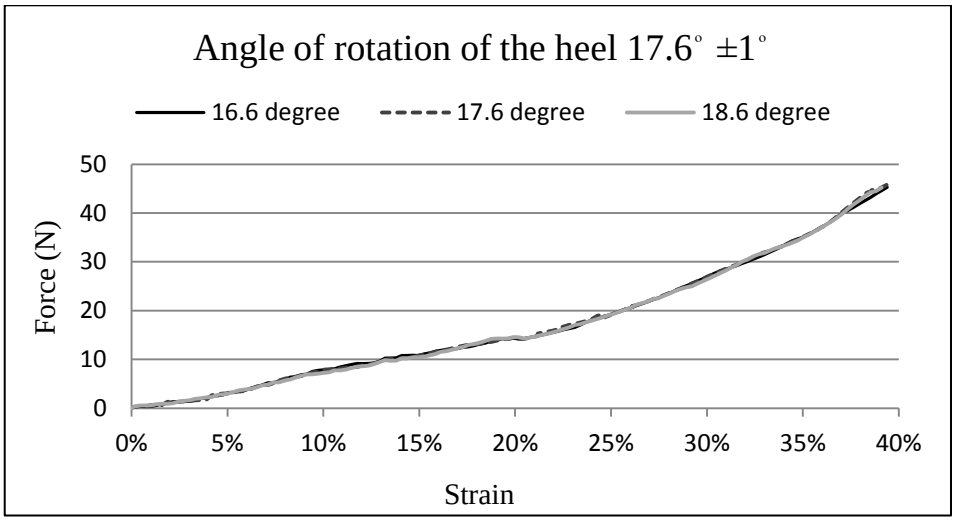

Figure 4.14: Effect of varying the angle of rotation of the FE model for ±1°.

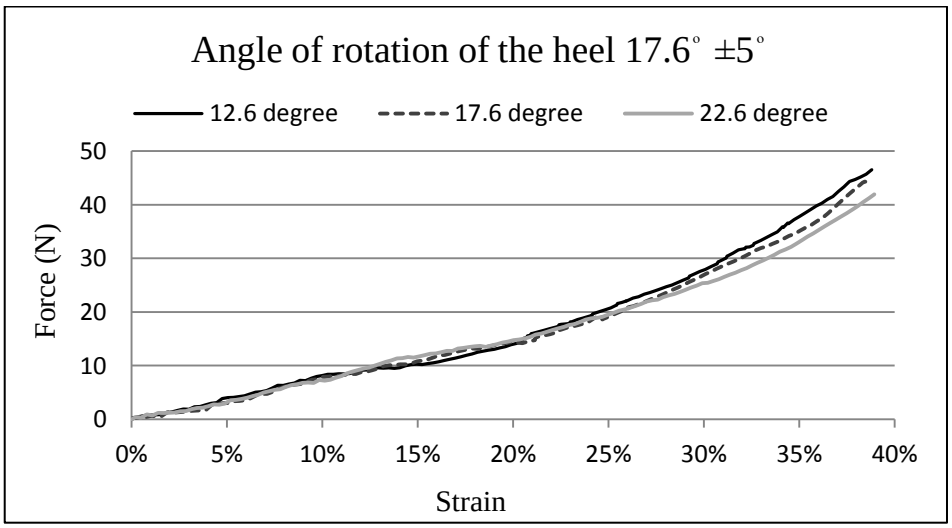

Figure 4.15: Effect of varying the angle of rotation of the FE modelfor ±5°

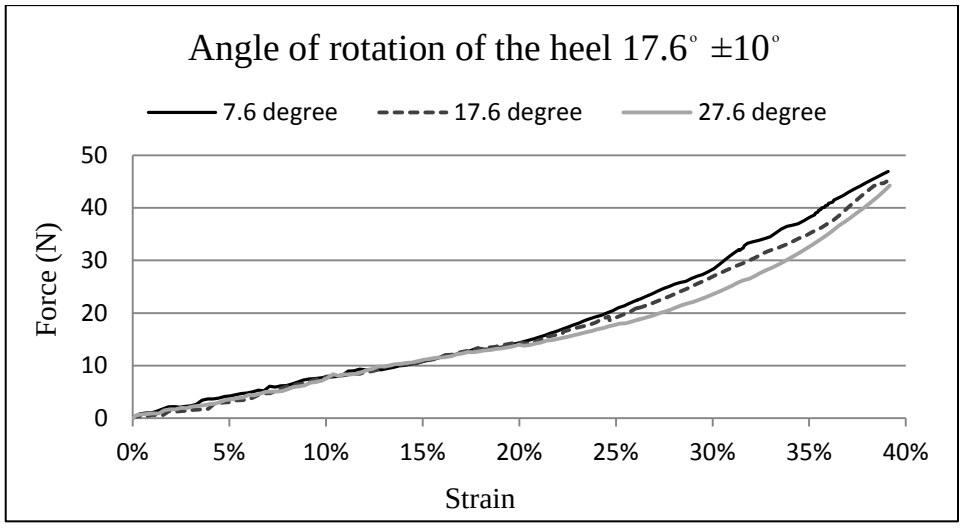

Figure 4.16: Effect of varying the angle of rotation of the FE modelfor ±10°

Table 4.4: Difference between the force-strain curves obtained for the model with the reference angle of rotation and the models with different angle of rotations.

Angle of rotation	18.6º (+1º)	16.6º (-1º)	22.6º (+5º)	12.6º (-5º)	27.6º (+10º)	7.6º (-10º)
RMS error (N)	0.47	0.31	1.40	0.99	1.64	1.43
RMS error (% Max force)	1.04	0.68	3.12	2.15	3.62	3.15

4.4 CONCLUSIONS

In recent years, several 3D FE models of the human foot have been generated to investigate the biomechanical behaviour of the heel pad. Although the macro-chamber, micro-chamber and skin have been distinguished different structures and material properties, in most of 3D FE models, they have been fused together to represent the soft tissue in the heel region (6, 73, 87, 102, 109, 110, 115). In some limited 3D FE models, the skin layer was separated from the macro-chamber and micro-chamber to investigate the material properties of the skin layer and gain better understanding of the heel pad biomechanical behaviour (7, 101, 103).

The aim of this chapter was to develop the 3D FE model of the heel region with size of 9.25cm from the back and 4.5cm from the bottom of the heel. The anatomically detailed

model of the heel region composed of the muscle tissue, plantar fascia, macro-chamber, micro-chamber and skin was generated based on created solid geometries in Chapter 3. The different structures in the model were meshed using hexahedral elements. The heel pad model was rotated for 17.6˚to replicate the position of the heel inside the test rig during physical tests. The indenter and the load cell were modelled and positioned under the calcaneus tuberosity to reproduce the compression tests conditions (see chapter 5). Loading and boundary conditions were applied to the model so that simulated the actual experimental conditions. To complete the FE model, the material properties obtained from the literature were applied to the FE model structures.

Some issues arose such as finding reliable material properties for the foot muscle tissue and the plantar fascia. In most of developed 3D FE model in the literature, the foot muscle tissue was merged with other soft tissues in the foot so identical material properties were assigned to them (73, 102, 109-111). The literature does not contain sufficient data regarding to the material properties of the foot muscle tissue and the results found for the plantar fascia were only tension material properties in its longitudinal axis (73, 97, 109, 110). Therefore, for muscle and plantar fascia parameters available in the literature were used initially and parametric studies were conducted to estimate the possible errors which might be induced to the FEA as results of not using accurate material properties. The parametric studies showed that the predicted force-strain responses of the heel pad were generally insensitive to the variation of the stiffness of the muscle tissue and plantar fascia in the commonly accepted ranges.

Another issue that was faced during the development of the FE model was measuring the angle of rotation of the heel in the test rig. Because of the narrow space between the foot brace and the heel pad indenter, it was not possible to use tools with high accuracy to measure the amount of rotation of the heel region during experiments. In addition, the compliance

within the brace system allowed small changes in the position of the foot inside the test rig. Therefore, another parametric study was performed to assess the effect of the rotation of the angle of the FE model on the predicted force-strain results. These results showed that the predicted results were only slightly influenced by variation of the angle of rotation by 1 degree (RMS error<1.5% max force). Larger changes were noticed for 5 and 10 degrees (RMS error<4% max force). By repeating the measurement at different times, the minimisation of the measurement error was ensured.

After completion of the study it was noticed that the hyperelastic Ogden material properties for macro-chamber, micro-chamber and skin layers obtained from literature as initial parameters to start FEA, were determined using a formula different from what was used in Ls-Dyna. Specifically, the shear modulus from literature (μ_l) was equal to ($\frac{1}{2}\ \mu_{ls}\alpha$), where μ_{ls} represents the shear modulus in Ls-Dyna and α is identical in both systems. This means that instead of 16.45kPa as shear modulus in Ls-Dyna, 4.82kPa should have been used. Further studies in Chapter 6 showed that when using 16.45kPa as shear modulus of the macro-chamber, the force-strain response of the tissue was still underestimated. Therefore, since this parameter was used as initial parameter to start FEA and did not affect the final results of this project, it was not necessary to repeat the studies using the corrected value.

The FE model with specifications described in this chapter was used to estimate the material properties for the heel pad sub-layers (see Chapter 6) and showing its application in studying the effects of experimental and geometrical conditions on the heel pad responses and also investigating the effect of foot wear design factors on the heel stress (see Chapter 7).

5. Chapter Five:

EXPERIMENTAL ACQUISITION OF FORCE AND TISSUE DISPLACEMENT DATA

5.1 INTRODUCTION

Several studies have been conducted to investigate the biomechanical behaviour of the human heel pad. Methods such as impact, compression, and indentation tests have been used *in-vivo* and *in-vitro*. Combined ultrasonic indentation systems composed of an ultrasound transducer and a load cell have been developed and shown to be a reliable tool to provide dynamic information about deformation of the heel pad under loading (8, 33).

The aim of this stage of the project was to perform a series of slow and rapid compression tests on the foot of a subject to obtain the force-strain responses of the heel pad and its sub-layers at different loading conditions. Compression tests were performed on the right foot of **Subject 1**, whose FE heel region model was generated. The experimental data obtained at slow compression tests and some of the data collected under rapid compression test were used as input for inverse FEA to estimate the hyperelastic and viscoelastic material properties of the heel pad sub-layers respectively (Chapter 6). The rest of rapid compression tests data were used for viscoelastic FE model validation (Chapter 6).

In this project a combined ultrasound and controlled compression device developed at the University of Salford and called STRIDE was used to study the non-linear viscoelastic behaviour of the heel pad sub-layers including the macro-chamber, micro-chamber and skin layers (118). This device (STRIDE) was designed to apply controlled and uniform vertical compression to the plantar tissue at large range of loading rates. Some limitations of the device are as follows.

- The ultrasound probe permits only 2D plane to be imaged and does not allow for a complete assessment of the plantar tissue deformation.
- The target strain could not be achieved in all conditions because of the compliance within the brace system.

- The restriction of the device to vertical compression does not permit complete simulation of gait.

This chapter starts with an introduction to the experimental device and the loading protocols used to perform different types of compression tests on the right foot of the subject. It continues with providing the results of the physical tests. Finally, a discussion of experimental findings is made in context of aims and objectives.

5.2 METHODS

5.2.1 Experimental Device

The Soft Tissue Response Imaging Device (STRIDE) developed at the University of Salford was used to apply compression to the heel pad (118). STRIDE is made of a combination of the ultrasound and indentation systems. It provides a simultaneous combined measurement of the deformation of the heel pad and the load experienced by the heel pad.

This device can only apply compression to the plantar tissue and it is not capable of complete simulation gait. During walking or running the foot and ankle are subjected to significant compressive and shear forces. Previous studies have indicated that the plantar foot ulceration are associated with both compressive and shear forces (119). Therefore, to study the behaviour of the heel during gait and simulate the heel injury, it is important to use shear and compression together. However, the vertical component of the foot motion is the predominant factor in the plantar tissue compression. In addition, during using the experimental data in estimation of the material properties of the plantar tissue in this project (Chapter 6), the model exactly replicates the experimental conditions and experimental vertical force-strain data are compared with the vertical predicted results. Thus, an effective estimation of the material properties of the plantar tissue, which is the main objective of this project, can be achieved using only the vertical component provided by STRIDE.

STRIDE is composed of a flat rigid ring shaped plate (150mm outer diameter and 21mm inner diameter) which is used to compress the heel pad uniformly to simulate the contact between the heel pad and a flat surface such as the ground or inside the shoe. This indenter plate has a circular plastic window (20mm diameter) at the centre of it. This window is designed to transmit load and ultrasound signals (Figure 5.1). An ultrasound probe (MyLab 70, Esaote, Italy), a 500lb Precision Miniature load cell (TC34, Amber Instrument, UK), and a Linear Variable Displacement Transducer (LVDT), (S-Series, Solartron, UK) are accommodated under the window at the centre of the indenter (Figure 5.1). A 0.5mm space between the indenter and the load cell caused the load passing through window to be decupled from load passing through the indenter plate.

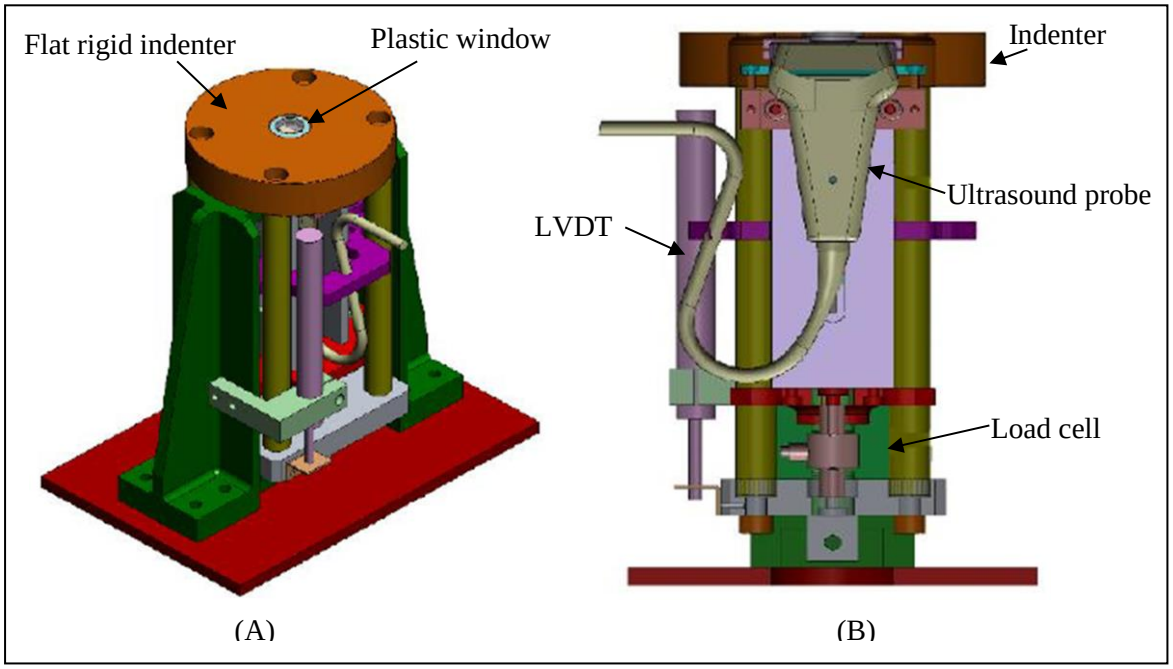

Figure 5.1: STRIDE: (A) Isometric view of STRIDE; (B) Section view of STRIDE

In this system, the ultrasound imaging data is recorded at 201Hz and the load cell and LVDT data are captured at 3000Hz. LVDT and load cell analogue data are converted to digital signals using a National Instruments Data Acquisition (NIDAQ) module. To establish synchronization between the ultrasound, LVDT and load cell output, a 5V square wave is

input to the ultrasound system and NIDAQ module. This system moves in the vertical direction and can apply controlled repeatable compression to the heel pad.

5.2.2 Foot Positioning

All tests were done while the subject was in standing position. The foot was placed in a foot brace (Aircast boot) which allowed vertical compression of the heel pad without lifting of the foot. In the foot brace, there was a rectangular 80×70mm aperture under the heel area that allowed the indenter to compress the heel pad. The calcaneus tuberosity was located above the center of the window during the compression tests.

This was achieved by finding the location of the calcaneus tuberosity using the ultrasound scanning and marking its location on the plantar surface. The subject was asked to sit on the examination table while her ankle was in neutral and the knee was in extended positions. The subject's foot was placed in an L-shaped frame that allowed intricate adjustment of foot position over the ultrasound probe in the medial-lateral and anterior-posterior directions. The probe was placed on the skin of the heel area in the medial-lateral direction and moved until the calcaneus tuberosity was aligned with the center of the probe. The position of the probe center was marked on the skin. The probe was then placed in the anterior-posterior direction aligned with the calcaneus tuberosity and another reference mark was made in-line with the center of the probe. Two reference lines at the plantar surface intersect at the location of the calcaneus tuberosity. Then the subject was asked to stand in the test rig and her foot was placed in the brace. The heel pad was positioned above the STRIDE using reference mark as a guide. Its position was adjusted until the calcaneus tuberosity was exactly located above the center of the window (Figure 5.2).

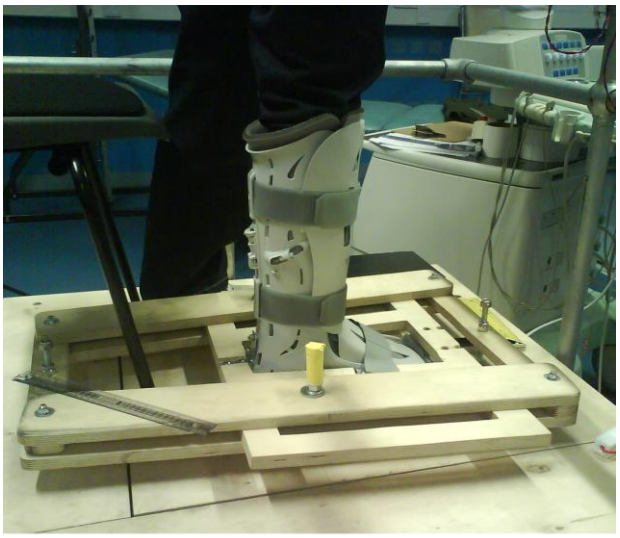

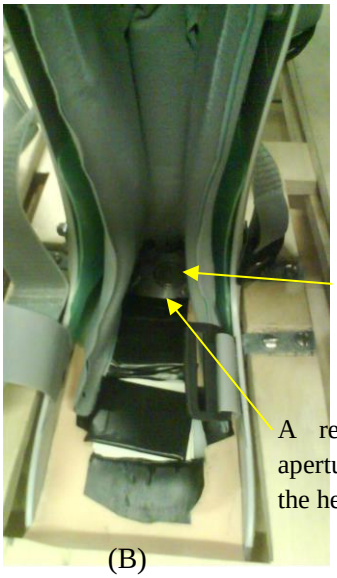

(A) (B)

Figure 5.2: Foot positioning: (A) The subject standing in the test rig; (B) The frontal view of the foot brace

5.2.3 Subjects Characteristics

A healthy female volunteer **(Subject 1)** was enrolled in this study. Ethical approval was granted by the University of Salford ethical committee. **Subject 1**, who provided the geometry of the heel region to develop the FE model in this study (see Chapter 3), was 34 years old with height of 164cm, weight of 63kg and shoe size 5UK at the time of study.

5.2.4 Loading Protocol

A series of slow and rapid compression tests were performed on the right foot of **Subject 1**, achieving up to ~40% of the unloaded thickness of the heel pad. Slow compression tests were conducted in order to determine the hyperelastic material properties of the heel pad sub-layers (see Chapter 6). Rapid compression tests were also carried out on the right foot of **Subject 1** to estimate the viscoelastic material parameters of the heel pad sub-layers and validation of the viscoelastic FE model (see Chapter 6).

At the beginning of each test, when the foot was placed in the foot brace and the heel pad was exactly positioned above the plastic window, the unloaded thickness of the heel pad sub-

layers was measured. This measurement was done using the ultrasound imaging system when the indenter just touches the plantar tissue and first ultrasound image was available. Prior to start compressing the heel pad, a layer of ultrasound gel was applied under the heel area to provide better quality of ultrasound image data. Force-strain responses of the heel pad were recorded as the output of the experimentations. While stress-strain is better representation of the response of the heel pad under loading without being affected by the size of the foot, because of the limitation of the device in measurement of the rapidly changing contact area, it was impossible to measure the stress accurately. On the other hand, the strain was chosen to represent the deformation of the heel pad and its sub-layers instead of displacement during experimentations to remove the effect of the thickness of the plantar tissues (the heel pad and its sub-layers) from the tissues' responses.

- **Slow compression tests**

In order to determine the acceptable displacement rate at which to obtain the hyperelastic material properties of the heel pad sub-layers, a series of compression tests at constant low velocities of 0.25, 0.5, 1, 2.5, and 5mm/s was performed on the heel pad of the subject. Each test at the specific displacement rate was repeated for five iterations to obtain the average results. The velocity of 0.25mm/s was the lowest rate that was possible to perform using STRIDE. The displacement rate of 5mm/s was chosen because it was close to the velocities of 5.2 and 5.7mm/s used in published works to determine the hyperelastic behaviour of the heel pad (4, 5). Another 3 velocities were also selected in between these values to investigate the effect of variation in low velocities on force-strain responses of the heel pad and determine the velocity at which the hyperelastic behaviour of the heel pad would be obtained.

Since the duration of the compression tests at velocities of 0.25 and 0.5mm/s was increased, the ultrasound data for these two tests were obtained at lower frequencies, which resulted in lower quality of the annotation of the images done by the user. Figure 5.3 shows the

ultrasound images recorded for compression test at velocities of 0.25 and 5mm/s. Results of 3 trials of compression test at the velocity of 0.5mm/s were saved in poor quality, thus discarded and the average result was obtained from only 2 trials for this particular loading velocity.

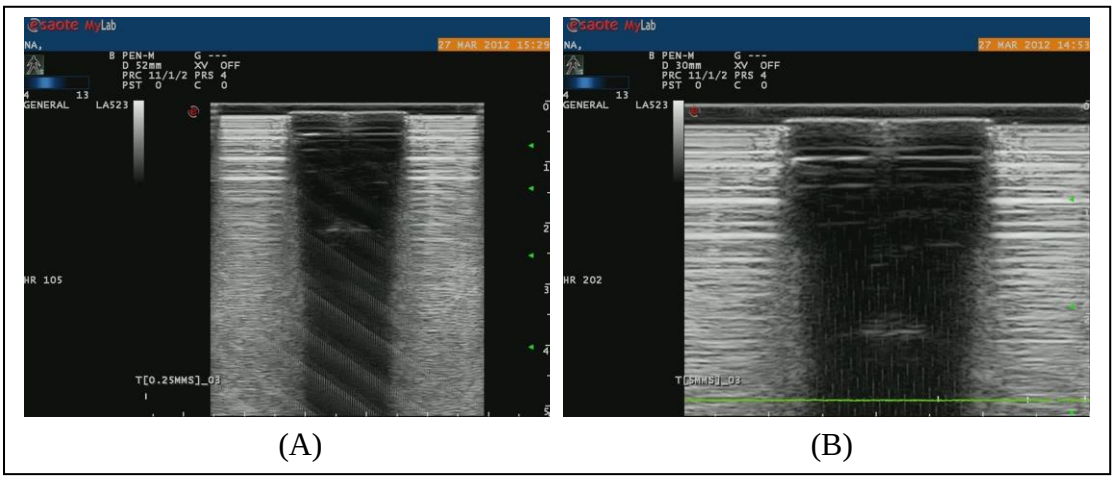

Figure 5.3: Ultrasound image recorded for different compression tests: (A) Ultrasound image recorded at lower frequency and higher beam penetration for compression test at 0.25mm/s; (B) Ultrasound image recorded at higher frequency and lower beam penetration for compression test at 5mm/s.

A triangular wave profile with constant displacement rate was used for slow compression tests. This profile started pre-contact with the plantar tissue to ensure that the indenter was moving at the constant rate when it started compressing the heel pad. The heel pad was compressed up to strain of ~40% before unloading at the same controlled displacement rate. The force-strain responses of the heel pad were obtained as outputs of slow compression tests. The loading profile for compression at displacement rate of 5mm/s is shown in Figure 5.4.

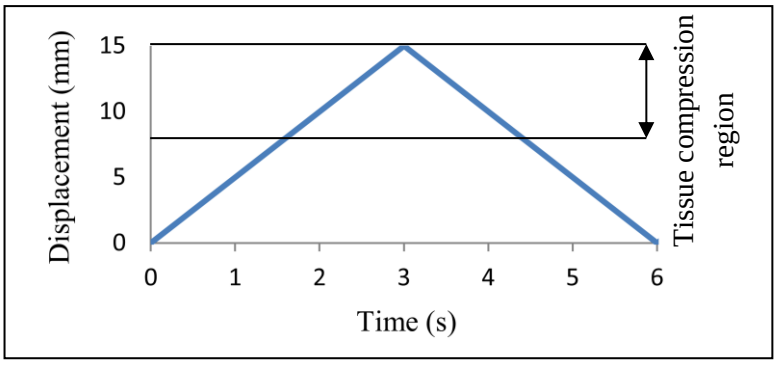

Figure 5.4: Slow compression test profile at displacement rate of 5mm/s

When the velocity was selected for slow compression test, then the heel pad of the subject was tested at this specific velocity to obtain the hyperelastic behaviour of the heel pad, macro-chamber, micro-chamber and skin layers. The compression tests were repeated for 5 iterations with 1 minutes rest time between each trial to allow for the heel pad recovery. The force and strain of the heel pad and its sub-layers were measured and recorded through the compression tests.

- **Rapid compression tests**

To obtain the viscoelastic material properties of the heel pad sub-layers a series of rapid compression tests was conducted at constant displacement rate of 225mm/s. The velocity of 225mm/s was selected because it was the highest constant displacement rate could be performed by STRIDE during loading-unloading cycle. The rapid loading profiles at 225mm/s included loading, hold and unloading tests. This profile started with a loading period at the constant displacement rate of 225mm/s. It continued with a hold period for 26ms at a constant displacement and ended with unloading period at the same constant displacement rate until the indenter reached the starting position (Figure 5.5).

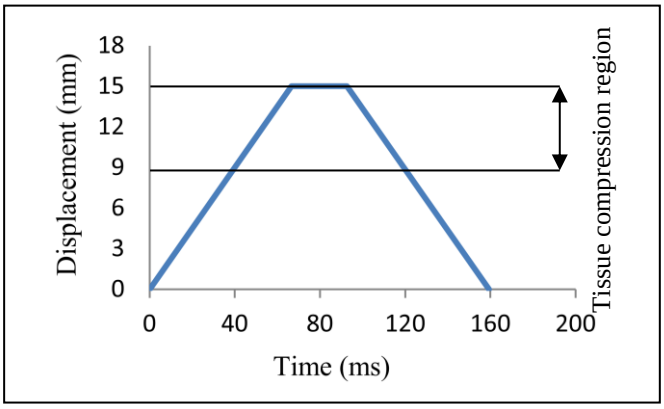

Figure 5.5: Rapid compression test profile at displacement rate of 225mm/s

During the rapid compression tests at 225mm/s, the heel pad was compressed up to strain of ~40%. The hold period was added to the rapid compression tests profile because the indenter was unable to reverse its direction to unload the heel pad at constant velocity after loading at

high velocity, but the hold period was minimised as far as possible. Five iterations were repeated with rest time of 1 minute between each test to allow for the heel pad recovery. The force-strain responses of the heel pad and its sub-layers were recorded for this series of tests.

Another two series of rapid compression tests at displacement rates of 141 and 300mm/s were also performed on the heel pad for viscoelastic FE model validation (see Chapter 6). Similar to the rapid compression test profile at 225mm/s, the loading profile at 141mm/s included loading, hold for 26ms at a constant displacement, and unloading periods. The loading and unloading periods were performed at constant velocity of 141mm/s (Figure 5.6). During the rapid compression tests at 141mm/s, the heel pad was compressed up to strain of ~40%. The test was repeated for 5 times with 1 minute break between each trial to allow tissue to recover.

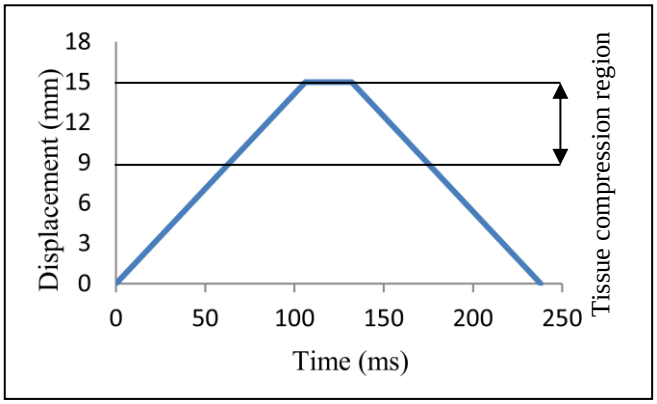

Figure 5.6: Rapid compression test profile at displacement rate of 141mm/s

A sinusoidal wave profile was used for the last rapid compression tests (Figure 5.7). In this sinusoidal loading, the velocity reaches to 300mm/s at its maximum point. The indenter is positioned under the tissue with distance equal to the value of the amplitude to ensure that the contact is made at maximum velocity. Then the velocity decreases to zero at maximum strain. The amplitude was set to 6mm to give a peak strain of about 40%. Based on the following equation the frequency was set to 8Hz.

$$V_{max} = 2\pi f A \tag{5.1}$$

Where V represents the maximum velocity and f and A represent the frequency and amplitude respectively. Aerts et al (15) called this a 'half cycle test' and used to replicate a pendulum test in which the contact starts at maximum velocity. Ker also claimed that this is a reasonable way to mimic the impact of the heel to the ground during locomotion (120). 5 cycles were repeated with 1 minute rest time for tissue recovery. All profiles started pre-contact with the plantar tissue to ensure that the indenter was moving at constant rate when compression started.

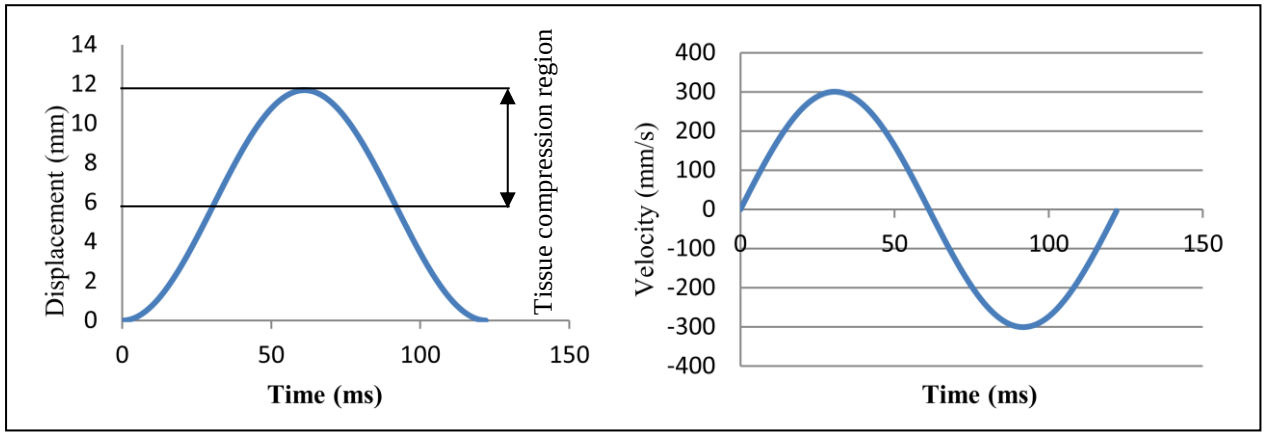

Figure 5.7: The sinusoidal loading profile with maximum velocity of 300mm/s

5.2.5 Ultrasound Data Processing

A standard clinical ultrasound probe with $5cm^2$ (5cm×1cm) imaging surface was used to collect the ultrasound imaging data during compression tests. The ultrasound system was set to 40mm imaging depth with operating frequency of 4-MHz to increase penetration through plastic window and multiple tissue interfaces. The ultrasound output data at 201Hz was saved as AVI (Audio Video Interleave) video files. The ultrasound videos were then imported into Avidemux version 2.5 to convert the images of a clip video to JPG format. Avidemux is an open source video editor, which can convert raw AVI clip into sequence of images. The image sequence was then exported to ImageJ software (National Institute of Health, Bethesda, USA) which is an image-processing program. The deformation of the heel pad sub-layers were tracked and measured in ImageJ with resolution of 0.077mm.

The boundary of the calcaneus could be seen as a white, thick arc at the lower part of the ultrasound images. The interface between the macro-chamber and micro-chamber was made of white thick layer in the middle of the ultrasound images. By adjusting the brightness and contrast of the images in ImageJ and make the images darker, the layers inside the macro-chamber were blurred and the white interface was clearer. The outer boundaries of skin layer were quite detectable as white bands, one adjacent to the plastic window and the other one forming the interface with the micro-chamber. The inner tissue of the skin and micro-chamber were distinct in the images. Watching the ultrasound videos of the indentation process showing the heel pad sub-layers deformation and their movements towards each other also was a great help in distinguishing the interface between sub-layers. Figure 5.8 shows ultrasound images of the heel pad at the area of the calcaneus tuberosity at unloaded and loaded position.

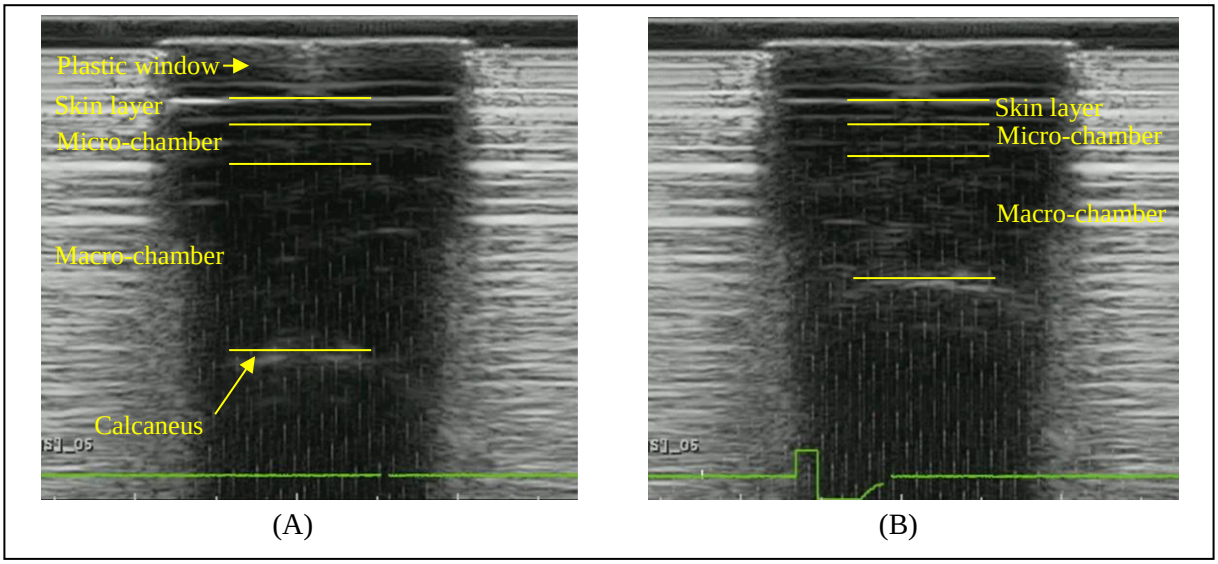

Figure 5.8: Ultrasound images for the frontal view at the location of calcaneus tuberosity: (A) Unloaded heel pad; (B) Loaded heel pad.

5.3 RESULTS AND DISCUSSION

In slow and rapid compression tests, the heel pad and its sub-layers exhibited non-linear behaviour. Under compression, they initially showed low stiff behaviour, and then they

became stiffer as the load was increased. The experimental results obtained from slow and rapid compression tests are provided here.

5.3.1 Slow Compression Tests

5.3.1.1 Selection of the Appropriate Low Displacement Rate

No significant difference was found between force-strain results obtained for slow compression tests at displacement rates of 0.25, 0.5, 1, 2.5, and 5 mm/s. The corresponding averages of the force-strain responses of the heel pad are plotted in Figure 5.9. The difference between force-strain results of the heel pad obtained from compression test at 5mm/s and other slow rates were calculated using RMS error provided in Table 5.1. According to this table, the maximum difference was measured between the results obtained at 5 and 0.25mm/s with RMS error of less than 4.5% of maximum force.

Table 5.1: Difference between force-strain curves resulted for compression tests at 5mm/s and other rates.

Compression test	2.5mm/s	1mm/s	0.5mm/s	0.25mm/s
RMS error (N)	0.98	0.92	2.13	3.23
RMS error (% Max force)	1.28	1.21	2.81	4.26

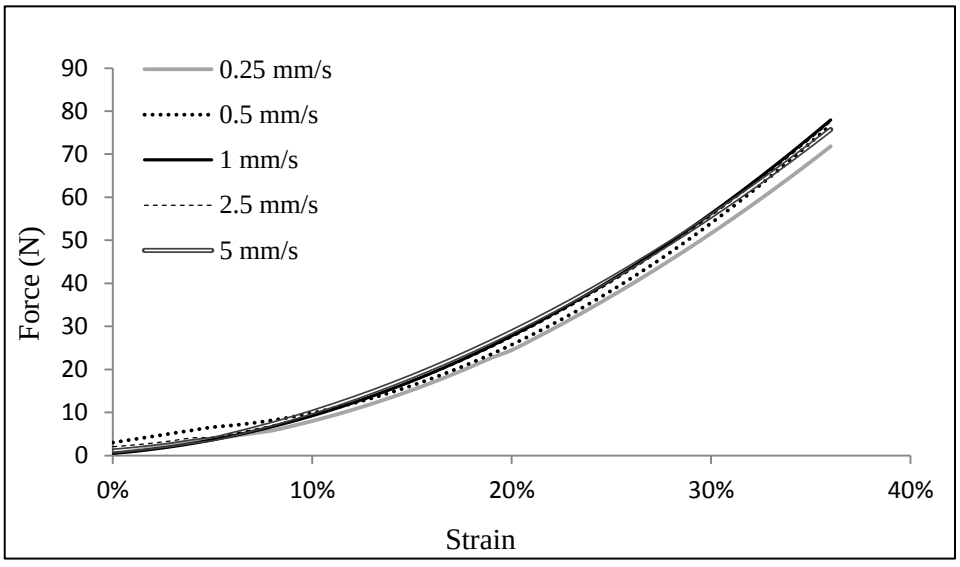

Figure 5.9: The average force-strain results for the heel pad at different displacement rates.

Certainly the hyperelastic behaviour of the heel pad could be better presented by the results obtained at the very low velocity of 0.25 and 0.5mm/s. However, the ultrasound data could be obtained at higher quality (refers to the ability to distinguish different tissues) for compression test at 5mm/s with only 3.23 and 2.13N differences from the results of 0.25 and 0.5mm/s. While ultrasound images at 5mm/s provided opportunity for more accurate deformation measurements of the heel pad, the lower quality of the images in low velocities increase the risk of misinterpretation. Besides, by increasing the loading time, the possibility of inducing error into results because of the slight changes in the standing posture of the subject in the test rig was also increased. Therefore, the displacement rate of 5mm/s was selected as a reference value because: (1) no important difference was found between slow compression tests results at different velocities; (2) the potential errors were smaller than other cases because of higher quality images and lower loading time; (3) it was close to other values used in literature (5.2 and 5.7mm/s) to determine hyperelastic behaviour of the heel pad. The force-strain results corresponding to slow compression tests at 0.5mm/s follows slightly different pattern from others. The possible reason is that the average result for this compression test was generated based on results of only 2 trials.

5.3.1.2 Slow Compression Tests at 5mm/s to Determine the Hyperelastic Material Properties

Based on the investigation in Subsection 5.3.1.1, the compression test at 5mm/s was selected as the low velocity to obtain the hyperelastic behaviour of the heel pad, macro-chamber, micro-chamber and skin layers. Figures 5.10-5.14 show the force-strain responses of the heel pad, its sub-layers and also total responses of the macro-chamber and micro-chamber under loading at 5mm/s. The force-strain results of each layer for 5 iterations did not overlap. Fontanella et al. also observed this feature in their results. They proposed that it might because the surrounding stiffer tissues constraining the movements of the heel pad, such as

calcaneus, could not be fixed relative to the measurement device. Therefore, the heel pad tissue might slightly rotate or translate during repetitive loading cycles. Also variations in liquid content such as blood perfusion might be another reason as loading might move liquid in muscles (101). The averages for the responses of the heel pad and its sub-layers are in Figure 5.15.

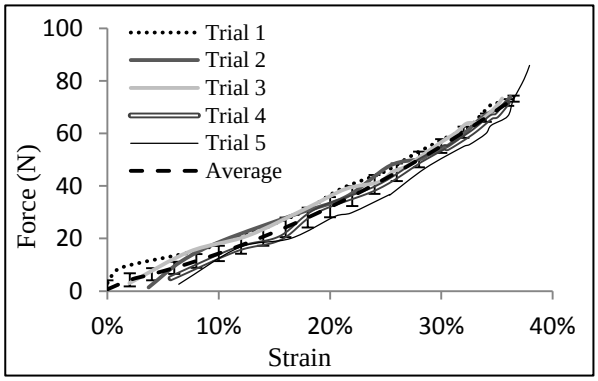

Figure 5.10: The heel pad behaviour at 5mm/s

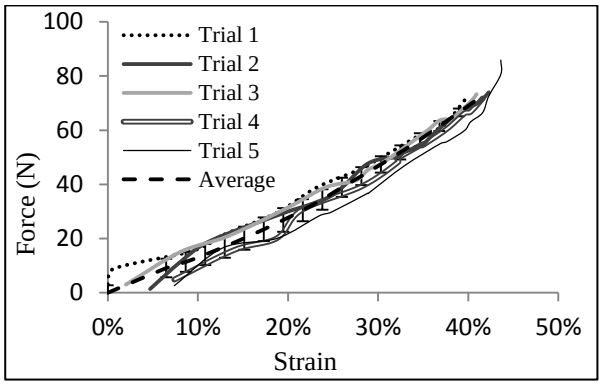

Figure 5.11: The macro-chamber behaviour at 5mm/s

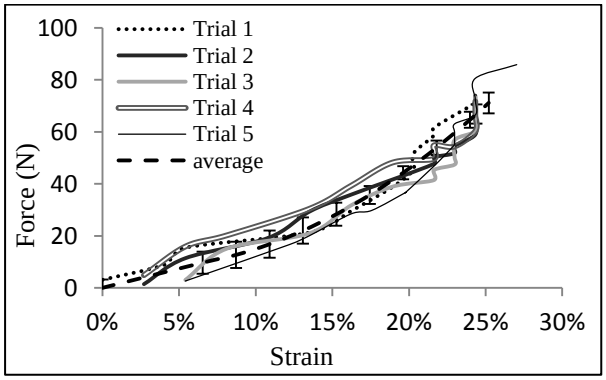

Figure 5.12: The micro-chamber behaviour at 5mm/s

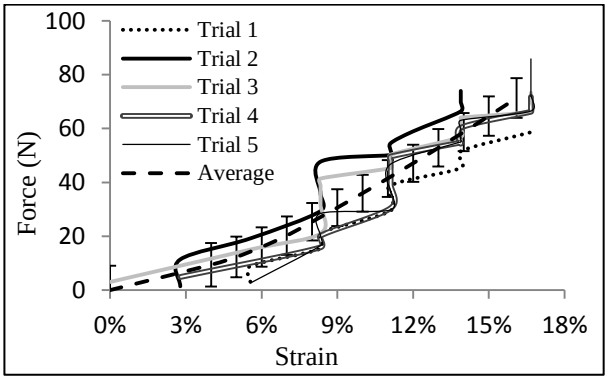

Figure 5.13: The skin behaviour at 5mm/s

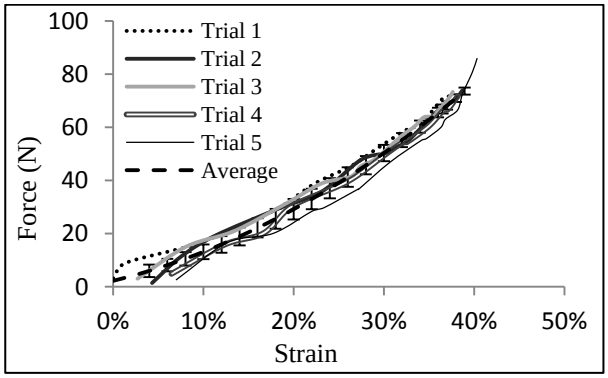

Figure 5.14: The behaviour of the total macro-chamber and micro-chamber at 5mm/s

The experimental results in Figure 5.15 highlight differences between biomechanical behaviours of the heel pad, macro-chamber, micro-chamber and skin layers under slow compression loading. According to the ultrasound image data, the heel pad was compressed up to average depth of 36.5% initial thickness (40% was the target). The experimental results were in agreement with the hypothesis of inhomogeneous nature of the heel pad tissue. As can be seen in Figure 5.15, the heel pad biomechanical behaviour under loading was close to the behaviour of the macro-chamber layer compared to the other layers. This is because of the greater volume of the macro-chamber layer in the heel pad compared to micro-chamber and skin layers.

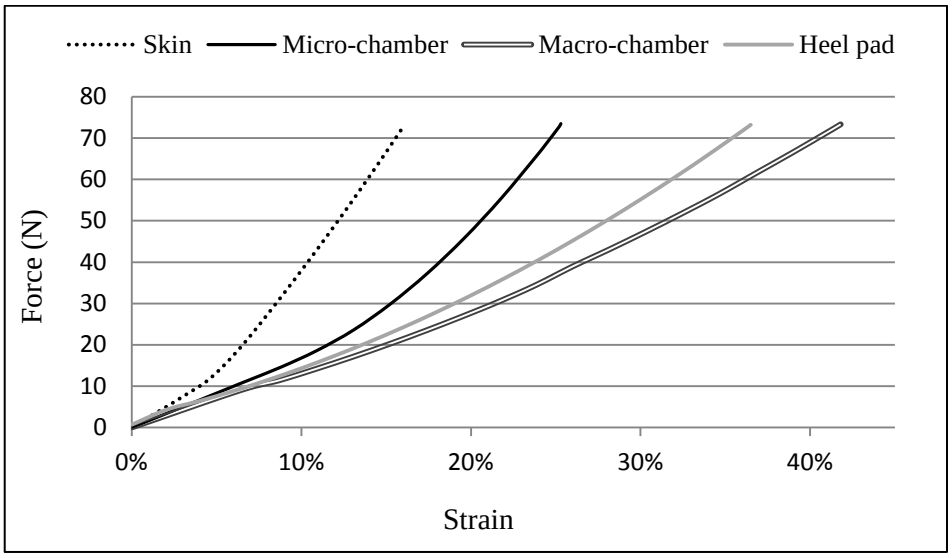

Figure 5.15: The averages of the force-strain responses of the heel pad and its sub-layers at 5mm/s.

In Table 5.2, deformation proportion of each layer shows the portion of the overall deformation of the heel pad that occurs in each of the heel pad sub-layers. For instance, 87.2% reflects the fact that this amount of deformation occurred in the macro-chamber layer. The results in Table 5.2 indicate that the macro-chamber, micro-chamber and skin layers formed 76.43, 14.65, and 8.92% of the unloaded heel pad thickness respectively.

Table 5.2: Mechanical information of the heel pad, macro-chamber, micro-chamber and skin layers under compression at 5mm/s.

	Heel pad	Macro-chamber	Micro-chamber	Skin
Unloaded thickness (mm)	15.7(0.2)	12.0 (0.2)	2.3 (0.1)	1.4 (0.1)
Strain (%)	36.5 (0.6)	41.8 (0.4)	25.3 (0.8)	16.1 (1.2)
Deformation proportion (%)	-	87.5	10.1	3.9

Values are means (SD)

The macro-chamber layer showed large strain under loading. At 36.5% deformation of the heel pad, the macro-chamber experienced a significantly greater deformation than the micro-chamber and skin layers as 87.5% vs 10.1% vs 3.9%. The micro-chamber layer responded to the loading with higher stiffness than the macro-chamber layer. At the beginning of the loading, the micro-chamber went under deformation, but this slowed as it became stiffer as load was increased. The skin layer responded to the loading with high stiffness compared to the macro-chamber and micro-chamber layers. Only ~4% of deformation of the heel pad at strain of 36.5% was related to the deformation of the skin layer. Since the skin was thin and its deformation under loading was very small, high measurement errors were expected.

Several research studies have been conducted to study the biomechanical behaviour of the heel pad under loading. In most of the previous studies, the heel pad has been considered as a single homogeneous layer. Although in some studies the heel pad has been investigated as a non-homogeneous two-layer tissue, in this project the behaviour of the heel pad and its 3 sub-layers were obtained *in-vivo* under slow compression. Spears and Miller-Young investigated the biomechanical behaviour of the skinned and skinless cadaveric heel pad in order to estimate the material properties of the skin and the fat pad (10, 12). They provided the force-displacement responses of the intact and skinless heel pad under loading. Hsu et al. used ultrasound-based loading device to study the behaviour of the macro-chamber and micro-chamber layer of the heel pad of 16 healthy subjects at age of about 55 years old during loading-unloading cycle *in-vivo* (33). However, according to the ultrasound images provided,

it seems likely that the thickness of the skin and micro-chamber were not measured separately and the total thickness of them was used to represent the thickness of the micro-chamber. The unloaded thickness of macro-chamber, micro-chamber and heel pad layers was measured about 13.9, 4.5, and 18.4mm respectively. The strain of the macro-chamber was 45.0%, significantly higher than the strain of micro-chamber of 10.4% for the heel pad maximum strain of 36.5%.

In this project, the strain of the macro-chamber (41.8%) at 36.5% strain of the heel pad was comparable with the one obtained from study conducted by Hsu et al. (45.0%). The strain of the total micro-chamber and skin layers was measured to compare with the result from Hsu's study. The comparison showed that 22% strain of the total micro-chamber and skin in this project is approximately double of the Hsu's result (10.4%). The difference in experimental technique, the age of the subjects, and the geometry of heel pads might be reasons for variation in the obtained results.

5.3.2 Rapid Compression Tests

5.3.2.1 Rapid Compression Test at 225mm/s

Although the loading device is a repeatable means of compressing, some differences appeared in the maximum strain of the heel pad between cycles. These differences were likely due to small positional changes of the foot as it was rapidly loaded with each cycle. Since the maximum strain of the heel pad affects the behaviour of the heel pad during hold and unloading periods, the behaviour of the heel pad during these periods for each iteration was considered separately. The repeatability of the loading device (STRIDE) was assured by the evaluation study of the device and test method in a prior published thesis (118). The evaluation study showed the ability of the drive mechanism, brace system and measurements apparatus to reproduce data with minimum error. Due to problem of different maximum strains explained earlier it was only possible to calculate an average result of 5 iterations for

the loading periods. Figures 5.16-5.20 show the force-strain responses of the heel pad, its sub-layers and the total responses of the macro-chamber and micro-chamber during the loading-hold-unloading cycle at the velocity of 225mm/s.

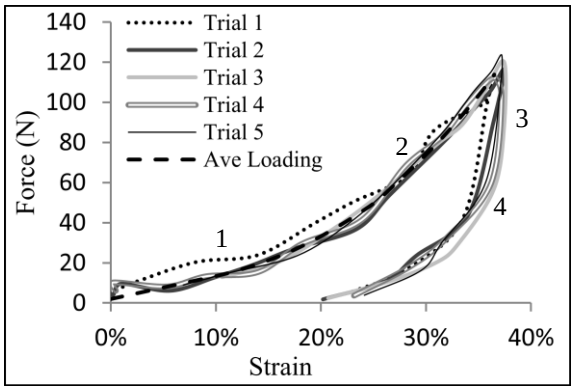

Figure 5.16: The heel pad behaviour at 225mm/s

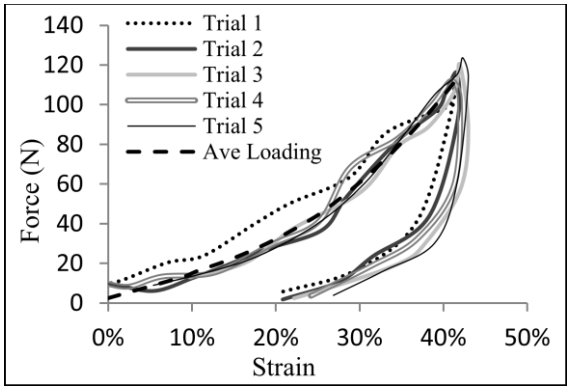

Figure 5.17: The macro-chamber behaviour at 225mm/s

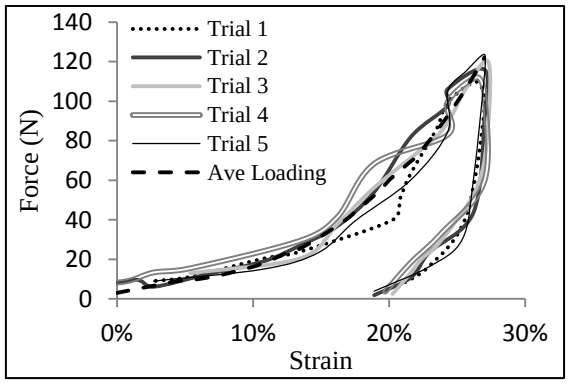

Figure 5.18: The micro-chamber behaviour at 225mm/s

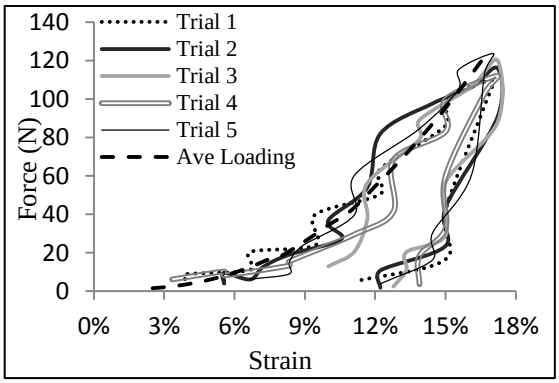

Figure 5.19: The skin behaviour at 225 mm/s

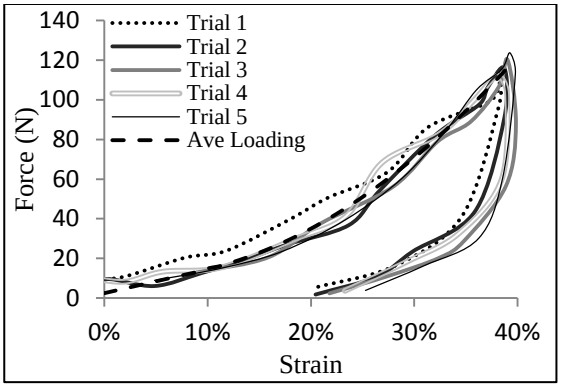

Figure 5.20: The behaviour of the total macro-chamber and micro-chamber at 225mm/s

The above results show that the heel pad was compressed to an average strain of 36.9% during testing (40% was the target). However, to compare these results with the findings

obtained from slow compression tests at 5mm/s, the responses of the heel pad and its sub-layers under loading were provided at the heel pad strain of 36.5%. Four regions could be identified in the behaviour of the heel pad and its sub-layers under loading-hold-unloading periods. These regions are numbered in Figure 5.16.

The loading period was started with initial compliant part (region 1) then followed by a nonlinear stiffer region (region 2). Although biological tissues are nonlinear viscoelastic materials, they show linear elastic behaviour for a relative strain under 10 to 15% (28). At higher level of strain, the collagen fibres in the heel pad tissue reach their natural lengths and come under tension, limiting more deformation of the tissue and increasing the tissue stiffness (121). During the hold period, while the displacement was kept constant, the load was decreased exhibiting stress-relaxation characteristic of the heel pad and its sub-layers (region 3). Finally the unloading period can be identified (region 4). At the unloading period, the heel pad tissue and the indenter lost contact around 20% strain. This can be explained by the fact that the heel pad could not return to its original shape with the same velocity as the indenter. Detailed information of the layers during loading period is given in Table 5.3.

Table 5.3: Mechanical information of the heel pad, macro-chamber, micro-chamber and skin layers during loading period at 225mm/s.

	Heel pad	Macro-chamber	Micro-chamber	Skin
Unloaded thickness (mm)	15.7 (0.2)	12.0 (0.2)	2.3 (0.1)	1.4 (0.1)
Strain (%)	36.50 (0.5)	41.7 (0.9)	26.3 (0.9)	16.1(1.0)
Deformation proportion (%)	-	87.2	10.5	3.9

Values are means (SD).

A comparison between Tables 5.3 and 5.2 revealed that the deformation proportions of the heel pad sub-layer under compression at 225mm/s were comparable to those obtained at 5mm/s. A review of the ultrasound images showed that the skin layer was deformed under

loading at the beginning of the loading and then its thickness was hardly changed more than ~16.1% of initial thickness. Similar to the previous tests, high measurement errors were expected for the skin layer (Figure 5.19). The macro-chamber layer showed significantly more deformation proportion than the micro-chamber and skin layers.

The heel pad and its sub-layers showed a non-linear viscoelastic biomechanical behaviour. The amount of energy lost during loading-hold-unloading periods was calculated for the heel pad under rapid compression test. The energy dissipation ratio (EDR) is measured using equation 5.2. The areas in equation 5.2 were calculated by numerical integration using trapezoidal rule. EDR was 76.10% (SD 4.47) for the heel pad at this test.

$$EDR\% = (\text{Bounded area} / \text{Area under loading curve}) \times 100 \quad (5.2)$$

5.3.2.2 Rapid Compression Test at 141mm/s

Although the loading device provides repeatable compression, the results showed that at each trial the heel pad was compressed up to a different maximum strain due to small positional changes of the foot. The maximum strain of the heel pad affected the behaviour of the heel pad during hold and unloading periods. Thus the behaviours of the heel pad and its sub-layers for different iterations were considered separately and it was only possible to calculate an average result for loading period. Figure 5.21 shows the force-strain responses of the heel pad during loading-hold-unloading periods at the velocity of 141mm/s. The average force-strain response of the heel pad during the loading period is also shown in Figure 5.21 with dashed line.

The energy dissipation ratio was measured as 63.3% (SD 4.29) whereas it was 76.1% (SD 4.47) for compression test at velocity of 225mm/s. This means that the increase in the loading velocity resulted in an increase in energy dissipated (EDR). The bounded area of the force-strain curve was increased at velocity of 225mm/s and resulted in growth of EDR. Similar to

findings in the previous experiment (rapid compression test at 225mm/s), the heel pad tissue and the indenter lost contact around 20-25% strain because the unloading velocity of the heel pad tissue was lower than the indenter velocity.

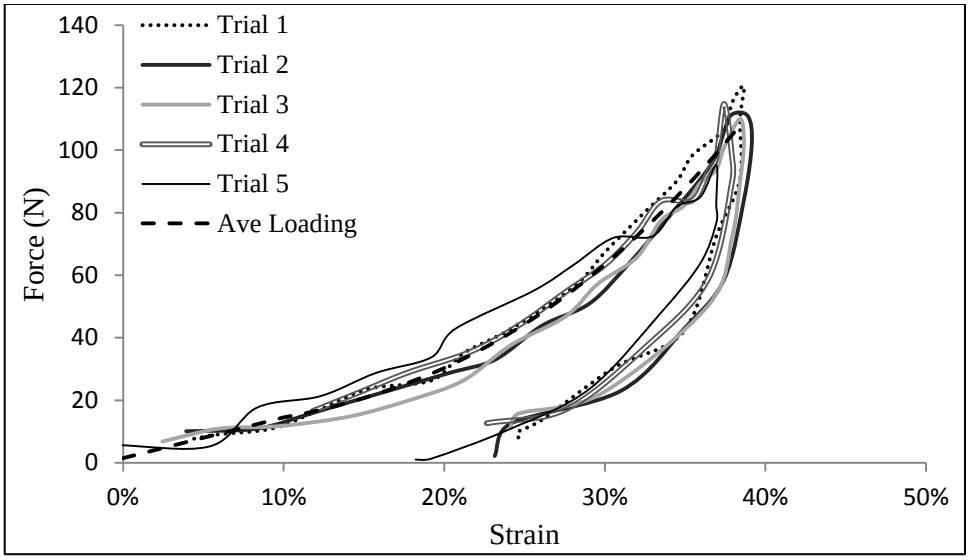

Figure 5.21: Force-strain relation of the heel pad for loading-hold-unloading periods at 141mm/s.

A comparison between the results obtained from rapid and slow compression tests demonstrated that the force-strain responses of the heel pad and its sub-layers are dependent on the loading velocity. While at slow compression test the average load of ~73N was required to apply 36.5% strain to the heel pad, the average loads of ~96 and ~114N were required to apply the same amount of strain to the heel pad at constant velocities of 141 and 225mm/s respectively. This means that the stiffness of the heel pad is increased by loading velocity. Larger differences in the applied force are expected for higher strains.

Spears et al. studied the behaviour of the heel pad under loading at 175 and 350mm/s, by performing compression tests on a cadaveric foot (10). The unloaded thickness of the heel pad was measured 13mm before start loading. A 20mm diameter indenter was used to compress the heel pad up to strain of 38.5%. Their findings also indicated a non-linear, velocity sensitive behaviour for the heel pad (Figure 5.22). The peak forces provided by them were

lower than the findings of this study which could be result of *in-vivo* versus *in-vitro* conditions.

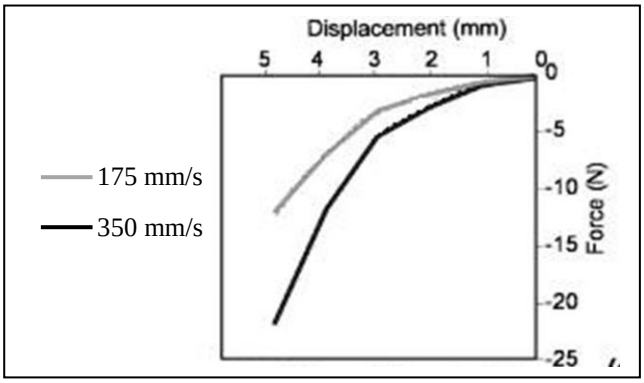

Figure 5.22: Force-deformation data for the heel pad at different loading rate obtained by Spears et al (10).

5.3.2.3 Rapid Compression Test under Sinusoidal Loading

Similar to the previous compression tests, at each trial the heel pad was compressed up to a different maximum strain because of small positional changes of the foot. Since the maximum strain could influence the behaviour of the heel pad during unloading period, the responses of the heel pad for each trial were considered separately. Figure 5.23 shows the force-strain responses of the heel pad for loading-unloading cycle under sinusoidal compression test.

The energy lost values (EDR) for the heel pad reported in literature are quite divergent. EDR values, obtained from ballistic pendulum test (85-90%) (50) and impact test (73-78%) (52), were found to be higher than those obtained from *in-vitro* compression test (30%) (60) or *in-vivo* slow indentation test (23-35.3%) (36) and during gait (17-19%) (31). Ledoux and Belvins showed that the energy loss is velocity sensitive and it increases with loading rate (13). Moreover, Jorgensen investigated the relationship between the heel pad thickness and its shock absorbency, proposed that shock absorption is lower in thinner heel pad (56). Hsu et al. suggested that because of loss of collagen and a decrease in the elastic fibrous tissue in heel pads of older adults, the heel pad shows poor recover response during unloading and EDR is increased (36). EDR was measured as approximately 78% (SD 5) during loading-unloading

cycle in this study. This value is in the range that obtained from impact test on healthy young and elderly adults (52). However because of the difference between the experimental methods, heel geometry and material properties of the tested heel in this study and those used in literature, making comparison is difficult.

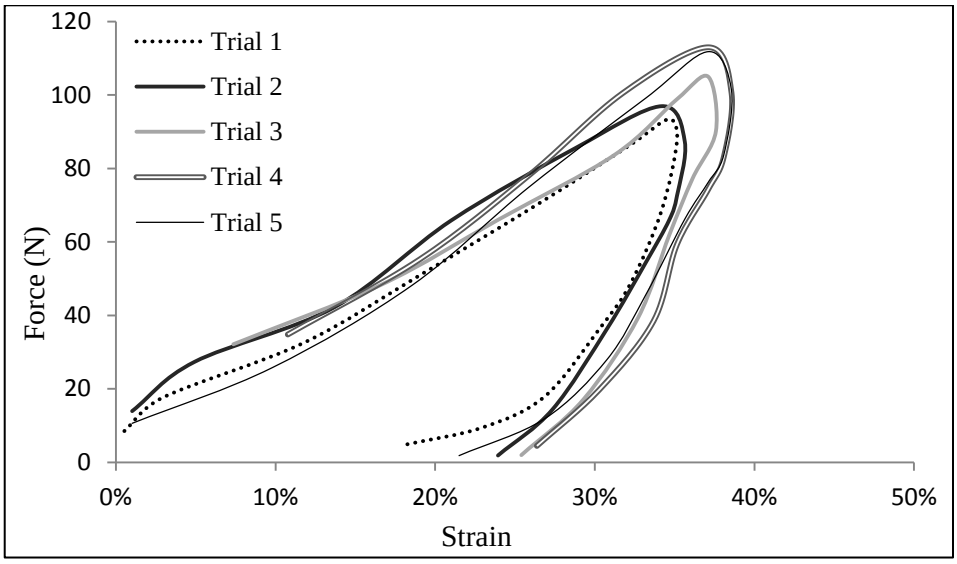

Figure 5.23: Force-strain relation of the heel pad under sinusoidal loading.

5.4 CONCLUSIONS

To investigate behaviours of the heel pad and its sub-layers and use their force-strain responses as input to inverse FEA, a series of slow and rapid compression tests were performed on the right heel of the subject, whose heel region FE model was developed in the previous chapter. The ultrasound and controlled compression device, used in this study, allowed the deformations of not only the heel pad but also its internal components (macro-chamber, micro-chamber and skin) to be measured during loading-unloading cycle. The large flat rigid indenter was used to compress the heel during experiments to reproduce the contact between the heel and the ground or inside of the shoe.

The slow compression test at constant speed of 5mm/s and rapid compression test at 225mm/s were designed to obtain the hyperelastic and viscoelastic force-strain responses of the heel

pad and the macro-chamber, micro-chamber and skin layers respectively. The same heel was also subjected to compression tests at constant rapid velocities of 141mm/s and sinusoidal loading (maximum force 300mm/s) to obtain the viscoelastic force-strain responses of the heel pad.

The data obtained at 5 and 225mm/s in this chapter were taken forward into Chapter 6 to be used as input to the initial FE model, generated in Chapter 4, for estimation of the hyperelastic and viscoelastic material properties of the heel pad sub-layers respectively. Furthermore, the results obtained at 141mm/s and sinusoidal loading and some of the results obtained at 225mm/s were used to validate the viscoelastic FE model in Chapter 6.

The force-strain responses of the heel pad and its sub-layers to different loading protocols indicated that their behaviours are nonlinear with initial compliant part followed by a stiffer region. Furthermore, it was noted that the behaviour of the heel pad was loading velocity sensitive. The stiffness of the heel pad was increased by the velocity. Also the increase in loading velocity resulted in an increase in EDR. The energy absorbed by the heel pad under sinusoidal loading was close to the findings for the impact and ballistic pendulum tests performed on healthy adults.

6. Chapter Six:

INVERSE FINITE ELEMENT ANALYSIS

6.1 INTRODUCTION

The aim of this chapter is to use the force-strain responses of the heel pad, macro-chamber and micro-chamber, obtained from the physical tests in Chapter 5, as inputs to inverse FEA to estimate the hyperelastic and viscoelastic material properties of the heel pad sub-layers. This is achieved by using the FE model of the heel region that was developed in Chapter 4.

Inverse FEA is a technique that is used to determine the target parameters (e.g. material properties) from the FE model by iteratively varying the parameters until the model predicted results are best fitted to the experimental measurements. In this method, an objective function is defined to measure the error between the model predicted and the experimental results. The optimum values of the target parameters are obtained through minimisation of the objective function. The RMS error, difference between maximum strains and difference between peak forces were used as objective functions in this study to measure the difference between the force-strain results obtained from the experiments performed on the heel region (see Chapter 5) and the predicted FE results. Figure 6.1 illustrates the procedure used for determination of the material properties.

After estimation of the hyperelastic and viscoelastic material parameters, the hyperelastic and viscoelastic FE models were validated against experimental data. The FE model validation refers to the process of studying the capability of FE models to simulate the actual behaviour of the heel pad. An effective way to evaluate the FE models predictions was to perform a series of tests on the heel pad used to develop the FE model geometries and record its responses to these tests. The validated models should have the ability to predict behaviours of the heel pad during different experiments. In this study, experimental data against which to compare FEA output was the heel pad thickness from MRI, the peak plantar pressure and force-strain responses of the heel pad under different rapid loading conditions. At the end of

this chapter the parametric studies conducted in Chapter 4 to evaluate the effects of the material properties of the muscle tissue and plantar fascia and changes of the angle of rotation of the heel on the force-strain responses of the heel pad were repeated after the heel pad sub-layer property derivation.

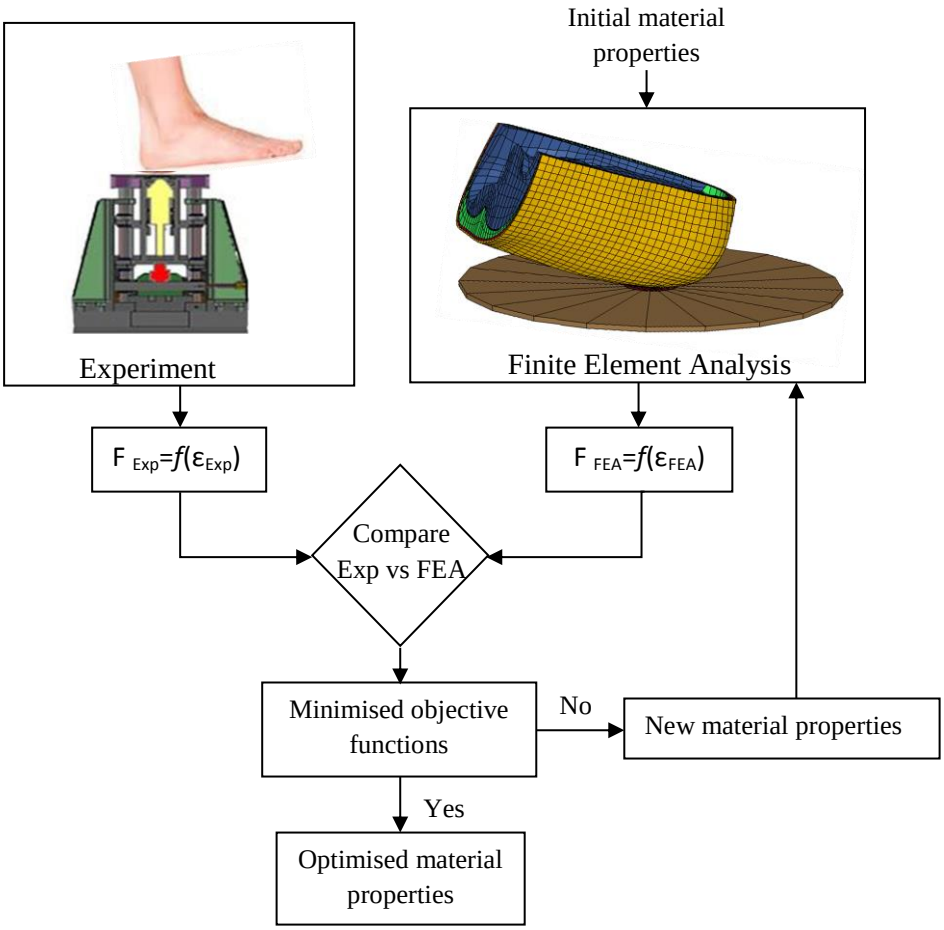

Figure 6.1: The procedure of the inverse FEA

In Figure 6.1, F and ε represent the force and strain respectively, whereas subscripts of $_{Exp}$ and $_{FEA}$ stand for experiment and finite element analysis.

6.2 METHODS

6.2.1 Hyperelastic Material Properties

To determine the hyperelastic material properties of the macro-chamber, micro-chamber and skin layers, the experimental data obtained in Chapter 5 at slow compression test (5mm/s) was used. The hyperelastic behaviour of the heel pad and its sub-layers can be investigated if the

displacement rate is kept low enough during compression. The hyperelastic behaviours of the heel pad and its sub-layers were represented by the Ogden material model in the FE model. In Ls-Dyna, for the Ogden material model, there are two hyperelastic material properties, μ and α, to be estimated for each layer (see Chapter 4). μ is the initial shear modulus and is linearly related to the initial elastic modulus. A variation in μ represents a change in low-strain response of the material. α value is the high-strain hardening exponent which reflects the high-strain slope of the resultant force-strain curve. Therefore, for the heel region model there were 6 hyperelastic material parameters to be estimated in total, three tissue layers with two Ogden material properties (μ and α) per layer.

It was complex to determine 6 unknown parameters from force-strain graphs at the same time while the complexity could be reduced by estimating 2 unknowns of one layer from the corresponding force-strain graph at each time. This process started with estimation of the material parameters of the macro-chamber layer at the absence of elements representing the micro-chamber and skin layer (one-layer model). The parameters determined at this stage were the initial estimates for the macro-chamber layer. Then, elements representing the micro-chamber were added to the model (two-layer model) and the first estimate for the material parameters of the micro-chamber layer and second estimates for macro-chamber layer were determined. Finally, the complete model incorporating macro-chamber, micro-chamber and skin layer (three-layer model) was used for estimation of the final values of the material parameters of the heel pad sub-layers. This process is shown in Figure 6.2 and explained in details in the following sections.

Changing this sequence, for example starting with estimation of initial material properties of the skin layer with using a one-layer model (with only two material parameters) without elements representing the macro-chamber and micro-chamber layers, results in a gap between the skin and muscle tissue and plantar fascia. Consequently, necessary boundary conditions

are removed and running of the analysis becomes impossible. Thus, this is the only sequence to ease the estimation of the material properties of three tissue layers.

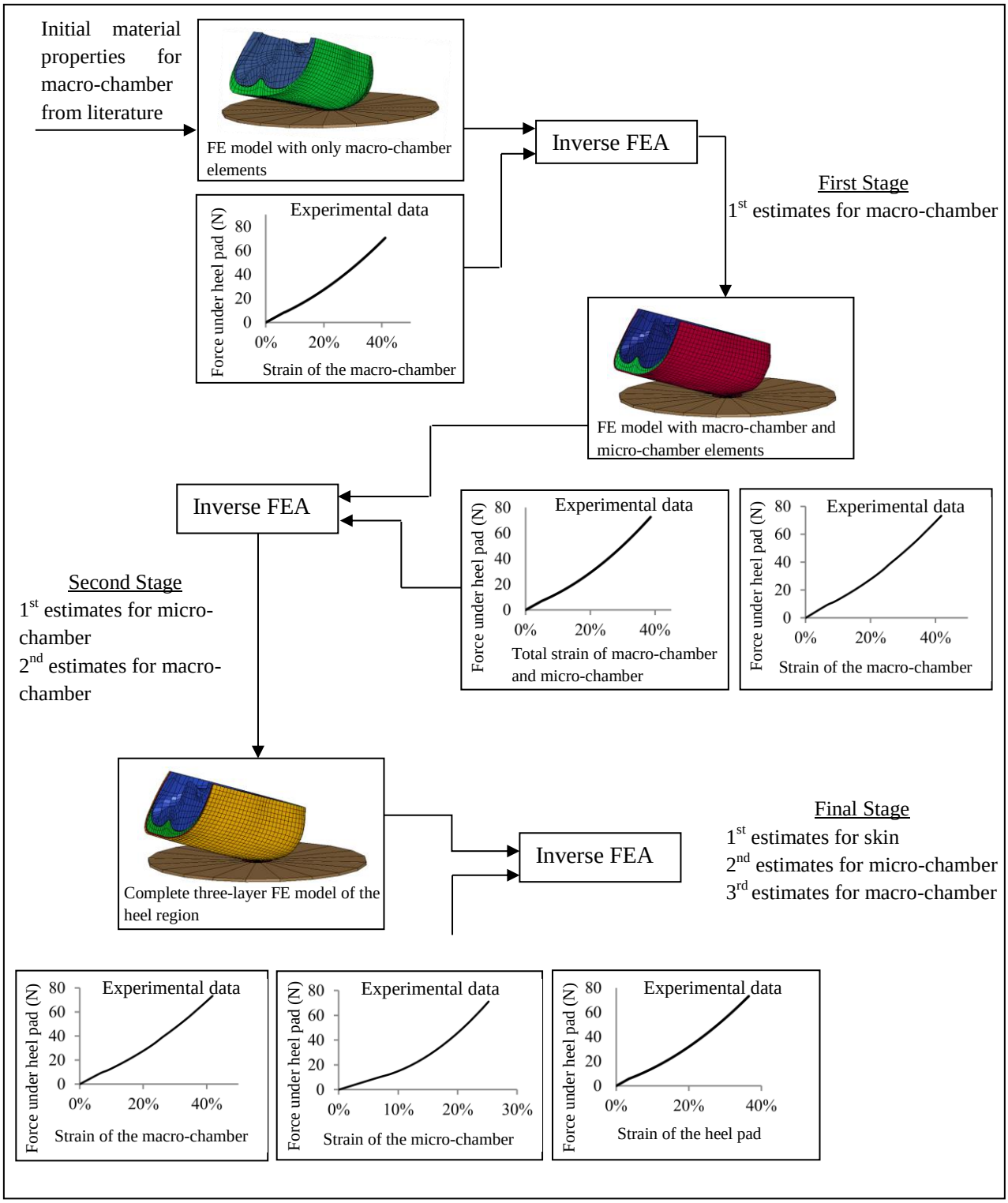

Figure 6.2: The process of estimation of the material properties of the macro-chamber, micro-chamber and skin layers.

6.2.1.1 Determination of the Hyperelastic Material Properties of the Macro-chamber Layer

The purpose of the first stage was to determine first estimates for the hyperelastic material properties of the macro-chamber layer. To achieve this, only elements representing the macro-chamber layer with 2 unknowns (μ and α) existed in the FE model (Figure 6.3). Two initial values of 16.45kPa and 6.82, obtained as the heel pad material properties in the published literature, were assigned to μ and α of macro-chamber elements (5). The FEA was run and the macro-chamber layer compressed with the indenter moving at the constant velocity of 5mm/s up to 41.8% strain to replicate the experimental condition. This is the maximum strain of the macro-chamber for 36.5% strain of the heel pad (see Chapter 5). The force was measured by the FE load cell model and the displacement of the macro-chamber in superior direction was measured by tracking movements of outer surface of elements adjacent to the center of the load cell. These data were extracted from the FE output files in Excel format. Having the unloaded thickness of the macro-chamber layer, its strain was calculated during loading and its force-strain response was generated.

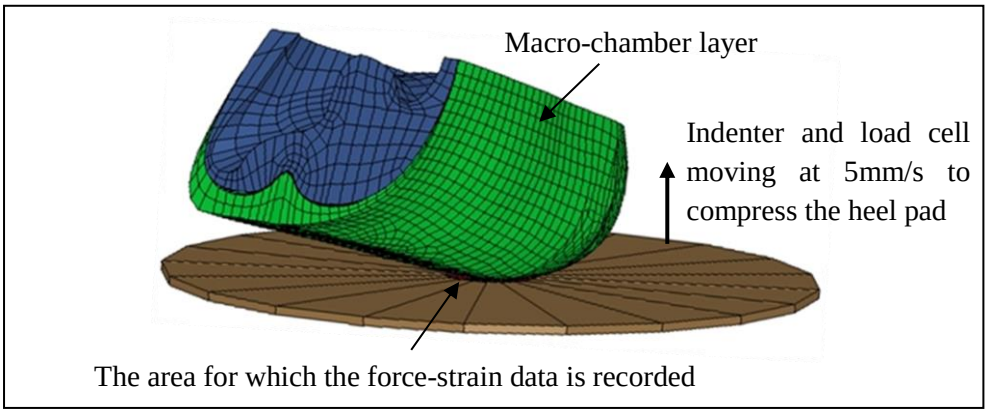

Figure 6.3: Determination of the macro-chamber hyperelastic material properties.

The RMS error between the experimental and predicted force-strain results as objective function was calculated for 999 data points, set by Ls-Dyna. The two material parameters of the macro-chamber, μ and α, were varied iteratively so that the predicted data were fitted to

the experimental data in low and high-strain regions whilst reviewing the RMS error for the whole loading sequence. The steps involved in the iterative curve fitting, called iterative curve fitting rule in this study, are as follows.

1. The most appropriate initial change increment for each material property was determined. This value was found through try and error by observing the effect of its variation on the response of the model. This increment was chosen so that the model response would gradually move towards the data curve during the following step.
2. Once the increments of changes in parameters were set, at each iteration only one parameter was varied (by its current increment) and the corresponding objective functions (e.g. RMS errors) were computed and stored. This process was repeated throughout successive iterations towards minimisation of the objective functions. This led to a point where any further variation of a parameter (by its current increment) would result in the increase of the objective functions.
3. At this point the current increment corresponding to that specific parameter was replaced by a smaller value (normally half of the current value).
4. Steps 2 and 3 were repeated until no more useful improvement were observed in reduction of the objective functions and the change in objective function between the current and previous iteration became negligible, and so continuing the process through further iterations was inefficient.

Throughout this process, visual assessment of the results helped to gain better understanding of the effects of parameter variations on the FE model responses, and consequently reducing the time needed for obtaining the optimum values of material parameters.

This process was repeated for 21 iterations until no useful improvement was observed in reduction of the RMS error (change in RMS error between the last two iterations<0.15N which is 0.2% maximum force). Continuing the curve fitting after 21 iterations was not

efficient since by increasing the computation time and cost, the RMS error was reduced by a very small amount.

It is important to remind that the material properties obtained at this stage were not the final values for the macro-chamber. During the experimental tests, the force was measured at the interface between the skin and the load cell. However, in this stage, the FE model provided the force at the contact area between the macro-chamber and the load cell ignoring the effects of the micro-chamber and skin layer on the macro-chamber layer behaviour. In reality, the micro-chamber and skin layers impose constraints to the macro-chamber layer which results in changes of the responses of the macro-chamber. Therefore, the estimates obtained at this stage were only used as initial properties to start the FEA of two-layer model towards determination of final material properties of the heel pad sub-layers.

6.2.1.2 Determination of the Hyperelastic Material Properties of the Micro-chamber Layer

The aim of this stage was to determine the first and second estimates for hyperelastic material parameters of the micro-chamber and macro-chamber layer respectively. The elements representing the micro-chamber layer were added to those of macro-chamber layer in the FE model (Figure 6.4) and the material parameters estimated for the macro-chamber in the previous stage were assigned to the micro-chamber elements to start the FEA. The indenter and the load cell compressed the two-layer model at 5mm/s up to 39% strain and the force-strain data was recorded. The value of 39% was the maximum strain induced to the total macro-chamber and micro-chamber for during experiments (see Chapter 5). RMS error was used as an objective function to quantify the quality of match between experimental data and model predictions. The error was calculated between the experimental and simulated force values for 999 data points set by Ls-Dyna.

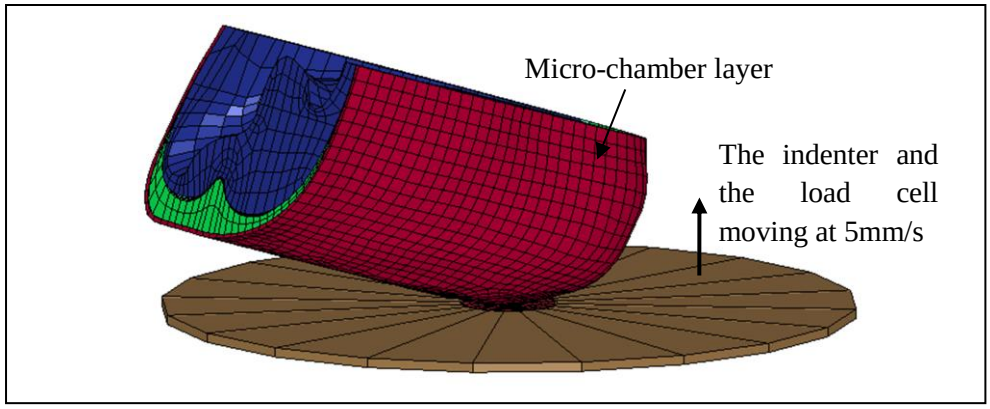

Figure 6.4: Determination of the micro-chamber hyperelastic material properties

The material parameters for the micro-chamber layer, μ and α, were varied based on the iterative curve fitting rule (see section 6.2.1.1) until the difference between the predicted force-strain result of two-layer model and the experimental data obtained for the total of the macro-chamber and micro-chamber layers was minimised. Additional constraints applied to the macro-chamber by the micro-chamber layer elements and changes in the parameters of the micro-chamber layer (micro-chamber stiffness) inevitably affected responses of the macro-chamber layer. Therefore, the behaviour of the macro-chamber layer was reviewed at each iteration and the macro-chamber parameters predicted in the previous stage were adjusted following iterative curve fitting rule (see section 6.2.1.1) until the predicted force-strain results were again fitted to the macro-chamber experimental data with possible minimum error. RMS error and difference between maximum strains were used as objective functions to evaluate the quality of the fit. Subsequently the material properties of the micro-chamber layer were adjusted.

The process of adjusting the material parameters of the macro-chamber and micro-chamber layers was repeated for 23 iterations until the objective functions of the macro-chamber layer and two-layer model did not change significantly between iterations (change in RMS error and maximum strain between the last two iterations<0.4N which is 0.5% maximum force and

0.05% strain respectively). Continuing curve fitting was not any more efficient in terms of error, while the computation time was increased.

A limitation of this stage was that the predicted force-strain result measured at the micro-chamber and the load cell interface were compared to the experimental force-strain result recorded at the skin and the load cell interface. This problem was resolved by modifying the estimates of the macro-chamber and micro-chamber material properties at the final stage. The material properties obtained for macro-chamber and micro-chamber at this stage were used as the initial properties to start the FEA of the complete three-layer FE model.

6.2.1.3 Determination of the Final Hyperelastic Material Properties of the Macro-chamber, Micro-chamber and Skin Layers

The aim of this stage was to estimate the final values of the material properties of the macro-chamber, micro-chamber and skin layers. The skin layer elements were added to those of macro-chamber and micro-chamber in the FE model (Figure 6.5). Initially the material properties obtained for the micro-chamber layer in the previous stage were assigned to the skin layer elements. The complete three-layer model was compressed by the indenter and the load cell at the speed of 5mm/s up to 36.5% strain to replicate the experiment. This is the maximum strain induced to the heel pad during the experiments (see Chapter 5). The predicted force-strain data was recorded. The force predicted by complete three-layer model was compared with the experimental force recorded at the interface between the skin and the load cell. RMS error was used as an objective function to quantify the quality of match between experimental data and model predictions. RMS error was calculated for 999 data points set by Ls-Dyna.

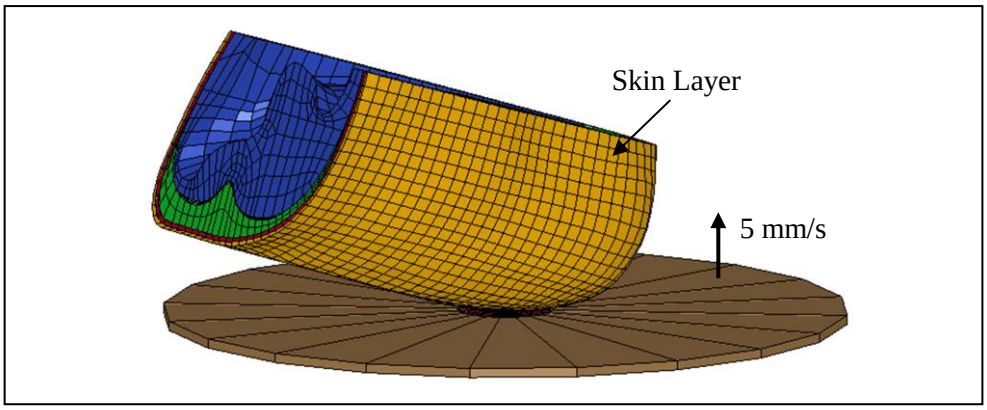

Figure 6.5: Determination of the hyperelastic material properties of the heel pad sub-layers

The material properties of the skin layer, μ and α, were iteratively varied based on iterative curve fitting rule (see section 6.2.1.1) until the difference between the simulated force-strain results for the three-layer heel pad model and the heel pad experimental data was minimised. The force-strain behaviours of the macro-chamber and micro-chamber layers predicted by the three-layer FE model were also reviewed at each iteration. It was noticed that their behaviours, observed in the two-layer FE model, changed and the corresponding errors increased. These changes were due to the additional constraints applied to the micro-chamber and macro-chamber by the skin layer and variation of the skin stiffness. Therefore, the material parameters of the macro-chamber and micro-chamber were also incrementally varied based on iterative curve fitting rule (see section 6.2.1.1) towards minimisation of objective functions. RMS errors and difference between maximum strains were used as objective functions to quantify the difference between predicted and experimental responses of the macro-chamber and micro-chamber layers. Subsequently the material properties of the skin layer were adjusted.

Adjustment of material properties of macro-chamber, micro-chamber and skin was continued for 71 iterations until the predicted results for the macro-chamber, micro-chamber, and three-layer model (heel pad) were fitted to a high standard to the corresponding experimental data. At this point no more useful improvement was observed in reduction of objective functions

(change in RMS error and maximum strain between the last two iterations <0.3N which is 0.4% maximum force and 0.2% strain respectively).

6.2.2 Validation of the Hyperelastic FE Model

The loaded thickness of the heel pad under compressive load and the peak plantar pressure under the heel was used to validate the hyperelastic FE model. MRI data was used to validate the FE models of the human soft tissues. Comparing the MRI of the loaded configurations with simulation results provides key information for validation. In some cases a comparison between simulated deformation of skin/fat and passive-muscle tissue and support material under loading and MRI results were used for validation (123, 124). The loaded thickness of the heel pad was obtained from the loaded MRI data from the right foot of the **Subject 1**. Unloaded MRI data of **Subject 1** was used previously to build model of this subject's foot (see Chapter 5). The T1 fast spin echo MRI scans were taken with 160×160 pixels and spacing of 5.5mm from the heel area in the coronal view.

A loading device was developed to compress the heel pad and apply load during the MRI scanning. This device consisted of a nonmagnetic back pack worn by subject and connected to wooden foot support via plastic side straps (Figure 6.6). The back pack was worn by the subject before she entered to the MRI unit. The back pack was firmly tightened over the subject's thorax and waist ensuring that it did not move during loading. During the MRI scanning, the subject was lying in the supine position and her right foot was placed against the foot support. The foot support was designed so that it kept the foot in a position whereby the ankle was rotated of about 17.6 degree to reproduce the experimental compression test (see Chapter 4). The load was applied to the heel pad by pulling the loose ends of the side straps connecting foot support housing and back.

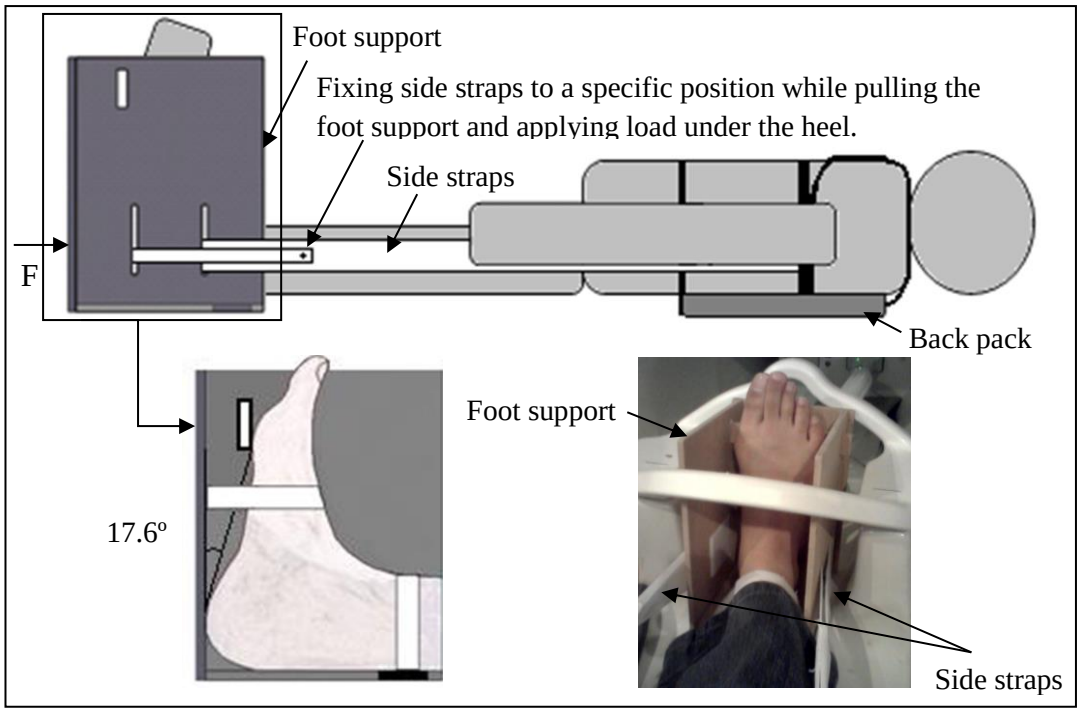

Figure 6.6: The heel pad loading device. The foot support kept the foot at angle of 17.6 degree to reproduce the position of the foot inside the test rig during experimentation and compressed the heel by pulling the loose ends of side straps.

The Pedar pressure insole system (Novel.de, Munich, Germany) was used to measure the load which was applied to the heel pad during the MRI scanning. Since it has metal/magnetic parts the insole system could not be used during scanning. Therefore, after the MRI scanning, the Pedar pressure insole was placed in the foot support under the heel area and the applied force under the heel pad was recorded over 30 seconds period. After MRI scanning the subject wearing the back pack lay down on the examination table in the supine position while her right foot was placed against the foot support. The loose ends of the side straps were pulled and fixed to the specific position marked on the side straps to compress the heel pad using the foot support for the same amount as applied during MRI scanning. Some pilot measurements were performed before and after MRI scanning to ensure that using the heel pad loading device provides consistent data out of and during MRI scanning.

30 seconds was enough to record the constant load under the heel area. This measurement was repeated 12 times with a few minutes rest between each trial to enable the heel pad to recover. The force was measured for 17 sensors with total area of 3295mm^2 under the heel region. Larger insole than the foot size was selected to ensure that not any load or pressure data of the heel is missed. Having the pressure data provided by Pedar system for each sensor and the area of each sensor, it was possible to calculate the applied force measured by each sensor. Then, the average force was calculated for each sensor during 30 seconds loading. The total of the average force of each sensor was set as the load applied to the heel for each repetition. A load of 315.14N (SD 7.8) was recorded under the heel pad for 12 repetitions. Figure 6.7 shows the plantar pressure distribution during loading using Pedar system.

The thickness of the heel pad under loading was then measured from the MRI scans. The loaded thickness of the heel pad was measured under the calcaneus tuberosity. The selected slice was 28.7mm from back of the foot. To predict the loaded thickness of the heel pad in the FE model, the indenter and load cell were replaced by a rectangular flat rigid plate in the FE model. The rectangular plate moved towards the heel pad and applied the load of 315N. The loaded thickness of the heel pad in the FE model was measured at the conjunction of the frontal and transverse planes almost 28.7mm from the back of the heel. The loaded thickness of the heel pad in both the MRI slice and FE cross section was measured at 34.5mm from the lateral side of the foot.

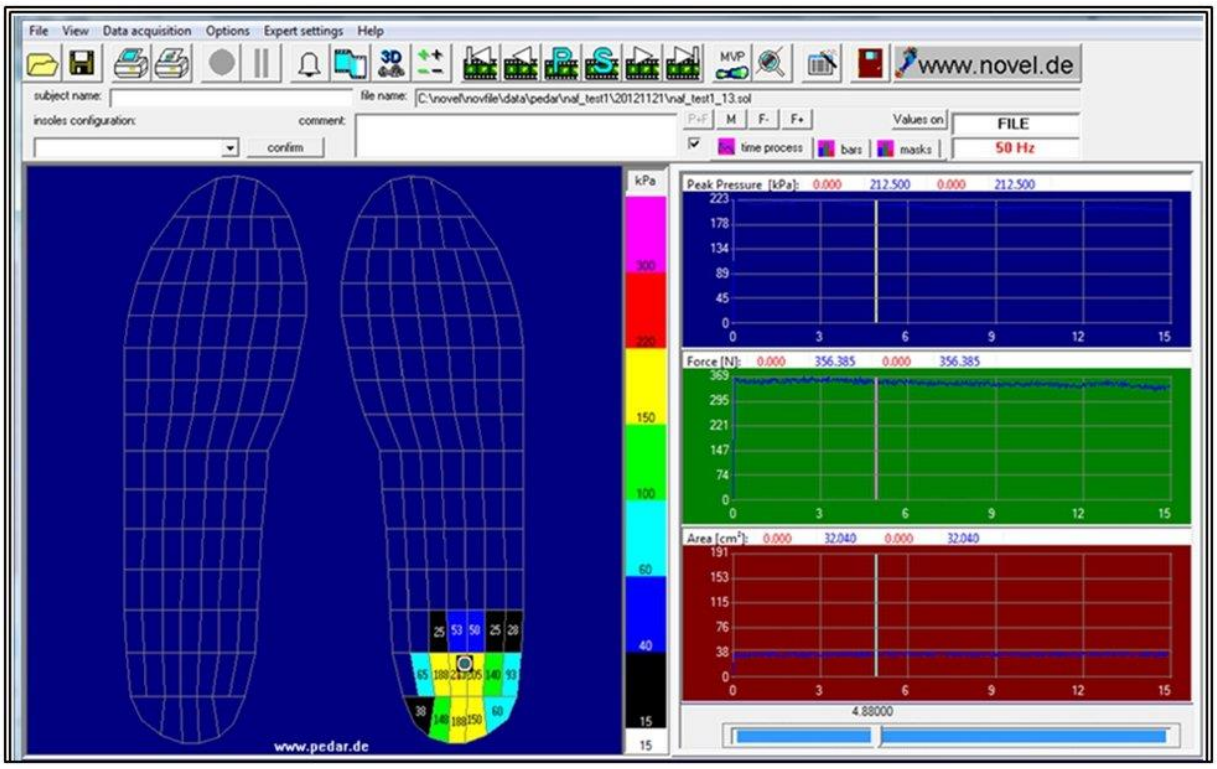

Figure 6.7: The heel region pressure distribution under loading measured by Pedar system

The second validation explored the capability of the model in prediction of the peak plantar pressure, which is a commonly used method in the biomechanics (5, 7, 9, 77) . For this purpose, the numerical result of peak plantar pressure was compared with the experimental data from the Pedar system under 315N from the previous validation study. The predicted peak plantar pressure was averaged over 10×19mm^2 which is close to the one sensor size in the Pedar insole (191mm^2).

6.2.3 Viscoelastic Material Properties

The viscoelastic material parameters of the macro-chamber, micro-chamber and skin layers could be estimated after determination of their hyperelastic material properties. The experimental data obtained for the macro-chamber, micro-chamber and heel pad under rapid compression test at 225mm/s (see Chapter 5) were used to estimate the viscoelastic material properties of the heel pad sub-layers. The force-strain results obtained from the compression

tests were used as inputs to the inverse FEA to determine the viscoelastic material properties of the heel pad sub-layers.

The Ogden material model in Ls-Dyna with optional "viscoelastic overstress" was chosen to simulate the viscoelastic behaviour of the heel pad and its sub-layers (see Chapter 4). In this model, viscoelastic behaviour is introduced via stress relaxation modulus, G, and viscoelastic decay constant, β (122). In total, 6 viscoelastic material parameters had to be estimated, three tissue layers with two viscoelastic parameters, G and β, for each layer. To reduce the complexity, a similar procedure to that used to obtain the hyperelastic material properties of the heel pad sub-layers was followed here (Figure 6.2). First, only the material parameters of the macro-chamber layer were determined from one layer FE model. These first estimates were not the final values for the properties of the macro-chamber layer and they were adjusted in the subsequent stages. Then, the first and second estimates for the material parameters of the micro-chamber and macro-chamber layers were determined from the two-layer FE model respectively. At last, the final values of the material parameters for the macro-chamber, micro-chamber and skin layers were estimated from the complete three-layer FE model. The complete process is explained in details as follows.

6.2.3.1 Determination of the Viscoelastic Material Properties of the Macro-chamber Layer

The aim of this stage was to predict the initial estimates for the viscoelastic material properties of the macro-chamber layer. To achieve this purpose, one-layer FE model with elements representing the macro-chamber layer with two unknowns (G and β) was used (Figure 6.3). Two initial values of 0.389MPa and $1ms^{-1}$ for G and β respectively, obtained for the skin layer in the published literature, were assigned to the macro-chamber elements (117). The macro-chamber layer was subjected to the loading-hold-unloading cycle up to 41.9% strain to replicate the experimental condition (see Chapter 5, trial 4). The macro-chamber was

loaded and unloaded at velocity of 225mm/s and its strain kept constant for 26ms before unloading and its force-strain relation was recorded for the loading-hold-unloading cycle. Two RMS errors, one measured during loading period and other measured for the unloading period, and the difference between peak forces at the maximum strain were used as objective functions to assess the quality of the match of the experimental and predicted results.

The RMS error for the loading period measured the difference between the predicted results and the average experimental data obtained for the loading period. The RMS error for the unloading period measured the difference between the predicted results and the experimental data of trial 4 out of 5 trials performed on the heel pad (see Chapter 5). Since the maximum strain, up to which the heel pad was compressed, were different in 5 trials, the experimental force-strain results were recorded for 5 different hold and unloading protocols and were different. Therefore, it was not possible to calculate the average of the hold-unloading results. Trial 4 was the median of the other trials. After estimation of the final material properties, comparison between predicted results and experimental data corresponding to other 4 trials was used as one of the validation methods (see section 6.2.4).

The viscoelastic material parameters of macro-chamber were iteratively adjusted based on iterative curve fitting rule (see section 6.2.1.1) for 16 iterations until no meaningful changes were observed in the reduction of objective functions (changes in RMS errors and difference in peak forces between the last two iterations<1N which is 0.8% maximum force). At this point by continuing the adjustment of material properties, the computation time was increased whereas only slight changes were occurred in decrease of the objective functions. The RMS errors were calculated for 993 data points set by Ls-Dyna.

As previously explained, the material properties obtained at this stage were not the final values. This was because of the difference between the force experienced at the interface of

the skin and the load cell in the experimental tests and the force predicted at the interface of macro-chamber and the load cell in the one-layer FE model, which ignored the effect of micro-chamber and skin on the responses of the macro-chamber layer. This problem was resolved by adjusting the material properties of the macro-chamber layer at the final stage where the effects of all three layers were taken into account.

6.2.3.2 Determination of the Viscoelastic Material Properties of the Micro-chamber Layer

The purpose of this stage was to predict the first and second estimates for viscoelastic material parameters of the micro-chamber and macro-chamber layers respectively. The elements representing the micro-chamber layer were added to macro-chamber elements in the FE model (Figure 6.4). The viscoelastic material parameters estimated for the macro-chamber layer in the previous stage were assigned to the micro-chamber elements to start the FEA. The two-layer FE model was subjected to the loading-hold-unloading cycle up to maximum strain of 38.9% to reproduce the experimental condition (see Chapter 5, trial 4). The FE model was loaded and unloaded at constant velocity of 225mm/s and its strain hold constant for 26ms before unloading started. The force-strain data were recorded for the loading-hold-unloading cycle.

Two RMS errors, measured during the loading and unloading periods, and the difference between the peak forces at the maximum strain were used as objective functions to quantify the quality of the fit between predicted results and experimental data. The RMS error for the loading period measured the difference between the values predicted by the FE model and the average of experimental data obtained during the loading period. The RMS error for the unloading period measured the difference between the predicted results and the experimental data of trial 4 during the unloading period (see Section 6.2.3.1). The RMS errors were

calculated between the experimental and simulated force values for 999 data point, set by Ls-Dyna.

The viscoelastic material parameters of the micro-chamber layer were iteratively varied based on iterative curve fitting rule (see section 6.2.1.1) until the fit between the predicted force-strain result of two-layer FE model and the corresponding experimental data was of a high standard. Already explained, adding the elements of micro-chamber layer to the FE model and adjusting its parameters (changing the stiffness) imposed extra constraints on the macro-chamber layer leading to variation in the macro-chamber behaviour. Therefore, the behaviour of the macro-chamber layer was reviewed at each iteration. The viscoelastic parameters of the macro-chamber were iteratively varied based on iterative curve fitting rule (see section 6.2.1.1) until the predicted force-strain results were fitted to the macro-chamber experimental data with possible minimum error. RMS errors, difference in peak forces and the maximum strains were used as objective functions. Subsequently the material properties of the micro-chamber layer were adjusted.

This adjustment of the material properties of the macro-chamber and the micro-chamber layers were continued for 24 iterations until improvements were very small (changes in RMS errors and difference between peak forces <0.94N which is 0.8% maximum force, change in difference between maximum strains was negligible). The material properties obtained at this stage were used as initial properties to start FEA of the complete three-layer model.

6.2.3.3 Determination of the Final Viscoelastic Material Properties of the Macro-chamber, Micro-chamber and Skin Layers

The aim of this stage was to determine the final estimates of the viscoelastic material properties for the macro-chamber, micro-chamber and skin layers. To achieve this, the elements of the skin layer were added to the macro-chamber and micro-chamber layers in the

FE model (Figure 6.5). The material properties obtained for the micro-chamber layer in the previous stage were assigned to the skin layer elements to start the FEA. The loading-hold-unloading cycle was performed on the three-layer model up to 37% maximum strain to replicate the experimental condition (see Chapter 5, trial4). The three-layer model was subjected to loading and unloading cycles at 225mm/s while its deformation kept constant for 26ms before unloading. The predicted force-strain results of the macro-chamber, micro-chamber and the heel pad were recorded. In this stage, the predicted force-strain behaviours of the heel pad and micro-chamber and macro-chamber could be properly compared to the experimental results since all the effects of the different heel pad sub-layers were considered.

Two RMS errors for the loading and unloading periods and the difference between peak forces at the maximum strain were used as objective functions to measure the quality of the match of predicted and experimental results of the heel pad. The RMS error for the loading period was calculated between the predicted results and the average of the experimental data during loading. As previously mentioned, the RMS error for the unloading period was calculated between the predicted results and the experimental data of trial 4 (see section 6.2.3.1). The RMS error was calculated for 999 data points, set by Ls-Dyna.

The material properties of the skin layer were iteratively varied based on the iterative curve fitting rule (see section 6.2.1.1) until the simulated force-strain result for the three-layer model was fitted to the heel pad experimental data to a high standard. Adding the skin elements to the FE model and also variation of its material properties (skin stiffness) affected the force-strain responses of the macro-chamber and micro-chamber layers. These changes were due to imposing extra confinements on the macro-chamber and micro-chamber layers. Thus, the behaviours of the macro-chamber and micro-chamber were also reviewed at each iteration. Their material parameters were changed incrementally based on iterative curve fitting rule (see section 6.2.1.1) until the predicted results for the macro-chamber and micro-chamber

layers were fitted to the corresponding experimental data with possible minimum error. RMS errors, difference in peak forces and maximum strains were used as objective functions. Subsequently the material properties of the skin layer were adjusted.

This process was repeated for 47 iterations until the errors did not change significantly (changes in of RMS errors and difference between peak forces<0.8N which is 0.7% maximum force, change in difference between maximum strains was negligible). The parameters obtained for macro-chamber, micro-chamber and skin layers in this stage were the final estimates.

6.2.4 Validation of the Viscoelastic FE Model

Two series of rapid compression tests were used to validate the viscoelastic FE model. For this purpose, the force-strain responses of the heel pad under loading-hold-unloading cycle at constant speed of 141mm/s and a 26ms hold time before unloading, and sinusoidal loading-unloading cycle with the maximum speed of 300mm/s were used (see Chapter 5). Five trials were available for each series of experiments with slightly different maximum strains. The 5 experimental conditions were applied to the viscoelastic FE model to reproduce the behaviour of the heel pad in each different experimental trial. In addition, to offer further validation, behaviours of the heel pad, micro-chamber and macro-chamber under loading-hold-unloading cycle with velocity of 225mm/s in the 4 trials not used to estimate material properties were compared to model simulation of the same data.

Two RMS errors for loading and unloading periods and difference between peak forces at the maximum strain were used to evaluate the quality of the viscoelastic FE model in reproducing the behaviour of the heel pad at rapid compression tests at 141mm/s and 225mm/s. Two RMS errors for loading and unloading periods were also used to assess the ability of the viscoelastic FE model in predicting the behaviour of the heel pad under sinusoidal loading-unloading tests with 300mm/s maximum velocity.

6.2.5 Parametric Studies

The series of parametric studies conducted in Chapter 4 to evaluate the effects of the material properties of the muscle tissue and plantar fascia and changes of the angle of rotation of the heel on the force-strain responses of the heel pad were repeated after estimation of the heel pad sub-layer properties. In this chapter, the parametric studies were conducted while the macro-chamber, micro-chamber and skin layers were assigned with the final material properties obtained from inverse FEA. The model was compressed at displacement rate of 5mm/s and the difference between the force-strain reactions of the model at different conditions were calculated using RMS error.

The first two parametric studies allowed estimation of the potential errors that might result from not using the material properties of the muscle tissue and plantar fascia for the test subject. To investigate the effect of stiffness of the muscle tissue on the heel pad responses three Young's modulus of 1.08, 14 and 55MPa were assigned to the muscle tissue to simulate its low, medium and high stiffness respectively. 5 Young's modulus of 10, 100, 250, 350 and 500MPa were assigned to the plantar fascia to evaluate the effect of its stiffness on the heel pad reactions. The final parametric study investigated the influence of variation in the angle of rotation of the foot on the heel pad force-strain responses. In this parametric study the reference angle of rotation of the model (17.6 degree) was varied for ±1º, ±5º and ±10º.

6.3 RESULTS AND DISCUSSION

6.3.1 Hyperelastic Material Properties of the Heel Pad Sub-layers

The aim of this section is to provide the results of the inverse FEA for the macro-chamber, micro-chamber and skin layers. This starts with providing initial estimates for material properties of the macro-chamber and micro-chamber layers obtained from one and two-layer FE models. Then, the final estimates for the hyperelastic properties of the macro-chamber,

micro-chamber and skin layers, determined from the complete three-layer FE model, are provided.

6.3.1.1 Initial Hyperelastic Material Properties of the Macro-chamber Layer

The initial estimates for the hyperelastic material properties of the macro-chamber layer, obtained from the one-layer FE model, are listed in Table 6.1. After 21 iterations a convergence with RMS error of 1.35N was reached between the predicted and the experimental results.

Table 6.1: Initial estimates for the hyperelastic material properties of the macro-chamber layer determined from one-layer FE model.

	μ (kPa)	α (-)	RMS error (N)	RMS error (% max force)
Macro-chamber	41	4.2	1.35	1.78

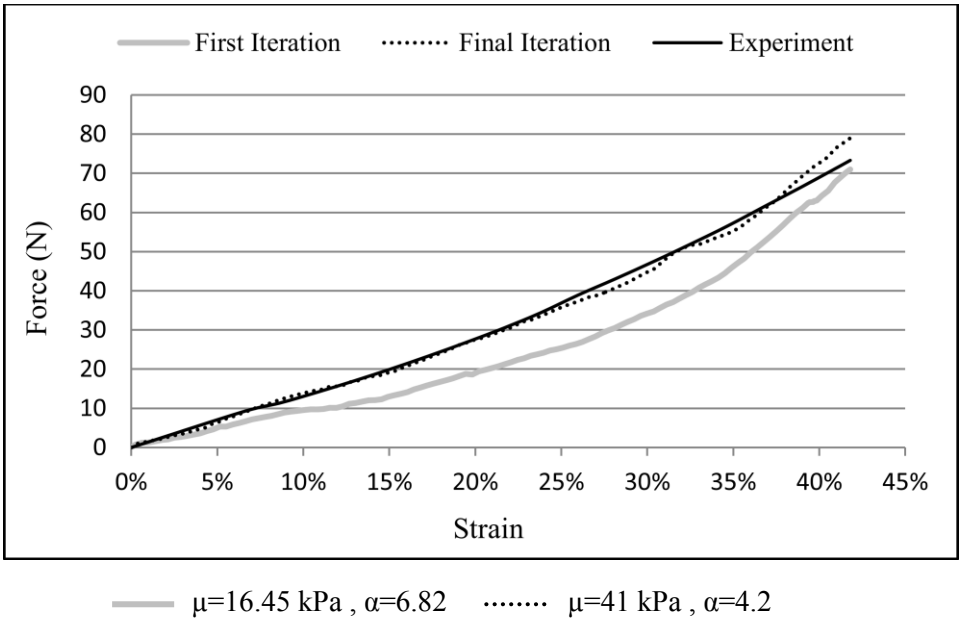

Figure 6.8: Force-strain relation of the macro-chamber layer predicted by the one-layer FE model.

Figure 6.8 shows the force-strain relations of the macro-chamber at the first and the final iterations using the material parameters derived from literature and those obtained from this study respectively. The RMS error was reduced by 5.9N from the first iteration to the final

iteration. Although the one-layer FE model at the final iteration overestimated the force at higher strains, it could predict the behaviour of the macro-chamber under compression up to strain of 37.4% with insignificant RMS error of 0.6N which is 0.9% maximum force (Figure 6.8).

6.3.1.2 Initial Hyperelastic Material Properties of the Micro-chamber Layer

The first estimates for the hyperelastic material properties of the micro-chamber layer and the second estimates for the hyperelastic material properties of the macro-chamber layer, obtained from the two-layer FE model, are provided in Table 6.2. A convergence was reached with RMS errors of 1.91 and 1.82N between the predicted and the experimental results for the two-layer FE model (total of the macro-chamber and micro-chamber) and the macro-chamber respectively after 23 iterations.

Table 6.2: The hyperelastic material properties of the micro-chamber and macro-chamber layers determined from two-layer model.

	μ (kPa)	α (-)	RMS error (N)	RMS error (% max force)	Difference between max strains
Micro-chamber	104	4.7	1.91 (for two-layer model)	2.56 (for two-layer model)	-
Macro-chamber	35	4.9	1.82	2.44	1.4

Figures 6.9 and 6.10 illustrate the force-strain relations of the macro-chamber layer and the two-layer model at the first and the final iterations predicted by the two-layer FE model. At the first iteration, the FEA was run while the micro-chamber layer was being assigned with the material parameters obtained for the macro-chamber layer in the previous stage. RMS error was reduced by 5.8N from the first iteration to the final iteration for the two-layer FE model.

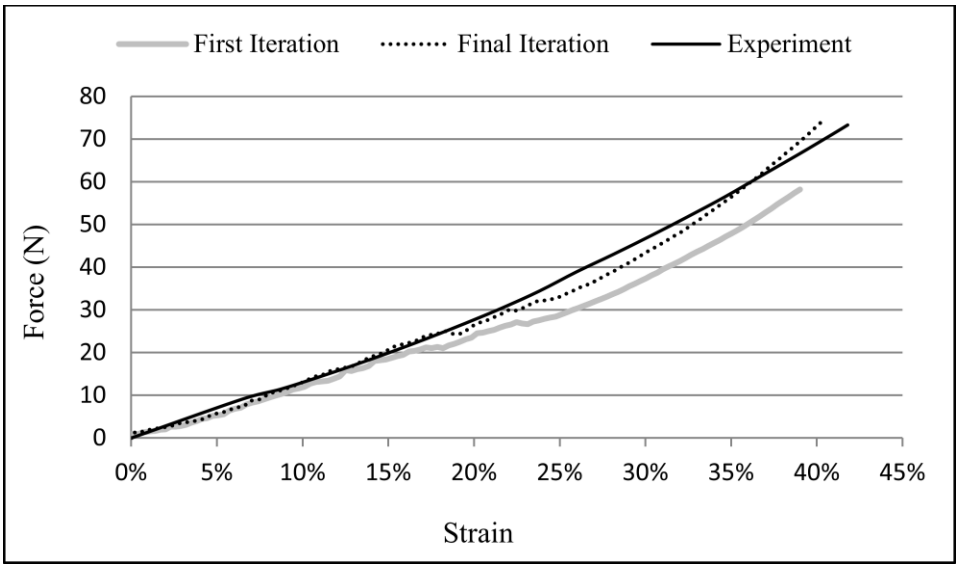

Macro-chamber: μ=41 kPa, α=4.2 ..... Macro-chamber: μ=35 kPa, α=4.9
Micro-chamber: μ=41 kPa, α=4.2 Micro-chamber: μ=104 kPa, α=4.7

Figure 6.9: Force-strain relation of the macro-chamber layer predicted by the two-layer FE model.

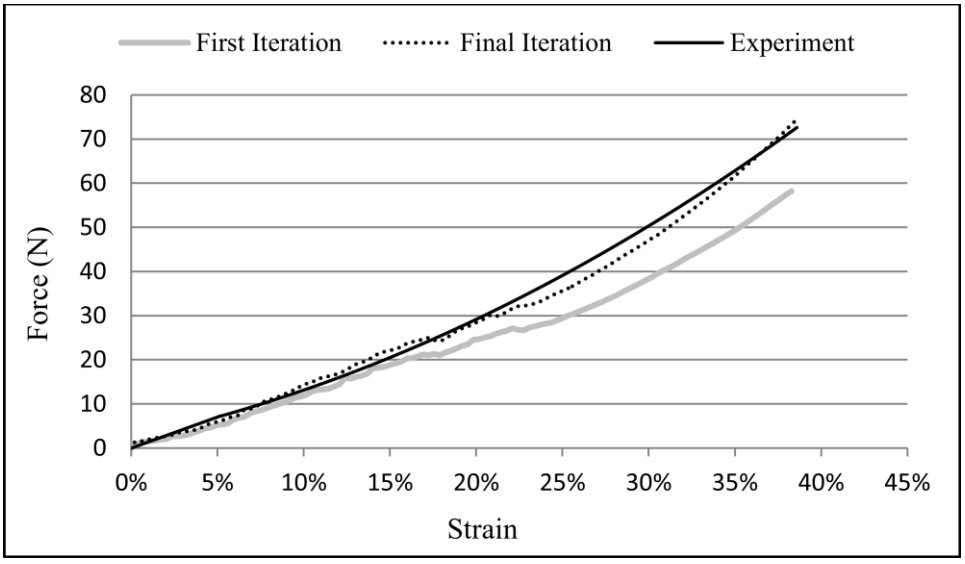

Macro-chamber: μ=41 kPa, α=4.2 .....Macro-chamber: μ=35 kPa, α=4.9
Micro-chamber: μ=41 kPa, α=4.2 Micro-chamber: μ=104 kPa, α=4.7

Figure 6.10: Force-strain relation of the two-layer FE model.

At the first iteration for 39.0% strain of the two-layer FE model, the macro-chamber was compresses only up to 39.0% strain, while 41.8% strain was expected (Figure 6.9). This can be explained by the fact that the micro-chamber layer was behaving with lower stiffness than *in-vivo,* being assigned with the material properties of the macro-chamber at the first iteration.

At the final iteration, when the stiffness of micro-chamber was increased, the simulation of the macro-chamber behaviour was improved and strain increased up to 40.4%, still 1.4 less than the experimental data. This issue was eliminated at the final stage. At the first iteration, the two-layer FE model underestimated the hyperelastic behaviour of the total of the macro-chamber and micro-chamber layers (Figure 6.10). At the first iteration, the FE model underestimated the behaviour of the total macro-chamber and micro chamber with ~58N for inducing 39% strain, whereas (~73N) was required based on experimental data. Thus model prediction had high error of approximately 15N (20% maximum force) initially.

6.3.1.3 Final Hyperelastic Material Properties of the Macro-chamber, Micro-chamber and Skin Layers

At this final stage, the final estimates for the hyperelastic material properties of the macro-chamber, micro-chamber and skin were determined using the complete three-layer FE model (the complete heel pad model). Table 6.3 provides the final material properties of the heel pad sub-layers and errors measured for the force-strain behaviours of the macro-chamber, micro-chamber and three-layer FE model. The total of 71 iterations were required to reach a convergence with RMS errors of 1.92, 3.73, and 1.98N between the predicted and experimental force-strain results for the macro-chamber, micro-chamber and the three-layer heel pad model respectively (Table 6.3). Figures 6.11-6.13 show the force-strain responses of the macro-chamber, micro-chamber, and the complete three-layer model at the first and the final iterations. RMS error was reduced by 4.3N from the first iteration to the final iteration for the three-layer model.

Table 6.3: Optimised final hyperelastic material properties for the macro-chamber, micro-chamber and skin layers

	μ (kPa)	α (-)	RMS error (N)	RMS error (% max force)	Difference between max strains
Skin	452	5.6	1.98 (for the heel pad model)	2.7 (for the heel pad model)	-
Micro-chamber	95	4.9	3.73	5.0	0.3
Macro-chamber	36	4.5	1.92	2.6	0.4

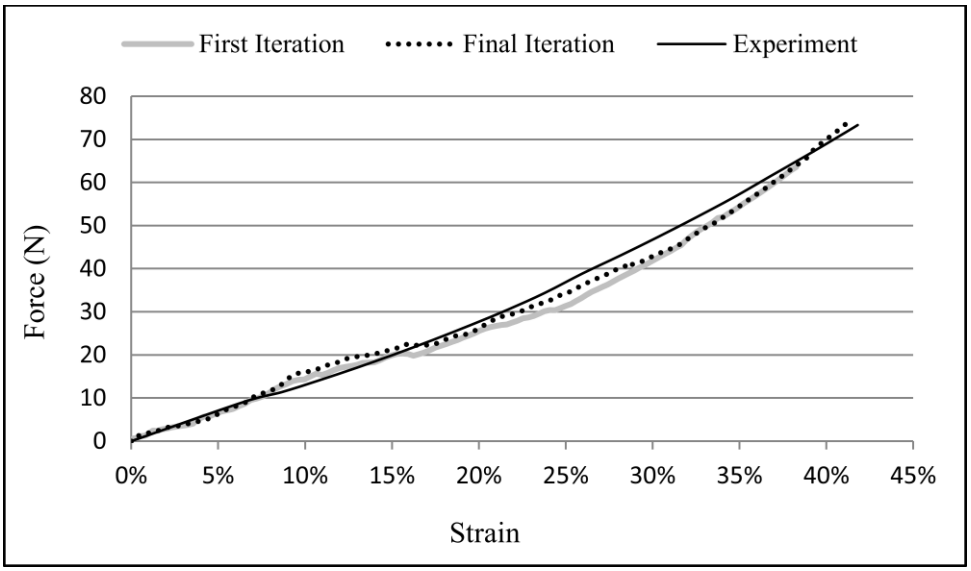

Macro-chamber: μ=35 kPa, α=4.9
Micro-chamber: μ=104 kPa, α=4.7
Skin: μ=104 kPa, α=4.7

Macro-chamber: μ=36 kPa, α=4.5
Micro-chamber: μ=95 kPa, α=4.9
Skin: μ=452 kPa, α=5.6

Figure 6.11: Force-strain relation of the macro-chamber layer predicted by the three-layer FE model.

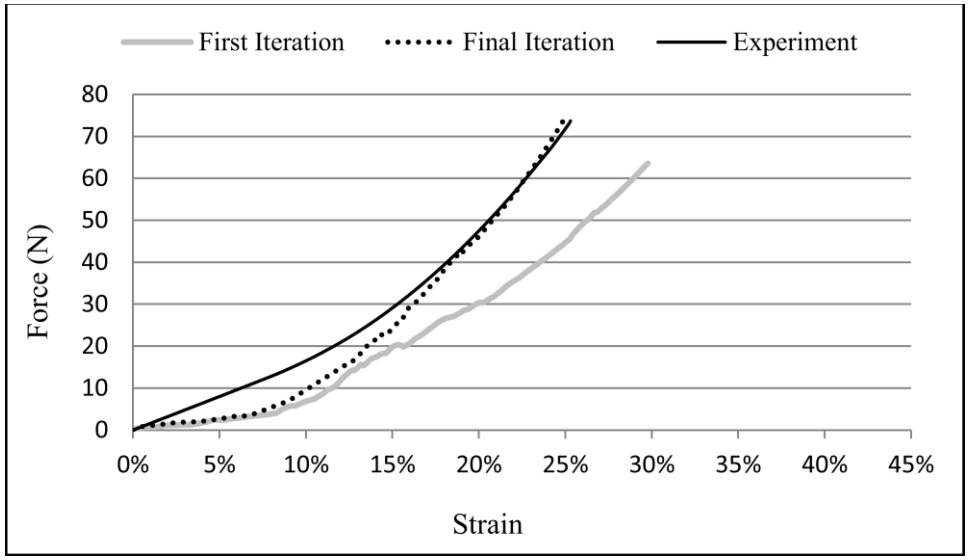

Macro-chamber: μ=35 kPa, α=4.9
Micro-chamber: μ=104 kPa, α=4.7
Skin: μ=104 kPa, α=4.7

Macro-chamber: μ=36 kPa, α=4.5
Micro-chamber: μ=95 kPa, α=4.9
Skin: μ=452 kPa, α=5.6

Figure 6.12: Force-strain relation of the micro-chamber layer predicted by the three-layer FE model.

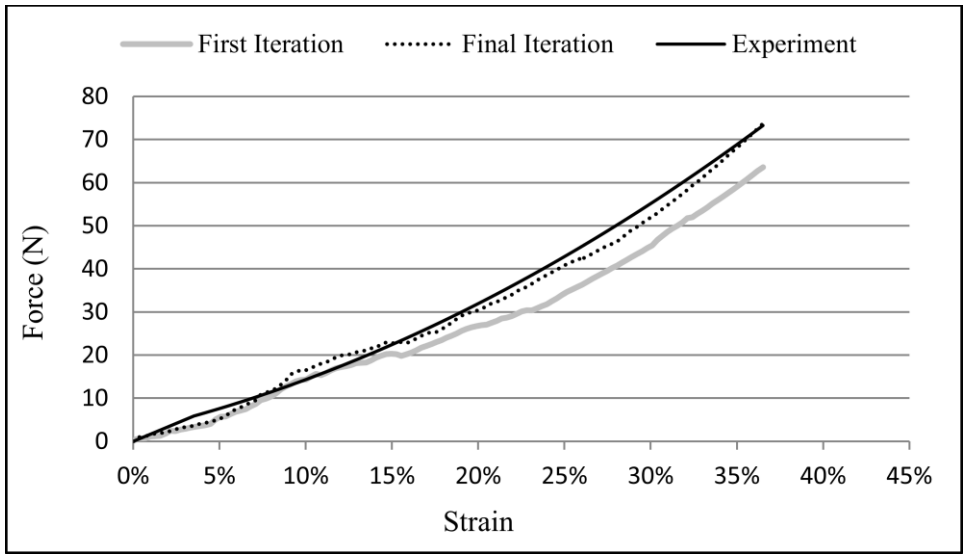

Macro-chamber: μ=35 kPa, α=4.9
Micro-chamber: μ=104 kPa, α=4.7
Skin: μ=104 kPa, α=4.7

Macro-chamber: μ=36 kPa, α=4.5
Micro-chamber: μ=95 kPa, α=4.9
Skin: μ=452 kPa, α=5.6

Figure 6.13: Force-strain relation of the three-layer FE model.

According to Figure 6.11, at the first iteration the macro-chamber-layer was compressed up to strain of 38.3% for 36.50% heel pad strain. However, the strain of 41.8% was expected according to the experimental results. On the other hand, Figure 6.12 reveals that the micro-chamber was compressed for 29.8% strain, whereas 25.3% strain was expected for 36.5% heel

pad strain based on experimental results. This might because of the skin and macro-chamber layers behaving with lower and higher stiffness than their actual ones respectively. It is clear that at the final iteration, by reducing the stiffness of the macro-chamber layer and also increasing the stiffness of the skin layer, the macro-chamber and micro-chamber hyperelastic behaviours were improved.

At the first iteration, where the skin stiffness was equal to the micro-chamber layer, the three-layer FE model underestimated the hyperelastic behaviour of the heel pad. To compress the heel pad up to 36.5% strain, a maximum load of ~64N was predicted with almost 9N difference (0.12% maximum force) with the experimental result of ~73N. The greatest difference between the values predicted by the FE model and experimental data can be seen in the hyperelastic behaviour of the micro-chamber layer. As can be seen in Figure 6.12 at final iteration, the FE model predicted the behaviour of the micro-chamber layer with a large error up to 0.15% strain.

According to the Ogden material model formulation in Ls-Dyna, the initial elastic modulus can be calculated as $3(\frac{1}{2}\mu\alpha)$ for an incompressible material. Therefore, the initial elastic modulus can be calculated as 3.797, 0.698 and 0.243MPa for the skin, micro-chamber and macro-chamber layers, respectively. In the literature, a wide range of values were reported for initial elastic modulus of the heel pad and its sub-layers. Gefen et al. reported the mean initial elastic modulus as 0.105MPa for the heel pad by conducting experiment on two healthy volunteers (31). In one study, the initial elastic modulus of the heel pad was reported as 0.050MPa using inverse FEA based on *in-vivo* experimental tests (5, 72). Hsu et al. reported 0.181 and 1.140MPa as elastic modulus of macro-chamber and micro-chamber, respectively based on *in-vivo* experiments on healthy subjects (33).

In-vitro results have also shown difference in initial elastic modulus. Value of 0.300MPa was reported for the heel pad using inverse FEA by fitting the predicted results to the experimental data obtained from an impact test on an isolated heel (9). However, in another case the initial elastic modulus of the heel pad was found as 0.003MPa using same method, but different experimental indentation data obtained using a spherical indenter and compression dominant loading on a heel specimen (6). In two cases the initial elastic modulus of the heel fat pad and skin were reported as 0.003-0.006MPa and 6.528-0.366MPa, respectively. In both cases the property of the fat pad was obtained by fitting the FE results to *in-vitro* experimental data, whereas *in-vivo* experimental data was used to determine the property of the skin layer (7, 11).

Depending upon the experimental test methods, subjects/samples, number of subjects/samples, and whether the study was conducted *in-vivo* or *in-vitro*, different initial elastic modulus have been reported for the heel pad and its sub-layers. Unique to this study, the material properties of three heel pad sub-layers (macro-chamber, micro-chamber and skin) were found based on *in-vivo* experimental data. Therefore, it is difficult to compare the property of the heel pad sub-layers with those provided for the heel pad as a single layer. Although the elastic modulus found for macro-chamber layer in this study (0.243MPa) is comparable with that obtained by Hsu et al. (0.181MPa), the micro-chamber property (0.698MPa) is approximately half of that reported by Hsu et al. (1.140MPa). This might because they considered the total of micro-chamber and skin layer as a micro-chamber layer resulting in a higher stiffness value for micro-chamber layer.

The property of the macro-chamber should approximately represent the heel pad's property because its behaviour is closest to the heel pad behaviour compared to the other sub-layers. In this study initial elastic modulus of macro-chamber (0.243MPa) is in the range of 0.050-0.300MPa provided for the heel pad in the literature, from both *in-vivo* and *in-vitro*

experimental data. The initial elastic modulus of the skin layer (3.797MPa) determined in this study can be compared to value of 6.528MPa obtained from *in-vivo* test for the skin layer. The difference between these two values might be due to the small value of 0.003MPa found for the fat pad leading to an increase in the property of the skin layer (6.528MPa) thus the whole model behaviour to be fitted to *in-vivo* experimental data. The fat pad property was obtained from an unconfined compression test conducted on isolated fat pads.

The material property of α can only be compared to studies which used Ogden material model. While Erdmir et al. reported value of 6.82 (SD 1.57) for the heel pad (5), values of 8.8-15.96 and 6.8-18 were found for the fat pad and skin respectively (7, 11). The values of 5.6, 4.9 and 4.5 found for skin, micro-chamber and macro-chamber in this study are close to value of 6.82 (SD 1.57) obtained using *in-vivo* test result. Similar to α values determined for the fat pad and skin layer in the literature, the values obtained for three heel pad sub-layers in this study are close to each other.

6.3.2 Validation of the Hyperelastic FE Model

To evaluate the accuracy of the FE model in prediction of the hyperelastic behaviour of the heel pad, the predicted loaded thickness of the heel pad under ~315N was compared with the experimental result, obtained from MRI. The loaded thickness of the heel pad was measured as 8.7mm under the calcaneus tuberosity at 34.5 and 28.7mm from the lateral side and the back of the foot respectively. The FE model predicted the loaded thickness of the heel pad as 9.3mm at the conjunction of the frontal and transverse planes at the same position in MRI data (Figure 6.14). Measurements and differences are provided in Table 6.4.

The result showed that the model was successful in matching the heel pad loaded thickness to the MRI data with 6.55% error. The errors propagated during the estimation of material properties for macro-chamber, micro-chamber and skin layers might be the source of this

error. The measurement of the applied load under the heel using Pedar system might be another source of our error.

Table 6.4: Difference between loaded heel pad thicknesses measured from the loaded MRI data and predicted by the FE model.

	Loaded MRI	FE model	Error (% max loaded thickness)
Loaded heel pad thickness	8.7 mm	9.3 mm	6.55

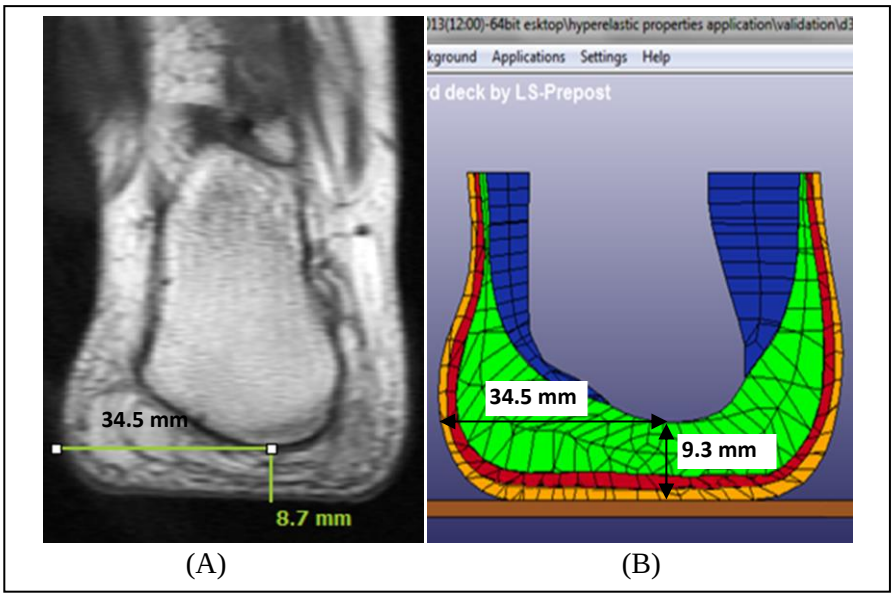

Figure 6.14: The loaded thickness of the heel pad subjected to a compressive load of 315.14N: (A) Loaded MR image of the heel pad; (B) FE model of the loaded heel pad.

In the second validation method, the model showed similar peak plantar pressure under the heel region compared to the experimental data from Pedar system. Figure 6.15 compares the numerical and experimental results of the peak plantar pressure under 315N. As shown by the contour plot of the numerical result, the peak pressure appeared in the central region of the heel with the value of 215kPa (averaged over area of $10\times19mm^2$). This is comparable with the result of Pedar system measurement with the value of 203kPa at a very similar location (5.58% maximum peak plantar pressure).

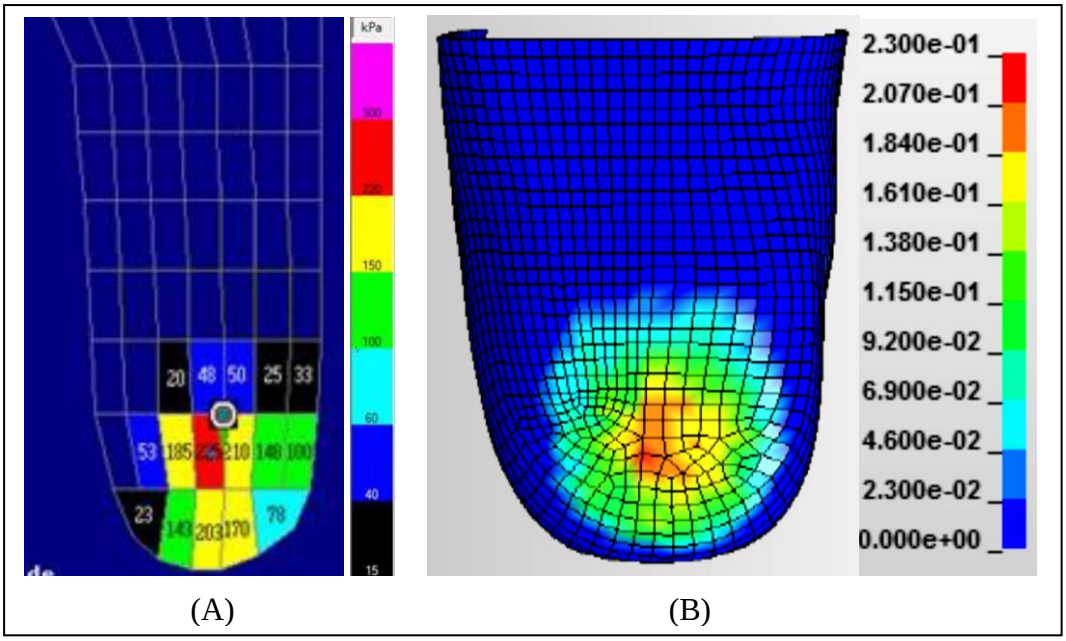

(A) (B)

Figure 6.15: Plantar pressure distribution of the heel with rotation angle of 17.6º under 315N: (A) Pedar pressure insole measurement; (B) FE model prediction.

6.3.3 Viscoelastic Material Properties of the Heel Pad Sub-layers

The purpose of this section is to provide the initial and final estimates of viscoelastic material properties for the macro-chamber, micro-chamber and skin layers based on inverse FEA. This starts with providing initial estimates for the macro-chamber and micro-chamber layers obtained from one and two-layer FE models. Then, the final estimates of the viscoelastic properties of the macro-chamber, micro-chamber and skin layers, determined from the complete three-layer FE model, are given.

6.3.3.1 Initial Viscoelastic Material Properties of the Macro-chamber Layer

The initial viscoelastic material properties of the macro-chamber layer and errors obtained at this stage are listed in Table 6.5. A convergence was reached with RMS errors of 9.24 and 5.66N for loading and unloading periods respectively after 16 iterations. The difference between the peak forces was measured 1.53N.

Table 6.5: The viscoelastic material properties of the macro-chamber layer determined from one-layer model. Values in parenthesis indicate the percentage of the error over maximum force.

	G (MPa)	β (ms^{-1})	RMS error Loading (N)	RMS error Unloading (N)	Difference between peak forces (N)
Macro-chamber	0.11	0.08	9.24 (8.4%)	5.66 (5.1%)	1.53 (1.4%)

Figure 6.16 shows the force-strain responses of the macro-chamber layer predicted by the one-layer FE model during the loading-hold-unloading cycle for the first and the final iterations. The RMS errors for the loading and unloading periods were reduced by 1.93 and 0.34N from the first iteration to the final iteration respectively. The difference between peak forces was reduced by 28.43N.

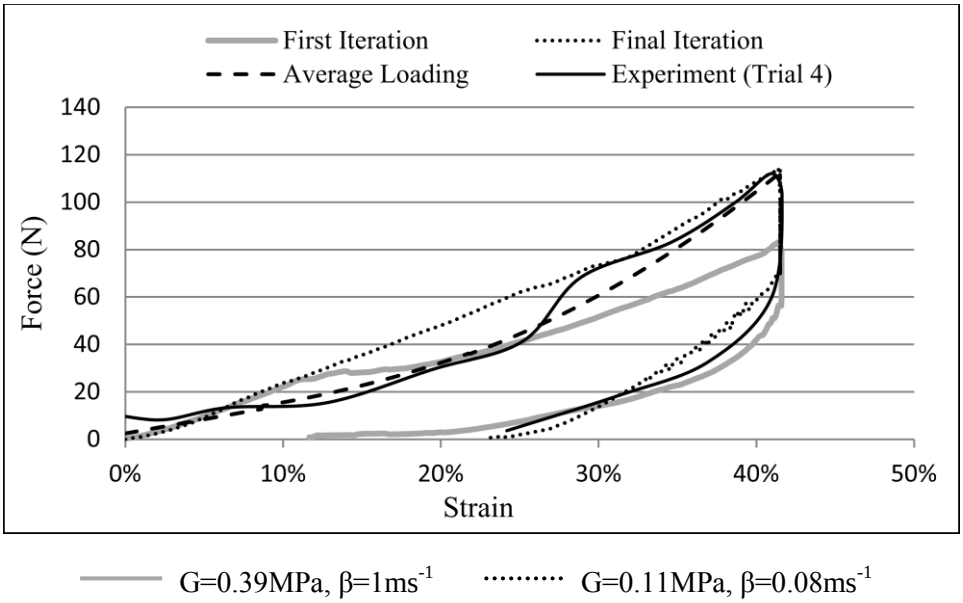

Figure 6.16: Force-strain relation of the macro-chamber layer predicted by the one-layer FE model.

At first iteration the behaviour of the macro-chamber could be predicted during loading up to 25% strain with RMS error of less than 4.35N. Then, the RMS error of loading was elevated by increasing the strain due to underestimation of the behaviour of the macro-chamber at high strains. In the final iteration, the maximum error was obtained for the middle portion of the loading period. While the experimental results showed the nonlinear behaviour for the macro-

chamber during the loading period, the FE model predicted almost linear behaviour. This might be because of the Ogden material model in which the spring of the viscoelastic overstress element was linear (see Chapter 4).

6.3.3.2 Initial Viscoelastic Material Properties of the Micro-chamber Layer

First estimates for the viscoelastic material properties of the micro-chamber layer and second estimates for the viscoelastic material properties of the macro-chamber layer and errors, obtained from the two-layer FE model, are provided in Table 6.6. Figures 6.17 and 6.18 show the force-strain responses of the macro-chamber layer and the total macro-chamber and micro-chamber predicted by the two-layer FE model during the loading-hold-unloading cycle for the first and the final iterations.

Table 6.6: The viscoelastic material properties of the micro-chamber and macro-chamber layers determined from the two-layer model. Values in parenthesis indicate the percentage of the error over the maximum force.

	G (MPa)	β (ms^{-1})	RMS error Loading (N)	RMS error Unloading (N)	Difference between peak forces (N)	Difference between max strains
Micro-chamber	0.46	0.06	10.82 (10.1%) (two-layer model)	4.65 (4.32%) (two-layer model)	4.06 (3.78%) (two-layer model)	-
Macro-chamber	0.14	0.06	9.24 (8.6%)	2.19 (2.04%)	-	0.4

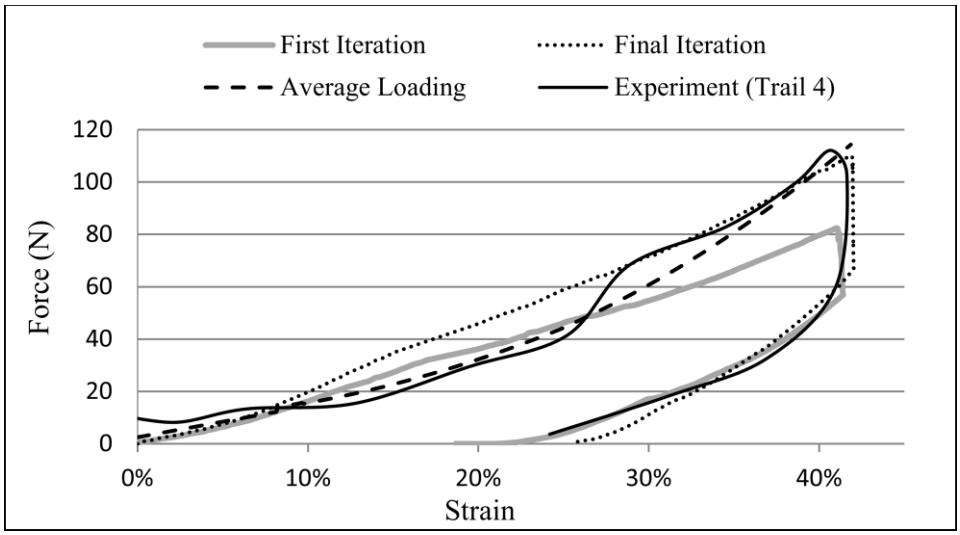

Macro-chamber: G=0.11MPa, β=0.08ms^{-1} ..... Macro-chamber: G=0.14MPa, β=0.06ms^{-1}
Micro-chamber: G=0.11MPa, β=0.08ms^{-1} Micro-chamber: G=0.46MPa, β=0.06ms^{-1}

Figure 6.17: Force-strain relation of the macro-chamber layer predicted by the two-layer FE model.

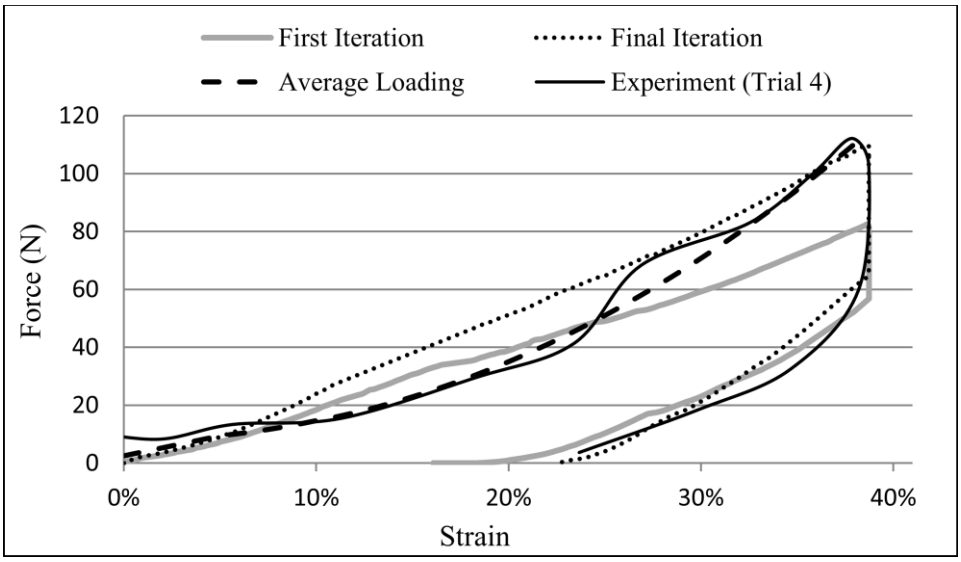

Macro-chamber:G=0.11MPa, β=0.08ms^{-1} ..... Macro-chamber:G=0.14MPa, β=0.06ms^{-1}
Micro-chamber:G=0.11MPa, β=0.08ms^{-1} Micro-chamber:G=0.46MPa, β=0.06ms^{-1}

Figure 6.18: Force-strain relation of the two-layer FE model at 225mm/s.

The first iteration predicted the behaviour of the macro-chamber and the two-layer FE model under loading up to 25% strain with small errors of 3.28 and 4.34N respectively. However, it underestimated the loading responses of the macro-chamber and two-layer model at high strains. Similar to the results of the one-layer FE model, at the final iteration the maximum error was obtained for the middle portion of the loading period (10-30% strain). While the

experimental data showed the nonlinear behaviour of the tissues during the loading period, the FE model simulated their response with almost linear behaviour. As previously proposed, this might be due to the linear viscoelastic overstress element in the Ogden material model. Although the macro-chamber and micro-chamber have different viscoelastic characteristics due to the amount of their liquid contents, the same decay constant was selected for them for simplicity.

6.3.3.3 Final Viscoelastic Material Properties of the Macro-chamber, Micro-chamber and Skin Layers

The final estimates for the viscoelastic material properties of the macro-chamber, micro-chamber and skin and the corresponding errors, obtained from the complete three-layer FE model, are listed in Table 6.7. The force-strain responses of the macro-chamber, micro-chamber, and the three-layer FE model predicted by the complete three-layer FE model are also shown in Figures 6.19-6.21 for the first and final iterations.

Table 6.7: The viscoelastic material properties of the heel pad sub-layers determined from three-layer complete model. Values in parenthesis indicate the percentage of the error over the maximum force.

	G (MPa)	β (ms^{-1})	RMS error Loading (N)	RMS error Unloading (N)	Difference between peak forces (N)	Difference between max strains
Skin	0.42	0.12	19.88 (17.1%) (three-layer model)	2.15 (1.8%) (three-layer model)	0.54 (0.4%) (three-layer model)	-
Micro-chamber	0.3	0.12	16.74 (14.4%)	7.44 (6.4%)	-	0.2
Macro-chamber	0.24	0.12	16.91 (14.5%)	3.59 (3.1%)	-	-

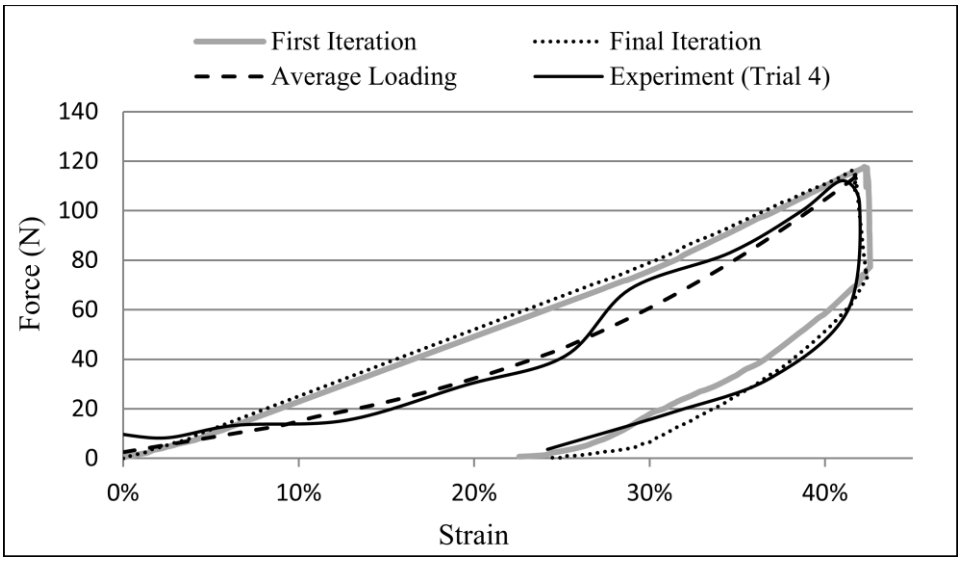

Macro-chamber: G=0.14MPa, β=0.06ms^{-1} Macro-chamber: G=0.24MPa, β=0.12ms^{-1}
Micro-chamber: G=0.46MPa, β=0.06ms^{-1} Micro-chamber: G=0.3MPa, β=0.12ms^{-1}
Skin: G=0.46MPa, β=0.06ms^{-1} Skin: G=0.42MPa, β=0.12ms^{-1}

Figure 6.19: Force-strain relation of the macro-chamber layer predicted by the three-layer FE model.

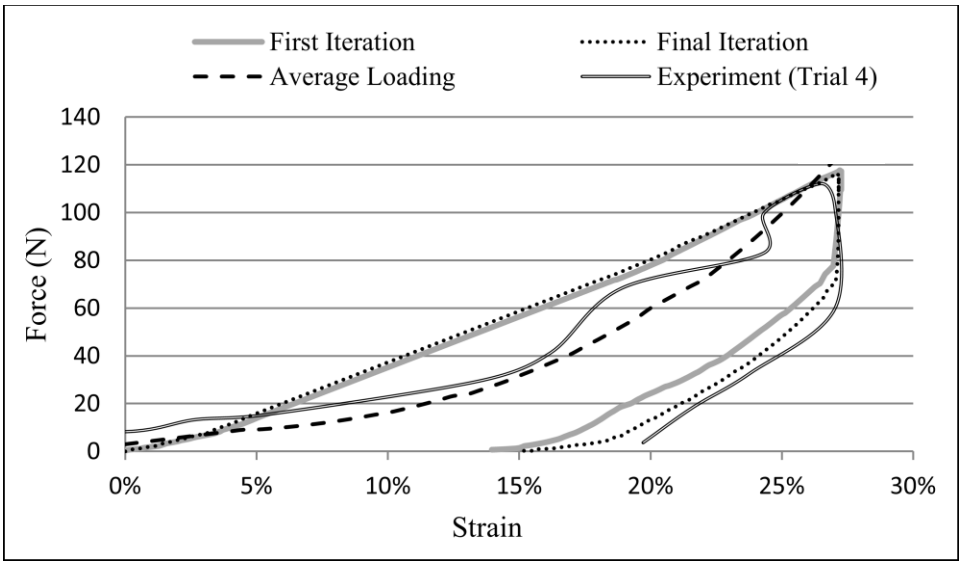

Macro-chamber: G=0.14MPa, β=0.06ms^{-1} Macro-chamber: G=0.24MPa, β=0.12ms^{-1}
Micro-chamber: G=0.46MPa, β=0.06ms^{-1} Micro-chamber: G=0.3MPa, β=0.12ms^{-1}
Skin: G=0.46MPa, β=0.06ms^{-1} Skin: G=0.42MPa, β=0.12ms^{-1}

Figure 6.20: Force-strain relation of the micro-chamber layer predicted by the three-layer FE model.

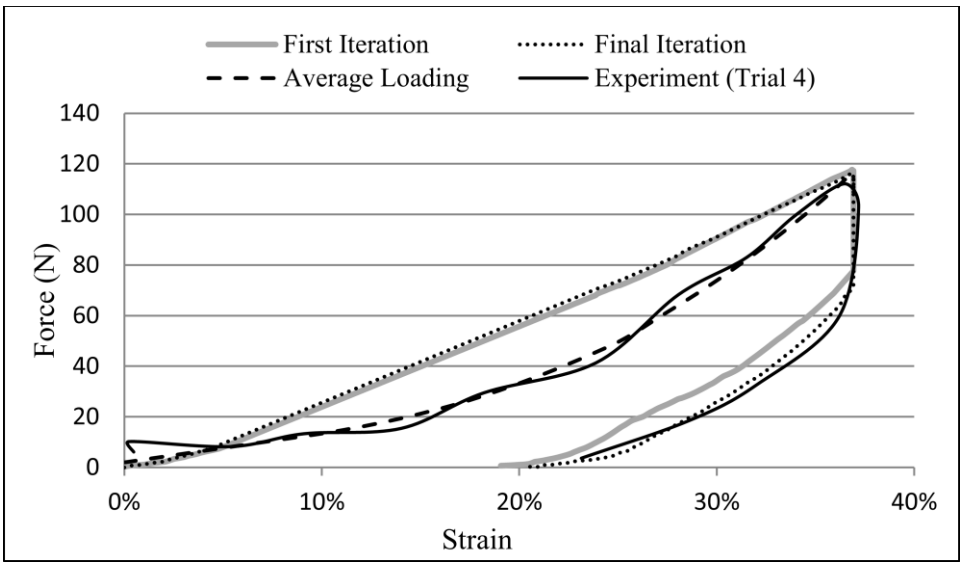

Macro-chamber: G=0.14MPa, β=0.06ms^{-1}
Micro-chamber: G=0.46MPa, β=0.06ms^{-1}
Skin: G=0.46MPa, β=0.06ms^{-1}

Macro-chamber: G=0.24MPa, β=0.12ms^{-1}
Micro-chamber: G=0.3MPa, β=0.12ms^{-1}
Skin: G=0.42MPa, β=0.12ms^{-1}

Figure 6.21: Force-strain relation of the three-layer FE model at 225mm/s.

From the first iteration to the final iteration, there was not much difference in the behaviour of the tissues during loading periods. However, the final iteration could better predict behaviours of the tissues during the unloading period. The RMS errors for the unloading period were reduced by 6.99N for the heel pad. Similar to the results obtained from one and two-layer FE model, the maximum difference between the predicted results and experimental data could be found in the middle portion of the loading period. It seems that the FE model was unable to simulate the nonlinear elastic behaviour of the heel pad sub-layers at high velocity during the loading period. To simplify the model, the identical decay constant was selected for heel pad sub-layers.

In two studies the viscoelastic material properties were found for the heel fat pad and skin layers. Identical viscoelastic properties were determined for the fat pad and skin. Values of 1 and 2ms have been reported as time constants (τ) and value of 0.99 has been found as relaxation coefficient (g) in different cases (10, 125). In other case the value of 0.5s was obtained as the time constant of the heel fat pad based on unconfined compression tests on

isolated fat pads (12). The time constant is the inverse of decay constant (β). In this study, the time constant of ~8ms was determined for all three heel pad sub-layers which is comparable to 1 and 2ms provided in the literature. Since the skin layer is stiffer than the other heel pad sub-layers (macro-chamber and micro-chamber) due to difference in liquid content, the skin layer is expected to have different time constant than other two layers. However, to simplify the model the same time constant was selected for the skin as the macro-chamber and micro-chamber layers. Modeling skin layer as only hyperelastic material, not considering its viscoelastic characteristics, might provide better results for simulating the heel pad behaviour.

Different relaxation modulus was used in different FEA software. For instance, Ls-Dyna used shear relaxation modulus (G) and ABAQUS used relaxation coefficient (g) which equals to G/G_0. G_0 is instantaneous shear relaxation modulus and equals to $G_\infty+G$. G_∞ is the long term shear relaxation modulus and it is related to the hyperelastic element of the model. Therefore, based on the above relations: $0 \leq g \leq 1$. When $g \rightarrow 1$ means that the material shows more viscous characteristics and when $g \rightarrow 0$ means that the material shows more elastic characteristics. Having the initial shear modulus of the skin, micro-chamber and macro-chamber (initial shear modulus$= \frac{1}{3}$ Elastic modulus), the relaxation coefficient (g) is approximately calculated for these layers as $\frac{0.42}{(>1.266)+0.42}$, $\frac{0.3}{(>0.233)+0.3}$ and $\frac{0.24}{(>0.08)+0.24}$ respectively. This approximate calculations show that from macro-chamber to skin layer, the elastic characteristic of the materials increases.

6.3.4 Validation of the Viscoelastic FE Model

Two series of rapid tests (loading-hold-unloading cycle at constant velocity of 141mm/s with 26ms hold time before unloading and sinusoidal loading with maximum velocity of 300mm/s) were used to evaluate the final viscoelastic FE model in simulation of the heel pad behaviour under rapid loadings. Two RMS errors for the loading and unloading periods and the

difference between peak forces were measured for 5 trials of each loading conditions. Table 6.8 provides errors obtained between the predicted results and the experimental results determined from rapid compression test of loading-hold-unloading cycle at 141mm/s. The experimental and predicted force-strain response of the heel pad for 5 different trials (different maximum strains) are shown in Figures 6.22-6.26. In the following figures, T stands for trial.

Table 6.8: Errors measured between the predicted results and the experimental data obtained at 141mm/s for different 5 trials with different maximum strains. Values in parenthesis indicate the percentage of the error over the maximum force.

	Maximum Strain	RMS error Loading (N)	RMS error Unloading (N)	Difference between peak forces (N)
Trial 1	38.60%	15.20 (14.1%)	3.44 (3.2%)	0.61 (0.5%)
Trial 2	39.20%	15.24 (13.8%)	3.85 (3.5%)	1.77 (1.6%)
Trial 3	38.60%	15.21 (14.1%)	2.94 (2.7%)	0.62 (0.5%)
Trial 4	37.90%	15.39 (14.7%)	1.69 (1.6%)	0.66 (0.6%)
Trial 5	36.90%	14.03 (14.6%)	5.01 (5.2%)	1.84 (1.9%)

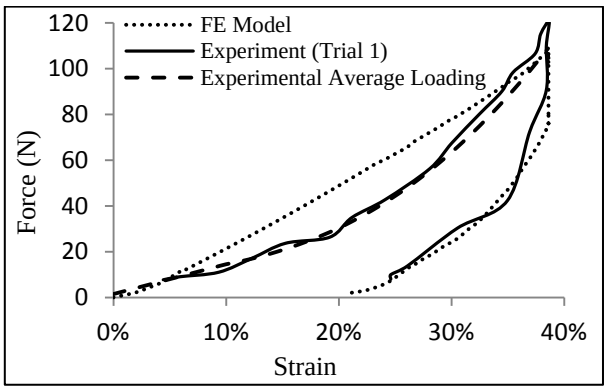

Figure 6.22: Heel pad behaviour at 141mm/s (T1)

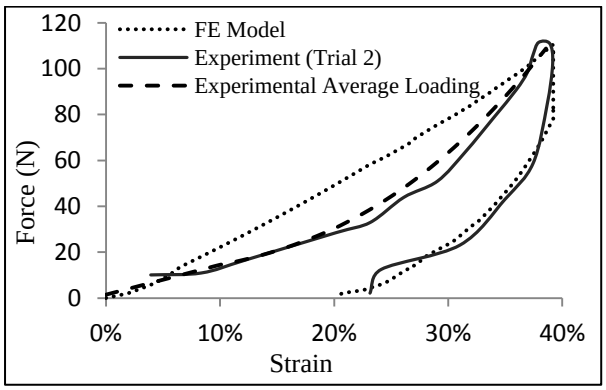

Figure 6.23: Heel pad behaviour at 141mm/s (T2)

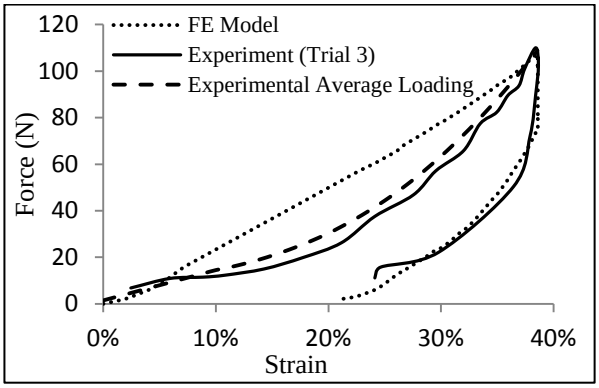

Figure 6.24: Heel pad behaviour at 141mm/s (T3)

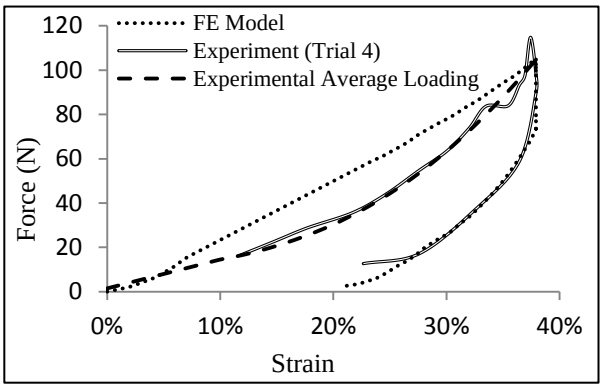

Figure 6.25: Heel pad behaviour at 141mm/s (T4)

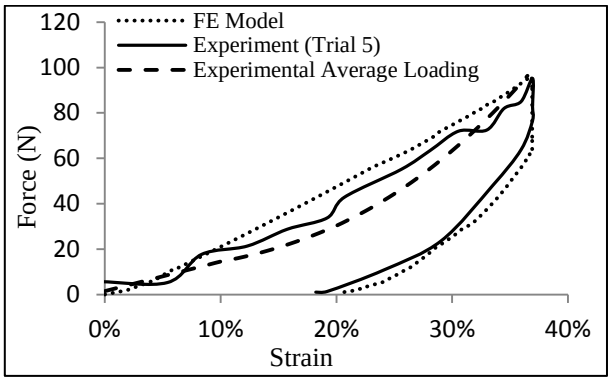

Figure 6.26: Heel pad behaviour at 141mm/s (T5)

Table 6.8 shows that the errors were comparable to those obtained for the heel pad during the rapid tests at loading-hold-unloading cycle at velocity of 225mm/s. For the series of rapid tests at 225mm/s, RMS errors for loading, unloading periods and the difference between peak forces ranged between 18.02-19.96N, 2.08-5.55N and 0.31-6.65N respectively. This demonstrates that the model could work with comparable performance at different constant rapid loading velocities. Similar to the predicted results obtained from the rapid test at 225mm/s, the maximum error obtained from rapid test at 141mm/s occurred during the middle portion of the loading period as it is due to more linear like response of the model during nonlinear *in-vivo* behaviour.

The RMS errors measured for unloading period are less than those measured for the loading period because of two reasons. Firstly, the experimental responses of the heel pad and its sub-layers show that during the hold time, the force experienced in the heel pad and sub-layers

was decreased and so the tissues did not show nonlinear behaviour during the unloading period as great as the loading period. Therefore the viscoelastic model could better simulate the unloading behaviour of the tissues. Secondly, during the unloading period in both physical testing and FE simulation, the materials lost their contact with the load cell at around 25% strain of the heel pad because the tissues recovered slower than the indenter velocity. If more data were available, greater RMS errors might be calculated during the unloading period.

Table 6.9 provides errors obtained between the predicted results and the experimental results determined from sinusoidal loading with 300mm/s maximum velocity. The predicted and experimental force-strain responses of the heel pad for each trial are shown in Figures 6.27-6.31.

Table 6.9: Errors measured between the predicted results and the experimental data obtained at sinusoidal loading for different five trials with different maximum strains. Values in parenthesis indicate the percentage of the error over the maximum force.

	Maximum Strain	RMS error Loading (N)	RMS error Unloading (N)
Trial 1	35.10%	8.33 (8.9%)	4.62 (4.9%)
Trial 2	35.70%	5.76 (5.9%)	5.61 (5.8%)
Trial 3	37.60%	8.29 (7.9%)	5.47 (5.2%)
Trial 4	38.60%	5.09 (4.5%)	5.3 (4.7%)
Trial 5	38.60%	7.94 (7.1%)	2.95 (2.6%)

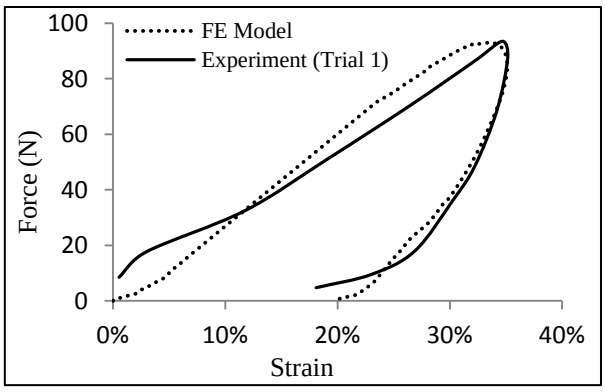

Figure 6.27: Heel pad behaviour under sinusoidal loading (T1)

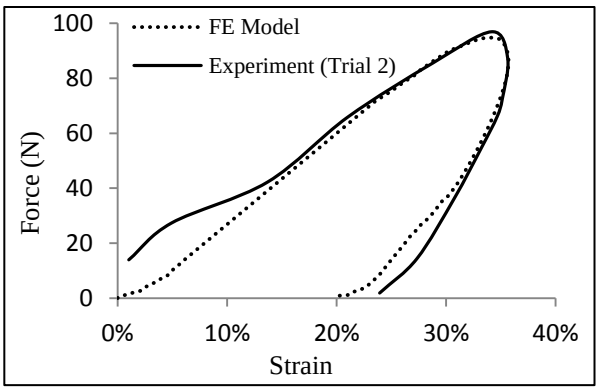

Figure 6.28: Heel pad behaviour under sinusoidal loading (T2)

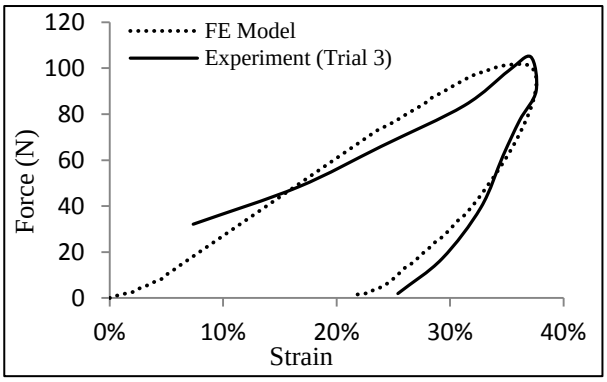

Figure 6.29: Heel pad behaviour under sinusoidal loading (T3)

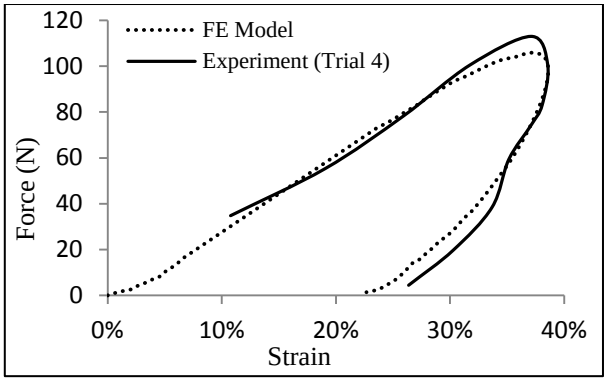

Figure 6.30: Heel pad behaviour under sinusoidal loading (T4)

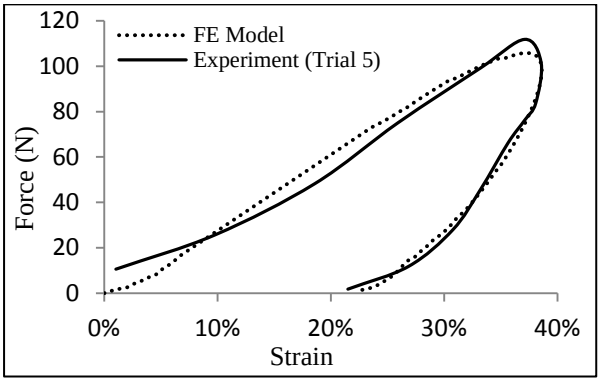

Figure 6.31: Heel pad behaviour under sinusoidal loading (T5)

Table 6.9 indicates that for 5 trials of rapid sinusoidal loading, RMS errors for the loading period were less than those measured at rapid tests at 225mm/s and 141mm/s. Since the experimental data during sinusoidal loading did not show nonlinear behaviour as much as those obtained under rapid constant loading, the FE model could better simulate the behaviour of the heel pad. Therefore, data used to test the model is important and can over/underestimate the model accuracy. A comparison between the RMS errors of the loading period obtained from different loading protocols suggests various loading scenarios are needed for estimation of the material properties and model validation. The RMS errors for the unloading period are comparable with the range reported for the rapid test at 225mm/s (2.08-5.55N).

Table 6.10 shows the errors for the loading and unloading periods and difference between the peak forces for the three-layer heel pad model, micro-chamber and macro-chamber layers for

4 trials with different maximum strain under 225mm/s. These are the data which were not used for material properties estimation.

Table 6.10: The errors measured between the predicted results and the experimental data for different 4 trials with different maximum strains. Values in parenthesis indicate the percentage of the error over the maximum force.

		RMS error Loading (N)	RMS error Unloading (N)	Difference between peak forces (N)
Trial 1 with max strain of 36.2%	Heel pad	19.96 (17.8%)	3.91 (3.5%)	2.78 (2.5%)
	Micro-chamber	16.84 (15.2%)	4.48 (4.0%)	-
	Macro-chamber	16.98 (15.3%)	6.66 (6.0%)	-
Trial 2 with max strain of 37.5%	Heel pad	18.02 (15.9%)	3.05 (2.7%)	6.65 (5.8%)
	Micro-chamber	14.78 (13.1%)	6.02 (5.3%)	-
	Macro-chamber	14.83 (13.1%)	10.62 (9.3%)	-
Trial 3 with max strain of 37.7%	Heel pad	18.03 (15.7%)	2.08 (1.8%)	6.08 (5.2%)
	Micro-chamber	14.76 (12.8%)	3.74 (3.2%)	-
	Macro-chamber	14.75 (12.8%)	4.88 (4.2%)	-
Trial 5 with max strain of 37.2 %	Heel pad	19.78 (16.9%)	5.55 (4.7%)	0.31 (0.2%)
	Micro-chamber	16.7 (14.3%)	10.10 (8.6%)	-
	Macro-chamber	16.88 (14.5%)	5.08 (4.3%)	-

Table 6.10 indicates that the maximum differences between the predicted results and the experimental data occurred in the loading period. Depending upon the unloading behaviours of the heel pad, macro-chamber and micro-chamber layers at different experimental trial the RMS error for the unloading period fluctuated between 1.8 to 9.3% maximum force which were comparable to those obtained between the predicted and experimental results of Trail 4, which was used for material properties estimation (1.8 to 6.4% maximum force). The results indicate that the model can predict behaviours of the heel pad and its sub-layers at 225mm/s up to different maximum strains comparable to the performance of the model during material properties estimation.

6.3.5 Parametric Studies

In agreement with the parametric study conducted in Chapter 4, the results indicate that the variation of stiffness of muscle tissue with Young's modulus of 1.08, 14 and 55MPa representing its low, medium and high stiffness, respectively, only had a small influence on the heel pad responses. The RMS errors showed almost 50% increase compared to the values obtained for the model with the heel pad sub-layers being assigned with material properties from the literature. However the differences are still insignificant and the influence of the variation of the muscle tissue stiffness in the accepted range is unimportant. The responses of the heel pad at different situations are shown in Figure 6.32 and the difference between force-strain results represented by RMS error is provided in Table 6.11.

Table 6.11: Difference between heel pad responses with different muscle tissue stiffness.

Muscle Stiffness	Low vs Medium	Low vs High	Medium vs High
RMS error (N)	1.15	1.08	0.74
RMS error (%Max force)	1.38	1.30	0.89

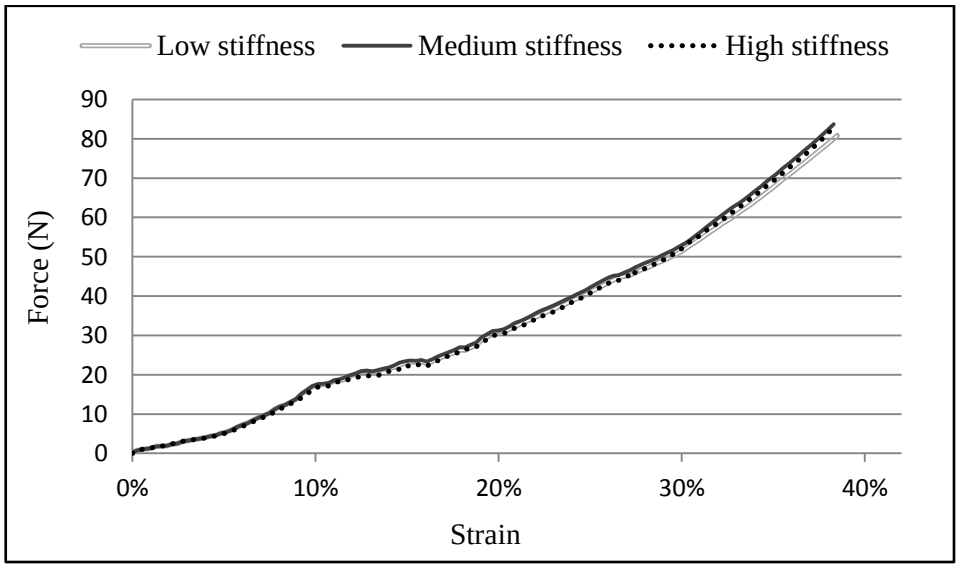

Figure 6.32: Effect of changing the stiffness of the muscle tissue

The predicted force-strain relationship of the heel pad for different stiffness of the plantar fascia (10, 100, 250, 350 and 500MPa) shows that the change of the material properties of the

plantar fascia in the accepted range has small effect on the heel pad responses. According to the results, the maximum difference occurs between reactions of the heel pad with lowest and highest stiffness of the plantar fascia with RMS error of 1.24% maximum force. This value is comparable with the result obtained for the model before estimation of the heel pad sub-layer parameters (RMS error<1.5% max force). Figure 6.33 shows the force-strain responses of the heel pad with different stiffness of the plantar fascia.

1:E=500MPa 2:E=350MPa 3:E=250MPa 4:E=100MPa 5:E=10MPa

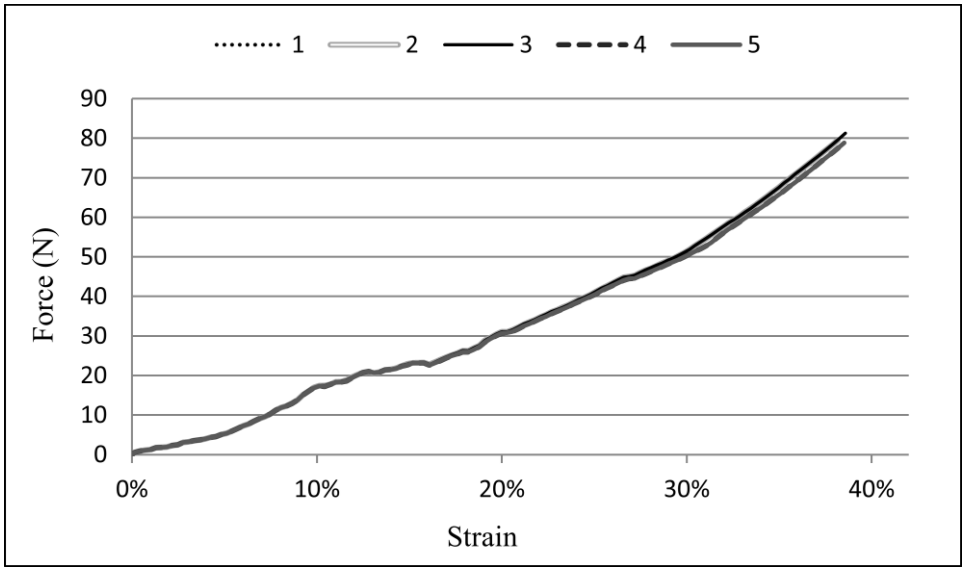

Figure 6.33: Effect of changing the stiffness of the plantar fascia

The varying the angle of rotation of the foot for ±1º, ±5º and ±10º showed to have small influence on the heel pad responses. The results obtained at this stage are comparable with those obtained for the model with material properties derived from the literature for the heel pad sub-layers in Chapter 4. Results indicate that change of the angle of rotation of the foot for 1 degree has small effect on the heel pad response (RMS error<2.5% max force). Extended changes to the angle of rotation increase the effect of the position of the heel on the heel pad responses (RMS error<4% max force). By increasing the angle of rotation, less material is compressed and therefore the force decreases. In low strains, approximately equivalent amount of material is compressed at different rotation of angle. The difference between the force-strain results obtained for the model with reference angle (17.6º) and

different angles are provided in Table 6.12. Figures 6.34-6.36 show the responses of the heel pad at different position.

Table 6.12: Difference between the force-strain responses of the heel pad at reference angle (17.6º) and different positions.

Angle of rotation	18.6º (+1º)	16.6º (-1º)	22.6º (+5º)	12.6º (-5º)	27.6º (+10º)	7.6º (-10º)
RMS error (N)	1.48	1.86	2.15	2.06	2.89	2.13
RMS error (%Max force)	1.86	2.33	2.69	2.58	3.62	2.67

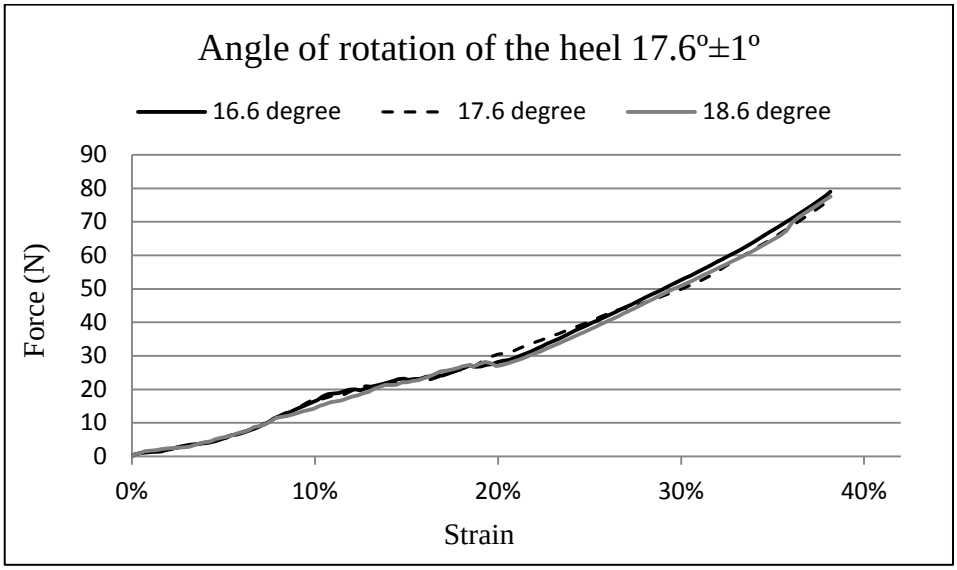

Figure 6.34: Effect of varying the angle of rotation of the FE model for ±1º

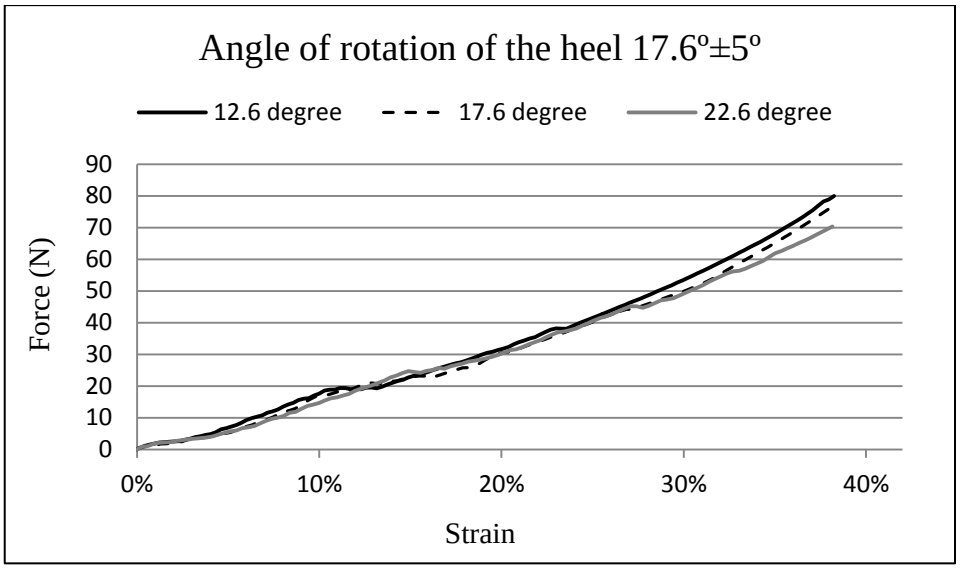

Figure 6.35: Effect of varying the angle of rotation of the FE model for ±5º

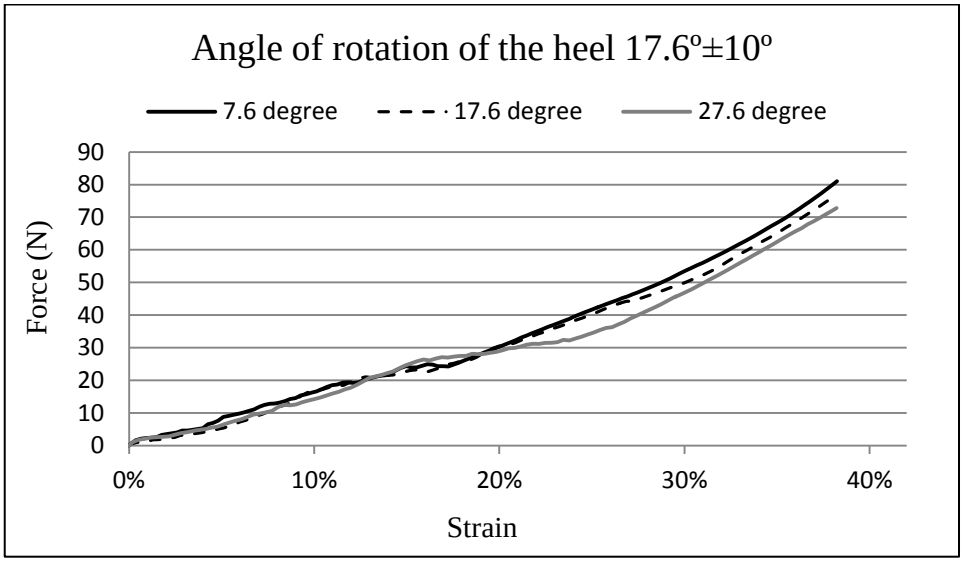

Figure 6.36: Effect of varying the angle of rotation of the FE model for ±10º

6.4CONCLUSIONS

The aim of this chapter was to use the force-strain experimental data of the heel pad and sub-layers, obtained at slow and rapid compression tests in Chapter 5, as input to inverse FEA to estimate the hyperelastic and viscoelastic material properties of the heel pad sub-layers using the FE model of the heel region, developed in Chapter 4. Two hyperelastic Ogden model material properties (μ and α) were estimated for each of the heel pad sub-layers. The force-

strain responses of the macro-chamber, micro-chamber and heel pad, obtained at constant velocity of 5mm/s, were entered into inverse FEA in three stages to determine their material parameters. During inverse FEA, RMS error and difference between maximum strains were used as objective functions. Two hyperelastic material parameters of each layer were estimated by being iteratively adjusted for 115 iterations until the objective functions were converged to the optimum points and no useful reduction of the RMS errors was observed in subsequent iterations. This process was performed based on iterative curve fitting rule derived for this project. It is acknowledged that the process of determination of the material properties is difficult to repeat and to remove the errors this process should be made into an algorithm. The loaded thickness of the heel pad and the peak plantar pressure under specific load were used to validate the hyperelastic FE model. The MRI was taken from the foot of **Subject 1**, whose foot structure the FE model was based upon. A brace was designed to apply a specific load under the heel area during the MR imaging. The FE model was subjected to the same load and the predicted loaded thickness were compared to the MRI data. For the second validation, the predicted plantar pressure was compared with Pedar pressure measurements. The results of both validation methods showed good agreement between experimental and modeling results.

After estimation of the final values for the hyperelastic material properties of the heel pad sub-layers, two optional viscoelastic parameters (G and β) of the Ogden material model in Ls-Dyna were added to the model for each of the heel pad sub-layers. The experimental force-strain responses of the macro-chamber, micro-chamber and the heel pad, obtained during loading-hold-unloading cycle at constant velocity of 225mm/s and 26ms hold time before unloading, were used to determine the viscoelastic parameters. The viscoelastic parameters were estimated by being changed for 87 iterations until the difference between the experimental data and the predicted results was minimised and no significant changes were

observed RMS errors of loading and unloading periods and difference between the peak forces and difference between maximum strains. The maximum error was obtained at the middle portion of the loading period where the Ogden material model was not able to simulate the nonlinear behaviour of the tissue accurately.

The viscoelastic behaviour of the FE model was validated by comparing experimental and predicted force-strain responses of the heel pad during the loading-hold-unloading periods at constant velocity of 141mm/s and hold time for 26ms and during sinusoidal loading with the maximum velocity of 300mm/s. Errors obtained for the test at velocity of 141mm/s were in the ranges reported for heel pad during the test at displacement rate of 225mm/s. The model could better simulate the viscoelastic behaviour of the heel pad particularly during unloading period under sinusoidal loading. Moreover, the viscoelastic behaviours of the heel pad, micro-chamber and macro-chamber were validated by comparing the predicted FE results with those obtained for 4 trials (other than Trial 4 which was used for material properties estimation) under rapid test at 225mm/s up to different maximum strains.

This project was successful in estimation of the hyperelastic and viscoelastic material properties of the macro-chamber, micro-chamber and skin layers in this stage. Inverse FEA method was used to determine the material properties using anatomically detailed FE model of the heel area and *in-vivo* experimental data. The hyperelastic model showed to have the capability in predicting behaviour of the heel pad with error of 6.55% maximum loaded thickness. The viscoelastic model could simulate the heel pad behaviour with higher RMS error of 13.8-17.8% and 1.6-5.2% maximum force for loading and unloading periods, respectively and 0.2-5.8% maximum difference in peak forces at rapid constant loadings. The viscoelastic model could better simulate the heel pad behaviour under sinusoidal loading with RMS error of 4.5-8.9% and 2.6-5.8% maximum force for loading and unloading periods, respectively.

At the end of this chapter, the parametric studies, performed in Chapter 4 to study the effect of the stiffness of the muscle tissue and plantar fascia and also the effect of the angle of rotation of the foot on the heel pad responses, were repeated while the final estimates for the heel pad sub-layers were assigned to the corresponding layers. In agreement with the results of these studies obtained at Chapter 4, the heel pad responses were generally insensitive (RMS error<1.5% max force) to variation of the stiffness of the muscle tissue and plantar fascia in the commonly accepted ranges. The change in angle of rotation showed to have small influence on the heel pad responses (RMS error<4% max force). These results are comparable to those obtained in Chapter 4.

The final estimates for material properties of the heel pad sub-layers obtained in this chapter were assigned to the corresponding layers. Then the FE model of the heel region was used in Chapter 7 to show some applications of the model in foot and footwear studies.

7. Chapter Seven:

MODEL APPLICATIONS

7.1 INTRODUCTION

The aim of this chapter is to show some applications of the human heel pad model developed in previous chapters with anatomically detailed geometry (Chapter 3 and 4) and appropriate material properties obtained for the heel pad sub-layers (Chapter 6). Biomechanical aspects of the heel pad and its interaction with foot support is still under investigation particularly when there is a disorder. Various clinical devices have been developed in order to obtain a quantitative evaluation of the heel pad behaviour during loading. However, data presented in the literature are wide-ranging, even for non-pathological cases. Using different experimental techniques, loading protocol, geometrical factors and material properties of the tissue may contribute to the inconsistencies in published data. Since some of the factors such as geometrical factors and gait patterns (loading protocol) cannot be controlled in clinical setting, the computational simulation of the heel pad could be used in order to provide information, which allows the description of the tissue. FE models of the human foot have been developed to overcome the limitation of clinical and cadaveric studies. However, majority of them have some geometric and material limitations, which were reviewed in Chapter 2. At this stage of this project with having anatomically detailed model of the heel pad and material properties determined for the heel pad sub-layers, it would be reasonable to show some of this model applications. Note that the model was validated against responses of the heel pad under loading (Chapter 6). The hyperelastic model could predict the deformation and plantar pressure of the heel pad with about 7% and 6% error, respectively. In the literature several FE models of the foot with validation result of 6-11% error, were used for insole designs and investigation of the heel pad behaviour at different loading and geometrical conditions (7, 76, 88). Hence, as the errors of this project are comparable to those in the literature, the model can be used for similar applications.

This chapter is divided into two sections: First, the applications of the model in studying the biomechanical aspects of the human heel pad; second, the applications of the model in footwear design research.

1) The first section divides into two case studies.

- In the first case study, some applications of the model in investigation of heel pad mechanical properties are shown. The FE model developed in this project is used to simulate different experimental designs and different heel geometry, to show how these can affect the force-displacement and force-strain heel pad responses.
- In the second case study, the robustness of the FE model in the estimation of the material properties of the heel pad sub-layers of another heel is evaluated.

2) In recent years, an increasing number of FE models have been used in footwear design research to reduce the cost and time required compared to physical experiments. The second section of this chapter uses the FE model within the footwear design field.

7.2 APPLICATIONS OF THE MODEL IN STUDYING THE BIOMECHANICAL ASPECTS OF THE HEEL PAD

Several research studies have been conducted and reported in the literature on the investigation of the heel pad mechanical properties based on the force-displacement or force-strain relationships. Although the stress-strain relationship can better represent the heel pad behaviour under loading than the force-strain or force-displacement results, it is not always possible to measure the contact stress during experiments because of the difficulty in measuring fast changing contact areas. The heel pad experimental data (e.g. force-strain, force-displacement, stress-strain, and stress-displacement) available in the literature were obtained at different experimental conditions (e.g. loading rate) and from heel pads with different geometries. Therefore, in the first case study, the FE model developed in this project is used to simulate different experimental designs and different heel geometry, to show how

these can affect the force-displacement and force-strain heel pad responses. In the second case study, the robustness of the FE model in determination of the material properties of the heel pad sub-layers of another heel is evaluated. This is undertaken to investigate how transferable the model may be to other individuals.

7.2.1 Effects of *In-vivo* Conditions (Case Study 1)

According to the published literature, the experimental conditions and the heel pad geometry affect the heel pad responses to the loading (10, 13, 59, 126). The FE model was used to investigate effects of different experimental and heel geometrical factors on the heel pad responses under loading. These factors were divided into some groups and sub-groups as it can be seen in the hierarchy chart 7.1.

Chart 7.1: The division of the effective factors on the heel pad responses under loading.

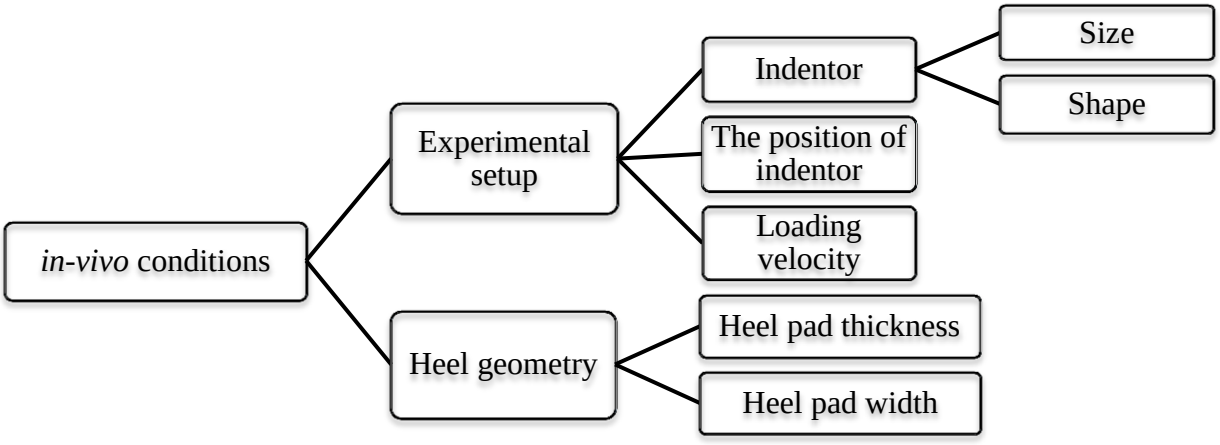

7.2.1.1 Effects of Experimental Setup Conditions

Researchers have used different experimental methods to investigate the biomechanical responses of the heel pad. For instance, indenters with different sizes and shapes have been used to compress the heel pad while these factors have been shown to produce different data (59, 126). Depends on the experimental setup the position of the indenter under the heel pad might be another factor affecting the obtained results. Moreover, because of the viscoelastic nature of the heel pad, the influence of the loading velocity on the heel pad behaviour is

inevitable. The FE model provides the opportunity to investigate the effect of the experimental setup on the heel pad responses systematically. The aim of this stage was to provide information on how the experimental setup factors (indenter size and shape, position of the indenter and loading velocity) affect the heel pad mechanical behaviour.

- **Methods**

The **size and shape of indenter** were the first experimental setup factors that were investigated. For this purpose, the developed hyperelastic FE model was used under loading at constant velocity of 5mm/s. The coefficient of friction between the heel pad tissue and the ground was set to 0.6 (109). The heel pad was subjected to the loading up to displacement of 6mm (38% strain) using flat and spherical indenters with diameters of 30 and 40mm (Figure 7.1). These sizes are close to those used in the literature (5, 6, 126).

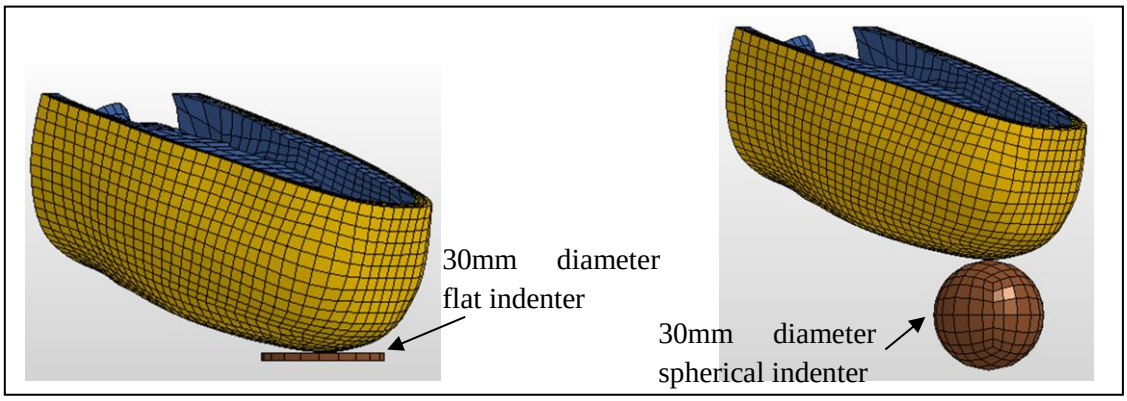

Figure 7.1: The flat and spherical indenter.

Since the mesh size of the model was obtained for the purpose of compression using a large indenter, indenting the model with a small indenter might cause mesh distortion around the indenter edges and inaccuracy in the results. Therefore, diameters of 30 and 40mm were selected for the indenters to reduce the resultant error, while the effect of the indenter size was investigated. The influence of the **position of the indenter** on the heel pad responses was investigated. Two flat indenters with diameters of 30mm (less than the maximum heel width) and 60mm (larger than the maximum heel width) were used to apply compression to the hyperelastic FE model at constant speed of 5mm/s. The location of the indenter under the

calcaneus tuberosity was changed by displacing it 7mm in the medial and lateral directions to investigate the effect of even small changes of the indenter position on the experimental data. The static coefficient of friction was 0.6 between the indenter and the tissue. The resultant contact force was measured between the indenter and the heel pad.

The **loading velocity** was the last physical factor that its effects on the heel pad responses were studied. The viscoelastic FE model was subjected to sinusoidal cyclic compression at five frequencies, 7.5, 10, 13, 15.5 and 18.5Hz. At these frequencies, the loading of the tissue was started at peak velocities of 270, 370, 470, 570 and 670mm/s and decreased to 0mm/s at 6mm deformation (38% strain) before unloading was started. These velocities are comparable to the vertical landing velocities of the heel during the slow and quick walking (51). A circular flat indenter with diameter of 60mm, which is larger than the maximum heel width, was used for the compression to mimic the condition that occurs during gait. The contact force was measured between the indenter and the heel and coefficient of friction was set to 0.6.

- **Results**

Results showed that both force-displacement and force-strain responses of the heel pad were affected by changes in the size and the shape of the indenter. The contact force was increased as indenter size increased for both flat and spherical shapes (Figures 7.2 and 7.3). To compress the heel pad for 6mm (38% strain) 262N was required using the large flat indenter (40mm diameter) whereas 210N was required using the small flat indenter (30mm diameter). This can be explained by equation 7.1, in which the force is related to the area. In equation 7.1, F, A, E, L and ΔL represent load, contact area, Young's modulus, thickness of material and amount of deformation respectively.

$$F \cong AE\frac{\Delta L}{L} \tag{7.1}$$

By increasing the size of the indenter, more material is required to be compressed, thus the contact load is increased. From the above figures, at low strains (up to approximately 25%

strain) small influence of the change of the indenter size was observed on the results. Up to this point the contact area for both indenters does not exceed the small indenter area. It means that using indenters with higher difference in their size results in more difference in the heel pad responses obtained by these indenters. A comparison between results obtained using small and large indenters might lead to a misconception that the tissue compressed by the larger indenter is stiffer than the other one. However, this difference is related to the contact area that gradually increases by the indentation depth using the larger indenter.

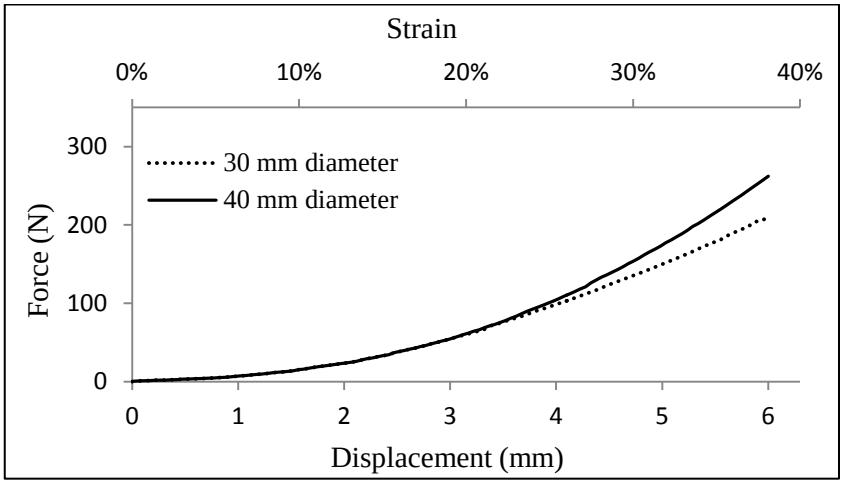

Figure 7.2: The force-displacement response of the heel pad compressed by small and large flat indenters.

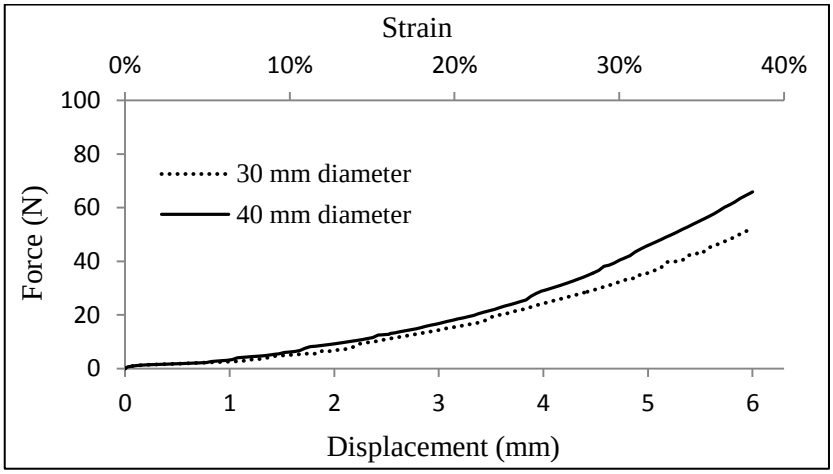

Figure 7.3: The force-displacement response of the heel pad compressed by small and large spherical indenters.

For the shape of the indenter (Figures 7.2 and 7.3), the force required to compress the heel pad using the sphere indenter was less than that required using the flat indenter. For example, to compress the heel pad 6mm (38% strain) using the 30mm diameter flat indenter, 210N was required whereas only 52N was measured for applying the same deformation to the heel pad using the same size sphere indenter. It is clear that by using the sphere indenter less material is compressed compared to the flat indenter for the same depth of compression. The mathematical explanation of these results can be simply expressed by equations 7.2 and 7.3. The contact between two elastic bodies first studied by Hertz (127). He showed the relationship between the applied force (F) and the indentation depth (d) for the flat indenter as follows.

$$F \cong \frac{2ERd}{(1-\nu^2)} \tag{7.2}$$

The E, R and ν are Young's modulus, indenter radius and Poisson's ratio respectively. For the sphere indenter the above relationship is expressed by equation 7.3.

$$F \cong \frac{4ER^{1/2}d^{3/2}}{3\,(1-\nu^2)} \tag{7.3}$$

A comparison between equations 7.2 and 7.3 indicates that the force required to apply deformation to the tissue using a flat indenter is greater than using a sphere indenter until the indentation depth is 2.25 times of the indenter radius.

The stress resulted from the flat indenter was also more than that from the sphere indenter. While the maximum compressive stress resulted from applying 6mm deformation on the heel pad using the large flat indenter was 0.421MPa, it was 0.313MPa using the large sphere indenter (Figure 7.4).

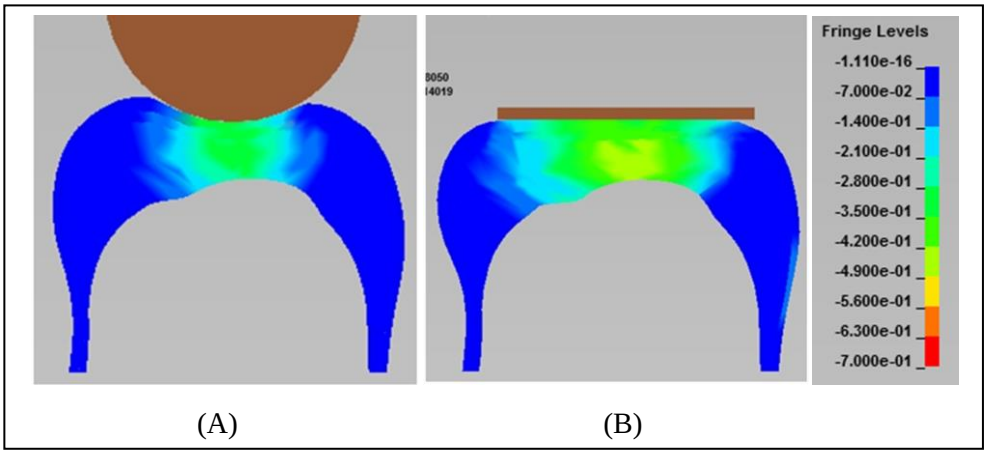

Figure 7.4: Compressive stress results for 6 mm deformation of the heel pad: (A) Indentation using the 40mm diameter sphere indenter; (B) Indentation using 40mm diameter flat indenter.

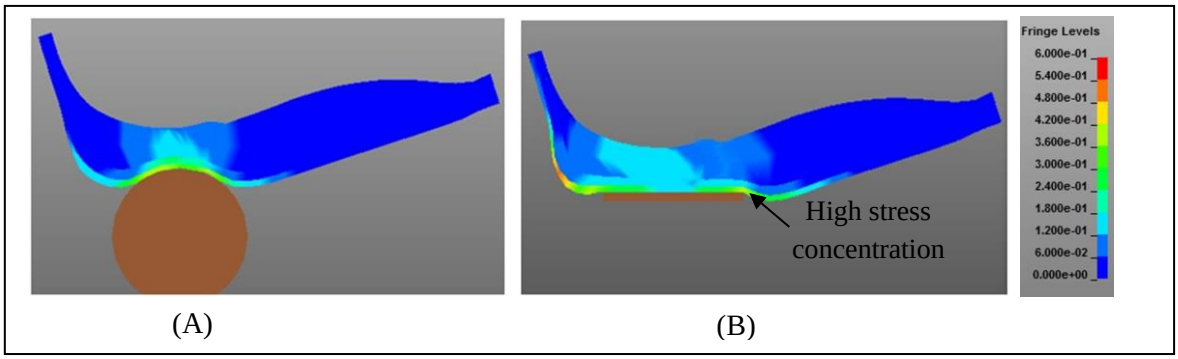

Figure 7.5: Von Mises stress results for 6 mm deformation of the heel pad: (A) Indentation using the 30mm diameter sphere indenter; (B) Indentation using 30mm diameter flat indenter.

Using the sphere indenter, the compressive stress was mostly concentrated under the indenter and the rest of the tissue was left unstressed. However, using the flat indenter, the compressive stress was spread out the wider area under indenter. Moreover, when the heel pad was loaded with the small flat indenter, stress concentration appeared around the edge of the indenter. This indenter caused the piling up of the material around its edges. Figure 7.5 shows resultant von Mises stress on the heel pad for 6mm deformation applied by small flat and sphere indenters. These results of this study are in consistent with those obtained by Robbins et al. and Matteoli et al. (59, 126). They showed that the response of the heel pad depends on the indentation technique with higher load in respond to flat indenter compared to sphere and larger indenter compared to smaller.

The position of the indenter under the heel pad also affects the heel pad behaviour whilst the predicted results revealed that the position of the large indenter does not influence the heel pad responses, the position of the small indenter results in different contact forces (Figure 7.6).

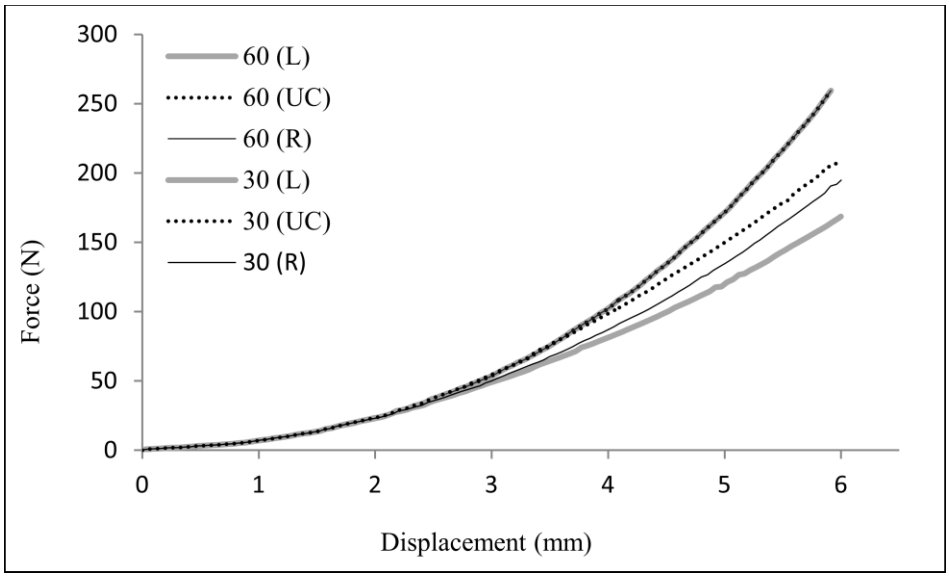

UC indicates Under Calcaneus tuberosity
R indicates 5mm towards Medial direction
L indicates 5mm towards Lateral direction

Figure 7.6: The effects of the position of the small (30mm) and large (60mm) indenters on the force-deformation response of the heel pad.

Since the shape of the calcaneal bone is neither uniform nor symmetrical, the thickness of the heel pad, measured from the skin surface to the calcaneus, varies beneath the calcaneus. Therefore, by changing the position of the small indenter under the heel area, the tissue thickness under the indenter changed and therefore different contact forces were obtained for the same indentation depth. Using the large indenter (60mm diameter), the heel pad responses were not affected by the position of the indenter because the indenter was large enough to compress the whole heel pad uniformly at each position located. In addition, no tissue contacted the edges of the indenter. These findings show that the force-displacement responses of the heel pad is sensitive to the position of the small indenter. It is suggested to either use a large indenter or employ consistent experimental setup based on appropriate

landmark such as calcaneus tuberosity for data collection. Some studies in literature used inappropriate position for indenter (e.g. a position on a line connecting the second toe and the mid-heel) which does not result in consistency in data collection (36, 59). Thus, different results might have been compared with each other.

Loading velocity had effect on heel pad responses during loading and unloading, especially at high strains (Figure 7.7).

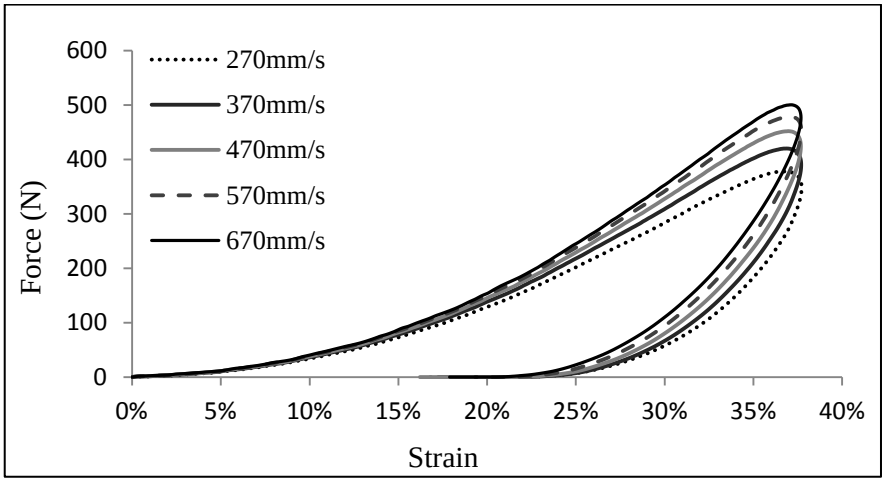

Figure 7.7: Force-strain response of the heel pad at different velocities.

Hysteresis in the behaviour of the heel pad can be observed in Figure 7.7. A diminishing trend in the increase of the peak force with increasing velocity can be noticed in the heel pad responses. For example the peak force was increased by 42.12N from the first cycle to the second cycle (maximum velocities of 270-370mm/s) while the increase was 22N for the last two cycles (maximum velocities of 570-670mm/s). This can be explained by viscoelastic material approach towards the so-called instantaneous stress response (128). During unloading, the tissue could not recover at the speed of the indenter and contact was lost around 25% strain.

Although in some experimental studies the effect of loading velocity on the heel pad responses was reported (12, 13), in some cases no significant changes in the stiffness and the percentage energy loss were found (15, 60). These results were obtained from *in-vitro*

experiments and loading velocity insensitivity of the heel pad tissue was reported for older cadaver (37-70 year old). On the other hand, a research study done by Jorgensen et al. found the relationship between the heel pad thickness and the energy loss with thinnest pads displaying lowest shock absorption characteristics (56). The FE model showed to be capable of investigation of the loading velocity effect on the heel pad responses for the same geometry and material properties of the tissue. Further investigations could provide valuable information about the effect of stiffness of material property and the heel geometry on the possible influence of the loading velocity on the heel pad responses.

These studies have shown model outputs under various experimental setups. The results demonstrated heel pad tissue responses to be sensitive to indenter size and shape, indenter position under the heel pad and loading velocity. When comparing data with those available in the literature all these effects should be also considered avoiding misconception. It is suggested that to get a series of consistent indentation test results using a small size indenter, a specific constant position under the heel is selected for all experimental iterations. By using a large indenter (larger than the maximum heel width), not only is the effect of position of indenter eliminated but also no stress concentration appears around the indenter edges. However, using a large indenter the size of the subject's heel becomes influential and it should be precisely considered since the measured force varies by the size of the heel (see section 7.2.2).

7.2.1.2 Effects of Heel Geometry

Various heel pad behaviours were reported in the literature based on force-displacement relationship. The divergence might be due to heel pad geometry. The aim of this stage was to investigate the effect of the heel pad geometry including heel pad thickness and heel width on heel pad responses.

- **Methods**

The effect of heel pad thickness and heel width on heel pad responses was studied. First, the hyperelastic FE model with thickness of 15.7mm was scaled in inferior-superior direction to achieve the original thickness±2 and ±4mm (11.7, 13.7, 17.7 and 19.7mm). The 5 hyperelastic FE models with different thicknesses were then subjected to compression at 5mm/s using flat 60mm diameter indenter up to 6mm deformation and the heel pad responses were recorded. The static coefficient of friction was set to 0.6 and the contact force was measured between the indenter and the tissue.

To investigate the effects of heel width on the heel pad responses, the original FE model with thickness of 15.7mm and the maximum heel width of 52.5mm was scaled in medial-lateral direction to achieve the initial heel width±5 and ±10mm (42.5, 47.5, 57.5 and 62.5mm). The 5 hyperelastic FE models were compressed at 5mm/s using circular flat indenter with diameter of 72mm up to 6mm deformation. The size of indenter was increased to 72mm to avoid edge effect observed in the prior study. The static coefficient of friction was set to 0.6 and the contact force was measured between the indenter and the tissue.

- **Results**

The force-displacement responses of the heel pad were affected by heel pad thickness. The thicker the tissue the less force was required to compress the heel pad for the same depth of indentation (Figure 7.8). For instance, to induce 6mm deformation to the heel pad with thickness of 11.7mm the load of 622N was required which is almost 4 times greater than the load that required for compressing the heel pad with thickness of 19.7mm for the same amount of displacement (160N). However, the results of this study showed that the heel pad force-strain responses are slightly affected by the tissue thickness (Figure 7.9). Note that inducing 6mm displacement into heel pad models with different thicknesses resulted in different strains.

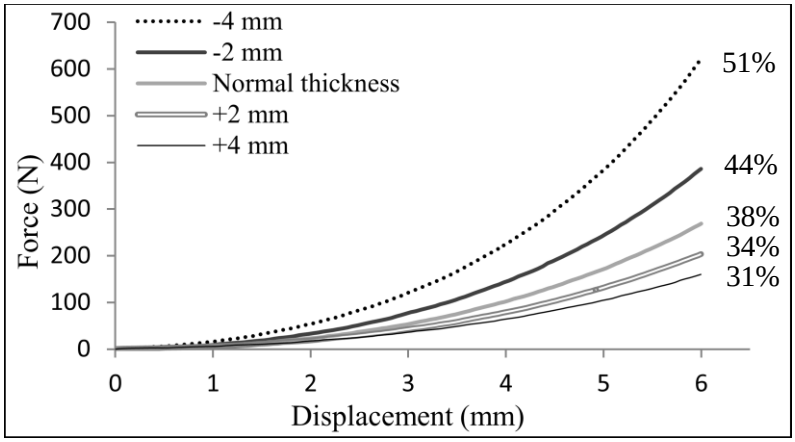

Figure 7.8: The effects of the heel pad thickness on the force-displacement response of the heel pad.

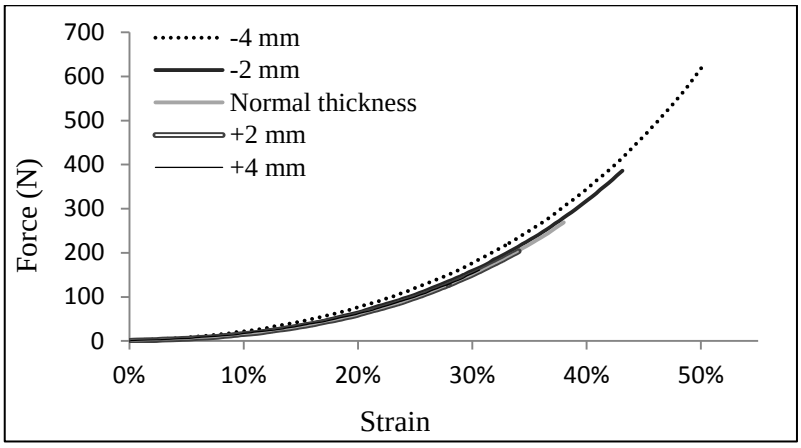

Figure 7.9: The effects of the heel pad thickness on the force-strain response of the heel pad.

Difference between force-displacement responses of the heel pad with different thickness can be explained by equation 7.1. While equation 7.1 is an approximate, it demonstrates the obvious point that the force required is inversely related to the thickness of the material. According to this equation for the same amount of strain, the equal forces are resulted for different heel pad thicknesses. The influence of the heel pad thickness on the peak contact pressure was also studied. The results revealed that the peak contact pressure decreases when the tissue thickness is increased (Figure 7.11). These results indicate that the force-strain response of the heel pad could better represent its behaviour. Force-displacement/strain responses of the heel pad are influenced by the heel width when the indenter is larger than the heel width (72mm diameter). Figure 7.10 shows the force-displacement/strain responses of the heel pad with different heel width under loading.

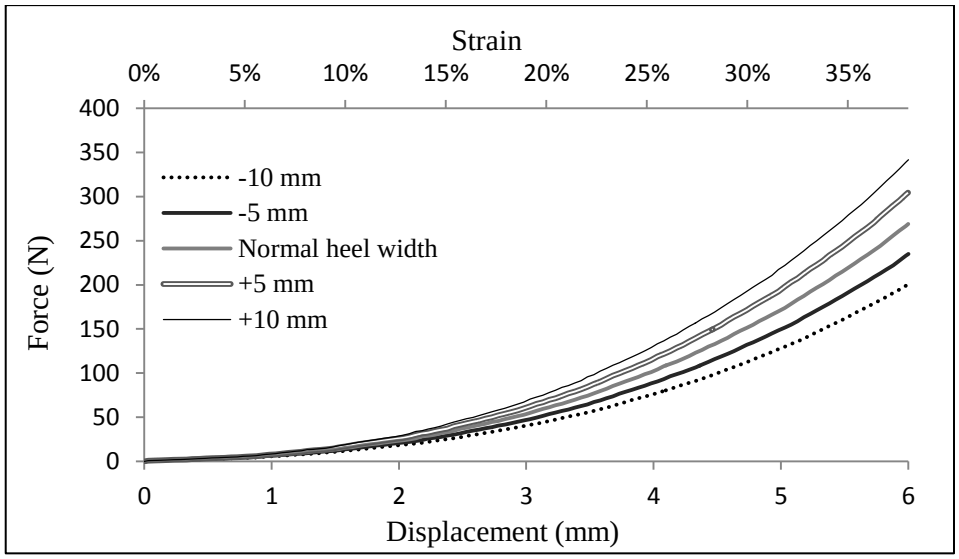

Figure 7.10: The effects of the heel width on the force-displacement response of the heel pad.

The contact pressure was only very gradually increased with the heel width (Figure 7.11) and the compressive stress did not vary with changes of the heel width (Figure 7.13). The peak contact pressure obtained from applying 6mm deformation to the FE models of the heel with different thickness and width are given in Figure 7.11. The pressure distribution and compressive stress obtained from inducing 6mm deformation to the FE models with heel width of 42.5, 52.5 and 62.5mm are illustrated in Figures 7.12 and 7.13.

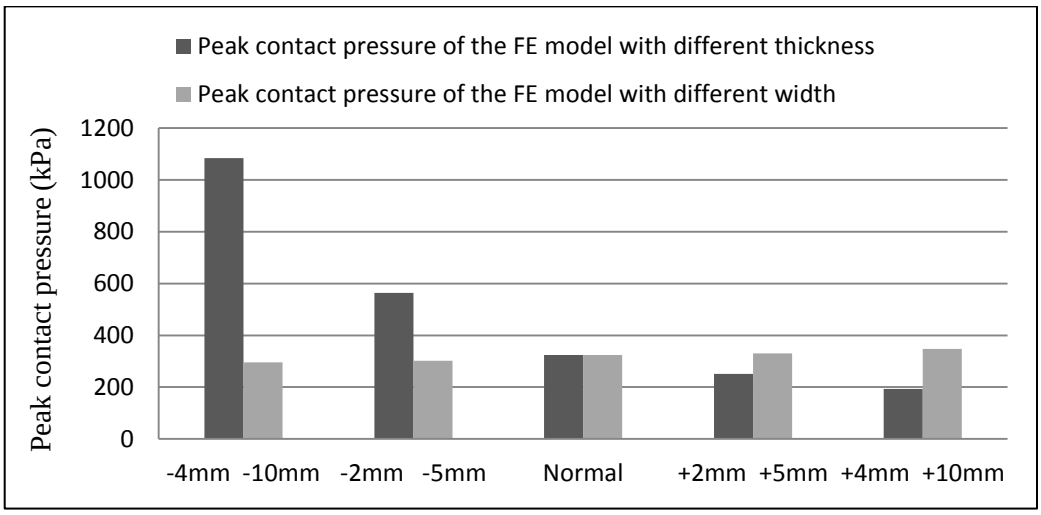

Figure 7.11: Contact pressure under the heel for inducing 6mm deformation to the FE models with different thickness and width.

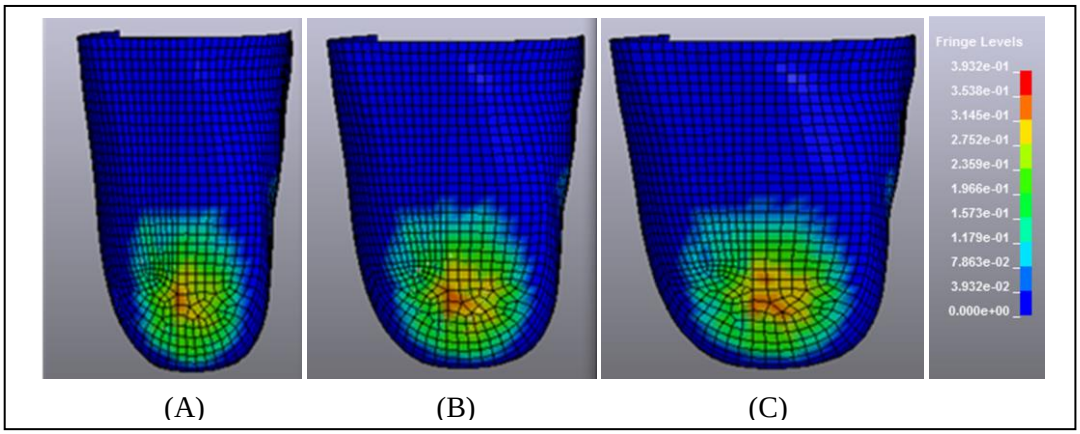

Figure 7.12: Pressure distribution under the heel for inducing 6mm deformation: (A) FE model with the maximum heel width of 42.5mm, (B) Original FE model with heel width of 52.5mm, (C) FE model with the maximum heel width of 62.5mm.

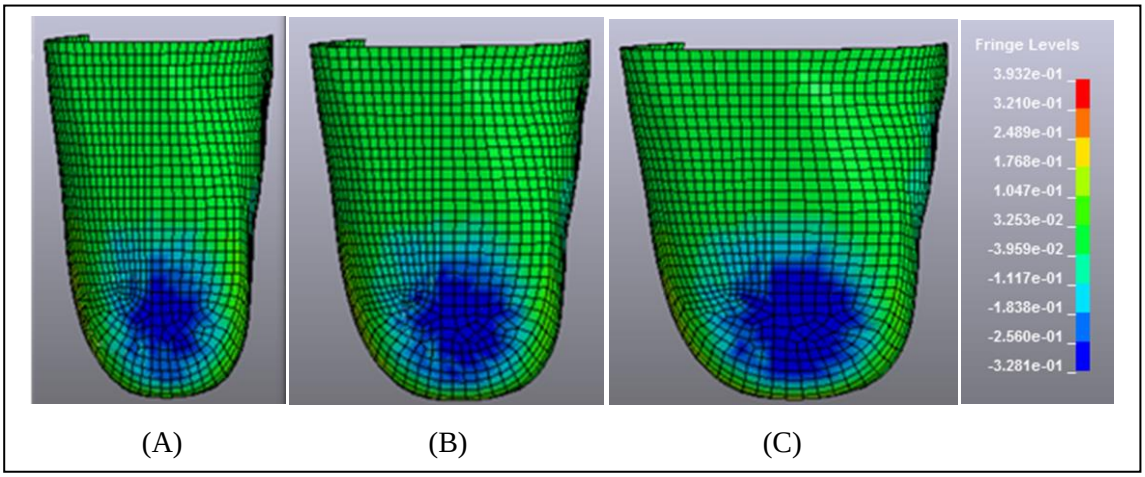

Figure 7.13: Compressive stress under the heel for inducing 6mm deformation: (A) FE model with the maximum heel width of 42.5mm, (B) Original FE model with heel width of 52.5mm, (C) FE model with the maximum heel width of 62.5mm.

The effect of the heel width on the load is related to the variation in the contact area that has direct relation with the force required to compress the heel pad (equation 7.1). Accordingly, the stress-strain relation is less affected by the heel size and can better represent the heel pad behaviour. In literature, some force-displacement/strain experimental data can be found which were obtained using a large indenter (29, 50, 60). However, they did not provide information regarding to the heel width, ignoring its effect. To eliminate the effect of the heel width, most of studies have started using a small indenter for obtaining the heel pad behaviours where

measuring the stress was not possible (5, 7, 32, 59, 126, 129). However, in these cases the resultant data could not represent the behaviour of the heel pad at conditions that occur during standing or gait and also the tissue had contact with the edges of the indenter resulting in stress concentration. Some conclusions can be made from these various studies.

- When studying heel pads with different thicknesses, the force-strain relationship can better represent heel pad behaviour because is less affected by variation of the thickness.
- For heel pads with different maximum heel widths, when it is not possible to measure the stress as the heel pad response, using a large indenter to compress the heel pads is suggested while the contact force is measured by a small load cell accommodated inside the large indenter. This indenter and load cell system is the same as that used in this project (see Chapter 5). In this system, while the heel pad is compressed by a large indenter to ensure that the responses of the heel pad during standing or gait are obtained and stress concentration does not occur around the edges of the indenter, the small load cell at the centre of the indenter is used to measure the force and ensure that results are not affected by the size of the heel.

7.2.2 Capability of the Developed FE Model in Determination of the Material Properties for another Heel Pad (Case Study 2)

The aim of this case study was to verify the capability of the FE model (generated for the heel area of **Subject 1**) in determination of the material properties of the other heels. To achieve this purpose another healthy female volunteer (**Subject 2**) was enrolled to this study. Ethical approval was granted by the University of Salford ethical committee. Table 7.1 provides information regarding to body characteristic and heel geometry of two subjects.

Table 7.1: Body characteristics and heel geometries of **Subjects 1** and **2**

	Body characteristics				Heel geometry			
	Age	Height	Weight	Shoe size	Heel pad thickness	Macro-chamber thickness	Micro-chamber thickness	Skin thickness
Subject 1	34Y	164cm	63kg	UK5	15.7mm	12.0mm	2.3mm	1.4mm
Subject 2	26Y	161cm	68.5kg	UK6	17.7mm	12.7mm	3.6mm	1.4mm

A series of slow compression tests were performed on the heel of **Subject 2** to obtain the responses of the heel pad and its sub-layers (as per slow compression test protocol in Chapter 5). The force-strain experimental data was used as an input to inverse FEA to assess the robustness of the FE model in estimation of hyperelastic material properties of the heel sub-layers of **Subject 2**. This case study is divided into two sub-sections. First sub-section is about experimental study of the heel pad of **Subject 2**. Second sub-section explains the method and results regarding to estimation of the hyperelastic material properties of the heel pad sub-layers of **Subjects 2**.

7.2.2.1 Slow Compression Test Performed on the Heel Pad of Subject 2

- **Methods**

The same method and compression device (STRIDE), used for performing experiments on the heel pad of **Subject 1** in Chapter 5, was used to obtain the heel behaviour of **Subject 2**. A series of slow compression tests at constant velocity of 5mm/s was performed on the right heel of **Subject 2**. The heel pad was compressed up to depth of ~40% initial thickness and the force-strain responses of the heel pad and its sub-layers were obtained. The compression test was repeated for 6 iterations with 1 minute rest time between each.

- **Results**

Figures 7.14-7.18 show the force-strain responses of the heel pad, its sub-layers and also responses of total macro-chamber and micro-chamber of **Subject 2** under loading. For 6 repetitions the heel pad was compressed up to average depth of 41.5% initial thickness (40%

was the target). The unloaded thickness, strain and deformation proportion of the heel pad and its sub-layers are provided in Table 7.2.

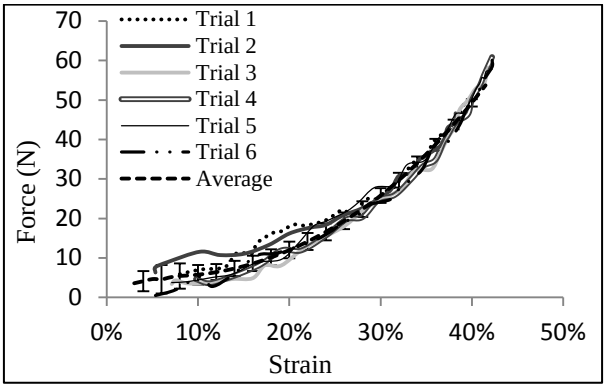

Figure 7.14: The heel pad behaviour at 5mm/s

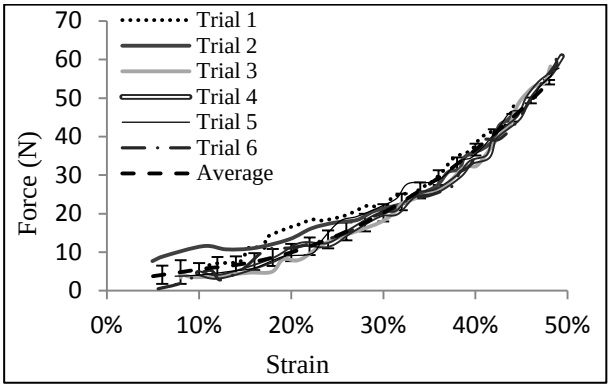

Figure 7.15: The macro-chamber behaviour at 5mm/s

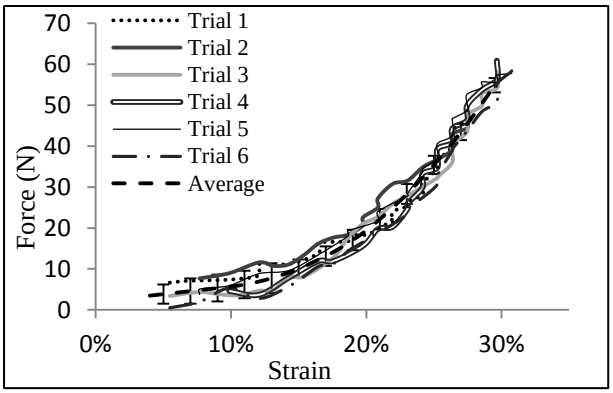

Figure 7.16: The micro-chamber behaviour at 5mm/s

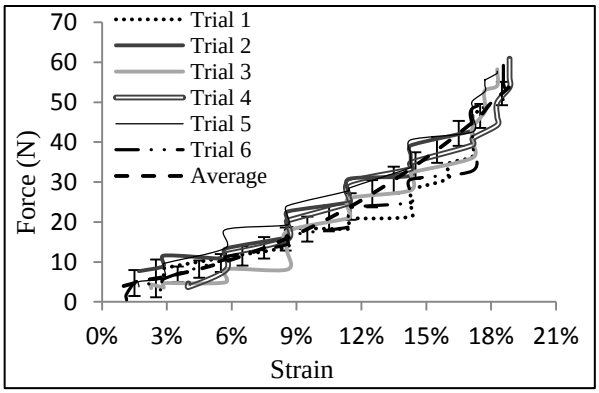

Figure 7.17: The skin behaviour at 5mm/s

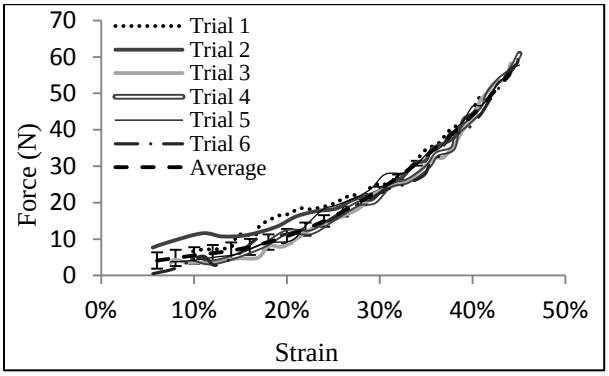

Figure 7.18: Behaviour of the total macro-chamber and micro-chamber at 5mm/s

Table 7.2: Mechanical information of the heel pad, macro-chamber, micro-chamber and skin layers under compression at 5mm/s (**Subject 2**).

	Heel pad	Macro-chamber	Micro-chamber	Skin
Unloaded thickness (mm)	17.7 (0.1)	12.7 (0.1)	3.6 (0.2)	1.4 (0.1)
Strain (%)	41.5 (0.7)	47.9 (0.5)	29.3 (0.4)	18.8 (0.5)
Deformation proportion (%)	-	82.8	14.3	3.6

Values are means (SD).

Similar to force-strain responses of the heel pad and its sub-layers of **Subject 1** (see Chapter 5), the responses of each layer for 6 iterations did not overlap. As explained earlier this might occur due to a small movement of the foot or changes in liquid content of the heel pad tissue.

According to Table 7.2, the macro-chamber, micro-chamber and skin layers formed 71.7%, 20.3%, and 7.9% of the heel pad thickness respectively. Like **Subject 1**, the heel pad and its sub-layers demonstrated highly non-linear behaviour. The macro-chamber layer underwent large deformations and showed higher compliance behaviour than the other two layers. For 41.5% strain of the heel pad, the macro-chamber experienced a significantly greater deformation proportion than the micro-chamber and skin layers (82.8% vs 14.3 vs 3.6). Since the skin layer was thin and demonstrated small deformation, a high amount of error was expected.

For inducing 41.5% strain to the heel pad of **Subject 2**, ~54N was required compared to ~73N for applying 36.5% strain to the heel pad of **Subject 1**. This comparison reveals that the heel pad of **Subject 1** is stiffer than **Subject 2**. **Subject 2** had a thicker and softer micro-chamber layer with more deformation under loading than **Subject 1** (deformation proportion of 14.3% vs 10.1%). The difference between force-strain relationship of the heel pad of **Subjects 1** and **2** is clearer in Figure 7.19. Both subjects were healthy and tested at the same experimental conditions including position of the foot, compression device, and loading velocity.

Therefore, the difference was possibly because of different materials of these heels. However, age can also affect tissue properties, although **Subject 1** still is younger than "aging" process. Hsu et al. showed that the age affects the mechanical properties of the heel pad. They conducted an examination on two groups of young (less than 40) and elderly (older than 60) volunteers. The results of their study indicate that the elasticity and compressibility of the heel pad are decreased in the older group (36). However, **Subjects 1** and **2** both are in "young" group by Hsu et al. definition.

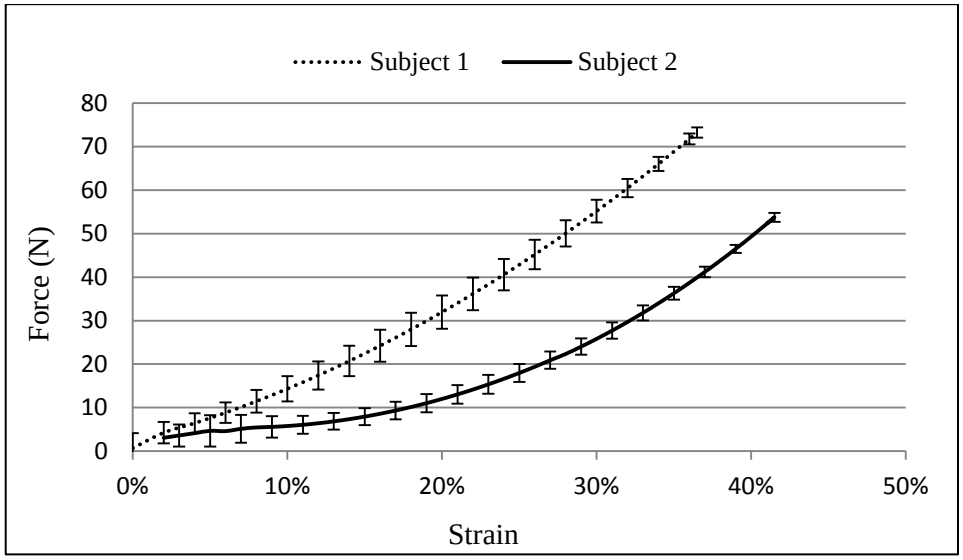

Figure 7.19: Force-strain relations of the heel pad obtained **Subjects 1** and **2**

7.2.2.2 Determination of the Hyperelastic Material Properties of the Heel Pad Sub-layers of Subject 2

- **Methods**

To estimate the material properties of the heel pad sub-layers of **Subject 2** using the FE model, the same method, used for **Subject 1**, was utilised (see Chapter 6). The estimation of the hyperelastic material properties was started with determination of initial estimates for the hyperelastic material properties (μ and α) of macro-chamber layer from the one-layer FE model. Two values of 36kPa and 4.5 for μ and α respectively were assigned to the macro-chamber layer to begin the FEA based on data obtained for macro-chamber of Subject 1 in

Chapter 6. The one-layer model was compressed up to 47.9% strain, which is the maximum strain experienced by the macro-chamber layer during physical testing for 41.5% heel strain (40% was the target), at velocity of 5mm/s. The predicted force-strain response of the macro-chamber was recorded and RMS error was measured between the predicted result and the experimental data. The material properties were varied iteratively following the iterative curve fitting rule (see Chapter 6) in order to minimise the RMS error.

The material properties determined for the macro-chamber layer were then assigned to the micro-chamber layer in the two-layer FE model. The two-layer FE model was compressed up to 43.7% strain, which is the maximum strain experimentally induced to the total macro-chamber and micro-chamber layer for 41.5% heel strain. The model predictions of the force-strain relationship for the total of macro-chamber and micro-chamber layers were compared to the corresponding experimental data. The material properties of macro-chamber and micro-chamber layers were adjusted following the iterative curve fitting rule (see Chapter 6) until no more important changes were observed in reduction of objective functions (variation in RMS errors <0.9N). RMS errors for macro-chamber and total of macro-chamber and micro-chamber layers and difference between maximum strains were used as objective functions.

Finally, the complete three-layer FE model was used to estimate the final material properties of the macro-chamber, micro-chamber and skin layers. The material properties of the micro-chamber layer determined from the two-layer FE model were assigned to the skin layer. The three-layer FE model was compressed up to 41.5% strain, the maximum strain of the heel pad measured during experimentation (40% was the target). The predicted force-strain responses of the macro-chamber, micro-chamber and three-layer model were recorded and compared with the corresponding experimental data. The hyperelastic material properties of the heel pad sub-layers were varied following the iterative curve fitting rule (see Chapter 6) until no more useful improvements were observed in reduction of objective functions (variation of RMS

errors<0.26N). RMS errors for macro-chamber, micro-chamber and heel pad and also difference between maximum strains were used as objective functions.

After estimation of the hyperelastic material properties of the heel pad sub-layers, the capability of the FE model in simulating the behaviour of the heel pad of **Subject 2** under loading was investigated. The maximum strain of the heel pad under specific plantar pressure was used as a measure of the FE model performance. The plantar pressure was selected because it is slightly affected by the size of the heel. The compression was performed under the heel pad of **Subject 2** using the loading device developed to apply load under the heel pad of **Subject 1** during MRI scanning. Complete details about the loading device can be found in Chapter 6. Some changes were applied to the structure of the wooden foot support in the loading device to allow visualization of the deformation of the heel pad under loading using ultrasound. For this purpose, a rectangular aperture was made under the heel area and then covered with rigid transparent thermoplastic Northplex material (North Sea Plastics Ltd, Glasgow, UK) which allows the ultrasound signal to pass (Figure 7.20).

To apply compression under the heel pad, **Subject 2** wore the back pack of the loading device in the supine position while her foot was placed against the foot support. The heel pad was compressed by pulling the loose ends of the side straps around the foot support housing and adjusting them to the marked position. The Pedar pressure insole was placed under the heel area to measure the plantar pressure (Figure 7.20). Then the insole was removed and the ultrasound probe was placed at the back of the foot support against the Northplex window under the calcaneus tuberosity. At this site the heel pad thickness and therefore the maximum strain were measure under loading (Figure 7.20).

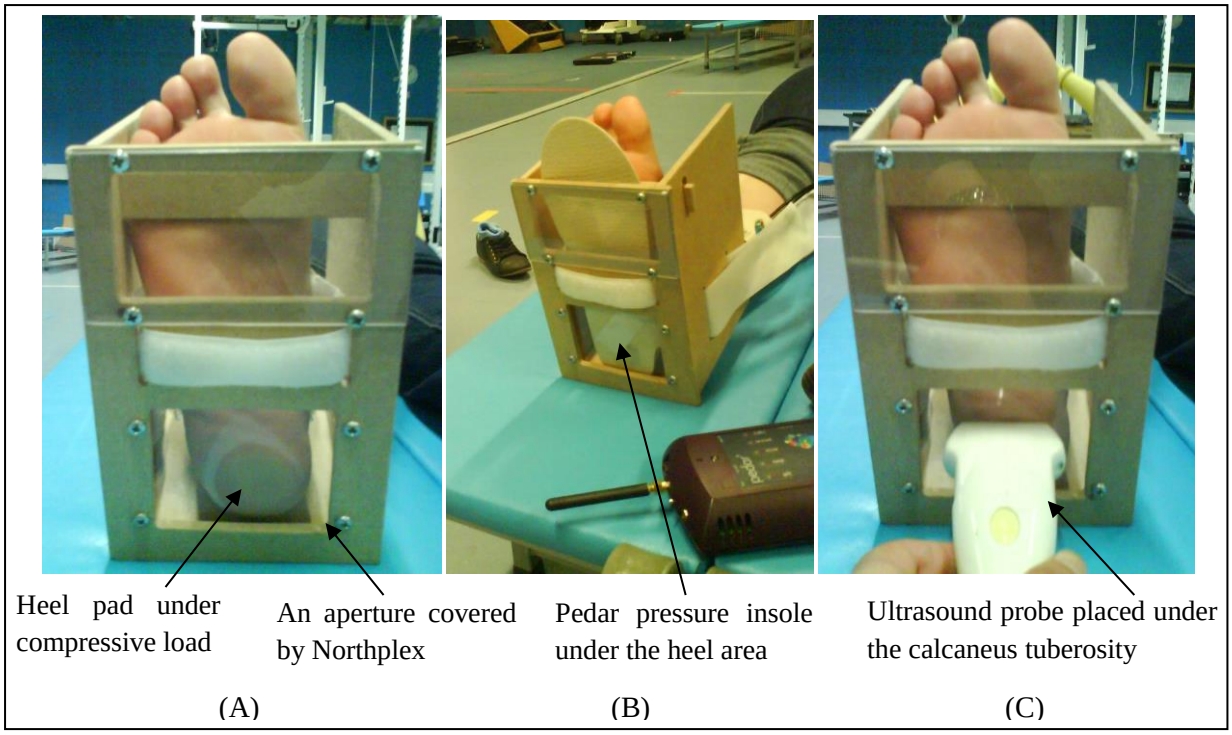

Figure 7.20: measuring loaded thickness of the heel pad under specific load: (A) Applying compression load under the heel pad using the loading device; (B) Measuring the compressive load using the Pedar pressure insole; (C) Measuring the loaded thickness of the heel pad using the ultrasound modality.

- **Results**

At the first step, the hyperelastic material properties of the macro-chamber were estimated. Only 2 iterations were required to reach a convergence with RMS error of 2.3N between the model predicted and the experimental results. The initial estimates for the hyperelastic material properties of the macro-chamber layer and the RMS error obtained at this stage are listed in Table 7.3. The force-strain relationships of the macro-chamber at the first and final iterations using the material parameters derived from literature and those obtained are plotted in Figure 7.21. The RMS error was reduced by 3.9N from the first to the final iteration.

Table 7.3: The hyperelastic material properties of the macro-chamber layer of Subject 2 determined from one-layer model.

	μ (kPa)	α (-)	RMS error (N)	RMS error (% max force)
Macro-chamber	16.45	6	2.3	4.2

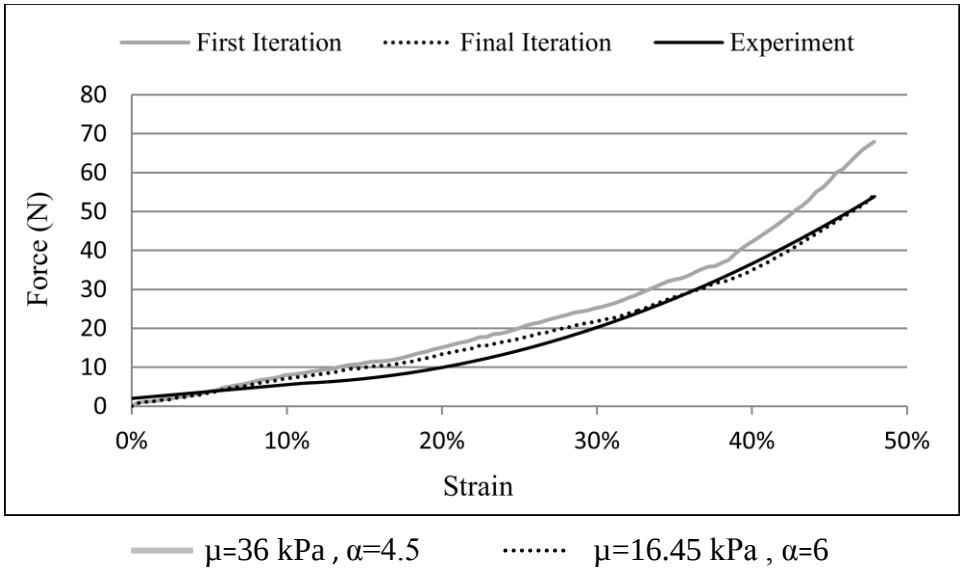

Figure 7.21: Force-strain relation of the macro-chamber layer of **Subject 2** predicted by one-layer FE model.

In the second step the first estimates for the hyperelastic material properties of the micro-chamber layer and the second estimates for the hyperelastic material properties of the macro-chamber layer were obtained. A convergence was reached after 12 iterations with the RMS errors of 2.05 and 2.95N between the FE predicted and the actual test results for the macro-chamber layer and two-layer FE model respectively. The estimates for the hyperelastic material properties of the micro-chamber and macro-chamber layers obtained at this stage are listed in Table 7.4. Figures 7.22 and 7.23 illustrate the force-strain relation of the macro-chamber layer and the two-layer model at the first and the final iterations starting from using the material parameters obtained for the macro-chamber layer in the previous stage to those obtained from the two-layer model.

Table 7.4: The hyperelastic material properties of the micro-chamber and macro-chamber layers of Subject 2 determined from two-layer model.

	μ (kPa)	α (-)	RMS error (N)	RMS error (% max force)	Difference between max strains
Micro-chamber	65	6	2.95 (for two-layer model)	5.6 (for two-layer model)	-
Macro-chamber	20	5	2.05	3.9	1.4

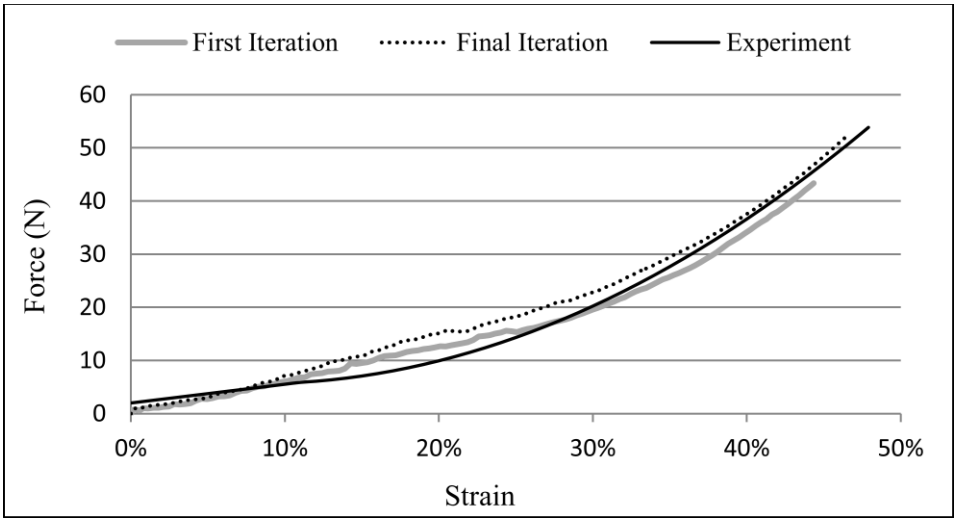

Macro-chamber: μ=16.45 kPa, α=6
Micro-chamber: μ=16.45 kPa, α=6
Macro-chamber: μ=20 kPa, α=5
Micro-chamber: μ=65 kPa, α=6

Figure 7.22: Force-strain relation of the macro-chamber layer of **Subject 2** predicted by the two-layer FE model.

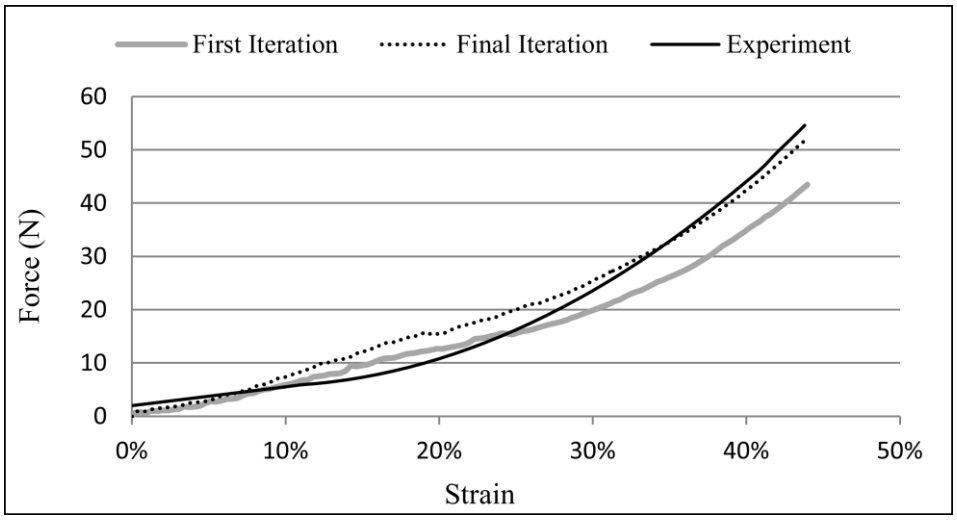

Macro-chamber: μ=16.45 kPa, α=6
Micro-chamber: μ=16.45 kPa, α=6
Macro-chamber: μ=20 kPa, α=5
Micro-chamber: μ=65 kPa, α=6

Figure 7.23: Force-strain relation of the two-layer FE model for **Subject 2**.

As can be seen in Figure 7.22, although the RMS error of the macro-chamber layer was small at first iteration (2.5N), the deformation of the macro-chamber was less than the experimental data. For 43.5% strain of two-layer FE model, the macro-chamber-layer was deformed up to strain of 43.2% while almost 47.9% was expected based on the experimental data. This

difference can be explained by the fact that at first iteration the micro-chamber layer, being assigned with material properties of macro-chamber layer, was behaving with lower stiffness than *in-vivo*. At the final iteration the stiffness of the micro-chamber layer had been adjusted and it was stiffer than the macro-chamber layer, as is case in experimental data. Therefore, the strain of the macro-chamber layer was improved up to 46.5% strain.

At the final step, after 33 iterations a convergence was reached with the RMS error of 3.76, 3.55, and 3.91N between the experimental and the predicted force-strain results for the macro-chamber layer, micro-chamber layer and the three-layer heel pad model respectively. The final estimates are listed in Table 7.5. Figures 7.24-7.26 show the force-strain responses of the macro-chamber layer, micro-chamber layer and the complete three-layer model at the first and the final iterations.

Table 7.5: Optimised final hyperelastic material properties for macro-chamber, micro-chamber and skin layers of **Subject 2**.

	μ (kPa)	α (-)	RMS error (N)	RMS error (% max force)	Difference between max strains
Skin	195	5.8	3.91 (for three-layer model)	7.4 (for three-layer model)	-
Micro-chamber	55	4.9	3.55	6.7	0.5
Macro-chamber	20	4.5	3.76	7.1	0.6

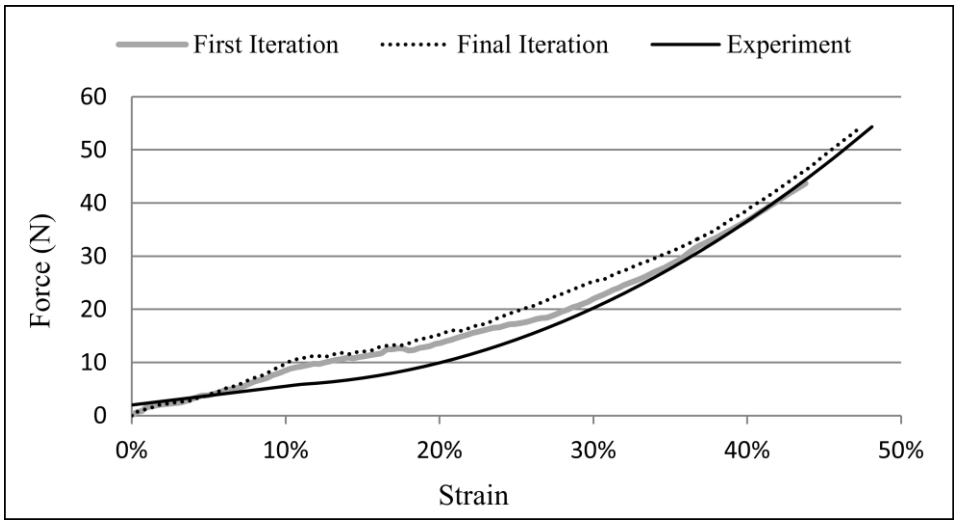

Macro-chamber: μ=20 kPa, α=5
Micro-chamber: μ=65 kPa, α=6
Skin: μ=65 kPa, α=6

Macro-chamber: μ=20 kPa, α=4.5
Micro-chamber: μ=55 kPa, α=4.9
Skin: μ=195 kPa, α=5.8

Figure 7.24: Force-strain relation of the macro-chamber layer of **Subject 2** predicted by three-layer FE model.

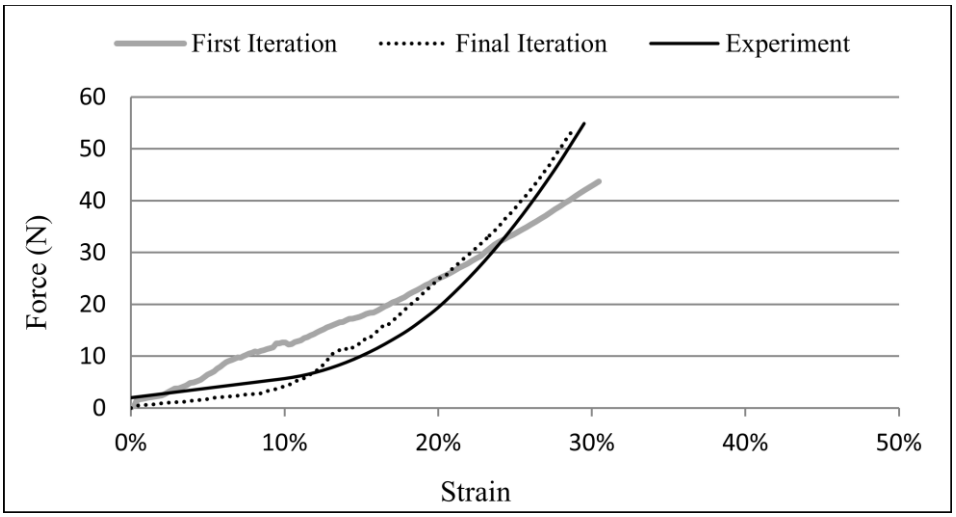

Macro-chamber: μ=20 kPa, α=5
Micro-chamber: μ=65 kPa, α=6
Skin: μ=65 kPa, α=6

Macro-chamber: μ=20 kPa, α=4.5
Micro-chamber: μ=55 kPa, α=4.9
Skin: μ=195 kPa, α=5.8

Figure 7.25: Force-strain relation of the micro-chamber layer of **Subject 2** predicted by three-layer FE model.

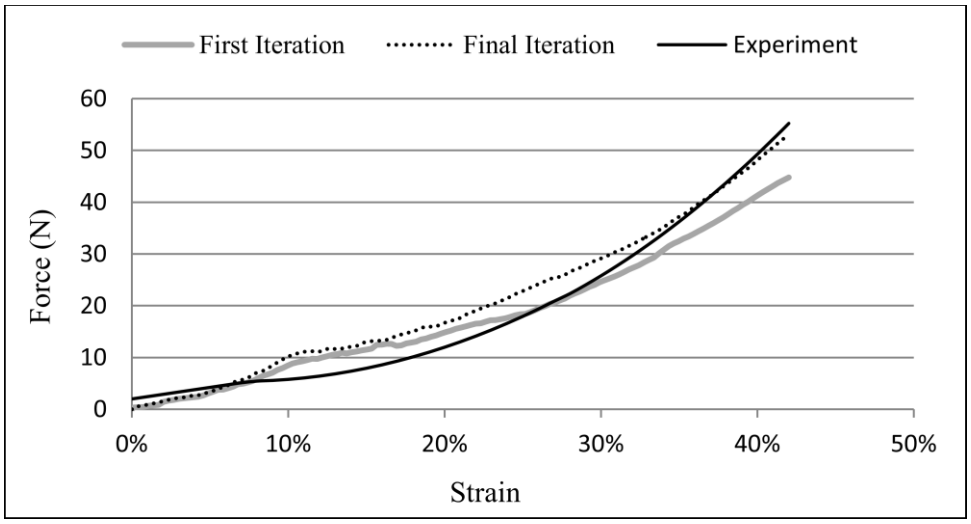

Macro-chamber: μ=20 kPa, α=5
Micro-chamber: μ=65 kPa, α=6
Skin: μ=65 kPa, α=6

Macro-chamber: μ=20 kPa, α=4.5
Micro-chamber: μ=55 kPa, α=4.9
Skin: μ=195 kPa, α=5.8

Figure 7.26: Force-strain relation of the three-layer FE model of Subject 2.

According to Figure 7.24, for 41.5% strain of the heel pad, the macro-chamber-layer was compressed up to 43.8% at first iteration while strain of almost 47.9% was expected according to the experimental results. Moreover, the micro-chamber was compressed for 30.4% while strain of almost 29.3% was expected (Figure 7.25). It seems that at the first iteration the stiffness of the macro-chamber was high while it was low for the skin layer. At the final iteration the strain of the macro-chamber and micro-chamber were improved to be 47.3 and 28.8%, with difference in maximum strains of 0.6 and 0.5, respectively. Since the thicknesses of the heel pad sub-layers of **Subject 2** were not proportional to the corresponding layers in the FE model, mathematically it was not possible to achieve same deformations achieved during experiments. Comparing the RMS errors measured between the predicted and experimental for **Subject 2** with those obtained for **Subject 1** (7.4% vs 2.7% for skin, 6.7% vs 5.0% for micro-chamber and 7.1% vs 2.6% for macro-chamber) and also difference between maximum strains (0.5 vs 0.3 for micro-chamber and 0.6 vs 0.4 for macro-chamber) shows that

the material properties for **Subject 2** were estimated with higher errors. More appropriate estimations might be achieved by running more iteration.

The maximum strain of the heel pad of **Subject 2** under compressive load was used to verify the capability of the FE model in simulating the behaviour of other heel pads. The peak plantar pressure was measured 137kPa (SD 12) for 13 sensors with area of 1970mm^2 under the heel region. For this amount of peak plantar pressure, the maximum strain of the heel pad was measured as 55.9%. The predicted strain of the FE model for peak plantar pressure of 137kPa was measured as 41.3%. A comparison between the experimental and predicted results showed the existence of high error, almost 26% maximum strain, whereas the FE model could predict the behaviour of the heel pad of **Subject 1** with 7% error. This illustrates the sensitivity of model predictions to the differences between individuals. Three specific reasons might explain this greater error. Since the calcaneus is a very stiff tissue, it sets constraints of heel pad behaviour. Thus, its shape might affect heel pad responses. Difference in the shape and the geometry of the calcaneus in the heel of **Subject 2** and the FE model might be a cause of the difference in the results.

- Since thicknesses of the heel pad sub-layers of **Subject 2** were not proportional to those in the FE model, mathematically it was not possible to appropriately simulate deformation of the heel pad of **Subject 2** with the FE model and fit the model predictions to the experimental data. Therefore the estimation of the material properties was prone to high errors. If there was a constant proportion relationship between thicknesses of the heel pad and its sub-layers of **Subject 2** and those in the FE model, better results might be obtained even if thickness of tissues differs.
- Higher errors propagated during the material properties estimation of **Subject 2** might be another source of the greater error.

It should be noted that this conclusion is based on study of only one other heel with different geometry than the FE model. It seems that the FE model might be used for estimation of material properties of other heels with different geometries if only homogeneous material properties of single layer heel pad are of interest. This could be done by scaling the FE model to fit the thickness and width of the tested heel. Doing so, the mathematical issue can be resolved. Further investigation is required to examine the robustness of the single layer FE model in material properties estimation and effect of the heel and calcaneus shape on the results.

7.3 THE APPLICATIONS OF THE MODEL IN FOOTWEAR DESIGN RESEARCH STUDY

Several studies have conducted experiments to investigate the effects of footwear design factors on the heel function. Effects of design factors were evaluated using the plantar pressure measurements. However, since the location immediately beneath the calcaneus tuberosity has been reported as the region of plantar heel pain (83), the stress within the heel tissues is the key to understand effects of design factors on pain relief. In contrast with experimental methods, FE models of the heel area are capable of studying the interaction between the foot and footwear based on internal stress. Furthermore, FE models can be used as powerful tools in footwear design research field instead of physical experiments that are very slow and expensive to perform. The aim of this stage was to show some of the applications of the developed hyperelastic FE model of the heel area in footwear design through investigation of the effects of 4 footwear design factors (insole and midsole thickness, insole and midsole material) on compressive stress reduction of the heel. A combined FEA and Taguchi method was used to find the optimum combination of the insole and midsole for footwear with minimum number of trials.

- **Methods**

When outputs of a process such as footwear design depend on several factors, Taguchi method can be used to economically run the process towards determination of optimum combination of factors with minimum trials. In Taguchi method, a process is designed based on factorial arrays. When running a process, varying factors simultaneously rather than one factor at a time is cost and time efficient. By systematically choosing combinations of factors, it is also possible to evaluate the effect of each factor. In this study, orthogonal array was used to investigate the effects of insole and midsole thickness and insole and midsole material on heel stress reduction.

An orthogonal array, denoted by $L_N(s^k)$, holds a subset of all possible combinations of test conditions in a way that any two columns have all combinations an equal number of times. $L_N(s^k)$ is a matrix with dimension of N×k, N (the number of required trials) is the number of rows and k (the number of design factors) is the number of columns in the orthogonal array. s represents the level of each design factors. For instance, $L_4(2^3)$, which is the smallest 2-level orthogonal array, is given in Table 7.6.

Table 7.6: The orthogonal arrayof $L_4(2^3)$

	Design Factor			Experimental Result
Trial	**A**	**B**	**C**	
1	1	1	1	η_1
2	1	2	2	η_2
3	2	1	2	η_3
4	2	2	1	η_4

As it can be seen in Table 7.6, the four ordered pairs of (1,1), (1,2), (2,1), and (2,2) appear once in any two columns which means that the levels of 1 and 2 occur the same number of times in each column (130). In Table 7.6, numbers under design factor represent the level of each design factor. Since each experiment is a combination of different design factor levels, it

is important to obtain the effect of each factor. At first step the overall mean is calculated using the equation 7.4 while m is the number of trial:

$$\eta = \frac{1}{\mathrm{m}} \sum_{i=1}^{m} \eta_i \tag{7.4}$$

Then the mean value of each level of a particular design factor is calculated as the average of the results values for the corresponding level. For example, the mean value of the level 2 of design factor B (η_{B2}) in Table 7.6 is calculated as:

$$\eta_{B2} = \frac{1}{2}(\eta_2 + \eta_4) \tag{7.5}$$

A statistical analysis of variance (ANOVA) was performed to investigate the significance of design factors (insole thickness, insole material, midsole thickness and midsole material) affecting the quality of interactions between the heel and footwear. The sensitivity of each design factor is measured by the sum of the squared deviations from the overall mean value (74, 131). For example, the sensitivity of design factor B is calculated as:

$$(\eta_{\mathrm{B1}} - \eta)^2 + (\eta_{\mathrm{B2}} - \eta)^2 \tag{7.6}$$

The percentage contribution of each of the design factors was measured as the sum of squared deviations of each design factor to the total sum of squared deviations.

In this study orthogonal array of $L_9(3^4)$ was selected. This means that 9 trials were required with 4 design factors at 3 levels to identify the optimum condition in which the maximum compressive stress were minimised (Table 7.9). The design factors and their 3 levels are provided in Table 7.7.

Table 7.7: Design factors and their levels

Design Factor	Level 1	Level 2	Level 3
Insole thickness	2mm	4mm	6mm
Midsole thickness	4mm	8mm	12mm
Insole material	Poron Cushioning	PPT	Microcel Puff
Midsole material	Plastazote Firm	Crepe Firm	Cork

Poron Cushioning (Open-cell polyurethane), PPT Regular (Open-cell polyurethane), and Microcel Puff (Closed-cell (EVA)) were used as soft, medium and firm insole materials respectively. Plastazote Firm (Closed-cell x-linked polyethylene), Crepe Firm (Closed-cell EVA/SBR blend), and Cork (Natural cellulose) were used as soft, medium and firm midsole materials respectively. The Hill Foam material model was chosen from the Ls-Dyna material library to define these insole and midsole materials. This is a suitable material model for highly compressible materials. The strain energy function of this kind of material model is expressed by the following equation.

$$W = \sum_{j=1}^{m} \frac{C_j}{b_j}\left[\lambda_1^{b_j} + \lambda_2^{b_j} + \lambda_3^{b_j} - 3 + \frac{1}{n}(J^{-nb_j} - 1)\right] \quad (7.7)$$

Where C_j, b_j and n indicate material parameters, λ_i are the principal stretches, m is order and $J= \lambda_1 \lambda_2 \lambda_3$ represents the volume ratio of the deformed to the unreformed state. The material parameters for Poron Cushioning, PPT Regular, Microcell Puff, Plastazote Firm, Crepe Firm and Cork obtained from literature are listed in Table 7.8 (132).

Table 7.8: Insole and midsole material parameters

Material	Mass density (g/mm^3)	n (-)	C_1 (MPa)	b_1 (-)
Porone Cushioning	2.4×10^{-4}	0.040	0.036	34.46
PPT Regular	1.7×10^{-4}	0.045	0.052	30.49
Microcel Puff	1.25×10^{-4}	0.061	0.095	28.14
Plastazote Firm	0.7×10^{-4}	0.067	0.073	25.91
Crepe Firm	2.6×10^{-4}	0.091	0.079	27.62
Cork	6.4×10^{-4}	0.170	0.187	21.83

To provide baseline data, the responses of the heel pad in barefoot condition (without insole or midsole) were initially investigated. The ground was modelled as a rigid 2mm thick material, moving towards the hyperelastic model at constant velocity of 5mm/s to apply load to the heel pad at nearly static condition (Figure 7.27). The friction coefficient of 0.6 was used

for foot-ground interface. The reaction of the heel pad was recorded under 160N (total displacement was 4.6mm). This load was about ¼ body weight of the subject whose foot model was generated. The maximum compressive stress and peak plantar pressure of the heel pad were recorded as results of the barefoot condition to be compared with results of other condition with insole and midsole.

Then the ground model was moved away from the heel pad model and the flat insole and midsole, bonded together, were inserted in this space, attached to the ground (Figure 7.27). The friction coefficient of 0.6 was set to skin-insole interface. The ground was moved in inferior-superior direction until 160N was applied to the heel pad. The maximum compressive stress for 9 trials at different combination of insole and midsole were recorded. The optimum level of each design factor that had the maximum effect on reduction of the compressive stress was identified. Finally, the FE model with optimum combination of insole and midsole was developed and its responses were compared with results of barefoot condition.

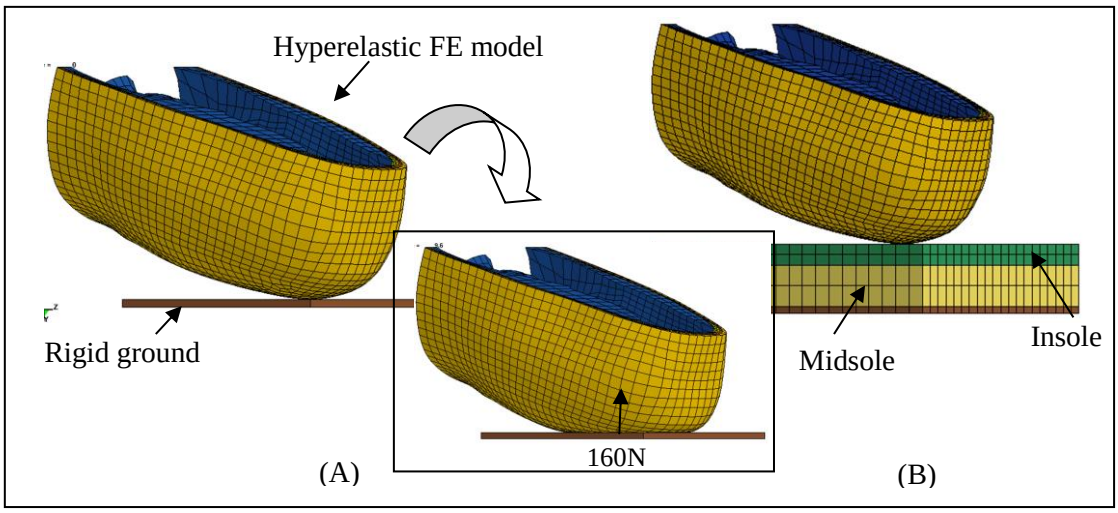

Figure 7.27: FE model of the heel pad at different conditions: (A) Barefoot condition; (B) Condition with insole, midsole and ground support.

- **Results**

The predicted maximum compressive stress of the heel pad obtained for 9 different combinations of the insole and midsole are listed in Table 7.9. The overall mean of the maximum compressive stress is 0.219MPa. The compressive stress averages of each design factor level are provided in Table 7.10 as the separate effect of each design factor level. These separate effects are plotted in Figure 7.28.

Table 7.9: L_9 orthogonal array table and the FE predicted results. Numbers under design factors indicate the levels of each design factor (Table 7.7).

Trial	Design factors				Maximum compressive stress (MPa)
	Insole thickness	Midsole thickness	Insole material	Midsole material	
1	1	1	1	1	0.218
2	1	2	2	2	0.221
3	1	3	3	3	0.245
4	2	1	2	3	0.223
5	2	2	3	1	0.219
6	2	3	1	2	0.207
7	3	1	3	2	0.225
8	3	2	1	3	0.213
9	3	3	2	1	0.206

Table 7.10: Response table of different factor levels

Levels	Average of compressive stress (MPa)			
	Insole thickness	Midsole thickness	Insole material	Midsole material
1	0.228	0.222	0.212	0.214
2	0.216	0.218	0.217	0.217
3	0.215	0.219	0.230	0.227

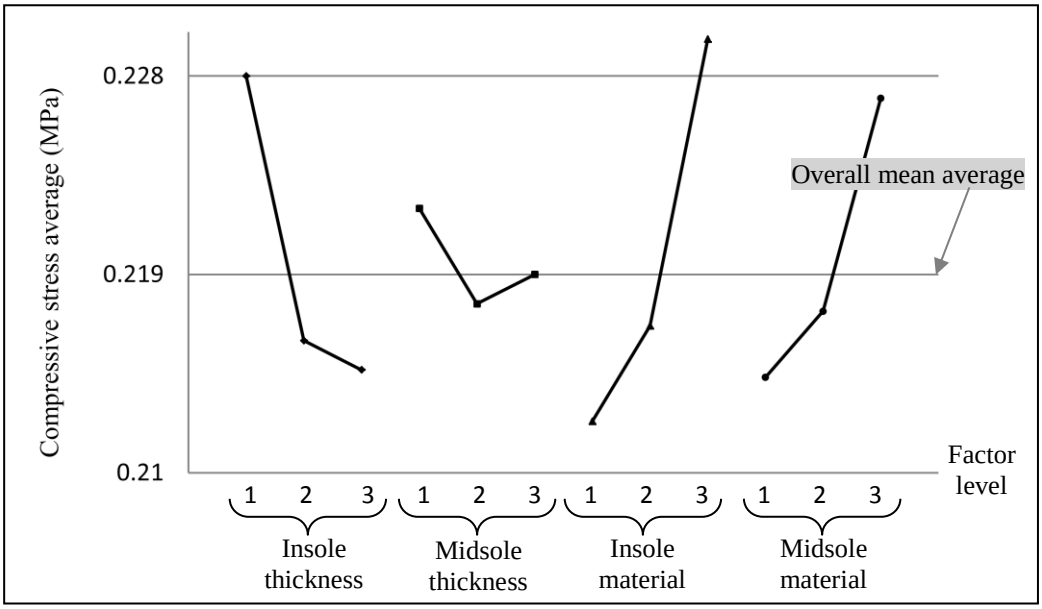

Figure 7.28: Response graph of design factors (Mean analysis)

In this study, the optimum level of each design factor is the level, which provides the minimum value of the mean effect. Therefore, according to Figure 7.28, the 6mm insole thickness (level 3), 8mm midsole thickness (level 2), Poron Cushioning as insole material (level 1), and Plastazote Firm as midsole material (level 1) were the optimum settings. The sensitivity of each design factor was calculated and provided in Table 7.11.

Table 7.11: The sensitivity of different design factors. Values in parenthesis represent the percentage of contribution.

	Design factor			
	Insole thickness	Midsole thickness	Insole material	Midsole material
Sensitivity of design factor (MPa^2)	1.1×10^{-4} (29.30%)	0.098×10^{-4} (2.68%)	1.6×10^{-4} (44.21%)	0.87×10^{-4} (23.81%)

Among the 4 design factors, the choice of insole material had the most effect on the stress reduction with 44.21% contribution. By softening the insole material, the compressive stress

was decreased. The insole thickness and midsole material were the next subsequent effective factors contributing to stress reduction (29.30 and 23.81% respectively). A reduction in compressive stress was observed by increasing the insole thickness from 2 to 6mm. A decrease in the stiffness of the midsole material reduced compressive stress. Although effect of varying midsole thickness was small on the stress reduction, the results showed that by increasing the midsole thickness from 8 to 12mm the stress slightly increased.

Responses of the FE model with optimum combination of insole and midsole (6mm insole thickness, 8mm midsole thickness, Poron cushioning for insole material and Plastazote Firm for midsole material) were compared with the barefoot condition (Figure 7.29). From the barefoot condition to the optimum condition, the external plantar pressure and maximum compressive stress were reduced by 0.062MPa (48.1% maximum pressure) and 0.081MPa (29.6% maximum compressive stress) respectively. The maximum deformation of the heel pad in inferior-superior direction was also reduced from 4.6mm for the barefoot to 3.5mm for the optimum condition.

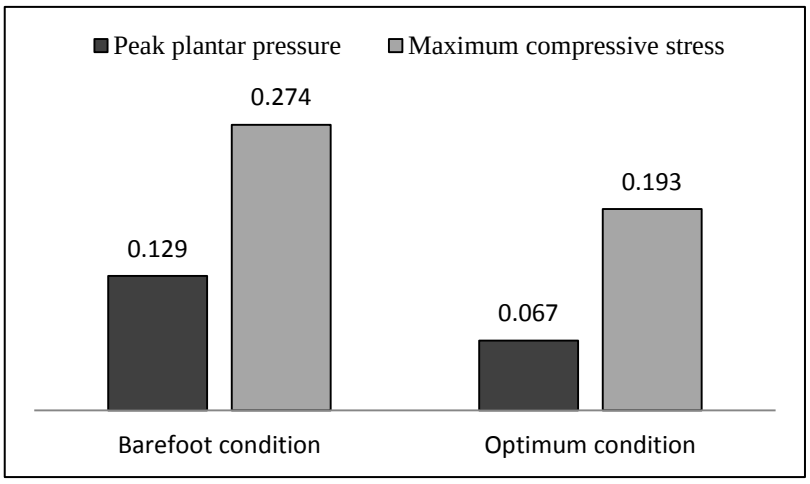

Figure 7.29: Difference between peak plantar pressure and maximum internal compressive stress for bare foot and optimum conditions. Values are in MPa.

The reduction in the plantar pressure can be explained by a possible reason. Using the softer insole increases the contact area, which is the principle cause of pressure reduction. The

contact area increased from approximately 1295mm^2 for the barefoot condition to approximately 2147mm^2 for the optimum condition. The reduction in the internal stress might because of the soft insole that deforms more easily to envelop the heel pad; therefore, restricts the excessive expansion of the heel pad in medial-lateral direction and deformation of the heel pad in superior direction (4.6mm heel pad deformation for the barefoot to 3.5mm for the optimum condition). It was expected for the maximum compressive stress measured in the optimum condition (0.193MPa) to be less than those measured in other combinations in 9 trials (Table 7.9).

According to Figure 7.29, the internal compressive stress is greater than the external pressure and there is not any constant relationship between them. The results of two studies in the literature demonstrated that the compressive internal stress is greater than the external pressure. One of them found the internal compressive stress of the foot to be site-dependent and 1.5-4.5 times greater than the external pressure. They were interested in the forefoot area (133). The other one indicated that the loading rate and sole angle affect the relationship between the internal stress and plantar pressure (125). From the barefoot condition to the optimum condition, the plantar pressure was more affected than the internal stress (Figure 7.29). Therefore, only using plantar pressure measurement to evaluate the effect of the combination of insole and midsole on heel behaviour might not be sufficient when designing footwear for pain relief is the main purpose. The stress distribution and deformation of the heel pad in both conditions are shown in Figures 7.30, 7.31, and 7.32.

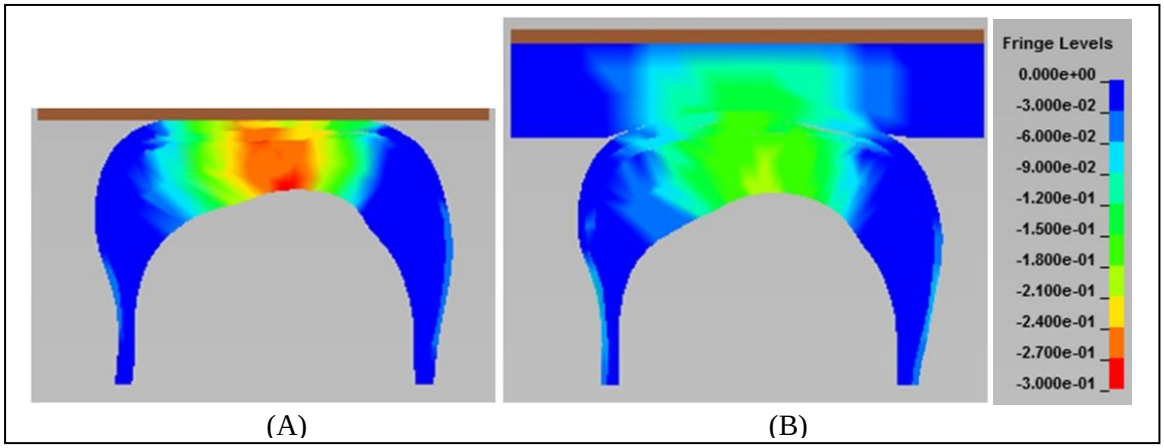

Figure 7.30: Distribution of compressive stress: (A) Bare foot condition; (B) optimum condition. Values are in MPa.

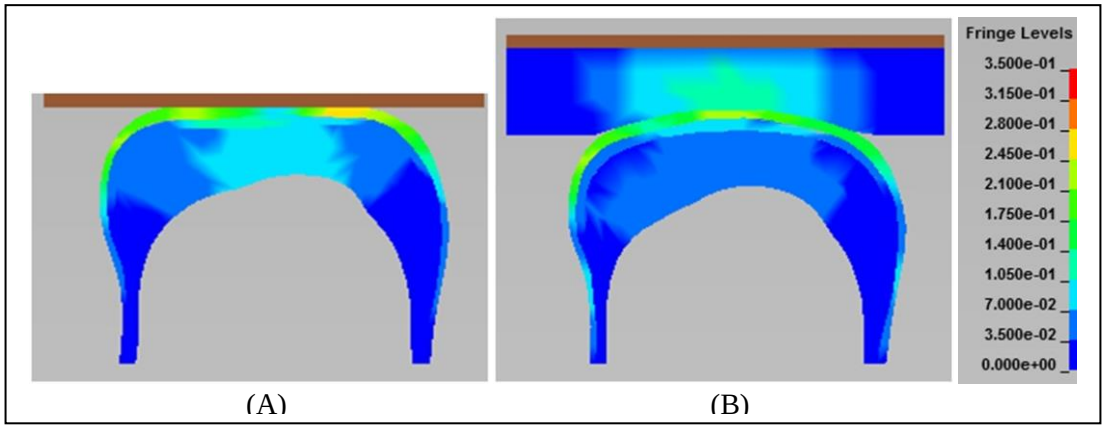

Figure 7.31: Von-Misses stress: (A) Bare foot condition; (B) Optimum condition. Values are in MPa.

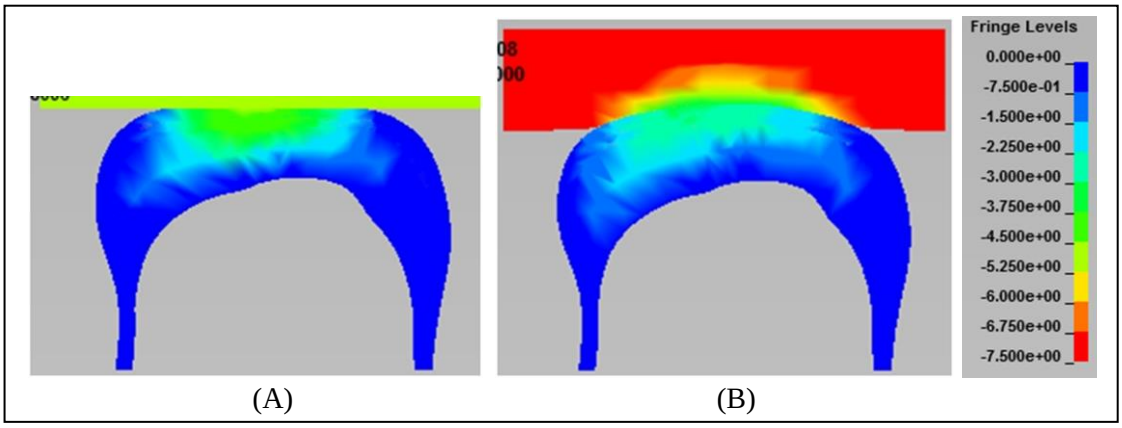

Figure 7.32: Displacement in inferior-superior direction: (A) Bare foot condition; (B) Optimum condition. Values are in MPa.

It was observed in all tests that the maximum compressive stress occurred at nodes representing calcaneus interface in the middle of the heel pad where the heel pad is thinnest (Figure 7.30) whereas, the maximum von Misses stress propagated in the skin layer (Figure 7.31). This was perhaps due to high tensile stress in the skin layer. From the results, it is clear that by using an appropriate combination of insole and midsole, the internal stress and plantar pressure can be modified.

Increasingly, FE models of the human foot have been used to identify the effects of footwear design factors on foot behaviours. Design factors such as the insole shape (e.g. flat and custom insole), insole and midsole thickness and insole and midsole material were of interest to most studies. The insole shape showed to have the most influence in reducing the plantar pressure and maximum stress with the full contact insole having the highest contribution (74, 77, 88). A study reported the greatest reduction in the maximum stress between 79-92% for a custom designed insole with non-friction and full friction contact, respectively (77), whereas another one demonstrated 24-40% relief in pressure for flat and full conforming insoles, respectively (88). The softer insole material was also found to be effective in the plantar pressure and stress relief with 35.75% contribution in pressure reduction (74, 77). Various results provided by different studies depend on the loading, material and geometry of the insole and midsole. Most studies investigated the effects of different design factors separately and none of them compared the results of the optimum condition with the barefoot condition. In this study, a comparison between the results of the optimum condition for the particular levels of design factors, used in this study, and barefoot condition showed a reduction of 48.1 and 29.5% in plantar pressure and compressive stress, respectively.

These results obtained for only hyperelastic characteristics of the heel under low loading velocity. Further investigations on identifying the effects of different design factors on viscoelastic behaviour of the heel pad under high loading velocity will provide valuable

information. For this study, the insole and midsole were modelled bonded together, simplifying the contact between them. The material used for the insole and midsole modelling were those usually used in the footwear industry and selected from the literature, so their stiffness were not systematically different. The predicted results are valid for the particular levels of the design factors and by changing them, different results might be obtained. For example, using different materials for insole or midsole with higher difference in their stiffness, their contributions and consequently the contributions of the insole and midsole thickness on the stress reduction might change. Because of observation of the small changes in the effect of the midsole thickness on the stress from 8 to 12mm, more investigations are required to ensure about this effect.

7.4 CONCLUSIONS

A wide range of responses were reported for the heel pad in different studies perhaps because of variations in testing techniques and subjects heel geometry and material properties. The first section was divided into two case studies. For the first case study, the FE model was used to investigate the effects of different experimental setup such as indenter size and shape, position of the indenter under the heel pad and loading velocity, and heel geometry on the mechanical heel pad responses.

Results showed that the size of indenter affects the force-displacement and force-strain responses of the heel pad. The larger the size of the indenter, the more contact force was reported. The shape of the indenter was also influential in the contact force and the internal stress: with a flat indenter inducing more force to the heel pad for the same indentation depth than a spherical indenter. A small flat indenter caused stress concentration in the heel pad around the indenter edges which resulted in variation in the stress inside the tissue. The results also revealed that the position of small indenter under the heel affect the heel pad responses. It

was due to changes of the heel pad thickness (existence of cushioning material) through different portions of the heel pad. Due to the viscoelastic characteristics of the heel pad sub-layers, hysteresis occurred in loading-unloading cycle and the contact force was increased by raising the loading velocity. A diminishing trend was observed in the increase of peak force with increase in velocity.

Evaluation of the effect of heel geometry showed that the thickness of the heel pad affects the stress and contact force. More force was required to achieve a specific displacement of the thinner heel pad compared to the thicker heel. The heel width was found to influence the contact force but when the large indenter (larger than the heel width) was used due to changes in the contact area.

Further findings were that the stress-strain relation could better present the behaviour of the heel pad than force-displacement/strain relationships since it is less affected by the test setup and heel geometry. When it is not possible to generate the stress-strain responses of the heel pad, force-strain is suggested. To eliminate the issue of stress concentration around the indenter edges caused by using small indenter, and also obtaining the heel pad behaviour during gait and standing situation when the heel pad is compressed by a large surface, using a large indenter is suggested. Moreover, to overcome effect of the maximum heel width on the heel pad responses when using a large indenter, measurement of the applied force by a small load cell accommodated inside the large indenter is recommended.

Throughout obtaining a series of consistent experimental data, experimental setups such as the indenter size and shape, position of the load cell and the loading velocity should be kept constant and to compare predicted or experimental results with those available in the literature, testing techniques and heel geometry should be considered carefully. The findings

of these studies might provide guidelines for researchers who are interested in studying the heel pad mechanical behaviour.

For the second case study, the capability of the FE model to estimate the material properties of another heel pad with different geometry was assessed. The response of the heel pad and its sub-layers of a second subject were obtained under loading at 5mm/s. The experimental data were used as input to inverse FEA to determine the material properties of the heel pad sub-Layers of **Subject 2** using the FE model developed based on geometry of the heel of **Subject 1**. Since the thickness of the heel pad sub-layers were not proportional to the corresponding layers in the FE model, mathematically it was not possible to reproduce the displacements reported for the experimental results in the FE model sub-layers. A comparison between the experimental and FE predictions revealed high error (26% maximum strain). This result was obtained based on study of only one other heel with different geometry than the FE model. Further investigation is required to examine the effect of the heel and calcaneus shape on the results. Up to this point, it is recommended not to use a FE model developed based on subject specific heel pad geometries for other heel pads with different.

In second section of this chapter, the influences of different design factors (insole and midsole thickness and insole and midsole material) on compressive stress were investigated. The Taguchi method was used with FE modeling to predict the optimum combination of insole and midsole with minimum simulation. For the particular levels of the design factors used in this study, the choice of insole material was found to be the most effective factor in stress with a 44.21% contribution. The insole thickness and midsole material were next most effective factors. A comparison of the results of optimum condition (with optimum combination of insole and midsole) and barefoot condition (without insole and midsole) revealed that the peak plantar pressure, maximum compressive stress and maximum displacement are reduced by 48.1%, 29.6% and 22.8% in the optimum condition.

Since no constant relationship could be found between the plantar pressure and the compressive stress, using only the plantar pressure measurement as a guide for footwear design might not be adequate. The FE prediction not only could provide information about the plantar pressure and overall displacement but also could report the distribution of the displacement and stress inside the heel pad tissue which could not be appropriately investigated by experiments.

The findings were obtained for the hyperelastic behaviour of the heel pad under ¼ body weight (160N) and they might be unique to these situations. In future studies the effects of the footwear design factors under rapid compression up to higher loadings can be investigated. Also understanding the influence of more effective footwear design factors such as insole conformity and incorporation of sidewalls of footwear seems interesting.

8. Chapter Eight:

CONCLUSIONS AND FUTURE WORK

Several studies have been conducted in the literature to investigate the biomechanical behaviour of the heel pad under loading. In most cases, although the human heel pad showed viscoelastic characteristics, only its nonlinear elastic behaviour was determined and it was assumed a homogeneous single layer material. Since the heel pad was studied using various methods with diverse heel geometry and experimental setup conditions, different biomechanical behaviours were determined for the heel pad.

In recent years, combined experimental and FEA methods have been used to study the mechanical properties of the human heel pad. Major issues of these FE models were the use of **simplified models** to simulate experiments, such as the use of hyperelastic material models to describe viscoelastic behaviour, ignoring experimental conditions and limiting models to 2D behaviour. Furthermore, the influence of the **sub-layers and geometry** of the different parts of the heel area on the biomechanical response were not considered. Some of these models were developed based on experimental results obtained from cadaveric tissue samples or at conditions which do not replicate the heel pad behaviour during gait (e.g. using a small indenter to compress the heel pad).

The aim of this project was to address these issues and limitations in the previous works and use a combined experimental and numerical method to develop a heel region model that can adequately represent *in-vivo* properties of the heel pad. Therefore, an anatomically detailed 3D model of the human heel area was developed based on unloaded MRI scan data of a heel region of a female volunteer. To address issues from some prior research, all boundary effects and confinements from surrounding tissues were represented and the heel pad was modeled as a composite three-layer material composing of the "**macro-chamber**", "**micro-chamber**" and "**skin**".

A combined ultrasound and controlled compression device was used to obtain the force-strain responses of the heel pad and its sub-layers during loading and unloading conditions *in-vivo*. A large indenter (150mm diameter) was used to compress the heel pad during physical testing to reproduce the contact between the heel and the ground or inside of the shoe, while a load cell (20mm diameter) at the centre of the indenter recorded the load experienced by the heel pad. The ultrasound system was used to simultaneously track and record the deformations of not only the heel pad but also its internal components.

Series of slow compression tests at constant speed of 5mm/s and rapid compression tests at 225mm/s were designed to obtain the hyperelastic and viscoelastic force-strain responses of the heel pad and its sub-layers respectively. These data were used as inputs to inverse FEA to estimate the hyperelastic and viscoelastic material properties of the heel pad sub-layers using the FE model. The loaded thickness of the heel pad, derived from MRI data when the foot was loaded was used as the first method to validate the hyperelastic FE model. For the second validation method, the predicted peak plantar pressure was compared with Pedar pressure measurements. The force-strain responses of the heel pad under rapid compression tests at constant velocities of 141mm/s and sinusoidal loading (maximum force 300mm/s) were used to validate the viscoelastic FE model. More validation was performed using the force-strain responses of the heel pad at 225mm/s with different maximum strains.

A total 115 iterations were required to estimate the final hyperelastic material properties of the macro-chamber, micro-chamber and skin layers. A comparison between the predicted and experimental results revealed that the hyperelastic FE model was successful in matching the heel pad loaded thickness to the MRI data with error of almost 7% maximum loaded thickness. The result of the second validation method revealed 6% maximum peak plantar pressure difference between predicted and experimental measurements. The errors propagated

during the estimation of material properties for macro-chamber, micro-chamber and skin layers and also the Pedar system force measurement might be the sources of this error.

Estimates of the viscoelastic parameters of the heel pad sub-layers were obtained after 87 iterations. The maximum difference between the force-strain experimental data and the predicted results were during the loading period. While the heel pad and its sub-layers showed nonlinear behaviour under rapid compression test, the overstress element of the Ogden material model predicted linear responses. Estimates for the viscoelastic material properties of the heel pad sub-layers obtained with RMS errors of 17.1 and 1.8% maximum force for loading and unloading periods respectively and there was a 0.54N difference between peak forces.

The viscoelastic FE model could predict the behaviour of the heel pad under compression test at 141mm/s with RMS errors of 14.3% (SD 0.3) and 3.2% (SD 1.2) for loading and unloading periods respectively and 1.1N (SD 0.57) difference between peak forces. The errors are comparable to those obtained during estimation of the viscoelastic properties while similarly the maximum difference occurred during the loading period. The viscoelastic FE model simulated the behaviour of the heel pad under sinusoidal loading with RMS errors of 6.9% (SD 1.5) and 4.6% (SD 1.1) for the loading and unloading periods. The results of validation of the FE model to compression tests at 225mm/s with different maximum strains showed RMS errors of 16.6% (SD 0.8) and 3.2% (SD 1.1) for the heel pad during the loading and unloading periods, respectively. A 3.9N (SD 2.6) difference was found between peak forces. A comparison between the results of sinusoidal loading with those obtained from constant loadings revealed that using only one loading scenario cannot evaluate the performance of the viscoelastic FE model.

The hyperelastic and viscoelastic FE models were used to show some functionality of the FE models of the heel pad in foot and footwear research. First the FE models were used to investigate the effects of the experimental setup conditions and the heel pad geometry on the biomechanical response of the heel pad. The results showed that indenter size and shape, its location under the heel and the loading velocity and heel pad geometry (heel pad thickness, heel width) can affect the internal stress, force-strain and force-displacement responses of the heel pad at different conditions.

Then, the hyperelastic FE model was used to evaluate the robustness of the FE model in estimation of the hyperelastic material properties of the heel pad sub-layers of another foot. The results revealed that the hyperelastic FE model could simulate the behaviour of the other heel with error of 26% maximum strain. This high error might be due to effect of the calcaneus shape and geometry and also difference between the thickness of the heel pad sub-layers of the other subject and the corresponding layers in the FE model. The errors propagated during material properties estimation might be another source of the high error.

Finally the hyperelastic FE model was used with the Taguchi method to investigate the effects of footwear design factors such as the material stiffness and thickness of insole and midsole on the compressive stress inside the heel tissue. The insole material showed to be the most effective design factor in stress reduction. The optimum combination of design factors was determined using the Taguchi method and compressive stress in the FE model compared to barefoot. The results revealed that the peak plantar pressure and the maximum compressive stress could be reduced by 48.1% and 29.6% respectively using optimum insole and midsole combinations.

In conclusion this project was successful in estimation of the hyperelastic and viscoelastic material properties of the macro-chamber, micro-chamber and skin layers. Inverse FEA

method was used to determine the material properties using anatomically detailed FE model of the heel area and *in-vivo* experimental data. Using the FE model, developed based on the MRI data of the subject who participated in the experiments, allowed for consideration of the effects of the heel pad sub-layers geometry and the calcaneus shape on the material properties estimation. The experimental data were obtained at the condition that the heel experiences during gait or standing. However, this study has some limitations as follows.

1. The hyperelastic and viscoelastic material properties were obtained for specific heel pad sub-layers. Therefore, all findings obtained in this study might be unique to the properties of this particular heel.
2. All results were obtained for only compression loading condition in the absence of the shear loading.
3. The determination of the material properties was performed based on iterative curve fitting rule derived for this project. Not using an algorithm for this process made it difficult to repeat and might increase the error.
4. Since only a part of the foot (heel region) was modeled in this project, the model developed in this project can only be used to investigate the behaviour of the heel area and also effects of heel part of insole and footwear on the rear foot area.
5. Effort was taken to create accurate detailed model of the heel region. However, because of manual intervention during segmentation and solid modeling, some differences between the model and real geometry might still exist.
6. Three heel pad sub-layers (macro-chamber, micro-chamber and skin) were considered to be bonded together without any shear contact between them.
7. The viscoelastic material properties of the heel pad sub-layers were estimated with RMS error 17.1% during loading period. The viscoelastic Ogden material model in

Ls-Dyna could not simulate the heel pad behaviour under constant rapid loading very accurately.

8. Based on literature, the heel skin, macro and micro-chambers should have different viscoelastic characteristics related to their amount of fluid contents. For example, since the water content of skin layer is less than macro and micro-chamber layers, it decays more slowly. However, for simplicity an identical decay constant was selected for all three heel pad sub-layers.
9. The combination of the insole and midsole were modelled as a simple structure than in reality. They were modelled as a flat structure and the contact between them was not considered.

The FE model has reasonable potential in the investigation of the heel pad behaviour through different loading conditions. The followings are potential further studies.

1. Improved properties

In this study the skin layer was modelled as a hyper viscoelastic material with the same decay constant as the macro-chamber and micro-chamber layers. In future study the skin layer can be modelled as hyperelastic material and compare heel pad responses with those obtained for viscoelastic skin. The purpose of this future study is to estimate more appropriate material properties for the skin layer leading to more accurately simulation of this layer behaviour. The precise FE model of the skin layer is important for investigation of some medical conditions such as heel ulcers.

Furthermore, it is suggested to use an optimization algorithm to iteratively solve the nonlinear RMS minimization problem in future study. Prior to use of an optimization algorithm, the suitability of it for determination of the material properties of more than one-layer tissue with two unknown parameters for each layer should be investigated. In this process, in addition to

RMS error, the difference between maximum strain and maximum force should be minimized as objective functions.

2. Further use to investigate the heel pad material stiffness and geometry

Since in this study the heel pad was designed as a composite three-layer material, by softening and stiffening of the material properties of each layer, it is possible to better understand the heel pad sub-layers functionalities and evaluate their variations effects on the heel pad behaviour. Therefore the biomechanical behaviour of the heel pad at different age or medical conditions can be better explained. The findings of this future study may be useful in preventing heel problems.

In future study the purpose is to use viscoelastic FE model to perform more investigation about geometrical effects on biomechanical behaviour of the heel pad. Investigation of the variation in factors such as the angle of rotation of the heel pad, the coefficient of friction, loading velocity may assist identifying the relationship between these factors and the plantar pressure and internal stresses experience by the heel.

3. Future use to investigate insoles/footwear

In this study, some of the FE model applications on studying the effects of the footwear design factors on the stress reduction in the heel pad were investigated. The results were obtained only under slow compression up to ¼ of body weight. In future studies the viscoelastic FE model can be used to study more effects of insoles/footwear on the heel area behaviour under rapid and higher loading. Furthermore, more realistic geometry of the insoles/footwear is developed to gain better understanding of the interactions between the heel and the insoles/footwear. The geometry development can include modeling sidewalls of footwear, conformity of the insole and contact between insole and midsole. This information is valuable in footwear design especially when heel pain relief is the main purpose.

APPENDIX A

This appendix include the process of the creation of the lofted surfaces representing the inner boundary of the micro-chamber layer, the outer boundary of the stiff tissue and muscle tissue and the interface between the plantar fascia and macro-chamber layer. These continuous smooth lofted surfaces were placed in the remaining part-1 (heel model without skin layer) subsequently and split it into five new solid parts. The process of separation of each structure from the remaining part-1 is also explained in detail in this Appendix.

After separation of the skin layer from the whole heel region solid model, it was time to separate the micro-chamber from the remaining part-1. For this task, a lofted surface representing the interface between micro-chamber and surrounding tissues was required. Therefore, the surface model of the micro-chamber layer generated in the ScanIP was imported into SolidWorks with STL format. The loft surface feature was then used to create the lofted splitting surface. Using the same iterative approach 10 profiles and 4 guide curves were required to generate the lofted surface representing the inner boundary of the micro-chamber layer so that the minimum difference targets were met (explained in Chapter 3). This smooth surface is shown in Figure A.1.

The continuous smooth lofted surface of the inner boundary of the micro-chamber layer was then placed in the remaining part-1 and split it into two new solid parts. The outer part was saved as the solid model of the micro-chamber layer and the inner part was called the "remaining part-2". The macro-chamber, plantar fascia, muscle and stiff tissue were still included in the remaining part-2. This process and two generated parts are shown in Figure A.2.

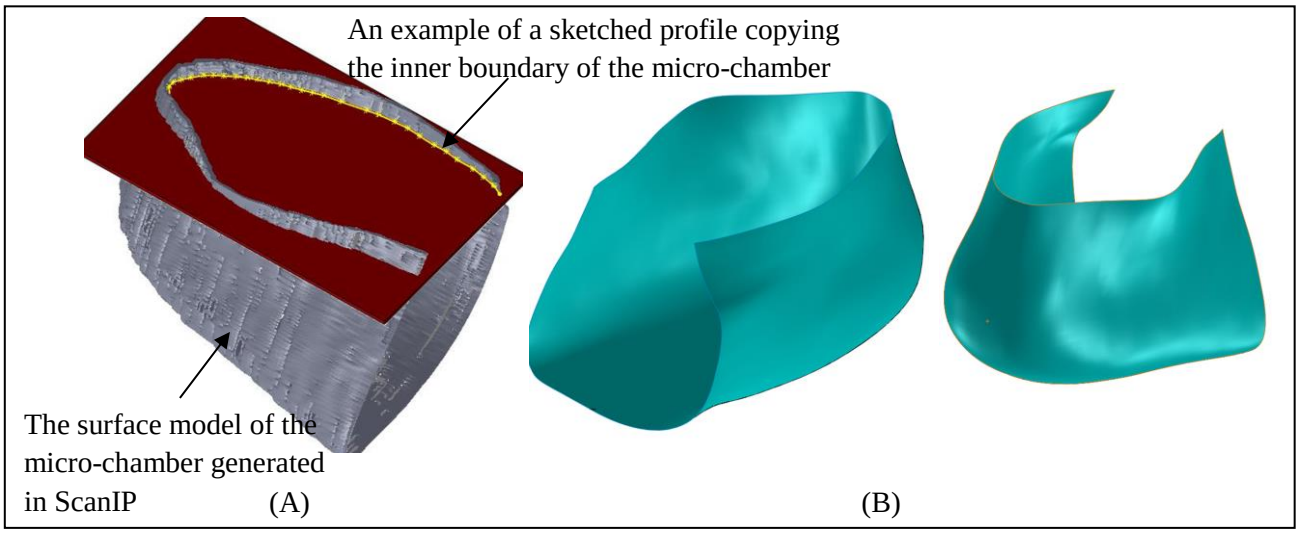

Figure A.1: Creation of the lofted surface representing the inner boundary of the micro-chamber layer: (A) Sketching a profile; (B) Splitting lofted surface.

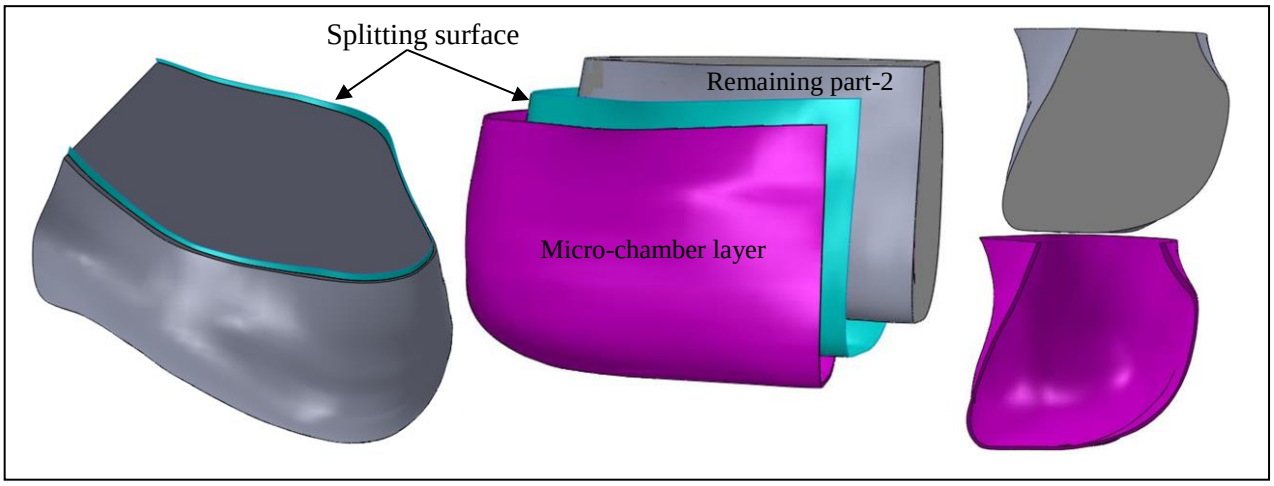

Figure A.2: Separation of the solid geometry of the micro-chamber from the heel region model.

The stiff tissue was the next part to be separated from the other remaining structures of the heel region. Hence, a lofted surface representing the interface between the stiff tissue and the surrounding tissues was required. Therefore, the surface model of the stiff tissue generated in ScanIP was imported into SolidWorks in STL format. Similar to the process used to create lofted surfaces for the skin and micro-chamber interfaces, loft surface feature in SolidWorks was used to create the desired geometry. In all, 9 profiles and 4 guide curves were required to

create the lofted surface replicating the outer boundary of the stiff tissue and with the maximum difference of 1.8mm from the surface geometry (Figure A.3).

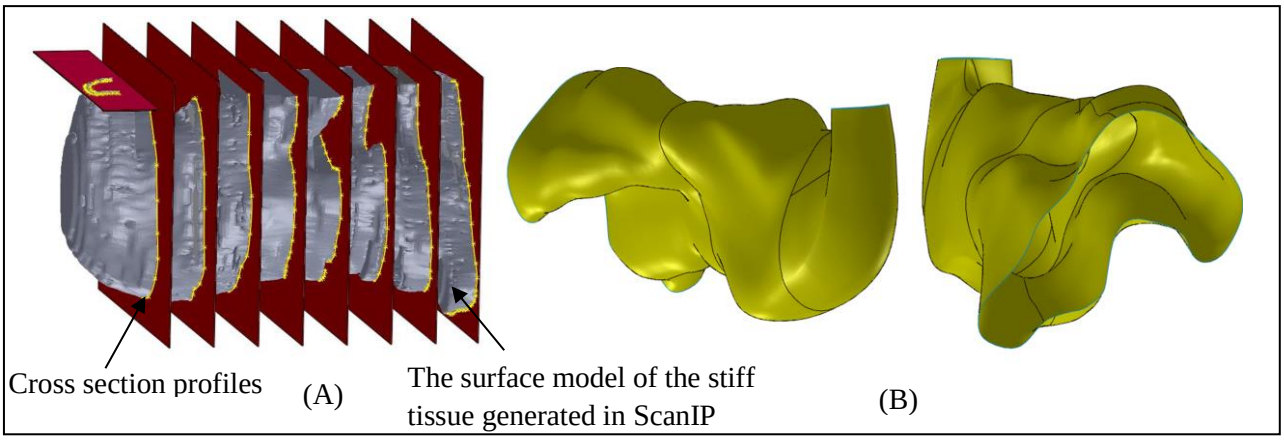

Figure A.3: Creation of the lofted surface representing the outer boundary of the stiff tissue: (A) Sketching the profiles; (B) Splitting lofted surface.

When the smooth lofted surface was constructed, it was placed in the remaining part-2 and played a role as a splitting surface to separate the stiff tissue from the remaining part-2. The separated part from the stiff tissue was called the "remaining part-3". This part was composed of the macro-chamber, the plantar fascia and the muscle tissue. The separation process and the two new parts are shown in Figure A.4.

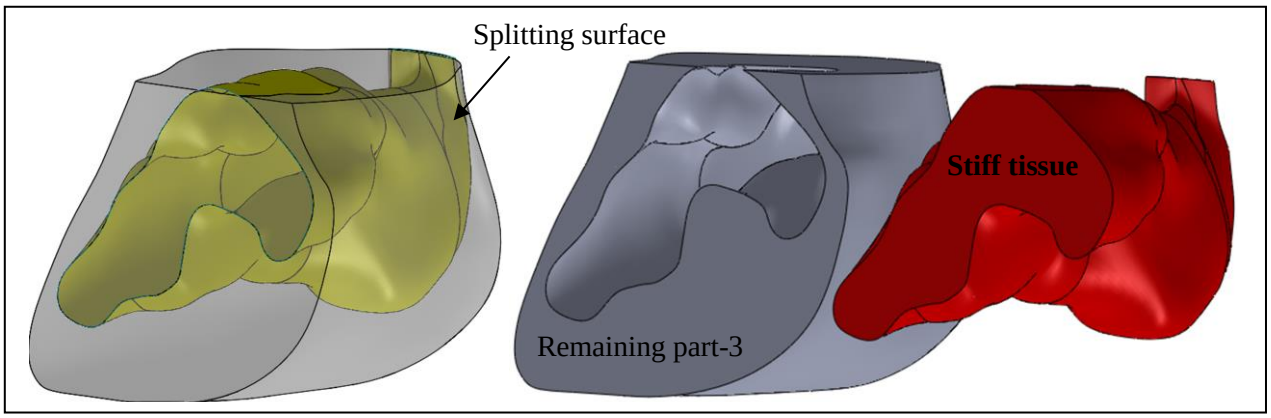

Figure A.4: Separation of the solid geometry of the stiff tissue from the remaining part of the heel region model.

In the next stage, the muscle tissue was separated from the remaining part-3. The separation process was the same as the procedure used to generate the solid model for the stiff tissue, the micro-chamber and the skin layer. This process starts with importing of the surface geometry

of the muscle tissue generated in ScanIP into SolidWorks with STL format. Then a splitting surface representing the outer boundary of the muscle tissue was developed by using the loft surface feature in SolidWorks and copying the outer boundary of the muscle tissue. 4 profiles and 10 guide curves were needed to create the splitting surface with maximum difference of 1.2mm from the surface geometry. The resulting surface is shown in Figure A.5.

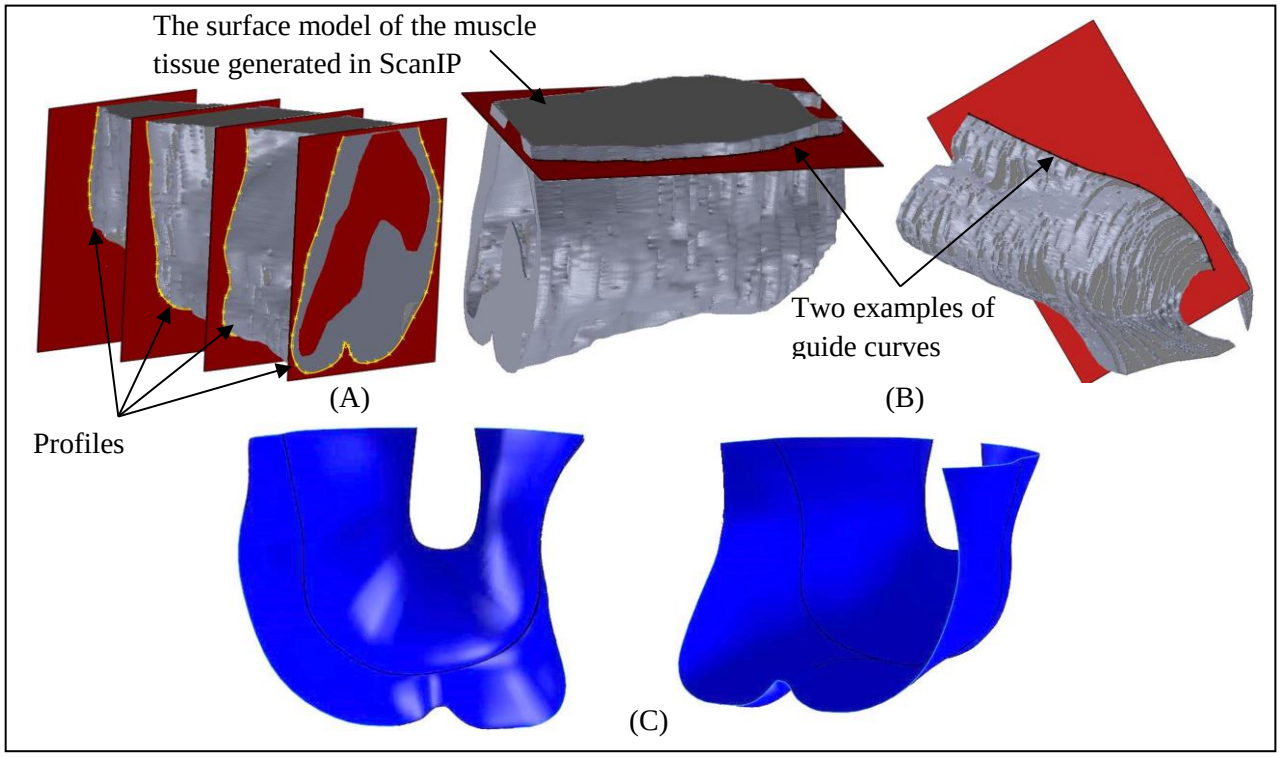

Figure A.5: Creation of the lofted surface representing the outer boundary of the muscle tissue: (A) Sketching the profiles; (B) Sketching guide curves; (C) Splitting lofted surface.

The splitting surface was placed in the remaining part-3 to scoop out the muscle from this part and two solid parts, the muscle tissue and the "remaining part-4", were created (Figure A.6). The remaining part-4 was made of the plantar fascia and the macro-chamber layer.

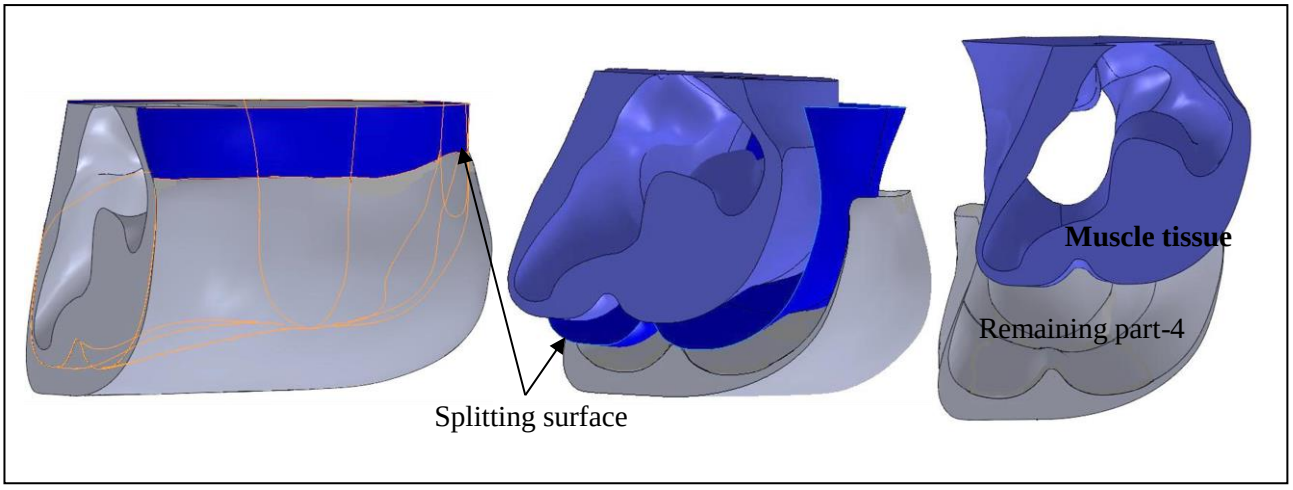

Figure A.6: Separation of the solid geometry of the muscle tissue from the remaining part of the heel region model.

At the final stage, only the plantar fascia was left to be separated from the macro-chamber layer. Therefore, a splitting lofted surface representing the interface between the plantar fascia and the macro-chamber layer was required to divide the remaining part-4 into the plantar fascia and macro-chamber layer. To generate the splitting surface, following the procedure used in the previous stages, first the surface geometry of the plantar fascia developed in ScanIP and was imported into SolidWorks in STL format. The splitting surface was then generated by making an exact copy of the outer boundary of the surface geometry of the plantar fascia using the loft surface feature. 4 profiles and 5 guide curves were needed to create the lofted surface with minimum difference from the original surface geometry to fulfil the difference investigation requirements explained in Chapter 3 (Figure A.7). The splitting surface was placed in the remaining part-4 and divided it into the plantar fascia and the macro-chamber layer. The last two solid models of the macro-chamber layer and the plantar fascia are shown in Figure A.8. These solid structures were assembled together in SolidWorks and created the whole solid geometry of the heel region (Chapter 3). The 3D solid model was used in Chapter 4 to create the FE model of the heel region.

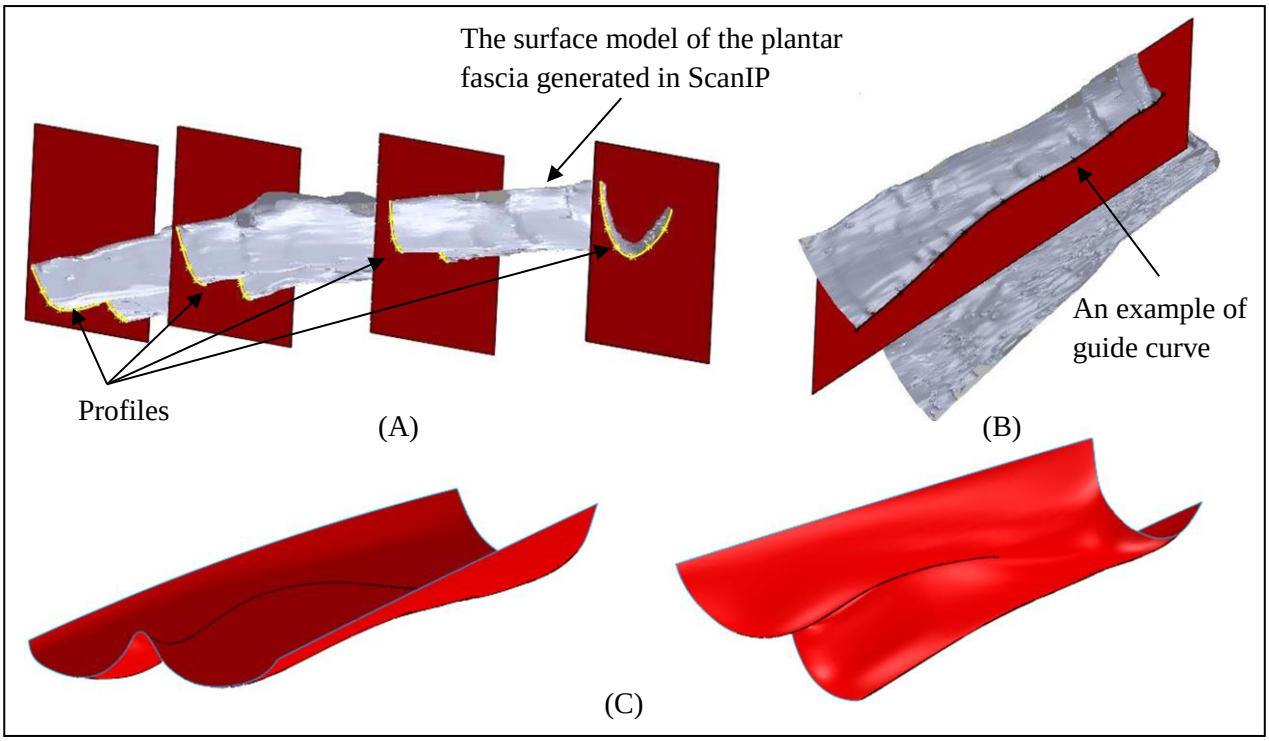

Figure A.7: Creation of the lofted surface representing interface between the plantar fascia and the macro-chamber layer: (A) Sketching profiles; (B) Sketching guide curves; (C) Splitting lofted surface.

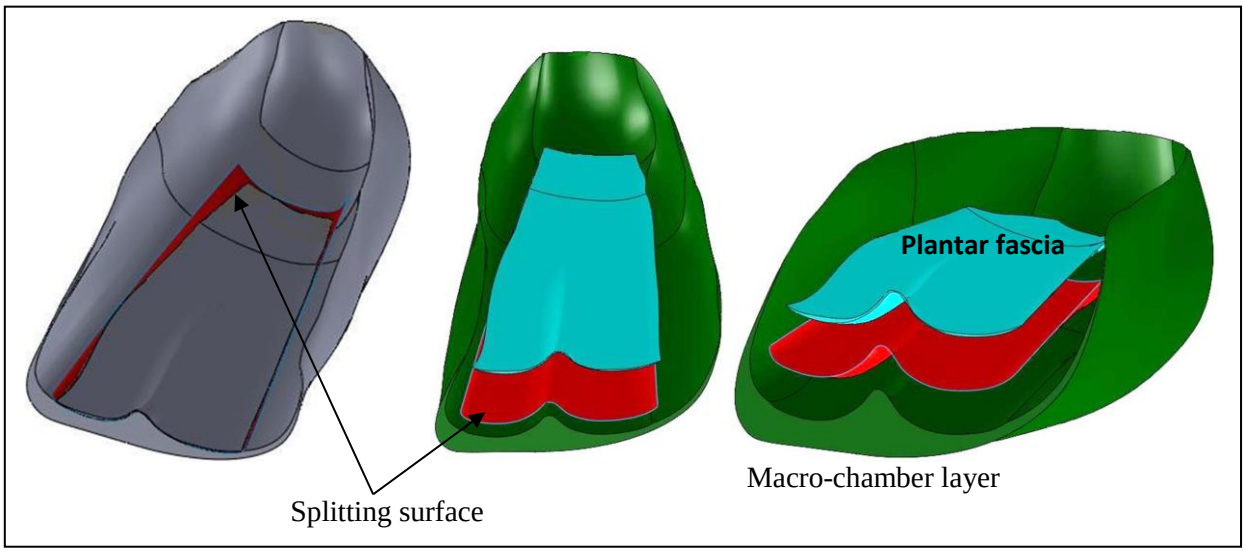

Figure A.8: Separation of the solid geometry of the plantar fascia from the macro-chamber layer.

REFERENCES

1. Zhang, W., H.Y. Chen, and G.S. Kassab, *A rate-insensitive linear viscoelastic model for soft tissues.* Biomaterials, 2007. **28**(24): p. 3579-3586.
2. Jahss, M.H., et al., *Investigations into the Fat Pads of the Sole of the Foot - Anatomy and Histology.* Foot & Ankle, 1992. **13**(5): p. 233-242.
3. Natali, A.N., C.G. Fontanella, and E.L. Carniel, *Constitutive formulation and analysis of heel pad tissues mechanics.* Medical Engineering & Physics, 2010. **32**(5): p. 516-522.
4. Hsu, C.C., et al., *Microchambers and macrochambers in heel pads: Are they functionally different?* Journal of Applied Physiology, 2007. **102**(6): p. 2227-2231.
5. Erdemir, A., et al., *An inverse finite-element model of heel-pad indentation.* Journal of Biomechanics, 2006. **39**(7): p. 1279-1286.
6. Chokhandre, S., et al., *A Three-Dimensional Inverse Finite Element Analysis of the Heel Pad.* Journal of Biomechanical Engineering-Transactions of the Asme, 2012. **134**(3).
7. Gu, Y.D., et al., *Heel skin stiffness effect on the hind foot biomechanics during heel strike.* Skin Research and Technology, 2010. **16**(3): p. 291-296.
8. Erdemir, A., et al, *Hyperelastic properties of normal and diabetic heel pads from an inverse finite element model of indentation.* 28th Annual Meeting of the American Siciety of Biomechanics 2004.
9. Verdejo, R. and N.J. Mills, *Heel--shoe interactions and the durability of EVA foam running-shoe midsoles.* Journal of Biomechanics, 2004. **37**(9): p. 1379-1386.
10. Spears, I.R. and J.E. Miller-Young, *The effect of heel-pad thickness and loading protocol on measured heel-pad stiffness and a standardized protocol for inter-subject comparability.* Clinical Biomechanics, 2006. **21**(2): p. 204-212.
11. Spears, I.R., et al., *The potential influence of the heel counter on internal stress during static standing: A combined finite element and positional MRI investigation.* Journal of Biomechanics, 2007. **40**(12): p. 2774-2780.
12. Miller-Young, J.E., N.A. Duncan, and G. Baroud, *Material properties of the human calcaneal fat pad in compression: experiment and theory.* Journal of Biomechanics, 2002. **35**(12): p. 1523-1531.
13. Ledoux, W.R. and J.J. Blevins, *The compressive material properties of the plantar soft tissue.* Journal of Biomechanics, 2007. **40**(13): p. 2975-2981.
14. Pain, M.T.G. and J.H. Challis, *The role of the heel pad and shank soft tissue during impacts: a further resolution of a paradox.* Journal of Biomechanics, 2001. **34**(3): p. 327-333.
15. Aerts, P., et al., *The mechanical properties of the human heel pad: A paradox resolved.* Journal of Biomechanics, 1995. **28**(11): p. 1299-1308.
16. Rome, K., et al., *Ultrasonic heel pad thickness measurements: a preliminary study.* British Journal of Radiology, 1998. **71**(851): p. 1149-1152.
17. Cavanagh, P.R., et al., *The relationship of static foot structure to dynamic foot function.* Journal of Biomechanics, 1997. **30**(3): p. 243-250.
18. Gooding, G.A.W., et al *Heel pad thickness: determination by high-resolution ultrasonography.* journal of Ultrasound Med, 1985. **4**: p. 173-174.
19. Levy, A.S., et al., *Magnetic-Resonance-Imaging Evaluation of Calcaneal Fat Pads in Patients with Os Calcis Fractures.* Foot & Ankle, 1992. **13**(2): p. 57-62.
20. Steinbach, H.L., and Russell, W., *Measurment of the heel-pad as an aid to diagnosis of acromegaly.* Radiology, 1964(82): p. 418-423.

21. Greene, E., *Plantar fasciitis and the plantar heel fat pad.* Austral Podiatr, 1995(12): p. 89-93.
22. Rome, K., *Mechanical properties of the heel pad: current theory and review of the litrature.* The Foot, 1998. **8**: p. 179-185.
23. Bletchschmidth, E., *The structure of the calcaneal padding.* Foot Ankle, 1982. **2**: p. 260-283.
24. Kelikian, A.S., Sarrafian, S.,, *Sarrafian's Anatomy of the Foot and Ankle: Descriptive, Topographic, Functional*. 1983.
25. Thoolen, M., T. J. Ryan, I. Bristow, *A study of the skin of the sole of the foot using high-frequency ultrasonography and histology.* The Foot, 2000. **10**: p. 14-17.
26. Hagisawa, S., Shimada, T.,, *Skin morphology and its mechanical properties assiciated with loading. In: Pressure ulcer research: Current and future perspectives.* 2005, Springer-Verlag: Berlin. p. 161-185.
27. Chao, C.Y.L., Y.P. Zheng, and G.L.Y. Cheing, *Epidermal Thickness and Biomechanical Properties of Plantar Tissues in Diabetic Foot.* Ultrasound in Medicine and Biology, 2011. **37**(7): p. 1029-1038.
28. Fung, Y.C., *Biomechanics: mechanical properties of living tissues*. 1993, New York, USA: Springer-Verlag Inc.
29. Aerts, P., et al., *The effects of isolation on the mechanics of the human heel pad.* Journal of Anatomy, 1996. **188**: p. 417-423.
30. Miller-Young, J.E., *Factors Affecting Human Heel Pad Mechanics: a Finite Element Study*, in *Mechanical Engineering*. 2003, University of Calgary.
31. Gefen, A., M. Megido-Ravid, and Y. Itzchak, *In vivo biomechanical behavior of the human heel pad during the stance phase of gait.* Journal of Biomechanics, 2001. **34**(12): p. 1661-1665.
32. Tong, J., Lim, C.S. ,Goh, O.L., *Technique to study the biomechanical properties of the human calcaneal heel pad.* The Foot, 2003. **13**: p. 83-91.
33. Hsu, C.C., et al., *Diabetic effects on microchambers and macrochambers tissue properties in human heel pads.* Clinical Biomechanics, 2009. **24**(8): p. 682-686.
34. Hsu, C.C., et al., *Effects of aging on the plantar soft tissue properties under the metatarsal heads at different impact velocities.* Ultrasound in Medicine and Biology, 2005. **31**(10): p. 1423-1429.
35. Hsu, T.C., Wang, C. L., Shau, Y. W., Tang, F.T., Li, K. L., Chen, C. Y., *Altered heel-pad mechanical properties in type 2 diabetic patients.* Diabetic Med, 2000. **17**: p. 854-859.
36. Hsu, T.C., et al., *Comparison of the mechanical properties of the heel pad between young and elderly adults.* Archives of Physical Medicine and Rehabilitation, 1998. **79**(9): p. 1101-1104.
37. Kao, P.F., B.L. Davis, and P.A. Hardy, *Characterization of the calcaneal fat pad in diabetic and nondiabetic patients using magnetic resonance imaging.* Magnetic Resonance Imaging, 1999. **17**(6): p. 851-857.
38. Hsu, T.C., Y.S. Lee, and Y.W. Shau, *Biomechanics of the heel pad for type 2 diabetic patients.* Clinical Biomechanics, 2002. **17**(4): p. 291-296.
39. Pai, S. and W.R. Ledoux, *The compressive mechanical properties of diabetic and non-diabetic plantar soft tissue.* Journal of Biomechanics, 2010. **43**(9): p. 1754-1760.
40. Buschmann, W.R., et al., *Histology and Histomorphometric Analysis of the Normal and Atrophic Heel Fat Pad.* Foot & Ankle International, 1995. **16**(5): p. 254-258.
41. Wang, C.L., et al., *Mechanical properties of heel pads reconstructed with flaps.* Journal of Bone and Joint Surgery-British Volume, 1999. **81B**(2): p. 207-211.

42. Prichasuk, S., P. Mulpruek, and P. Siriwongpairat, *The Heel-Pad Compressibility.* Clinical Orthopaedics and Related Research, 1994(300): p. 197-200.
43. Brinckmann, P., *Musculoskeletal Biomechanics*. 2002, New York: Thieme.
44. Prichasuk, S., *The Heel Pad in Plantar Heel Pain.* Journal of Bone and Joint Surgery-British Volume, 1994. **76B**(1): p. 140-142.
45. Berlowitz, D.R., Brienza, D.M., *Are all pressure ulcers the result of deep tissue injury? A review of the literaturet*. Journal of Ostomy Wound Manage, 2007. **53**(10): p. 34-38. Churchill Livingston.
46. Stekelenburg, A., Gawlitta, D., Bader, D.L., Oomens, C.W., *Deep tissue injury: how deep is our understanding?* Journal of Physical Medicine and Rehabilitation, 2008. **89**(7): p. 1410-1413.
47. Gefen, A., *The biomechanics of heel ulcers.* Journal of Tissue Viability, 2010. **19**(4): p. 124-131.
48. Le, K.M., et al., *An in-Depth Look at Pressure Sores Using Monolithic Silicon Pressure Sensors.* Plastic and Reconstructive Surgery, 1984. **74**(6): p. 745-754.
49. Brand, P.W., *The Pathomechanics of the Diabetic Neurotrophic Ulcer and Its Conservative Treatment.* Acta Orthopaedica Scandinavica, 1982. **53**(2): p. 309-309.
50. Cavanagh, P.R., et al, *Biological aspect of modelling shoe/foot interaction during running.* In Sport Shoes and Playing Surfaces, 1984: p. 24-46.
51. Aerts, P., Declercq, D.,, *Deformation characteristics of the heel region of the shod foot during a simulated heel strike: the effect of varying midsole hardness.* Journal of Sport Science, 1993. **11**: p. 449-461.
52. Kinoshita, H., et al., *In-Vivo Examination of the Dynamic Properties of the Human Heel Pad.* International Journal of Sports Medicine, 1993. **14**(6): p. 312-319.
53. Zheng, Y.P., et al., *Biomechanical assessment of plantar foot tissue in diabetic patients using an ultrasound indentation system.* Ultrasound in Medicine and Biology, 2000. **26**(3): p. 451-456.
54. Han, L.H., J.A. Noble, and M. Burcher, *A novel ultrasound indentation system for measuring biomechanical properties of in vivo soft tissue.* Ultrasound in Medicine and Biology, 2003. **29**(6): p. 813-823.
55. Nigg, B.M.D., J., *Sportplatzbelage (Playing surfaces).* Juris Verlag: Zurich, 1980.
56. Jorgensen, U., E. Larsen, and J.E. Varmarken, *The Hpc-Device - a Method to Quantify the Heel Pad Shock Absorbency.* Foot & Ankle, 1989. **10**(2): p. 93-98.
57. De Wit, B., D. De Clercq, and P. Aerts, *Biomechanical analysis of the stance phase during barefoot and shod running.* Journal of Biomechanics, 2000. **33**(3): p. 269-278.
58. Declercq, D., P. Aerts, and M. Kunnen, *The Mechanical Characteristics of the Human Heel Pad during Foot Strike in Running - an in-Vivo Cineradiographic Study.* Journal of Biomechanics, 1994. **27**(10): p. 1213-&.
59. Robbins, S.E., G.J. Gouw, and A.M. Hanna, *Running-Related Injury Prevention through Innate Impact-Moderating Behavior.* Medicine and Science in Sports and Exercise, 1989. **21**(2): p. 130-139.
60. Bennett, M.B., Ker, R. F.,, *The mechanical properties of the human subcalcaneal fat pad in compression.* Journal of Anatomy, 1990(171): p. 131-138.
61. Alcover, E.A., *Differences Between Machine and Human Testing of Shock Absorbing System,* in *Health, Biological and Enviromental Sciences*. 2000, Middlesex University: Middlesex.
62. Kuhns, J.G., *Changes in Elastic Adipose Tissue.* Journal of Bone and Joint Surgery-American Volume, 1949. **31-A**(3): p. 541-547.
63. Higa, M., et al., *Passive mechanical properties of large intestine under in vivo and in vitro compression.* Medical Engineering & Physics, 2007. **29**(8): p. 840-844.

64. Miller, K., *Constitutive model of brain tissue suitable for finite element analysis of surgical procedures.* Journal of Biomechanics, 1999. **32**(5): p. 531-537.
65. Ivanco. Vladimir. *Nonlinear Finite Element Analysis*. 2011.
66. *Understanding Nonlinear Analysis.* www.solidworks.com.
67. Bamford., D.J., *Computational Methods in Solid Mechanics.* www.mcise.uri.edu.
68. Buchler, P., et al., *A finite element model of the shoulder: application to the comparison of normal and osteoarthritic joints.* Clinical Biomechanics, 2002. **17**(9-10): p. 630-639.
69. Toosizadeh, N. and M. Haghpanahi, *Generating a finite element model of the cervical spine: Estimating muscle forces and internal loads.* Scientia Iranica, 2011. **18**(6): p. 1237-1245.
70. Schutte, S., et al., *A finite-element analysis model of orbital biomechanics.* Vision Research, 2006. **46**(11): p. 1724-1731.
71. Prendergast, P.J., Lennon, A. B.,, *An Introduction to the Workshop on Finite Element Modelling in Biomechanics and Mechanobiology*, in *Finite Element Modelling in Biomechanics and Mechanobiology*. 2007, Trinity Centre for Bioenginnering: Dublin.
72. Lemmon, D., et al., *The effect of insoles in therapeutic footwear--A finite element approach.* Journal of Biomechanics, 1997. **30**(6): p. 615-620.
73. Cheung, J.T.-M., et al., *Three-dimensional finite element analysis of the foot during standing--a material sensitivity study.* Journal of Biomechanics, 2005. **38**(5): p. 1045-1054.
74. Cheung, J.T.M. and M. Zhang, *Parametric design of pressure-relieving foot orthosis using statistics-based finite element method.* Medical Engineering & Physics, 2008. **30**(3): p. 269-277.
75. Qian, Z.H., L. Ren, and L.Q. Ren, *A Coupling Analysis of the Biomechanical Functions of Human Foot Complex during Locomotion.* Journal of Bionic Engineering, 2010. **7**: p. S150-S157.
76. Gu, Y.D., et al., *Foot contact surface effect to the metatarsals loading character during inversion landing.* International Journal for Numerical Methods in Biomedical Engineering, 2011. **27**(4): p. 476-484.
77. Luo, G.M., et al., *Finite element analysis of heel pad with insoles.* Journal of Biomechanics, 2011. **44**(8): p. 1559-1565.
78. Manschot, J.F.M. and A.J.M. Brakkee, *The Measurement and Modeling of the Mechanical-Properties of Human-Skin Invivo .1. The Measurement.* Journal of Biomechanics, 1986. **19**(7): p. 511-515.
79. Manschot, J.F.M. and A.J.M. Brakkee, *The Measurement and Modeling of the Mechanical-Properties of Human-Skin Invivo .2. The Model.* Journal of Biomechanics, 1986. **19**(7): p. 517-521.
80. Erdemir, A., et al., *An Elaborate Data Set Characterizing the Mechanical Response of the Foot.* Journal of Biomechanical Engineering-Transactions of the Asme, 2009. **131**(9).
81. Petre, M., *Investigating the Internal Stress/Strain State of the Foot Using Magnetic Resonance Imaging and Finite Element Analysis*, in *Department of Biomedical Engineering*. 2007, Case Western Reserve University.
82. Delbridge, L., et al., *The Etiology of Diabetic Neuropathic Ulceration of the Foot.* British Journal of Surgery, 1985. **72**(1): p. 1-6.
83. Tsai, W.C., et al., *The mechanical properties of the heel pad in unilateral plantar heel pain syndrome.* Foot & Ankle International, 1999. **20**(10): p. 663-668.
84. Rome, K., et al., *Reliability of weight-bearing heel pad thickness measurements by ultrasound.* Clinical Biomechanics, 1998. **13**(4-5): p. 374-375.

85. Bus, S.A., J.S. Ulbrecht, and P.R. Cavanagh, *Pressure relief and load redistribution by custom-made insoles in diabetic patients with neuropathy and foot deformity.* Clinical Biomechanics, 2004. **19**(6): p. 629-638.
86. Brown, M., S. Rudicel, and A. Esquenazi, *Measurement of dynamic pressures at the shoe-foot interface during normal walking with various foot orthoses using the FSCAN system.* Foot & Ankle International, 1996. **17**(3): p. 152-156.
87. Chen, W.P., C.W. Ju, and F.T. Tang, *Effects of total contact insoles on the plantar stress redistribution: a finite element analysis.* Clinical Biomechanics, 2003. **18**(6): p. S17-S24.
88. Goske, S., et al., *Reduction of plantar heel pressures: Insole design using finite element analysis.* Journal of Biomechanics, 2006. **39**(13): p. 2363-2370.
89. Ballinger, R. *MRI Tutor and MRI/Radiology Files*. 2009; http://www.mritutor.org/.
90. *Foundations of FMRI: How Does MRI work?* . http://people.ee.duke.edu/~jshorey/MRIHomepage/work.html].
91. Rull, G., *Magnetic Resonance Imaging.* www.patient.co.uk, 2013.
92. Laboratory, N.H.M.F. *MRI Tutorial*.
93. Hornak, J.P., *The Basics of MRI*. 2011.
94. Wieringa, H.J. and M.J. Peters, *Processing Mri Data for Electromagnetic Source Imaging.* Medical & Biological Engineering & Computing, 1993. **31**(6): p. 600-606.
95. *Segmentation*. 2010: Biomathematics & Statistics Scotland.
96. Ilic. S., U.B. *Seeded Region Growing Method for Imaging Segmentation*. 2000; Available from: www.lab.geog.ntu.edu.tw.
97. Wu, L.J., *Nonlinear finite element analysis for musculoskeletal biomechanics of medial and lateral plantar longitudinal arch of Virtual Chinese Human after plantar ligamentous structure failures.* Clinical Biomechanics, 2007. **22**(2): p. 221-229.
98. Buter. G. *Tips and Tricks for Using the Solidworks Loft Feature*. 2013; Available from: www.mcad.com.
99. Fontanella, C.G., et al., *Analysis of heel pad tissues mechanics at the heel strike in bare and shod conditions.* Medical Engineering & Physics, 2013. **35**(4): p. 441-447.
100. SIMULIA, *Abaqus 6.10-EF Documentation*. www.abaqus.ethz.ch.
101. Fontanella, C.G., et al., *Investigation on the load-displacement curves of a human healthy heel pad: In vivo compression data compared to numerical results.* Medical Engineering & Physics, 2012. **34**(9): p. 1253-1259.
102. Tao, K., et al., *An In Vivo Experimental Validation of a Computational Model of Human Foot.* Journal of Bionic Engineering, 2009. **6**(4): p. 387-397.
103. Sopher, R., et al., *The influence of foot posture, support stiffness, heel pad loading and tissue mechanical properties on biomechanical factors associated with a risk of heel ulceration.* Journal of the Mechanical Behavior of Biomedical Materials, 2011. **4**(4): p. 572-582.
104. Tadepalli, S.C., A. Erdemir, and P.R. Cavanagh, *Comparison of hexahedral and tetrahedral elements in finite element analysis of the foot and footwear.* Journal of Biomechanics, 2011. **44**(12): p. 2337-2343.
105. Bower, A.F., *Applied Mechanics of Solids*. 2010: CRC Press, Taylor & Francis Group.
106. Laursen, T.A., *Computational Contact and Impact Mechanics: Fundamentals of Modelling Interfacial Phenomena In Nonlinear Finite Element Analysis*. 2003, Berlin: Springer.
107. Bala, S., *Contact Modeling in LsDYNA*, L.S.T. Corporation, Editor. 2001.
108. Cheung, J.T.M., M. Zhang, and K.N. An, *Effects of plantar fascia stiffness on the biomechanical responses of the ankle-foot complex.* Clinical Biomechanics, 2004. **19**(8): p. 839-846.

109. Isvilanonda, V., et al., *Finite element analysis of the foot: Model validation and comparison between two common treatments of the clawed hallux deformity.* Clinical Biomechanics, 2012. **27**(8): p. 837-844.
110. Antunes, P.J., et al., *Nonlinear 3D foot FEA modelling from CT scan medical images.* Computational Vision and Medical Imaging Processing, 2008: p. 135-141.
111. Gefen, A., Megido-Ravid, M., Itzchak, Y., Arcan, M.,, *Biomechanical Evaluation of Surgical Plantar Fascia Release Effects*, in *www.content.lib.utah.edu*.
112. Wright, D.G. and D.C. Rennels, *A Study of the Elastic Properties of Plantar Fascia.* Journal of Bone and Joint Surgery-American Volume, 1964. **46**(3): p. 482-492.
113. Kitaoka, H.B., et al., *Material Properties of the Plantar Aponeurosis.* Foot & Ankle International, 1994. **15**(10): p. 557-560.
114. Gefen, A., *The in vivo elastic properties of the plantar fascia during the contact phase of walking.* Foot & Ankle International, 2003. **24**(3): p. 238-244.
115. Qiu, T.X., et al., *Finite element modeling of a 3D coupled foot-boot model.* Medical Engineering & Physics, 2011. **33**(10): p. 1228-1233.
116. Ogden, R.W., *Large Deformation Isotropic Elasticity - Correlation of Theory and Experiment for Incompressible Rubberlike Solids.* Proceedings of the Royal Society of London Series a-Mathematical and Physical Sciences, 1972. **326**(1567): p. 565-&.
117. Costin, U., Shin, Jaeho., Crandall, Jeff., Crino, Scott.,, *Development and validation of a headform impactor finite element model with application to vehicle hood design for pedestrian protection*, in *9th International LS-DYNA Users Conference*.
118. Parker, D., *Characterising the Biomechanical Properties of the Plantar Soft Tissue under the Conditions of Simulated Gait*, in *Health Sciences*. 2013, University of Salford: Salford.
119. Mori, T., Hamatani, M., Noguchi, H., Oe, M., Sanada, H.,, *Insole-Type Simultaneous Measurment System of Plantar Pressure and Shear Force During Gait for Diabetic Patients.* Journal of Robotics and Mechatronics, 2012. **24**(5): p. 766-772.
120. Ker, R.F., *The time-dependent mechanical properties of the human heel pad in the context of locomotion.* Journal of Experimental Biology, 1996. **199**(7): p. 1501-1508.
121. Ogden, R.W., *Nonlinear Elasticity, Anisotropy, Material Stability and Residual Stresses in Soft Tissue*, in *Biomechanics of Soft Tissue in Cardiovascular Systems*. 2003, Springer: University of Glasgow.
122. Kauer, M., et al., *Inverse finite element characterization of soft tissues.* Medical Image Analysis, 2002. **6**(3): p. 275-287.
123. Vogl, T.J., et al., *Mechanical Soft Tissue Property Validation in Tissue Engineering Using Magnetic Resonance Imaging: Experimental Research.* Academic Radiology, 2010. **17**(12): p. 1486-1491.
124. Makhsous, M., et al., *Finite element analysis for evaluation of pressure ulcer on the buttock: Development and validation.* Ieee Transactions on Neural Systems and Rehabilitation Engineering, 2007. **15**(4): p. 517-525.
125. Spears, I.R., et al., *The effect of loading conditions on stress in the barefooted heel pad.* Medicine and Science in Sports and Exercise, 2005. **37**(6): p. 1030-1036.
126. Matteoli, S., Fontanella, C., Virga, A., Wilhjelm, J. E., Corvi, A., Natali, A. N.,, *Mechanical behaviour of the heel pad:experimental and numerical approach*, in *GNB 2012*. 2012: Roma, Italy.
127. Hertz, H., *Uber die beruhrung fester elastischer korper (on the contact of elastic solids).* Journal of reine und angewandte Mathematik, 1882. **94**: p. 156-171.
128. Marvalova, B., *Viscoelastic properties of filled rubber. Experimental observations and material modelling.* Constitutive Models for Rubber V, 2008: p. 79-84.

129. Rome, K., et al., *Heel pad stiffness in runners with plantar heel pain.* Clinical Biomechanics, 2001. **16**(10): p. 901-905.
130. Roy, R.K., *A Primer on the Taguchi Method*. 2010: SME, Technology and Engineering.
131. Lee, W.C.C. and M. Zhang, *Design of monolimb using finite element modelling and statistics-based Taguchi method.* Clinical Biomechanics, 2005. **20**(7): p. 759-766.
132. Petre, M., Erdemir, A., Cavanagh, P. R.,, *Determination of Elastomeric Foam Parameters for Simulations of Complex Loading.* Computer Methods in Biomechanics and Biomedical Engineering, 2006. **9**(4): p. 231-242.
133. Chen, W.M., et al., *Investigation of Plantar Barefoot Pressure and Soft-tissue Internal Stress: A Three-Dimensional Finite Element Analysis.* 13th International Conference on Biomedical Engineering, Vols 1-3, 2009. **23**(1-3): p. 1817-1820.